frontiers | Research Topics

# Current research on spin glasses

**Edited by**
Stefan Boettcher, Ralph Chamberlin, Gregory Kenning and Federico Ricci-Tersenghi

**Published in**
Frontiers in Physics

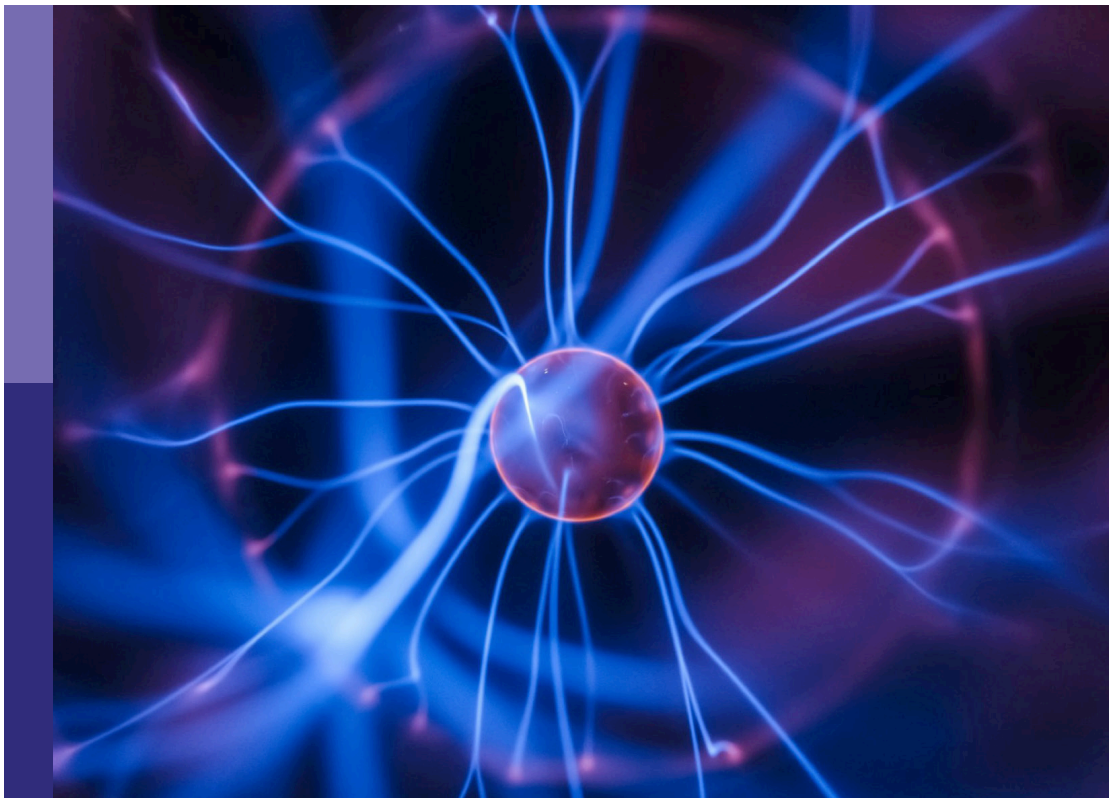

ISSN 1664-8714
ISBN 978-2-8325-6160-7
DOI 10.3389/978-2-8325-6160-7

## About Frontiers

Frontiers is more than just an open access publisher of scholarly articles: it is a pioneering approach to the world of academia, radically improving the way scholarly research is managed. The grand vision of Frontiers is a world where all people have an equal opportunity to seek, share and generate knowledge. Frontiers provides immediate and permanent online open access to all its publications, but this alone is not enough to realize our grand goals.

## Frontiers journal series

The Frontiers journal series is a multi-tier and interdisciplinary set of open-access, online journals, promising a paradigm shift from the current review, selection and dissemination processes in academic publishing. All Frontiers journals are driven by researchers for researchers; therefore, they constitute a service to the scholarly community. At the same time, the *Frontiers journal series* operates on a revolutionary invention, the tiered publishing system, initially addressing specific communities of scholars, and gradually climbing up to broader public understanding, thus serving the interests of the lay society, too.

## Dedication to quality

Each Frontiers article is a landmark of the highest quality, thanks to genuinely collaborative interactions between authors and review editors, who include some of the world's best academicians. Research must be certified by peers before entering a stream of knowledge that may eventually reach the public - and shape society; therefore, Frontiers only applies the most rigorous and unbiased reviews. Frontiers revolutionizes research publishing by freely delivering the most outstanding research, evaluated with no bias from both the academic and social point of view. By applying the most advanced information technologies, Frontiers is catapulting scholarly publishing into a new generation.

## What are Frontiers Research Topics?

Frontiers Research Topics are very popular trademarks of the *Frontiers journals series*: they are collections of at least ten articles, all centered on a particular subject. With their unique mix of varied contributions from Original Research to Review Articles, Frontiers Research Topics unify the most influential researchers, the latest key findings and historical advances in a hot research area.

Find out more on how to host your own Frontiers Research Topic or contribute to one as an author by contacting the Frontiers editorial office: frontiersin.org/about/contact

# Current research on spin glasses

**Topic editors**
Stefan Boettcher — Emory University, United States
Ralph Chamberlin — Arizona State University, United States
Gregory Kenning — Indiana University of Pennsylvania, United States
Federico Ricci-Tersenghi — Sapienza University of Rome, Italy

**Citation**
Boettcher, S., Chamberlin, R., Kenning, G., Ricci-Tersenghi, F., eds. (2025). *Current research on spin glasses*. Lausanne: Frontiers Media SA.
doi: 10.3389/978-2-8325-6160-7

*This Research Topic is dedicated to the fond memory of Professor Paolo Sibani, prematurely passed away in April 2023. At the time of his passing Professor Sibani was working as a co-editor of this collection.*

# Table of contents

frontiers | Frontiers in Physics

TYPE Editorial
PUBLISHED 11 March 2025
DOI 10.3389/fphy.2025.1563982



OPEN ACCESS

EDITED AND REVIEWED BY
James Avery Sauls,
Louisiana State University, United States

*CORRESPONDENCE
Gregory Kenning,
ccpm@iup.edu

RECEIVED 20 January 2025
ACCEPTED 24 February 2025
PUBLISHED 11 March 2025

CITATION
Boettcher S, Chamberlin R, Kenning G and Ricci Tersenghi F (2025) Editorial: Current research on spin glasses.
*Front. Phys.* 13:1563982.
doi: 10.3389/fphy.2025.1563982



# Editorial: Current research on spin glasses

Stefan Boettcher[1], Ralph Chamberlin[2], Gregory Kenning[3]* and Federico Ricci Tersenghi[4]

[1]Department of Physics, Emory University, Atlanta, GA, United States, [2]Department of Physics, Arizona State University, Tempe, AZ, United States, [3]Department of Physics, Indiana University of Pennsylvania, Indiana, PA, United States, [4]Dipartimento di Fisica, Sapienza Università di Roma, Rome, Italy

KEYWORDS

**spin glass, magnetism, phase transitions, disorder, complexity on multiple length and time scales, fluctuations, Monte Carlo methods, Markov chains**

Editorial on the Research Topic
Current Research on Spin Glasses

## Overview

Fifty years after the discovery of phase transition-like behavior in random-dilute magnetic alloys, the spin-glass state is still not fully understood. Interpreting spin-glass behavior is of practical importance for understanding cooperative behavior in random systems, and fundamental interest for insight into complexity that occurs across multiple times and spatial scales. In recent years, great strides have been made towards clarifying the spin-glass problem utilizing novel experimental techniques, detailed simulations of microscopic models, and analytical analyses of mean-field and scaling theories.

Our goal for this Research Topic was to gather recent developments in the general area of spin-glass-like behavior into a review that can guide future progress. Specifically, we have assembled a range of recent studies from diverse disciplines to provide up-to-date insight into the behavior of complex systems. The volume contains a series of papers that can provide readily accessible (open access) content from top researchers in the field. We briefly summarize the papers in this Research Topic.

## Experimental papers

The experimental papers in this Research Topic clearly show that even 50 years after the discovery of the spin glass state, much about the state is not understood and spin glasses remain a rich environment for discovery. Some of the main issues that come up in these papers include the exact experimental nature of the 3D phase transition, probing the large finite-size effects and time dependencies associated with crossing the Lower Critical Dimension of the phase transition, as well as investigations, in the spin glass phase, of the myriad of interesting time dependencies including memory, rejuvenation and temperature chaos.

In this Research Topic, Pradham et al. provide the first comparative study (on the same sample) of a variety of techniques (FC, ZFC, AC, onset of remanence) as a function of magnetic field and temperature, that in the past have been used to determine the spin glass transition temperature. Kenning et al. have used ultra-high sensitivity DC SQUID

magnetometry to probe close to the transition temperature elucidating for the first time, the strong time, temperature and magnetic field dependencies of the Thermal Remanent Magnetization (TRM) observed in this region.

Zhai and Orbach probe the time dependencies observed in spin glass thin films as a function of layer thickness, probing through the lower critical dimension. They compare the data with data found in large scale simulations and both neutron and muon spin scattering and provide analysis in terms of correlated growth in-plane and out-of-plane.

Well below the spin glass phase transition temperature, many time-dependent effects have been observed. Freedberg and Dahlberg explore both memory and rejuvenation and their experimental signatures as observed with in-phase and out-of-phase susceptibility and DC magnetization techniques.

Harrison discusses transport measurements in spin glasses, in particular Universal Conductance Fluctuations, to probe the spin glass state as a function of frequency and temperature.

## Theoretical/computational papers

Theoretical developments that were originally spawned by the discovery of glassy behavior in disordered spin systems have, of course, expanded way beyond the confines of real materials. Mean field replica theory (honored with the Physics Nobel prize for G. Parisi in 2021) has inspired myriad of uses, not only in physics but also in computer sciences, engineering, as well as laying the foundations to machine learning (honored with the Physics Nobel prize for J. Hopfield in 2024). However, its applicability to actual magnetic materials in finite dimensions, specifically to the Edwards-Anderson lattice spin glass model, remains a widely discussed issue. It is its very glassy nature, entailing slow equilibration and the need of extensive disorder averaging, that is also the obstacle to provide conclusive insights with simulations of low-temperature behavior in and out of equilibrium. In turn, these challenges have driven many fruitful designs of ever more ingenious mathematical concepts, computational techniques, and algorithms, some of which we showcase in this Research Topic.

The complexities of bringing traditional Monte Carlo techniques, so well-honed for ordinary materials, to bare on the thermodynamic behavior of magnetic glasses is exemplified in the review by Münster and Weigel, concerning the application of cluster algorithms to expedite equilibration near the phase transition. Similarly, Hukushima and Krauth explore the evolution of Markov chains to establish empirical as well as rigorous bounds on mixing and equilibration for the Edwards-Anderson model in 3d, in light of some recent algorithmic breakthroughs for structural glasses such as the hard-sphere model.

The breadth that the spin glass paradigm has taken on since its inception is demonstrated by Lanthier et al., who study the application of tensor networks to reduce the complexity, without or with only minimal loss of accuracy, in sparsely connected mean-field spin glasses with general p-spin coupling terms, which proves effective beyond expectations near the zero-temperature SAT/UNSAT transition. This has been an exceedingly fruitful area of research at the interface of spin glass theory and combinatorial optimization problems in computer science, such as SATisfiability.

A similar reduction in complexity is employed by Boettcher to heuristically search for ground states of the Edwards-Anderson model, which is an (NP-)hard optimization problem deep in the UNSAT regime, to measure the energy cost of domain wall excitations in dimensions d = 3, …,8. Finally, Newman and Stein take a mathematically rigorous approach to such droplet excitations that are central to an understanding of the nature of ground states in the Edwards-Anderson model, showing that the relevance of replica theory to finite dimensional glasses is equivalent to the presence of certain critical droplets in the infinite lattice.

## Dedication: in memory of Paolo Sibani

The guest editors would like to dedicate our work on this Research Topic to our dear friend and fellow scientist Paolo Sibani. Until his sudden passing, Paolo was a co-editor on this Research Topic. Paolo felt that this type of spin glass Research Topic, which includes both experimental and theoretical/computational papers and expresses the current state of the field, was both timely and necessary. In his work on this Research Topic Paolo brought the same joy and enthusiasm that he brought to life and everything he worked on. His friendship will be greatly missed!

## Author contributions

SB: Writing–original draft, Writing–review and editing. RC: Writing–original draft, Writing–review and editing. GK: Writing–original draft, Writing–review and editing. FR: Writing–original draft, Writing–review and editing.

## Funding

The author(s) declare that no financial support was received for the research, authorship, and/or publication of this article.

## Conflict of interest

The authors declare that the research was conducted in the absence of any commercial or financial relationships that could be construed as a potential conflict of interest.

## Generative AI statement

The author(s) declare that no Generative AI was used in the creation of this manuscript.

## Publisher's note

frontiers | Frontiers in Physics

TYPE Original Research
PUBLISHED 20 March 2024
DOI 10.3389/fphy.2024.1370278



OPEN ACCESS

EDITED BY
Federico Ricci-Tersenghi,
Sapienza University of Rome, Italy

REVIEWED BY
Qiang Zhai,
Xi'an Jiaotong University, China
Luca Leuzzi,
National Research Council (CNR), Italy

*CORRESPONDENCE
R. L. Orbach,
orbach@utexas.edu

RECEIVED 14 January 2024
ACCEPTED 20 February 2024
PUBLISHED 20 March 2024

CITATION
He J and Orbach RL (2024), Spin glass dynamics through the lens of the coherence length. *Front. Phys.* 12:1370278. doi: 10.3389/fphy.2024.1370278



# Spin glass dynamics through the lens of the coherence length

J. He and R. L. Orbach*

Texas Materials Institute, The University of Texas at Austin, Austin, TX, United States

Spin glass coherence lengths can be extracted from experiment and from numerical simulations. They encompasses the correlated region, and their growth in time makes them a useful tool for exploration of spin glass dynamics. Because they play the role of a fundamental length scale, they control the transition from the reversible to the chaotic state. This review explores their use for spin glass properties, ranging from scaling laws to rejuvenation and memory.

KEYWORDS

**spin glass dynamics, coherence length, rejuvenation, memory, numerical simulation, scaling law**

## 1 Introduction

The dynamical processes found in spin glasses mimic those from a wide variety of physical systems, not limited to glass formers, polymers, granular materials, phase separation in the early Universe, and the social sciences. Because their dynamical properties can be measured directly, they provide a window into the behavior of far-from-equilibrium systems. This review will explore the spin glass coherence length, $\xi(t, t_w; H)$, its definition, extraction from experiment and simulations, and applications. Here, $t_w$ is the age of the spin glass system before the measurement time, $t$ begins, and $H$ is the magnetic field. An inherent advantage of the use of $\xi(t, t_w; H)$ to describe dynamical properties is that the spin glass transition temperature, $T_g$ is implicit. A precise value of $T_g$ is not required even for explorations close to $T_g$.

The first explicit experimental procedure for extraction of the spin glass was proposed and demonstrated by Joh et al. [1]. They noted that the relevant free energy barrier energy change from imposition of a magnetic field $H$ was given by what they termed the "Zeeman" energy, $E_Z$ where,

$$E_Z = N_s \chi_{\rm FC} H^2 \ . \tag{1}$$

Here, $N_s$ is the number of spins in a volume subtended by $\xi(t, t_w; H)$, and $\chi_{\rm FC}$ is the field-cooled susceptibility *per spin*. They took $N_s = (4/3)\pi[\xi(t, t_w; H)]^3$ whereas, subsequently, a value based on the structure of the four spin coherence length was introduced [2],

$$N_s = [\xi(t, t_w; H)]^{D-(\theta/2)} \tag{2}$$

where $\theta$ is the replicon exponent [3].

The Sherrington-Kirpatrick (SK) infinite range exchange Hamiltonian [4] for spin glasses exhibits states within an ultrametric geometry [5] which has a pictorial equivalent [6] of an hierarchical organization. Free energy barriers separate states with occupancies that increase exponentially with diminishing overlap. The Parisi solution [7, 8] of the SK model are "pure states" separated by infinite barriers. This geometry was shown by analogy to replicate dynamical transitions between states with finite free energy barriers [9]. Putting

all these factors together leads to an inflection point in the time dependence of the magnetization, and hence a maximum in the logarithmic derivative of the time dependent magnetization, known as $S(t, t_w; H)$, the relaxation function:

$$S(t, t_w; H) = \frac{d\,M(t, t_w; H)}{d\,ln\,t} \quad . \tag{3}$$

Experimentally, the magnetization is measured at constant temperature $T$ after an aging time $t_w$. Empirically, the maximum of $S(t, t_w; H)$ occurs at a time $t \approx t_w$ [10] associated with the largest free energy barrier generated by the growth of the spin glass coherence length $\xi(t, t_w; H)$ where $H$ is the magnetic field.

In a thermoremanent magnetization (TRM) experiment, $H$ is applied in the paramagnetic state, kept constant as the spin glass is cooled to a temperature $T$ below the condensation temperature $T_g$, and the magnetization is measured after the time $t_w$ when $H$ is changed (most often, cut to zero). In a zero-field cooled (ZFC) experiment, $H = 0$ initially as the spin glass is cooled to T, and the magnetization measured upon application of $H$ after the time $t_w$. It is important to understand that the free energy barriers are not "chemical" in their origin. Rather, they are created by larger and larger numbers of correlated spins, the volume containing $N_s$ subtended by $\xi(t, t_w; H)$ according to Eq. 2.

Thus, the maximum free energy barrier height, $\Delta_{max}$ is associated with $t_w$ according to an Arrhenius law,

$$\Delta_{max} \approx k_B T\ ln\left[\frac{t_w}{\tau_0}\right] \tag{4}$$

where $\tau_0$ is an exchange time usually taken as $\hbar/k_B T_g$. From Eq. 1, we can define an "effective" waiting time $t_w^{eff}$ in the presence of a magnetic field as,

$$\Delta_{max} - N_s \chi_{FC} H^2 = k_B T\, ln\, t_w^{eff} - k_B T\, ln\, \tau_0 \ , \tag{5}$$

where $t_w^{eff}$ is taken as the time when $S(t, t_w; H)$ reaches its peak in the absence/presence of $H$ for TRM/ZFC experiments, respectively.

Combining Eqs 1, 5 enables the only means for extraction of the spin glass coherence length from experiment. In order to keep this value explicit, we shall label it $\xi_{Zeeman}$.

Mathematical simulations from the Janus Collaboration [11], using a special purpose computer, can address the value of $\xi$ directly. In temperature cycling experiments that will be addressed below, they project (at least) two different coherence lengths [12].

The first is $\xi_{micro}(t_w, T)$, the microscopic coherence length computed directly from the replicon propagator [13, 14] in Eq. 6

$$\mathcal{G}_R(\mathbf{r}, t, T) = \frac{1}{V}\sum_{\mathbf{x}} \overline{\left(\langle s_{\mathbf{x},t} s_{\mathbf{x}+\mathbf{r},t}\rangle_T - \langle s_{\mathbf{x},t}\rangle_T \langle s_{\mathbf{x}+\mathbf{r},t}\rangle_T\right)^2}, \tag{6}$$

where for Ising spins, $s_x = \pm 1$. The replicon correlator $\mathcal{G}_R$ decays to zero in the long-distance limit. One therefore computes $\xi_{micro}(t_w, H)$ by exploiting the integral estimators [15, 16] in Eqs 7 and 8

$$I_k(t, T) = \int_0^\infty d\,r\, r^k \mathcal{G}(\mathbf{r}, t; T), \tag{7}$$

and

$$\xi_{k,k+1}(t, T) = \frac{I_{k+1}(t, T)}{I_k(t, T)} \quad . \tag{8}$$

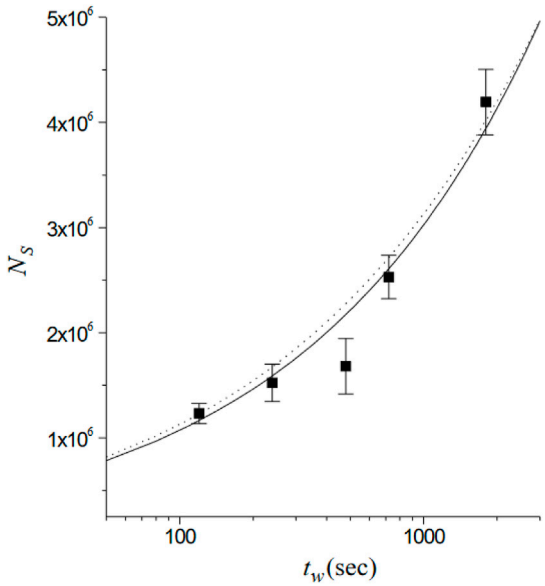


FIGURE 1
A plot of $N_s$ reproduced from [1] for CuMn 6 at.% vs. $t_w$ on a log scale at fixed temperature $T = 0.89\ T_g = 28$ K. The solid curve drawn through the points is the prediction for power law dynamics [20], while the dashed curve is the prediction for activated dynamics [21], with their exchange factor set equal to $T_g$ (i.e., independent of $T$ and $t$). As is seen from the two curves, the two fits are equally good.

The $\xi_{1,2}(t_w, T)$ is designated as the microscopic coherence length $\xi_{micro}(t_w, T)$.

Physically [12], "$\xi_{micro}(t_w, T)$ is the size of the (glassy) domains within the sample (it is the largest length scale at which we can regard the system as ordered at time $t_w$."

Another length scale is introduced in simulations [12] when comparing the same system at two times $t_1$ and $t_2$ ($t_1 < t_2$): $\zeta(t_1, t_2)$. It "characterizes the long-distance decay of the pair-correlation function corresponding to the set of spins taking opposite signs at times $t_1$ and $t_2$. Physically, $\zeta(t_1, t_2)$ is the typical size of regions where coherent rearrangements have occurred between times $t_1$ and $t_2$ . . . because of the ongoing formation of a new spin order at time $t_2$. For fixed $t_1$, $\zeta(t_1, t_2)$ grows with $t_2$ starting from $\zeta(t_1, t_2 = t_1) = 0$."

At a given temperature, $\xi_{Zeeman}(t_w, T)$ "fairly closely follows the behavior of the microscopic length $\xi_{micro}(t_w, T)$" [12, 17–19] so that, for all practical purposes, they can be taken equal. For varying temperature protocols, the scenario is more intricate because of the presence of temperature chaos at large temperature changes. The length scales are quantitatively compared in Figure 5 of [18].

Now that we have defined the relevant length scales, we show in the next section how they elucidate the dynamical properties of spin glasses.

## 2 Physical properties

The first experimental extraction of $\xi_{Zeeman}(t_w, T)$ [1] compared results from two approaches: power law dynamics

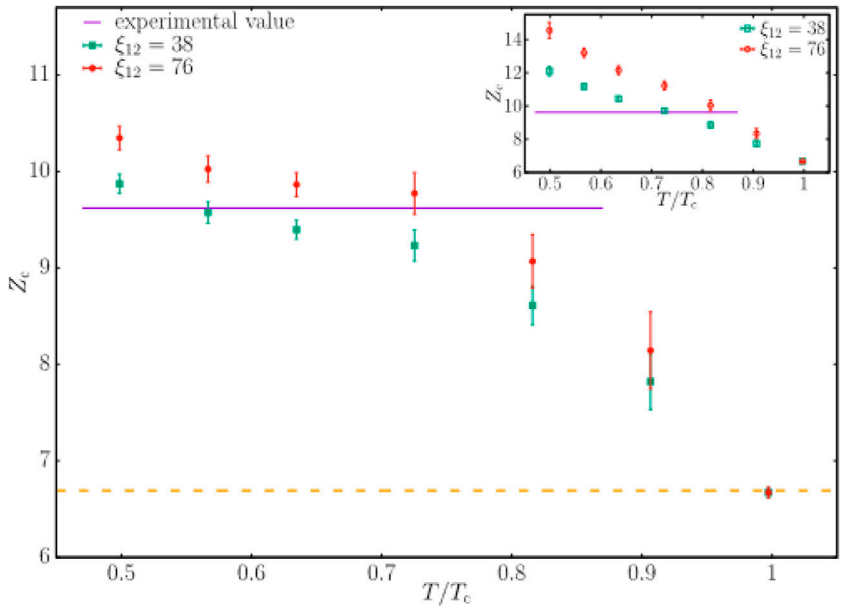


FIGURE 2
Value of the experimental aging rate for spin glasses $Z_c(T) = z_c(T, \xi)T/T_c$, reproduced from Ref. [22]. The straight line is the experimental value of $z_c(T) \approx 9.62$ from Ref. [23].

[20] vs. activated dynamics [21]. The results are reproduced in Figure 1. Knowing $\chi_{FC}$ per spin from other measurements allows for the extraction of $\xi_{Zeeman}(t_w, T)$ from Eq. 2. For example, from Figure 1 at $t_w = 1,000$ s, $N_s \approx 3 \times 10^6$ spins. They set $\xi(t_w, T) \approx [N_s(t_w, T)]^{1/3}$ giving $\xi(t_w = 1,000, T = 28\text{ K}) = 100\ a_0$, where $a_0$ is the average distance between Mn ions. Subsequently it was shown [3] that the correct extraction of $\xi(t_w, T)$ is given by $[N_s(t_w, T)]^{1/d_f}$, where $d_f$ is the fractal dimension equal to $D - (\theta/2)$, with $\theta$ the replicon exponent [16]. In general, $\theta \sim 0.3$–$0.4$ so that its omission in Ref. [1] results in only a small error.

The uses of $\xi(t_w, T)$ to describe physical processes provides a powerful quantitative tool. Pertinent examples are described below.

## 2.1 Slowing down of the growth of $\xi(t_w, T)$

The Janus Collaboration utilizes a special purpose-built computer [16] to examine the dynamics of the Ising spin glass. They were able to explore the (re-normalized) aging rate [22],

$$z_c(T, \xi) = \frac{T}{T_g} \frac{d\,ln\,t_w}{d\,ln\,\xi} \ . \tag{9}$$

The re-normalizing factor $T/T_g$ makes $z_c(T, \xi) \approx z_c(\xi)$ [23].

We can rewrite Eq. 9 as Eq. 10,

$$ln\,t_w = \frac{z_c T_g}{T}\, ln\,\xi + \text{const} \tag{10}$$

The aging rate, $z_c$, was found to vary substantially from experiment to experiments, depending upon the temperature and nature of the spin glass sample. For example, for a bulk polycrystalline sample of CuMn (6 at%) [1] found $z_c = 5.917$ at a reduced temperature of $T/T_g = 0.89$. For a polycrystalline bulk spinel they found $z_c = 7.576$ at a reduced temperature of $T/T_g = 0.72$.

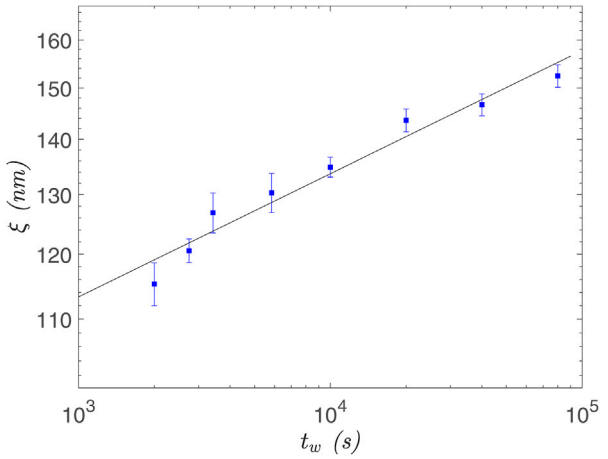


FIGURE 3
$\xi(t_w, T)$ as a function of the waiting time $t_w$ at a measuring temperature of $T = 28$ K ($T_g = 31.5$ K) reproduced from Ref. [26]. The staight line is a fit to $\ln t_w = (z_c T_g/T) \ln \xi + \text{const.}$ [recall Eq. 10], yielding $Z_c = 12.37 \pm 1.07$.

In thin films [24] found for 11.7 at. % that $z_c = 9.62$ at reduced temperatures of $T/T_g = 0.43, 0.59$, and $0.78$. Working at $T/T_g = 0.95$ [25], found $z_c = 6.80$ in bulk polycrystalline CuMn (5 at%).

The Janus collaboration [22] found a hint to reconcile these apparently conflicting values from experiment by computing $\xi$ over a temperature range $0.5 \le T/T_g \le 1$. Figure 2 exhibits their results.

Experimentally, there is a significant confirmation for this variation of $z_c$. Ref. [22] found that the growth of $\xi(t_w, T)$ slows down as $\xi(t_w, T)$ increases. That is, $z_c$ *increases* as $\xi(t_w, T)$ *increases*.

In order to achieve large values of $\xi(t_w, T)$ to test this simulation prediction, we were blessed with a single crystal of CuMn, 6 at%, grown by Dr. D.L.Schagel, the description of which is contained in Ref. [26]. By working at 28 K ($T_g = 31.5$ K) and at long waiting times (up to $10_5$ s), the value extracted for $\xi(t_w, T)$ reached 150 nm, the largest coherence length ever reported for a glassy system [26]. The value of $\xi(t_w, T)$ vs. $t_w$ is plotted in Figure 3, from which $z_c = 12.37 \pm 1.07$ can be extracted. This is to be compared with $z_c \approx 9.62$ extracted at shorter waiting times for smaller values of $\xi(t_w, T)$.

## 2.2 Scaling law

The coherence length $\xi(t_w, T)$ can be measured precisely for spin glasses both in experiment and through simulations. However, known analysis methods lead to discrepancies either for large external magnetic fields or close to the transition temperature. This problem can be solved through introduction of a scaling law that takes into account both the magnetic field and the time-dependent coherence length. This is especially important because temperatures $T \approx T_g$ are most relevant for the study of glass formers ($\xi$ is restricted to a very narrow window of variation if one moves away from $T_g$).

Historically, non-linear magnetization effects, and their scaling properties in spin glasses, were first introduced by Malozemoff, Barbara, and Imry [27–29] who introduced the relation for the singular part of the magnetic susceptibility,

$$\chi_s = H^{2/\delta} f\left(t_r / H^{2/\phi}\right), \tag{11}$$

where $f(x)$ is a constant for $x \to 0$; $f(x) = x^{-\gamma}$ for $x \to \infty$; $\phi = \gamma\delta/(\delta - 1) \equiv \beta\delta$; and $t_r$ is the reduced temperature $T/T_g$.

This form was used by Lévy and Ogielski [30], and Lévy [31] who measured the AC non-linear susceptibilities of very dilute AgMn alloys above and below $T_g$ as a function of frequency, temperature, and magnetic field. Their critical exponents from Eq. 11 differed substantially from Monte Carlo simulations for short-range Ising systems [32]. The discrepancy in their value of $\gamma$ was very large, and most probably arose from the lack of an exact value for $T_g$ in their experiments. This illustrates the value of and need for a different approach for scaling the non-linear magnetization of spin glasses in the vicinity of $T_g$.

The scaling argument goes as follows. Let $M(t, t_w; H)$ be the magnetization per spin. The generalized susceptibilities $\chi_1, \chi_3, \chi_5, \ldots$ are defined through the Taylor expansion,

$$M(H) = \chi_1 H + \frac{\chi_3}{3!} H^3 + \frac{\chi_5}{5!} H^5 + \mathcal{O}(H^7). \tag{12}$$

We have omitted $t$ and $t_w$ for brevity. Our hypothesis is that, in the non-equilibrium regime for a spin glass close to $T_g$ in the presence of a small magnetic field,

$$M(t, t_w; H) = [\xi(t + t_w)]^{y_H - D} \times \mathcal{F}\left(H[\xi(t + t_w)]^{y_H}, \frac{\xi(t + t_w)}{\xi(t_w)}\right) \tag{13}$$

According to full-aging spin-glass dynamics [30] Eq. 13 tells us that $\xi(t + t_w)/\xi(t_w)$ will be approximately constant close to the maximum of the relaxation rate [i.e., peak of $S(t)$], so that we omit this dependence. Thus, combining Eqs 12, 13, one can express the generalized susceptibilities $\chi_1, \chi_3, \chi_5, \ldots$ in terms of the spin glass coherence length $\xi(t, t_w; H)$:

$$\chi_{2n-1} \propto |\xi(t_w)|^{2ny_H - D}, \tag{14}$$

where we have omitted the arguments $t$ and $H$ for convenience, and Eq. 15

$$2y_H = D - \frac{\theta(\bar{x})}{2}, \tag{15}$$

with $\theta(\bar{x})$ the replicon exponent [3].

The first term of $M(H)$ in Eq. 12 is $\chi_1$, which contains the linear term as well as the first non-linear scaling term, so that we write,

$$\chi_1 = \frac{\hat{S}}{T} + \frac{a_1(T)}{\xi^{\theta(\bar{x})/2}} \tag{16}$$

where $a_1(T)$ is some unknown constant, hopefully varying smoothly with temperature.

The free-energy variation per spin in the presence of a magnetic field can be derived by integrating the magnetic density Eq. 12 with respect to the magnetic field in Eq. 17,

$$\Delta F = -\left[\frac{\chi_1}{2} H^2 + \frac{\chi_3}{4!} H^4 + \frac{\chi_5}{6!} H^6 + \mathcal{O}(H^8)\right]. \tag{17}$$

Substituting the scaling from Eqs 14, 16, the free energy $\Delta F$ can be written as (we drop the $\bar{x}$ dependence of $\theta$ for brevity) in Eq. 18,

$$\Delta F = -\left[\frac{\hat{S}}{2T} H^2 + \frac{a_1(T)}{\xi^{\theta/2}} H^2 + a_3(T)\xi^{D-\theta} H^4 + a_5(T)\xi^{2D-(3\theta/2)} H^6 + \mathcal{O}(H^8)\right], \tag{18}$$

where again the $a_n(T)$ are unknowns and hopefully again smoothly varying functions of temperature. Using the effective response time, $t_H^{\text{eff}}$, to reflect the total free-energy change at magnetic field $H$ with respect to $H \to 0^+$,

$$ln\left[\frac{t_H^{\text{eff}}}{t_{H\to 0^+}^{\text{eff}}}\right] = N_s \Delta F = -b\left[\left(\frac{\hat{S}}{2T} + \frac{a_1(T)}{\xi^{\theta/2}}\right)\xi^{D-(\theta/2)} H^2\right] + a_3(T)\xi^{2D-(3\theta/2)} H^4 + a_5(T)\xi^{3D-2\theta} H^6 + \mathcal{O}(H^8)\Big] \tag{19}$$

where the coefficient $b$ is a geometrical factor, and we have absorbed the $k_B T$ term in the $a_n(T)$ coefficients. The correction term $a_1(T)/\xi^{\theta(\bar{x})/2}$ is small compared to $\hat{S}/T$, so it will be neglected in subsequent expressions. Equation 19 shows that the higher order terms have the functional form, in Eq. 20,

$$\chi_{2n-1} \frac{H^{2n}}{(2n)!} = a_{2n-1}(T)\xi^{-\theta(\bar{x})/2}\left[\xi^{2y_H} H^2\right]^n \tag{20}$$

where, in Eq. 21

$$2y_H = D - \frac{\theta(\tilde{x})}{2} \tag{21}$$

This leads to the new scaling relation,

$$ln\left(\frac{t_H^{\text{eff}}}{t_{H\to O^+}^{\text{eff}}}\right) = \frac{\hat{S}}{T}\xi^{D-(\theta/2)} H^2 + \xi^{-\theta/2}\mathcal{G}\left(\xi^{D-(\theta/2)} H^2; T\right)\Big). \tag{22}$$

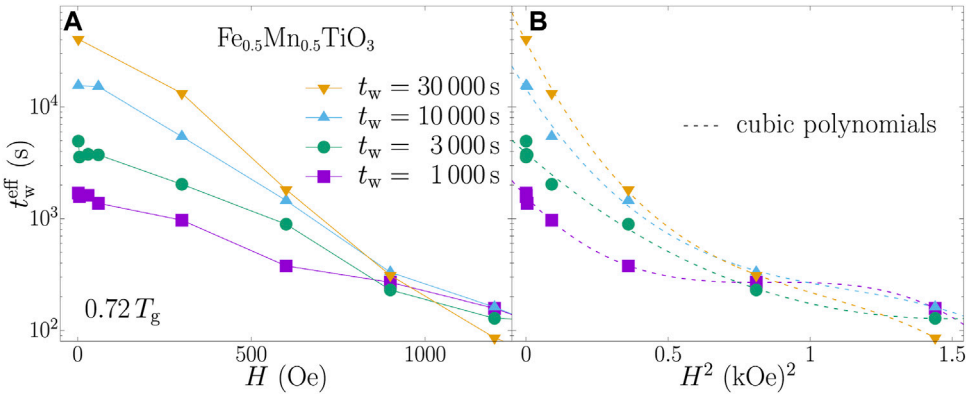


FIGURE 4
**(A)** Effective waiting times (log scale) derived from field-change experiments on an Ising sample ($Fe_{0.5}Mn_{0.5}TiO_3$) as a function of magnetic field $H$. The plot reproduces Figure 10 of Paga *et al.* [17] (solid lines are linear interpolations to data with the same $t_w$). **(B)** The same data plotted against $H^2$. The dotted lines are fits to Eq. 19.

where the geometrical factor $b$ has been absorbed into the scaling function $\mathcal{G}$).

Among the many uses of Eq. 22, two can be highlighted. The first is the issue surrounding the magnetization encompassed in $\xi_{Zeeman}(t_w, T)$. The original introduction proposal, Ref. [1], envisaged the reduction of the barrier heights $\Delta(t_w, T)$ by $E_Z$ [Eq. 1] to be caused by the magnetization induced by the magnetic field within the volume subtended by the spin glass coherence length $\xi(t_w, T)$, viz Eq. 1. A subsequent treatment [33] associated $E_Z$ with the magnetization associated with the fluctuations of the entire system of N spins, namely, $\propto \sqrt{N}$. The magnetic field dependence is very different, the former $E_z \propto H^2$ while the latter $E_Z \propto H$.

A comparison of the two was exhibited in Fig. 10 of Ref. [17], reproduced here as Figure 4. The magnitude of the magnetic fields contained in Figure 4 are quite large. The authors of Ref. [33] state that the proportionality to $H$ fails at low magnetic fields. The reader can judge whether a linear fit to $H$ is obeyed by the left-hand of Figure 4. The right-hand of Figure 4 is the fit to the scaling law, valid over the full range of $H$, large and small. Again, the reader can judge which fit is preferable.

The second is the value of the condensation temperature, $T_g$. In principle, determination of $T_g$ would require an infinite $t_w$ because $\xi(T) \to \infty$ when $T \to T_g$. One expects that any experiment at finite $t_w$ would yield a maximum for the non-linear susceptibility at a temperature we shall call $T_g\,(t_w)$ because $t_w$ is finite.

In principle then, by measuring $T_g\,(t_w)$ for ever larger $t_w$, one could extrapolate to the true $t_w \to \infty$ condensation temperature $T_g$. If nothing else, measurements at large values of $t_w$ on laboratory time scales could establish an upper bound for $T_g$.

The non-linear susceptibility $\chi_3$ diverges as Eq. 23

$$\chi_3\,(t_w \to \infty\,; T) = \chi_0\,\frac{T_g\,(t_w \to \infty)}{|T_g\,(t_w \to \infty) - T|^{\gamma}}, \tag{23}$$

where $\chi_0$ is a constant independent of temperature, and $\gamma = 6.13\,(11)$ from Ref. [32]. For *finite* $t_W$, $\chi_3\,(t_w, T)$ only has a maximum as a function of temperature. A way of arriving at this maximum would be to fit the data to the function, in Eq. 24

$$\chi_3\,(t_w, T) = \chi_0\,\frac{T_g\,(t_w)}{|T_g\,(t_w) - T|^{\gamma}}, \tag{24}$$

and then use data points from just two or three temperatures to extract $T_g\,(t_w)$. For larger and larger $t_w$, one could in principle extrapolate to the true $T_g$. This is just a suggestion for a feasible process for taking laboratory data for finite $t_w$ and extrapolating to find $T_g\,(t_w \to \infty)$.

## 2.3 Temperature chaos

Temperature chaos is one of the outstanding mysteries posed by spin glasses. It consists of the complete reorganization of the equilibrium configurations by the slighted change in temperature." [34] These are the opening lines of a major paper titled "Temperature chaos is a non-local effect" and set the stage for this section. Even the existence of temperature chaos in spin glasses has been questioned [35–38]. Recent experiments [39] and simulations [40] have shed light on its existence and nature, but there are many questions that remain.

From this article's perspective, the opening gambit was the renormalization group perspective of Bray and Moore [41]. They introduced a length scale associated with temperature chaos that, for all practical purposes, can be simplified to,

$$\ell_c\,(T_1, T_2) = a_0\left[\frac{T_2}{T_1 - T_2}\right]^{1/\zeta} \tag{25}$$

where $\zeta = d_s - \theta$, $d_s$ the fractal dimension of the correlated region, and $\theta$ is the replicon exponent. The system is in an equilibrium state at a temperature $T_1$, after which the temperature is dropped to $T_2$. Temperature chaos obtains with a length scale $\ell_c$. The reason that $\ell_c$ is important is that, for a coherence length $\xi(t_w, T)$ not infinite, temperature chaos requires a finite temperature drop. The condiction is, shown in Eq. 26

$$\begin{aligned} \text{Temperature chaos:} \quad & \ell_c\,(T_1, T_2) \le \xi\,(t_w, T_1), \\ \text{Reversible:} \quad & \ell_c\,(T_1, T_2) \ge \xi\,(t_w, T_1), \end{aligned} \tag{26}$$

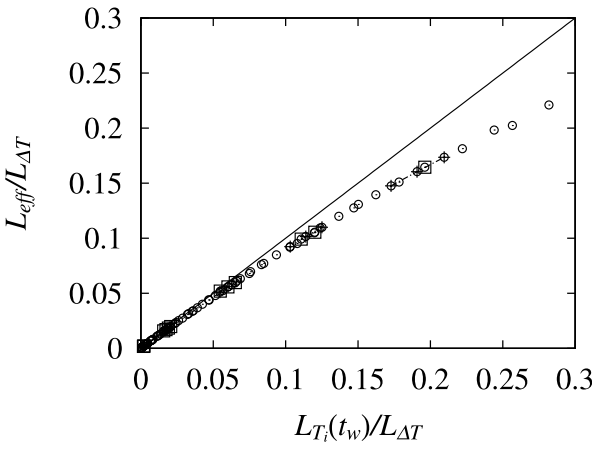


FIGURE 5
Reproduced from Figure 4 in [42]. Scaling plot of $L_{\rm eff}$ with $L_{\Delta T} = L_0 (c\Delta T/J)^{-2.6}$ with $c$ = 5. The solid straight line represents scaling in the absence of temperature chaos.

where by "reversible" we mean that the system "remembers where it came from" when the temperature is dropped from $T_1$ to $T_2$, i.e., no temperature chaos.

Though the relationship Eq. 25 is for a spin glass in equilibrium, realistically, this is never the case. Fortunately, recently an analysis was provided [40] which is titled "Temperature chaos is present in off-equilibrium spin-glass dynamics," so that we can use the relationship Eq. 25 experimentally. Note that both $t_w$ and $\Delta T = T_1 - T_2$ are controllable parameters. Hence, we can probe the onset of temperature chaos by examining spin glass dynamics under difference conditions, and in particular, can control its onset.

Experiments have probed temperature chaos. The first definitive paper [42] defined the length scale for chaos as $L_{\Delta T}$ given by Eq. 27,

$$L_{\Delta T} \sim L_0 |\Delta T / J|^{-1/\zeta} \tag{27}$$

equivalent to our Eq. 25 with $L_{\Delta T} \equiv \ell_c\,(T_1, T_2)$, and $J$ an exchange energy in units of temperature. They extract and effective chaos length scale, $L_{\rm eff}$ from the following plot (their Figure 4, our Figure 5): Their plot generates $1/\zeta = 2.6$ or $\zeta = 0.38$. This value is a factor of nearly 3 below the rather universally accepted value of $\zeta = 1.1$ (see Appendix B in Ref. [39], for a full listing of theoretical values for $\zeta$).

It is difficult to understand why their value for $\zeta$ was so far off from what is now regarded as the fairly accepted value near unity. An origin may be lie in their measurement protocol, namely, a zero-field magnetization measurement where the magnetic field is applied after cycling to $T_1$. Magnetic field chaos [43, 44] could then be compounded with temperature chaos, and distort the extraction of a value for $1/\zeta$.

In order to circumvent this possibility, Zhai et al. [39] worked with a protocol where the magnetic field remained constant across temperature cycling. The idea was to use the field-cooled magnetization to investigate temperature chaos in spin glasses. This protocol involved turning on a magnetic field $H$ above the condensation temperature, $T_g$, keeping it constant throughout the temperature cycling protocol.

The specific steps were as follows. The decay of the field cooled (FC) magnetization, $M_{FC}(t,\ T_1,\ H)$ is measured at the first temperature stop $T_1$ after cooling in the current magnetic field and waiting a time $t_{w1}$. The decay curve is denoted as the "reference curve." Then, temperature cycling is engaged, where one first cools to temperature $T_1$, waits a time $t_{w1}$, cools to $T_2$, waits a time $t_{w2}$, then rapidly warms back to $T_1$, and measures the decay of the magnetization $M_{FC}(t,\ T_1,\ H)$.

In order to observe TC, $T_1$ was fixed and the temperature $T_2$ was gradually lowered in separate experimental runs to $T_2 = T_1 - \Delta T$. Following the temperature drop, if,

$$x = \frac{\ell_c\,(T_1, T_2)}{\xi\,(T_1, t_{w1})} \geq 1, \tag{28}$$

the coherence length will continue to grow, and one remains in the reversible state. However, in Eq. 29

$$x = \frac{\ell_c\,(T_1, T_2)}{\xi\,(T_1, t_{w1})} \leq 1 \tag{29}$$

temperature chaos sets in and one finds a diminished coherence length after heating back to temperature $T_1$ (see the discussion below of memory).

As a consequence, under reversible dynamics, Eq. 28, the decay curve of $M_{FC}(t,\ T_1,\ H)$ *after temperature cycling* can be superposed on the reference decay curve, allowing for a positive shift in time for $M_{FC}(t, T_1, H)$ during the time that $T < T_1$. However, after the onset of temperature chaos, The decay curves cannot be superposed for any positive shift of $M_{FC}(t,\ T_1,\ H)$ in time.

This is seen explicitly in Figure 6 which was reproduced from Figure 1 of Ref [39]. By changing $T_1$, $t_{w1}$, Eq. 25 can be probed to yield a value for $1/\zeta$. A value for $\zeta \approx 1.1$ was extracted in [39], very close to a majority of the theoretical values.

This experimental evidence for the existence of temperature chaos in spin glasses will prove important in our subsequent treatments of rejuvenation and memory. We shall argue that temperature chaos is responsible for the former, and plays an important role in a quantitative treatment of the latter. In any case, the experiments of Ref. [34] have shown that temperature chaos is present in spin glasses, and will be shown to have a profound impact in other dynamical spin glass phenomena.

## 2.4 Rejuvenation

The singular publication that engendered the attention of both theorists and experimentalists for over three decades was that of Jonason et al. [45] titled "Memory and Chaos Effects in Spin Glasses." They displayed the remarkable figure (Figure 7 reproduced from Figure 1 in their paper). The system is "aged" at 12 K, becoming "older." Upon lowering the temperature, it returns to the reference curve, thus becoming "younger". This is termed "rejuvenation." It was attributed to temperature chaos, namely, the spin glass "forgot" its previous history of aging when the temperature was lowered beyond the threshold for temperature chaos.

This assignment has yet to be proven unequivocally. A very recent paper [18] by Paga et al. displayed the results of temperature cycling to explore this claim, and indeed to relate rejuvenation to the

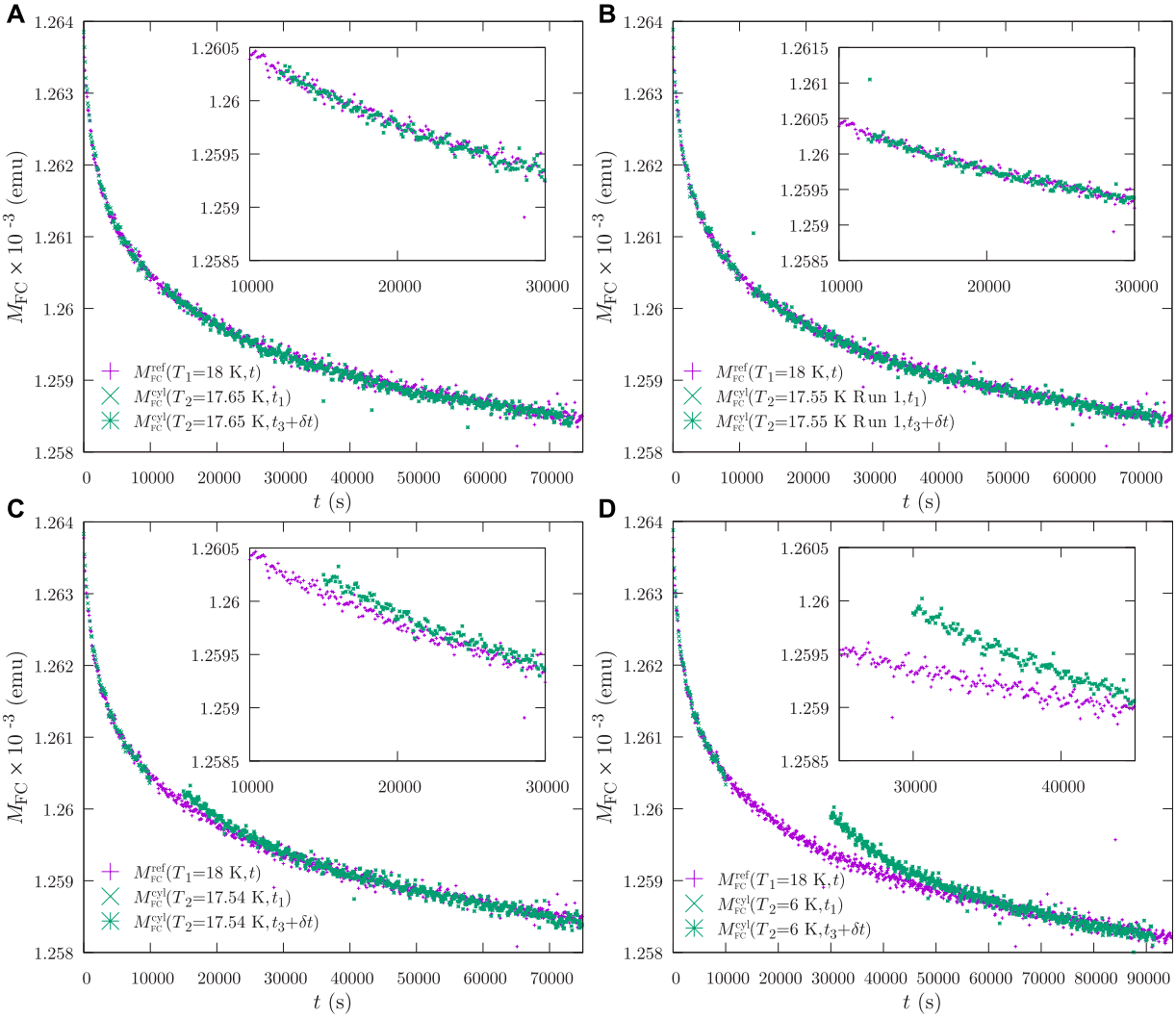


FIGURE 6
The example of $T_1$ = 18 K, reproduced from Figure 1 in [39]. The temperature is gradually lowered to $T_2$ after $t_{w1} = 10^4$ s and heated back to $T_1$ after $t_{w2} = 10^3$ s. The temperature cycling curve is then shifted by $\delta t$ to overlap the reference curve. In the reversible temperature range, **(A)** and **(B)**, the cycling curve can be overlapped with the reference curve over the whole period $\approx 7 \times 10^4$ s. In the chaotic range, **(C)** and **(D)**, the cycling curve can only be partially overlapped. Hence, temperature chaos, at $T_1$ = 18 K, $t_{w1} = 10^4$ s, sets in for $\Delta T > 450$ mK.

spin glass coherence length. Figure 8 reproduces their Figure 2. While Figure 8 appears definitive, there needs to be an exploration of $t_w^{\text{eff}}$ for temperature above and below the temperature for the onset of temperature chaos to arrive at an unequivocal relationship between rejuvenation and temperature chaos. For the moment, Figure 8 seems entirely consistent with that interpretation.

## 2.5 Memory

Though rejuvenation in spin glasses is remarkable, the even more remarkable is memory. Once the system has rejuvenated back to the reference curve, upon reheating it traces out the same behavior as it exhibited upon cooling, even with temperature chaos between $T_1$ and $T_2$. This is explicitly demonstrated in Figure 7. On the surface it seems quite inconsistent. How can the system exhibit memory when it has experienced temperature chaos? There have been a multitude of papers and models that addressed this conundrum. Most involve heuristic models with adjustable parameters that can fit the data represented in Figure 7. A recent treatment [18] gives an interpretation that is free of real space models and the concomitant adjustable parameters, and is based upon the behavior of the spin glass coherence length. The beauty of this formulation is that every term in its interpretation can be tested experimentally, something that previous models lack.

The concept is as follows. Upon cooling the spin glass from above $T_g$ to the first measuring temperature $T_1$, the system is aged for a time $t_{w1}$. As a consequence, the spin glass coherence length grow from nucleation to $\xi(t_{w1}, T)$. When the temperature is then lowered to $T_2$, the correlations created at $T_1$ are essentially frozen. This concept has been introduced by Bouchaud et al. [45]. What is new is that, when the system is aged at $T_2$ for a time $t_{w2}$, the system has created new coherent regions that have nothing to do with those

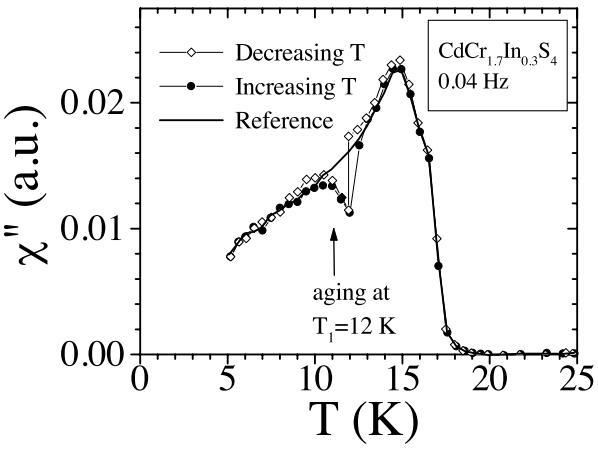


FIGURE 7
Reproduced from Figure 1 of Ref. [45]. Out-of-phase susceptibility $\chi''$ of the $CdCr_{1.7}In_{0.3}S_4$ spin glass. The solid line is measured upon heating the sample at a constant rate on 0.1 K/min (reference curve). Open diamonds: the measurement is done during cooling at this same rate, except that the cooling procedure has been stopped at 12 K during 7 h to allow for aging. Cooling then resumes down to 5 K: $\chi''$ is not influenced and goes back to the reference curve (chaos). This is termed rejuvenation. Solid circles: after this cooling procedure, the data is taken while reheating at the previous constant rate, exhibiting memory of the aging stage at 12 K.

created at $T_1$. Hence, when heating back to $T_2$, the two correlated regions *interfere*, thereby reducing the spin glass coherence length from the native value created at $T_1$, $t_{w1}$.

This is exhibited explicitly in Figure 8 in the lower part of the figure. The $C_n$ represent three separate temperature and waiting time cycles, and illustrate unequivocally the relationship between memory and competing coherence lengths. Each of the cycles has three steps: 1) the system is "prepared" at $T_1$ = 30 K by waiting for the same time $t_{w1}$ = 1 h 2) The temperature is then dropped to $T_2$ and the system is aged for $t_{w2}$. 3) The system is than heated back to $T_1$ = 30 K and $t_w^{\rm eff}$ measured as rapidly as possible. $C_1$ sets $T_2$ = 26 K and $t_{w2}$ = 1/6 h. $C_2$ sets $T_2$ = 26 K and $t_{w2}$ = 3 h. Finally, $C_3$ sets $T_2$ = 16 K and $t_{w2}$ = 3 h. Memory is quantified by comparing the magnitude of the coherence length measured at step (3) with the native coherence length [the coherence length of the initially prepared state at step (1)]. If the two lengths are the same, memory is perfect. If after step (3), the measured coherence length is smaller than the initially prepared state at step (1), memory is less, a direct result of the interference of the two states. The slopes in Figure 8 are steeper, the larger the coherence length being measured because the volume of the correlated region is larger [Eq. 1].

Consider $C_1$. The system has "morphed" from the prepared state into a chaotic regime, but only aged for a short time (1/6 h). The coherence length in the chaotic state has grown during this time, so that its interference with the initially prepared coherence length is significant. Hence, the memory is less, exhibited by the shallower slope as compared to the native slope exhibited in Figure 8. Now, $C_2$ *increases* $t_{w2}$ to 3 h, so that the coherence length in the chaotic state can grow beyond it is value in $C_1$. This should lead to greater interference, a smaller memory, and a more shallow slope than found for $C_1$. This is explicit in Figure 8.

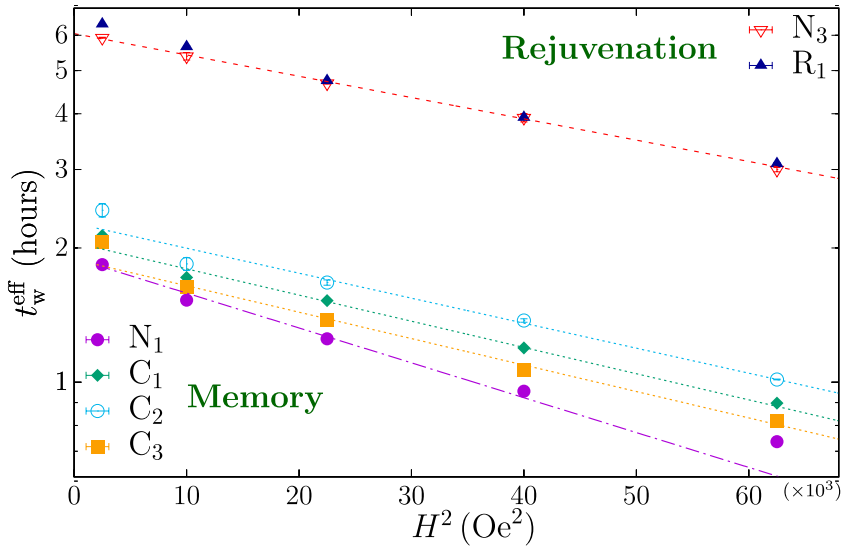


FIGURE 8
Reproduced from Figure 2 of Ref. [18]. We use the abbreviations N (native), R (rejuvenation), and C (cycle). By native, we mean the temperature is lowered from above $T_g$ (here, $T_g$ = 41.6 K to the lower temperature $T_2$ in the usual cycling protocol (here, $T_2$ = 26 K, $t_{w2}$ = 3 h), and the effective waiting time is given by the peak in $S(t)$ for different magnetic fields $H$. The points are labeled $N_3$ in Figure 8. Next, the system is cooled from above $T_g$ to the temperature $T_1$ = 30 K and aged for 1 h. The temperature is then dropped to $T_2$ = 26 K, and aged for 3 h. The points are labelled $R_1$ in Figure 8. As can be seen from the figure, the two procedures yield nearly exactly the same $t_w^{\rm eff}$ for all values of $H^2$, *independent of the aging at* $T_1$. This is a clear demonstration of rejuvenation. In addition, the spin glass coherence lengths can be extracted from the slope of $t_w^{\rm eff}$ *vs* $H^2$. One finds $\xi_{N_3}/a_0$ = 11.96 (9) and $\xi_{R_1}/a_0$ = 11.787 (8), showing the development of spin glass order is the same without and with aging at $T_1$. Memory is measured through a full temperature cycle, from $T_1$, $t_{w1} \rightarrow T_2$, $t_{w2} \rightarrow T_1$ when $t_w^{\rm eff}$ is measured as rapidly as possible. The text discusses the physical meaning for the three protocols, $C_1$, $C_2$, and $C_3$.

Finally, the $C_3$ protocol has the same $t_{w2}$ as $C_2$, but the temperature drop to $T_2$ is much greater, $T_2 = 16\,K$. At such a low temperature, the growth of the chaotic coherence length is very slow (almost none), so there should be almost no interference, and the memory should be nearly perfect. This again is explicitly exhibited in Figure 8 where the slope of $C_3$ is close to the slope for the native slope.

These three temperature cycles, and their properties exhibited in Figure 8, are strong evidence for the interpretation of memory through interfering coherence volumes. This is at odds with Ref. [46] where it is argued that the coherence length returned to the native value upon reheating. By adjusting $t_{w2}$ one can change the value of $\xi(T_1, t_{w1}, T_2, t_{w2})$ at will, from no loss to complete loss of memory. This have been born out in our Figure 8, and also in independent experiments by Freedberg et al. [47].

## 3 Summary

The purpose of this paper is to display spin glass dynamics through the lens of the spin glass coherence length. We have shown how it use can unite the seeming independent features observed both in the laboratory and through simulations. They provide a unifying picture for what seem to be independent complex phenomena.

## Data availability statement

The raw data supporting the conclusions of this article will be made available by the authors, without undue reservation.

## Author contributions

JH: Visualization, Writing–original draft, Writing–review and editing. RO: Conceptualization, Data curation, Formal Analysis, Funding acquisition, Investigation, Project administration, Resources, Supervision, Validation, Visualization, Writing–original draft, Writing–review and editing.

## Funding

The author(s) declare that financial support was received for the research, authorship, and/or publication of this article. This work has been supported by the U.S. Department of Energy, Office of Basic Energy Sciences, Division of Materials Science and Engineering, under Award DE-SC0013599.

## Acknowledgments

We thank Dr. I. Paga for a close reading of this manuscript, and for her important insights.

## Conflict of interest

The authors declare that the research was conducted in the absence of any commercial or financial relationships that could be construed as a potential conflict of interest.

The handling editor FRT declared a past co-authorship with the author RO.

## Publisher's note



## References

1. Joh YG, Orbach R, Wood GG, Hammann J, Vincent E. Extraction of the spin glass correlation length. *Phys Rev Lett* (1999) 82:438–41. doi:10.1103/PhysRevLett.82.438

2. Marinari E, Parisi G, Ruiz-Lorenzo J, Ritort F. Numerical evidence for spontaneously broken replica symmetry in 3d spin glasses. *Phys Rev Lett* (1996) 76:843–6. doi:10.1103/PhysRevLett.76.843

3. Baity-Jesi M, Calore E, Cruz A, Fernandez LA, Gil-Narvion JM, Gordillo-Guerrero A, et al. Matching microscopic and macroscopic responses in glasses. *Phys Rev Lett* (2017) 118:157202. doi:10.1103/PhysRevLett.118.157202

4. Sherrington D, Kirkpatrick S. Solvable model of a spin-glass. *Phys Rev Lett* (1975) 35:1792–6. doi:10.1103/PhysRevLett.35.1792

5. Mézard M, Parisi G, Sourlas N, Toulouse G, Virasoro M. Replica symmetry breaking and the nature of the spin glass phase. *J Phys France* (1984) 45:843–54. doi:10.1051/jphys:01984004505084300

6. Parisi G. Spin glasses and fragile glasses: statics, dynamics, and complexity. *Proc Natl Acad Sci* (2006) 103:7948–55. doi:10.1073/pnas.0601120103

7. Parisi G. Toward a mean field theory for spin glasses. *Phys Lett A* (1979) 73:203–5. doi:10.1016/0375-9601(79)90708-4

8. Parisi G. A sequence of approximated solutions to the s-k model for spin glasses. *J Phys A: Math Gen* (1980) 13:L115–21. doi:10.1088/0305-4470/13/4/009

9. Hammann J, Lederman M, Ocio M, Orbach R, Vincent E. Spin-glass dynamics Relation between theory and experiment: a beginning. *Physica A Stat Mech its Appl* (1992) 185:278–94. doi:10.1016/0378-4371(92)90467-5

10. Nordblad P, Svedlindh P, Lundgren L, Sandlund L. Time decay of the remanent magnetization in a cumn spin glass. *Phys Rev B* (1986) 33:645–8. doi:10.1103/PhysRevB.33.645

11. Baity-Jesi M, Baños R, Cruz A, Fernandez L, Gil-Narvion J, Gordillo-Guerrero A, et al. Janus ii: a new generation application-driven computer for spin-system simulations. *Comput Phys Commun* (2014) 185:550–9. doi:10.1016/j.cpc.2013.10.019

12. Baity-Jesi M, Calore E, Cruz A, Fernandez LA, Gil-Narvion JM, Gonzalez-Adalid Pemartin I, et al. Memory and rejuvenation effects in spin glasses are governed by more than one length scale. *Nat Phys* (2023) 19:978–85. doi:10.1038/s41567-023-02014-6

13. de Almeida JRL, Thouless DJ. Stability of the sherrington-kirkpatrick solution of a spin glass model. *J Phys A: Math Gen* (1978) 11:983–90. doi:10.1088/0305-4470/11/5/028

14. De Dominicis C, Giardina I. *Random fields and spin glasses: a field theory approach*. Cambridge University Press (2006). doi:10.1017/CBO9780511534836

15. Belletti F, Cotallo M, Cruz A, Fernandez LA, Gordillo-Guerrero A, Guidetti M, et al. Nonequilibrium spin-glass dynamics from picoseconds to a tenth of a second. *Phys Rev Lett* (2008) 101:157201. doi:10.1103/PhysRevLett.101.157201

16. Belletti F, Cruz A, Fernandez LA, Gordillo-Guerrero A, Guidetti M, Maiorano A, et al. An in-depth view of the microscopic dynamics of ising spin glasses at fixed temperature. *J Stat Phys* (2009) 135:1121–58. doi:10.1007/s10955-009-9727-z

17. Paga I, Zhai Q, Baity-Jesi M, Calore E, Cruz A, Fernandez LA, et al. Spin-glass dynamics in the presence of a magnetic field: exploration of microscopic properties. *J Stat Mech Theor Exp* (2021) 2021:033301. doi:10.1088/1742-5468/abdfca

18. Collaboration J, Paga I, He J, Baity-Jesi M, Calore E, Cruz A, et al. *arxiv: quantifying memory in spin glasses* (2023).

19. Paga I, Zhai Q, Baity-Jesi M, Calore E, Cruz A, Cummings C, et al. Superposition principle and nonlinear response in spin glasses. *Phys Rev B* (2023) 107:214436. doi:10.1103/PhysRevB.107.214436

20. Koper GJM, Hilhorst HJ. A domain theory for linear and nonlinear aging effects in spin glasses. *J Phys France* (1988) 49:429–43. doi:10.1051/jphys:01988004903042900

21. Fisher DS, Huse DA. Nonequilibrium dynamics of spin glasses. *Phys Rev B* (1988) 38:373–85. doi:10.1103/PhysRevB.38.373

22. Baity-Jesi M, Calore E, Cruz A, Fernandez LA, Gil-Narvion JM, Gordillo-Guerrero A, et al. Aging rate of spin glasses from simulations matches experiments. *Phys Rev Lett* (2018) 120:267203. doi:10.1103/PhysRevLett.120.267203

23. Zinn-Justin J. Quantum field theory and critical phenomena. In: *International series of monographs on physics*. Oxford University Press (2021). General theoretical arguments suggest that $z_c$ is is also $\xi$ independent at exactly $T = T_g$.

24. Zhai Q, Harrison DC, Tennant D, Dahlberg ED, Kenning GG, Orbach RL. Glassy dynamics in cumn thin-film multilayers. *Phys Rev B* (2017) 95:054304. doi:10.1103/PhysRevB.95.054304

25. Kenning GG, Tennant DM, Rost CM, da Silva FG, Walters BJ, Zhai Q, et al. End of aging as a probe of finite-size effects near the spin-glass transition temperature. *Phys Rev B* (2018) 98:104436. doi:10.1103/PhysRevB.98.104436

26. Zhai Q, Martin-Mayor V, Schlagel DL, Kenning GG, Orbach RL. Slowing down of spin glass correlation length growth: simulations meet experiments. *Phys Rev B* (2019) 100:094202. doi:10.1103/PhysRevB.100.094202

27. Malozemoff AP, Barbara B, Imry Y. Further studies of nonlinear susceptibility of GdAl and MnCu spin glasses. *J Appl Phys* (1982) 53:2205–7. doi:10.1063/1.330818

28. Malozemoff AP, Imry Y, Barbara B. Scaling of susceptibility and the size of the critical region in an amorphous GdAl spin glass (invited). *J Appl Phys* (1982) 53:7672–7. doi:10.1063/1.330179

29. Chandra P, Coleman P, Ritchey I. The anisotropic kagome antiferromagnet: a topological spin glass? *J Phys France* (1993) 3:591–610. doi:10.1051/jp1:1993104

30. Lévy LP, Ogielski AT. Nonlinear dynamic susceptibilities at the spin-glass transition of ag:mn. *Phys Rev Lett* (1986) 57:3288–91. doi:10.1103/PhysRevLett.57.3288

31. Lévy LP. Critical dynamics of metallic spin glasses. *Phys Rev B* (1988) 38:4963–73. doi:10.1103/PhysRevB.38.4963

32. Baity-Jesi M, Baños RA, Cruz A, Fernandez LA, Gil-Narvion JM, Gordillo-Guerrero A, et al. Critical parameters of the three-dimensional ising spin glass. *Phys Rev B* (2013) 88:224416. doi:10.1103/PhysRevB.88.224416

33. Bert F, Dupuis V, Vincent E, Hammann J, Bouchaud JP. Spin anisotropy and slow dynamics in spin glasses. *Phys Rev Lett* (2004) 92:167203. doi:10.1103/PhysRevLett.92.167203

34. Fernandez LA, Marinari E, Martin-Mayor V, Parisi G, Yllanes D. Temperature chaos is a non-local effect. *J Stat Mech Theor Exp* (2016) 2016:123301. doi:10.1088/1742-5468/2016/12/123301

35. Sasaki M, Nemoto K. Memory effect, rejuvenation and chaos effect in the multi-layer random energy model. *J Phys Soc Jpn* (2000) 69:2283–90. doi:10.1143/JPSJ.69.2283

36. Sasaki M, Martin OC. Discreteness and entropic fluctuations in generalized-random-energy-model-like systems. *Phys Rev B* (2002) 66:174411. doi:10.1103/PhysRevB.66.174411

37. Sales M, Bouchaud JP, Ritort F. Temperature shifts in the sinai model: static and dynamical effects. *J Phys A: Math Gen* (2003) 36:665–84. doi:10.1088/0305-4470/36/3/306

38. Rizzo T. Ultrametricity between states at different temperatures in spin-glasses. *Eur Phys J B* (2002) 29:425–35. doi:10.1140/epjb/e2002-00274-x

39. Zhai Q, Orbach RL, Schlagel DL. Evidence for temperature chaos in spin glasses. *Phys Rev B* (2022) 105:014434. doi:10.1103/PhysRevB.105.014434

40. Baity-Jesi M, Calore E, Cruz A, Fernandez LA, Gil-Narvion J, Gonzalez-Adalid Pemartin I, et al. Temperature chaos is present in off-equilibrium spin-glass dynamics. *Commun Phys* (2021) 4:74. doi:10.1038/s42005-021-00565-9

41. Bray AJ, Moore MA. Chaotic nature of the spin-glass phase. *Phys Rev Lett* (1987) 58:57–60. doi:10.1103/PhysRevLett.58.57

42. Jönsson PE, Yoshino H, Nordblad P. Symmetrical temperature-chaos effect with positive and negative temperature shifts in a spin glass. *Phys Rev Lett* (2002) 89:097201. doi:10.1103/PhysRevLett.89.097201

43. Kondor I. On chaos in spin glasses. *J Phys A: Math Gen* (1989) 22:L163–8. doi:10.1088/0305-4470/22/5/005

44. Billoire A, Coluzzi B. Magnetic field chaos in the sherrington-kirkpatrick model. *Phys Rev E* (2003) 67:036108. doi:10.1103/PhysRevE.67.036108

45. Jonason K, Vincent E, Hammann J, Bouchaud JP, Nordblad P. Memory and chaos effects in spin glasses. *Phys Rev Lett* (1998) 81:3243–6. doi:10.1103/PhysRevLett.81.3243

46. Bouchaud JP, Dupuis V, Hammann J, Vincent E. Separation of time and length scales in spin glasses: temperature as a microscope. *Phys Rev B* (2001) 65:024439. doi:10.1103/PhysRevB.65.024439

47. Freedberg J, Meese WJ, He J, Schlagel DL, Dahlberg ED, Orbach RL. *arxiv: on the nature of memory and rejuvenation in glassy systems* (2023).

frontiers | Frontiers in Physics

TYPE Mini Review
PUBLISHED 16 August 2024
DOI 10.3389/fphy.2024.1448175



OPEN ACCESS

EDITED BY
Gregory Kenning,
Indiana University of Pennsylvania,
United States

REVIEWED BY
Raymond Orbach,
The University of Texas at Austin, United States

*CORRESPONDENCE
Martin Weigel,
martin.weigel@physik.tu-chemnitz.de

RECEIVED 12 June 2024
ACCEPTED 01 July 2024
PUBLISHED 16 August 2024

CITATION
Münster L and Weigel M (2024), Spin glasses and percolation.
*Front. Phys.* 12:1448175.
doi: 10.3389/fphy.2024.1448175



# Spin glasses and percolation

Lambert Münster and Martin Weigel*

Institut für Physik, Technische Universität Chemnitz, Chemnitz, Germany

The description of thermodynamic phase transitions in terms of percolation transitions of suitably defined clusters has a long tradition and boasts a number of important successes, the most prominent ones being in ferromagnetic lattice models. Spin glasses and other frustrated systems are not among them as the clusters of aligned spins usually considered in this context start to percolate in the disordered phase and hence fail to indicate the onset of ordering. In this mini-review we provide an overview of the state of the art in this field, including recent advances, and outline the main open questions in the area.

KEYWORDS

**spin glasses, percolation, lattice models, Monte Carlo simulations, phase transitions, quenched disorder**

## 1 Introduction

Percolation models were first proposed and studied by Flory and Stockmeyer in the context of polymer gelation [1, 2], and they have found applications in an astonishingly broad range of areas, from forest fires [3], over porous media in oil fields [4], to electric conductivity [5] and all the way to complex networks [6]. For lattice systems, Broadbent and Hammersley [7] first proposed the idea of what is today known as *bond percolation*, where the edges of a lattice are occupied at random with a probability $p$, and the resulting structure of connected components is investigated [8]. This model provides one of the simplest and most fundamental examples of a (usually continuous) phase transition. For percolation, the transition is characterized by the appearance of a spanning or *incipient percolating* cluster that connects opposite edges of the system and is of infinite size in the thermodynamic limit. At the transition point, $p_c$, clusters exist on all length scales and the system is correlated up to the largest distances, forming a (stochastic) self-similar fractal [3].

This behavior is reminiscent of the spatial correlations observed in other systems near criticality, for instance in the magnetic ordering transition of lattice spin models [9]. In view of the success and intuitive appeal of the percolation picture, it has been a longstanding goal in the description of phase transitions and critical phenomena to represent the ordering process in general systems as a percolation transition of suitably defined structures or *droplets* in the substance that form as the phase changes [10]. Fisher proposed a model [11] that postulated droplets of a certain free energy whose average size diverges at the critical point and that feature a cluster size distribution whose exponents are related to the critical indices of the thermal transition. A microscopic definition of such droplets, however, was initially not available. While it was clear that they must correspond to a spatially *correlated* percolation problem, it soon became clear that the clusters (connected components) of like spins do *not* fit Fisher's description as they percolate away from the thermal critical point [12]. Coniglio and Klein [13] first realized that suitable clusters resulted from a merely *probabilistic* occupation of bonds between like spins if the occupation probability was chosen as $p = 1 - \exp(-2\beta J)$, where $\beta$ is the inverse temperature and $J$ denotes the ferromagnetic exchange coupling. Independently, Fortuin and Kasteleyn [14] had provided a representation of the Potts model in form of a correlated percolation model that contained the same cluster definition. The resulting

Fortuin-Kasteleyn-Coniglio-Klein (FKCK) clusters percolate at the thermal transition point and their structure encodes the nature of spin-spin correlations. They are also the basis for powerful numerical simulation schemes in form of the cluster algorithms of Swendsen and Wang [15] as well as Wolff [16].

While these ideas are rather straightforwardly generalized from Ising to Potts variables, as well as to continuous spins [16], and even to disordered ferromagnets [17], they fail as soon as competing interactions and frustration come into play [18, 19]. Further, while FKCK clusters can be easily generalized to this case by focusing on (parallel or antiparallel) spin pairs with *satisfied* bonds, it is found that in three dimensions such clusters percolate far away from the spin-glass transition point as they, in fact, do *not* encode the relevant correlations at the spin-glass transition [20]. Instead, it has been proposed that one should consider cluster definitions based on overlap variables, as they encode the order parameter of the spin-glass transition [21]. Further, it appears that a more subtle property of clusters than the mere onset of percolation might be associated with the occurrence of the spin-glass transition. Only in two dimensions, where the situation is somewhat different as the spin-glass transition is shifted to zero temperature, does one observe for some types of overlap-based clusters the percolation points asymptotically approach the spin-glass transition [22].

Based on some of these observations, a number of cluster-update algorithms for spin glasses have been proposed, the general target being to ensure that the updated clusters undergo a percolation transition at or close to the spin-glass transition, and that the structure of clusters encodes the correlations of the underlying spin model. A general solution to this problem has not been found to date, but some approaches provide reasonably good performance for systems in two dimensions [23], for spin glasses on diluted lattices [24], or for an intermediate size range in three and higher dimensions [25]. In the remainder of this mini-review, we will provide a more detailed discussion of the connection between percolation and the spin-glass transition and the simulation algorithms based on these observations.

## 2 Spin clusters

While some of what is discussed below can be generalized to the cases of Potts spins as well as continuous models such as the *XY* and Heisenberg spin glasses, to be specific we focus on the case of the short-range (Edwards-Anderson) Ising spin glass with Hamiltonian [26]

$$\mathcal{H} = -\sum_{\langle i,j\rangle} J_{ij}\sigma_i\sigma_j, \tag{1}$$

where $\sigma_i = \pm 1$ and the sum is taken over nearest-neighbor pairs of the lattice only. To allow for a spin-glass phase, the distribution of the quenched couplings $J_{ij}$ should include values of both signs, the most common cases being the bimodal and Gaussian distributions. In a natural generalization from the cases of ferromagnetic Ising and Potts models, FKCK clusters may be constructed for such a system by occupying bonds between *satisfied* spin pairs, i.e., those with $J_{ij}\sigma_i\sigma_j > 0$, with probability

$$p_{\mathrm{FKCK}} = 1 - \exp\left[-2\beta|J_{ij}|\right]. \tag{2}$$

There is clear numerical evidence that such clusters percolate at temperatures far above the spin-glass transition, for instance at $T_{\mathrm{c,FKCK}} = 3.934\,(3)$ for the three-dimensional symmetric $\pm J$ model [19, 20] as compared to the spin-glass transition temperature at $T_{\mathrm{SG}} = 1.101\,(5)$ [27] (a similar difference is expected for the model with Gaussian couplings). In two dimensions, these clusters percolate at $T_{\mathrm{SG}} = 1.1894\,(3)$ for the Gaussian model [22], while the spin-glass transition only occurs for $T \to 0$ [28]. More generally, for a bimodal model with a fraction $x$ of antiferromagnetic bonds with $J_{ij} < 0$, a coincidence of the percolation transition and the thermal transition point is only observed for $x = 0$ [20]. This behavior is rather plausible since FKCK clusters do not represent the relevant spin correlations in these systems. While for the ferromagnet [29]

$$\langle s_i s_j\rangle = \mathrm{Prob}\,(i \text{ and } j \text{ are connected by occupied bonds}), \tag{3}$$

the situation for spin glasses is more subtle, and one can show that in this case [21, 30]

$$\begin{aligned}\langle s_i s_j\rangle = {} & \mathrm{Prob}\,(i \text{ and } j \text{ are connected by an even number}\\ & \text{of occupied antiferromagnetic bonds})\\ & -\mathrm{Prob}\,(i \text{ and } j \text{ are connected by an odd number}\\ & \text{of occupied antiferromagnetic bonds}).\end{aligned} \tag{4}$$

Hence, the percolation of FKCK clusters no longer implies the presence of long-range order. Since the percolation transition of FKCK clusters does not encode spin-glass criticality (but see Ref. [31] for a possible connection to damage spreading), it is expected that it is in the universality class of random percolation, and this expectation is borne out by the results of numerical simulation studies [20, 22, 32] as well as rigorous analysis [33, 34].

## 3 Overlap clusters

This failure is not surprising in view of the fact that the magnetization is no order parameter for the spin-glass transition and, instead, for its description one needs to turn to *overlap* variables [35]. Several cluster definitions have been suggested based on the site or link overlap of two spin configurations using the same disorder realization. Initially in the context of random-field models, Chayes, Machta and Redner [36] proposed a representation where doubly satisfied ("blue") bonds in a two-replica representation are occupied with a probability

$$p_{\mathrm{CMR,blue}} = 1 - \exp\left[-4\beta|J_{ij}|\right], \tag{5}$$

while, additionally, singly satisfied ("red") bonds are occupied with probability

$$p_{\mathrm{CMR,red}} = 1 - \exp\left[-2\beta|J_{ij}|\right].$$

Then, it is possible to relate the percolation properties of such clusters to the occurrence of symmetry breaking of the spin system [21]: in contrast to the ferromagnet, where the appearance of a percolating cluster suffices to indicate the onset of the ordered phase, for spin glass there should be a "blue" cluster of strictly larger density than any other cluster [37]. In practise, one observes the occurrence

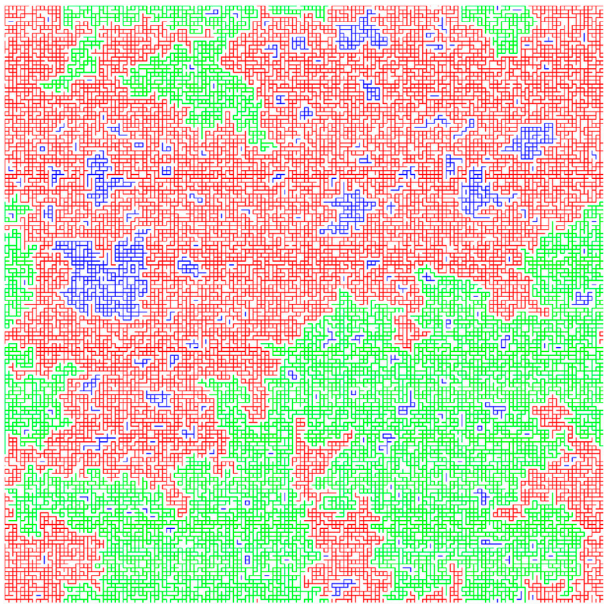

FIGURE 1
Typical configuration of CMR "blue" clusters in a sample of the 2D Gaussian Edwards-Anderson spin-glass model at low temperature ($\beta = 3$). The red and green bonds correspond to the largest and second largest clusters, respectively.

of *two* percolating clusters of opposite overlap that develop a density difference at the spin-glass transition [21, 22]. A corresponding overlap configuration is shown in Figure 1 for the example of the 2D Gaussian spin glass, illustrating that there are mainly two large clusters of opposite overlap, with any further clusters being much smaller. If the weight of such smaller clusters diminishes for systems of increasing sizes, the overlap $q$ (i.e., the order parameter) is connected to the density difference of the two largest clusters. This is rigorously the case in the mean-field Sherrington-Kirkpatrick model [21], and numerical data in 3D [21] and 2D [22] are also consistent with such a picture—for the 2D case this is demonstrated by the data shown in Figure 2 that consist of the densities of the three largest clusters as a function of inverse temperature and for different lattice sizes. The onset of percolation of CMR blue clusters itself again occurs away from the spin-glass transition, with $T_{\mathrm{c,CMR}} \approx 3.85$ for the 3D bimodal model [21] (which is surprisingly close to $T_{\mathrm{c,FKCK}}$); in 2D the CMR percolation temperatures of finite lattices converge to $T = 0$ for $L \to \infty$ [22], consistent with the spin-glass transition temperature there.

Another possible cluster definition based on the overlap of two replicas results from a simple duplication of the FKCK construction on the two spin configurations, i.e., bonds are occupied independently in the two replicas according to the FKCK probability (Eq. 2), and clusters are constructed over all bonds simultaneously occupied in *both* replicas [38]. This is equivalent to a bond occupation probability

$$p_{\mathrm{TRFK}} = \left(1 - \exp\left[-2\beta|J_{ij}|\right]\right)^2 \tag{6}$$

for doubly satisfied bonds. Such clusters might be referred to as two-replica Fortuin-Kasteleyn (TRFK) clusters. These clusters behave rather similarly to the CMR ones [21, 22], which is not surprising as they follow the same construction apart from the smaller bond occupation probability $p_{\mathrm{TRFK}} \leq p_{\mathrm{CMR,blue}}$. The latter leads to a significant suppression of the percolation point which now occurs for $T_{\mathrm{c,TRFK}} \approx 1.77$ [21].

Finally, a cluster definition based on a *site* percolation problem rather that a *bond* percolation one was first proposed in connection with a specific cluster-update algorithm for spin glasses in 2D [23]. There, clusters are grown in regions of constant overlap, and neighboring sites of the same overlap are *unconditionally* added to the cluster, such that the effective bond occupation probability is

$$p_{\mathrm{Houdayer}} = 1.$$

One might hence think of these as some form of *geometric clusters* in overlap space [39]. The CMR and TRFK clusters clearly are subregions of the Houdayer clusters as for the latter one does not take into account whether a given bond is satisfied or not. In many 3D lattices such as the simple cubic one, such clusters percolate already for $T_{\mathrm{c,Houdayer}} = \infty$ as their site percolation thresholds are $p_{\mathrm{c}} < 0.5$. Hence they have not been studied in much detail there. In 2D, on the other hand, they again percolate at a sequence of temperatures that approaches $T_{\mathrm{SG}} = 0$, but they are found to be in general larger that the CMR and TRFK clusters [22].

## 4 Cluster updates

In view of the spectacular success of cluster updates in alleviating critical slowing down for ferromagnetic spin models [15, 16] it has been a natural idea to use cluster moves to counter the dramatically slow dynamics observed in spin-glass systems. In fact, the first proposal in this direction [40] even (slightly) predates the ferromagnetic algorithms. Unfortunately, the cluster component in this approach was not found to be extremely efficient, while the replica component eventually lead to the development of the replica exchange or parallel tempering method [41, 42] that is the *de facto* standard for spin-glass simulations.

Houdayer's proposal [23] for a cluster update for 2D models was in this sense more successful. Geometric clusters are constructed in the way described above, by connecting neighboring sites of equal overlap, and an update consists of flipping the spins inside a cluster in *both* replicas. Crucially, such updates can be performed unconditionally, i.e., without adding an extra acceptance step, since they leave the total energy of the replicated system invariant. Usage of more than two replicas (per temperature) is possible, but usually not found to be efficient computationally [43]. Due to the fixed energy, it is clear that such updates are not ergodic, and hence need to be complemented, e.g., by single-spin flip moves. While this approach works well on the square lattice, where the percolation threshold $p_{\mathrm{c}} \approx 0.59 > \frac{1}{2}$ and the percolation points of Houdayer clusters approach $T_{\mathrm{SG}} = 0$ for $L \to \infty$ [22], the method is not very efficient in 3D, which is blamed on the fact that, for most lattices in 3D, $p_{\mathrm{c}} < \frac{1}{2}$ [23]. In an attempt to improve on this aspect, Zhu et al. [25] proposed a modification of Houdayer's method where

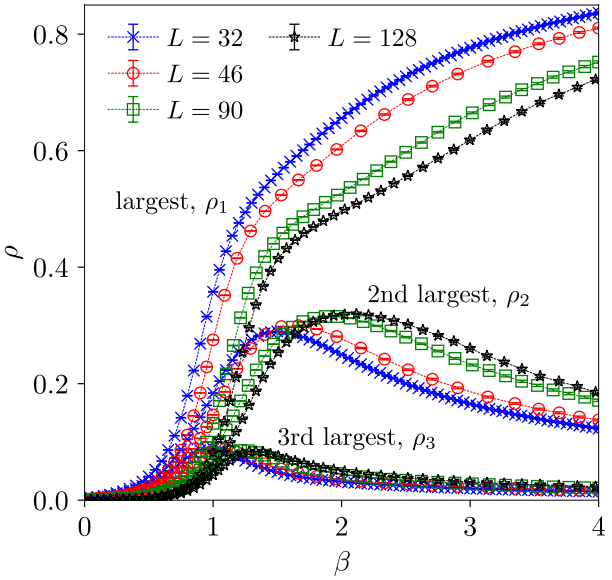


FIGURE 2
Average densities $\rho$ of the largest three CMR clusters in the 2D Gaussian Edwards-Anderson spin-glass model as a function of inverse temperature $\beta$ for different lattice sizes $L$. At low temperatures, the combined weight of the two largest clusters increases with $L$.

they grow a single cluster in the *minority* phase of the overlap, which is claimed to somewhat improve the performance in 3D. More recently, the cluster selection for updates has been scrutinized in a multi-cluster version of the algorithm discussed in the context of combinatorial optimization problems [44], a close relative of spin-glass problems (see, e.g., Ref. [45]).

The CMR representation also suggests several cluster updates. Constructing only the blue clusters, these can flip freely as the cluster construction rules together with the bond occupation probability (Eq. 5) mean that the update satisfies detailed balance with respect to the equilibrium distribution [22]. This was used by Jörg [24] to efficiently simulate spin glasses on diluted lattices, leading to overall smaller clusters. By construction, however, the update is not ergodic since spins connected by (partially) unsatisfied bonds cannot be updated. An extension proposed in Ref. [36] (see also [21]) uses both red and blue bonds to construct blue and *grey* clusters, leading to a rejection-free and ergodic update which, however, is still found to be relatively inefficient due to the onset of cluster percolation above $T_{SG}$ [21].

## 5 Discussion

While a percolation perspective onto spin glasses and other frustrated systems has not led to the same level of revolutionary success this approach has seen for ferromagnets, significant progress has been possible. The cluster construction rules used for ferromagnets (Fortuin-Kasteleyn–Coniglio-Klein), while applicable to spin glasses, do not lead to structures that reflect spin-glass correlations. Instead, clusters must be constructed in overlap space, corresponding to the order parameter of the spin-glass transition. While there is no one-to-one correspondence between the spin-glass transition and a simple percolation transition of a cluster type that has been investigated to date, an intriguing picture has emerged: for the CMR and TRFK clusters defined on two replicas *two* equally large percolating clusters appear significantly above the spin-glass transition, and it is only at the spin-glass transition that their densities start to differ [21, 22]. It appears that below the percolation point smaller clusters beneath the two dominating ones are asymptotically irrelevant.

Regarding cluster updates, a fundamentally efficient algorithm only exists in two dimensions, while attempts for more general, and in particular, 3D systems have only partially been successful. While some improved results where found in cases where the average sizes of clusters constructed are reduced such as in diluted systems [24] or with algorithmic modifications [25], it is not fully clear whether such size reduction is a sufficient condition for improving performance.

In view of this state of affairs a number of interesting questions remain to be addressed in future studies. Is it possible to construct clusters that percolate at or very close to the temperature of the spin-glass transition? One promising direction in this respect is the study of *multi-replica* overlaps [22]. In view of Eq. 6 it is clear that, depending on their precise construction, such clusters could percolate at lower and lower temperatures as the number of replicas is increased. Regarding the algorithms, it was seen that for blue clusters there are two very dominant large clusters in the vicinity of the glass transition, such that in contrast to the ferromagnetic case close to the transition there is no multi-scale nature of spin updates for such blue clusters close to the spin-glass transition. This is likely the prime reason for the unsatisfactory performance of such algorithms. In contrast, for Houdayer's algorithm and its extensions, what is the cluster-size distribution? How do multi-cluster variants of such algorithms perform as compared to the default single-cluster ones? Answers to (some of) these questions hold the potential for significantly advancing our understanding of the spin-glass transition while simultaneously facilitating much improved efficiency in simulating spin-glass systems with the hope of answering some more of the fundamental open questions of this field.

## Author contributions

LM: Conceptualization, Investigation, Writing–original draft, Writing–review and editing. MW: Conceptualization, Investigation, Writing–original draft, Writing–review and editing.

## Funding

The authors declare that no financial support was received for the research, authorship, and/or publication of this article.

## Conflict of interest

The authors declare that the research was conducted in the absence of any commercial or financial relationships that could be construed as a potential conflict of interest.

## Publisher's note



## References

1. Flory PJ. Molecular size distribution in three dimensional polymers. I. Gelation. *J Am Chem Soc* (1941) 63:3083–90. doi:10.1021/ja01856a061

2. Stockmayer WH. Theory of molecular size distribution and gel formation in branched-chain polymers. *J Chem Phys* (1943) 11:45–55. doi:10.1063/1.1723803

3. Stauffer D, Aharony A. *Introduction to percolation theory*. 2nd ed. London: Taylor and Francis (1994).

4. King P, Buldyrev S, Dokholyan NV, Havlin S, Lee Y, Paul G, et al. Predicting oil recovery using percolation theory. *Pet Geosci* (2001) 7:S105–S107. doi:10.1144/petgeo.7.s.s105

5. Efros A, Shklovskii BI. Critical behaviour of conductivity and dielectric constant near the metal-non-metal transition threshold. *Phys Status Solidi B* (1976) 76:475–85. doi:10.1002/pssb.2220760205

6. Cohen R, Erez K, Ben-Avraham D, Havlin S. Resilience of the internet to random breakdowns. *Phys Rev Lett* (2000) 85:4626–8. doi:10.1103/physrevlett.85.4626

7. Broadbent SR, Hammersley JM. (1957). Percolation processes: I. Crystals and mazes. *Math Proc Camb Phil Soc* 53, 629–41. (Cambridge University Press), doi:10.1017/s0305004100032680

8. Grimmett G. *The random-cluster model*. Berlin: Springer (2006).

9. McCoy BM, Wu TT. *The two-dimensional Ising model*. Massachusetts: Harvard University Press (1973).

10. Stanley HE, Ostrowsky N. Correlations and connectivity: geometric aspects of physics. In: *Chemistry and biology, vol. 188 of NATO Science Series E*. Springer (1990).

11. Fisher ME. The theory of condensation and the critical point. *Physics* (1967) 3:255–83. doi:10.1103/physicsphysiquefizika.3.255

12. Müller-Krumbhaar H. Percolation in a lattice system with particle interaction. *Phys Lett A* (1974) 50:27–8. doi:10.1016/0375-9601(74)90337-5

13. Coniglio A, Klein W. Clusters and Ising critical droplets: a renormalisation group approach. *J Phys A* (1980) 13:2775–80. doi:10.1088/0305-4470/13/8/025

14. Fortuin CM, Kasteleyn PW. On the random-cluster model I. Introduction and relation to other models. *Physica* (1972) 57:536–64. doi:10.1016/0031-8914(72)90045-6

15. Swendsen RH, Wang JS. Nonuniversal critical dynamics in Monte Carlo simulations. *Phys Rev Lett* (1987) 58:86–8. doi:10.1103/PhysRevLett.58.86

16. Wolff U. Collective Monte Carlo updating for spin systems. *Phys Rev Lett* (1989) 62:361–4. doi:10.1103/PhysRevLett.62.361

17. Ballesteros HG, Fernández LA, Martín-Mayor V, Muñoz Sudupe A, Parisi G, Ruiz-Lorenzo JJ. Critical exponents of the three dimensional diluted Ising model. *Phys Rev B* (1998) 58:2740–7. doi:10.1103/physrevb.58.2740

18. Kessler DA, Bretz M. Unbridled growth of spin-glass clusters. *Phys Rev B* (1990) 41:4778–80. doi:10.1103/PhysRevB.41.4778

19. De Arcangelis L, Coniglio A, Peruggi F. Percolation transition in spin glasses. *EPL* (1991) 14:515–9. doi:10.1209/0295-5075/14/6/003

20. Fajen H, Hartmann AK, Young AP. Percolation of Fortuin-Kasteleyn clusters for the random-bond Ising model. *Phys Rev E* (2020) 102:012131. doi:10.1103/PhysRevE.102.012131

21. Machta J, Newman CM, Stein DL. The percolation signature of the spin glass transition. *J Stat Phys* (2008) 130:113–28. doi:10.1007/s10955-007-9446-2

22. Münster L, Weigel M. Cluster percolation in the two-dimensional Ising spin glass. *Phys Rev E* (2023) 107:054103. doi:10.1103/physreve.107.054103

23. Houdayer J. A cluster Monte Carlo algorithm for 2-dimensional spin glasses. *Eur Phys J B* (2001) 22:479–84. doi:10.1007/PL00011151

24. Jörg T. Cluster Monte Carlo algorithms for diluted spin glasses. *Prog Theor Phys Supp* (2005) 157:349–52. doi:10.1143/ptps.157.349

25. Zhu Z, Ochoa AJ, Katzgraber HG. Efficient cluster algorithm for spin glasses in any space dimension. *Phys Rev Lett* (2015) 115:077201. doi:10.1103/physrevlett.115.077201

26. Edwards SF, Anderson PW. Theory of spin glasses. *J Phys F* (1975) 5:965–74. doi:10.1088/0305-4608/5/5/017

27. Hasenbusch M, Pelissetto A, Vicari E. The critical behavior of 3D Ising spin glass models: universality and scaling corrections. *J Stat Mech Theor Exp* (2008) 2008:L02001. doi:10.1088/1742-5468/2008/02/l02001

28. Hartmann AK, Young AP. Lower critical dimension of Ising spin glasses. *Phys Rev B* (2001) 64:180404. doi:10.1103/physrevb.64.180404

29. Edwards RG, Sokal AD. Generalization of the Fortuin-Kasteleyn-Swendsen-Wang representation and Monte Carlo algorithm. *Phys Rev D* (1988) 38:2009–12. doi:10.1103/PhysRevD.38.2009

30. Coniglio A, di Liberto F, Monroy G, Peruggi F. Cluster approach to spin glasses and the frustrated-percolation problem. *Phys Rev B* (1991) 44:12605–8. doi:10.1103/physrevb.44.12605

31. Lundow PH, Campbell I. Fortuin-Kasteleyn and damage-spreading transitions in random-bond Ising lattices. *Phys Rev E* (2012) 86:041121. doi:10.1103/physreve.86.041121

32. Imaoka H, Ikeda H, Kasai Y. Percolation transition in two-dimensional ±J Ising spin glasses. *Physica A* (1997) 246:18–26. doi:10.1016/s0378-4371(97)00351-8

33. De Santis E, Gandolfi A. Bond percolation in frustrated systems. *Ann Prob* (1999) 27:1781–808. doi:10.1214/aop/1022677548

34. Gandolfi A. A remark on gauge symmetries in Ising spin glasses. *Probab Theor Relat. Fields* (1999) 114:419–30. doi:10.1007/s004400050230

35. Parisi G. Infinite number of order parameters for spin-glasses. *Phys Rev Lett* (1979) 43:1754–6. doi:10.1103/physrevlett.43.1754

36. Chayes L, Machta J, Redner O. Graphical representations for Ising systems in external fields. *J Stat Phys* (1998) 93:17–32. doi:10.1023/b:joss.0000026726.43558.80

37. Machta J, Newman CM, Stein DL. A percolation-theoretic approach to spin glass phase transitions. In: de Monvel AB, Bovier A, editors. *Spin glasses: statics and dynamics*. Basel: Birkhäuser (2009). p. 205.

38. Newman CM, Stein DL. Short-range spin glasses: results and speculations. In: Bolthausen E, Bovier A, editors. *Spin glasses*. Berlin, Heidelberg: Springer (2007). p. 159.

39. Akritidis M, Fytas NG, Weigel M. Geometric clusters in the overlap of the Ising model. *Phys Rev E* (2023) 108:044145. doi:10.1103/physreve.108.044145

40. Swendsen RH, Wang JS. Replica Monte Carlo simulation of spin glasses. *Phys Rev Lett* (1986) 57:2607–9. doi:10.1103/physrevlett.57.2607

41. Geyer CJ. Markov chain Monte Carlo maximum likelihood. In: *Computing science and statistics: proceedings of the 23rd symposium on the interface*. New York: American Statistical Association (1991). p. 156–163.

42. Hukushima K, Nemoto K. Exchange Monte Carlo method and application to spin glass simulations. *J Phys Soc Jpn* (1996) 65:1604–8. doi:10.1143/JPSJ.65.1604

43. Kumar R, Gross J, Janke W, Weigel M. Massively parallel simulations for disordered systems. *Eur Phys J B* (2020) 93:79–13. doi:10.1140/epjb/e2020-100535-0

44. Vandenbroucque A, Chiacchio EIR, Munro E. *The Houdayer algorithm: overview, extensions, and applications* Preprint arXiv:2211 (2022). p. 11556.

45. Perera D, Hamze F, Raymond J, Weigel M, Katzgraber HG. Computational hardness of spin-glass problems with tile-planted solutions. *Phys Rev E* (2020) 101:023316. doi:10.1103/PhysRevE.101.023316

frontiers | Frontiers in Physics

TYPE Original Research
PUBLISHED 27 August 2024
DOI 10.3389/fphy.2024.1443298



OPEN ACCESS

EDITED BY
Constantinos Simserides,
National and Kapodistrian University of Athens, Greece

REVIEWED BY
Maciej Sawicki,
Polish Academy of Sciences, Poland
Katarzyna Gas,
Tohoku University, Japan

*CORRESPONDENCE
G. G. Kenning,
gregory.kenning@iup.edu

RECEIVED 03 June 2024
ACCEPTED 26 July 2024
PUBLISHED 27 August 2024

CITATION
Kenning GG, Brandt M, Brake R, Hepler M and Tennant D (2024) Observation of critical scaling in spin glasses below $T_c$ using thermoremanent magnetization.
*Front. Phys.* 12:1443298.
doi: 10.3389/fphy.2024.1443298



# Observation of critical scaling in spin glasses below $T_c$ using thermoremanent magnetization

G. G. Kenning[1]*, M. Brandt[1], R. Brake[1], M. Hepler[1] and D. Tennant[2]

[1]Madia Department of Chemistry, Biochemistry, Physics and Engineering, Indiana University of Pennsylvania, Indiana, PA, United States, [2]Texas Materials Institute, The University of Texas at Austin, Austin, TX, United States

Time-dependent thermoremanent magnetization (TRM) studies have been instrumental in probing energy dynamics within the spin glass phase. In this paper, we review the evolution of the TRM experiment over the last half century and discuss some aspects related to how it has been used in the understanding of spin glasses. We also report on recent experiments using high-resolution DC SQUID magnetometry to probe the TRM at temperatures less than but near to the transition temperature $T_c$. These experiments have been performed as a function of waiting time, temperature, and five different magnetic fields. We find that as the transition temperature is approached from below, the characteristic time scale of TRM is suppressed up to several orders of magnitude in time. In the highest-temperature region, we find that the waiting time effect subsides, and a waiting time-independent crossover line is reached. We also find that increasing the magnetic field further suppresses the crossover line. Using a first-principles energy argument across the crossover line, we derive an equation that is an excellent fit to the crossover lines for all magnetic fields probed. The data show strong evidence for critical slowing down and an $H = 0$ *Oe* phase transition.

KEYWORDS

**spin glass dynamics, critical dynamics, phase transition, scaling theory, critical slowing down, coherence length**

## 1 Introduction

The main goal of this paper is to present the data and analysis which use the thermoremanent magnetization (TRM) waiting time effect in spin glasses as a probe of the critical region near the spin glass phase transition. In the spirit of this collection, we begin with a brief historical perspective and a primer on several magnetic signatures found in spin glasses. This introductory section includes a description of the experiments, field cooled/zero field cooled (FC/ZFC) and field cooled-thermoremanent magnetization/zero field cooled magnetization (FC-TRM/ZFC-TRM), the waiting time effect, and the relationships between them. We then review the structure of the FC-TRM decay and discuss several experiments and simulations that are important for understanding the data and the analysis to follow. This is not meant to be a comprehensive review. Since the measurements presented in this paper represent an improvement in experimental design and an improved signal-to-noise ratio, Section 2, *Experimental methods*, is more detailed and may be of use to experts in the field. Finally, in Section 3 and Section 4, we present the data and analysis which encompass using the TRM and waiting time effect in spin glasses as a probe of the critical region near the spin glass phase transition.

The history of experimental and numerical studies in spin glasses follows the development of technology itself, and it can be argued that the challenges of exploring the nature of the spin glass phase have driven aspects of technology forward. Early numerical studies on this NP hard problem [1] began in the 1980s with simulations on smaller than 16 spins. Today, with the advent of large-scale computing, dedicated computers, and advances in algorithms, simulations are done with more than $1.67x10^7$ spins [2]. Even as we reach toward large-scale neural networks [3] and quantum computing [4], the spin glass algorithm is seen as a fundamental starting point.

From the experimental side, in small magnetic fields, the spin glass state has, by its random nature, a small magnetic signal. Elucidating the much smaller time dependencies of the magnetization signals makes the measurement sensitivity of primary importance. These signals approach zero at several limits, ($H \rightarrow 0\ Oe$, $T \rightarrow T_g$, and $t \rightarrow \infty$), making the signal-to-noise ratio crucial in investigations of these limits. Over the last five decades, spin glass experiments have increased orders of magnitude in their sensitivity, stability, and time scales. From direct Faraday-effect measurements to AC measurements with lock in amplifiers, RF SQUIDS, and DC SQUIDS, sensitivity has increased, and new regions of the spin glass state have become accessible. The PC control of the experiments now allows us to perform experiments that were not possible before 1980. We can now perform many automated experiments with temperatures controlled to the ± $\mu$K resolution for long periods of time.

The first TRM measurements were made by [5], using Faraday techniques, only 2 years after the discovery of the spin glass phase [6]. This measurement was made by cooling the spin glass below its transition temperature, in a magnetic field, to a measuring temperature. These measurements were often made by physically pulling the sample out of a sensing coil, thereby inducing a magnetic flux change in the coil and then electronically integrating the signal to obtain total magnetization. Other "static" measurements then evolved, including the first field-cooled/zero field-cooled (FC/ZFC) measurements. They were performed on $Gd_{0.37}Al_{0.63}$ [7] and shortly afterward on the "canonical" spin glasses AuFe [8] and CuMn [9], cementing the FC/ZFC magnetization curves as a spin glass signature. This measurement became a quick way of determining the approximate spin glass transition temperature with both a peak in the ZFC and the onset of irreversibility occurring at a temperature approximately equal to the peak temperature of the low-frequency AC susceptibility.

To understand the FC-TRM decay measurement, the corresponding ZFC-TRM measurement, and the subtle differences between them, it is useful to analyze the FC/ZFC magnetization of the spin glass state as a function of temperature. Figure 1 displays the field cooled (FC) and zero field-cooled (ZFC) magnetization curves for a poly-crystalline $Cu_{0.95}Mn_{0.05}$ sample. These measurements were taken using the Quantum Design DC SQUID MPMS magnetometer at the University of Texas. To produce this curve, one starts in a zero magnetic field, at a high temperature (in this case, 40 K), above the spin glass transition temperature (in this case, approximately 28.7 K). The sample is then rapidly cooled down to a temperature below the spin glass transition temperature (in this case, 10 K). A field of 10 Oe is then applied. The magnetization

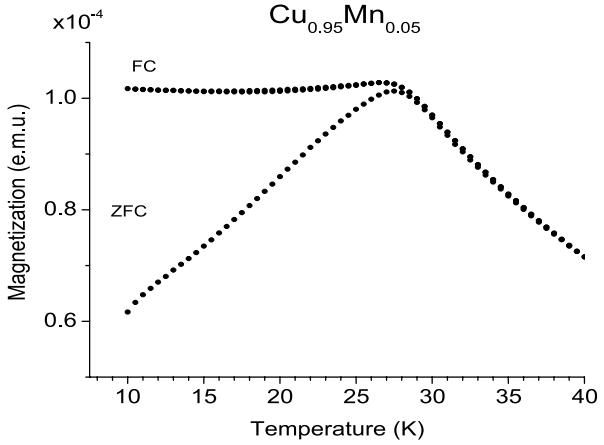


FIGURE 1
ZFC and FC magnetization curves in a 10-Oe magnetic field for bulk $Cu_{0.95}Mn_{0.05}$. Tg for the sample used in this study was determined to be 28.7 K.

makes a rapid jump of approximately $6x10^{-5}$ emu, and the magnetization value is read. The temperature is incremented (in this case, by 0.5 K), and at each point up to the maximum temperature, the magnetization is recorded. This curve is the ZFC curve. Starting from that same high temperature in the same field (10 Oe), the temperature is then lowered in similar temperature increments and magnetization measured at each temperature all the way down to the lowest temperature. This is the FC magnetization curve.

One problem that arises in the experimental spin glass field is that unlike numerical studies, which determine $T_c$ from the Binder cumulant, it is difficult to experimentally determine the actual zero-field spin glass phase transition temperature $T_c$. Perhaps, the best attempt was made by [10], who extrapolated the diverging terms in non-linear susceptibility. This, however, is a difficult measurement to perform, and more rapid approximations of $T_g$ have been made from the FC/ZFC or AC measurements. In this paper, we call the experimental approximation of the phase transition temperature, $T_g$. In this collection, [11], compare the values of $T_g$ obtained from different techniques and showed the limitations to these methods. In this paper, we use the $H \rightarrow 0$ Oe extrapolated value of the onset of irreversibility to determine a value of $T_g = 28.7\ K$ for the $Cu_{0.95}Mn_{0.05}$ polycrystalline sample measured in Figure 1 and $T_g$ = 31.5 $K$ for the single-crystal $Cu_{0.94}Mn_{0.06}$ sample used in all other experiments in this paper.

Getting back to the FC/ZFC curves, above $T_g$, the FC and ZFC magnetization overlap displaying the reversible Curie–Weiss behavior of a paramagnetic phase. At a temperature near the transition temperature, FC magnetization becomes approximately constant and remains close to that value throughout most of the spin glass phase. At first observation, it looks like the spin glass magnetization (and spin configuration) freezes at Tg. It can be observed that there is a peak in the ZFC curve, which is often used as a determination of $T_g$ [12]. It can also be observed that near the peak temperature, the FC and ZFC curves split, indicating the onset of magnetic irreversibility in the system. This onset temperature has also been used to determine the transition temperature [13]. The

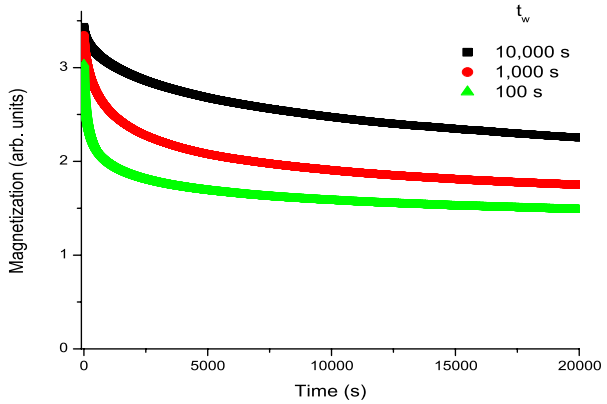


FIGURE 2
TRM waiting time effect for the $Cu_{0.94}Mn_{0.06}$ single-crystal sample. The sample was field-cooled from 40 K in a 16-Oe magnetic field to a measuring temperature of 25 K ($0.8T_g$). The sample was maintained at 25 K for time $t_w$, field set to 0.0 Oe, and the above decays measured.

peak in the ZFC magnetization appears to be field-independent, while the onset of irreversibility has a definite magnetic field dependence, weakly shifting down in temperature as the magnetic field increases. The ZFC-TRM and the FC-TRM both measure time dependencies of this irreversibility.

In 1983, [14] reported both a time-dependent decay of the ZFC-TRM and the waiting time effect using RF-SQUID magnetometry. In the ZFC-TRM, the sample is cooled in a zero magnetic field from a high temperature above the transition temperature to some measuring temperature within the spin glass state. Since the sample is cooled in a zero magnetic field, the random nature of the spin glass state implies zero magnetization (time reversal symmetry applies). In this zero-magnetization state, the sample is maintained at the measuring temperature for time $t_w$, after which the magnetic field is turned on and the magnetization measured at small time intervals for a measuring time $t_m$. On application of the magnetic field, there is a rapid magnetization jump to a value approximately equal to the ZFC magnetization at that temperature (with a small systematic difference due to the waiting time effect), and then, a slow increase occurs. This increase is the ZFC-TRM. Previously, it was generally assumed that the increase would come to equilibrium magnetization at the FC line; however, this has been called into question by the weak logarithmic time dependencies of the FC magnetization [15, 16].

In 1984, [17] reported similar time dependencies (including the waiting time effect) in RF-SQUID-aided measurements of the FC-TRM measurement. In the FC-TRM measurement, the sample is cooled in a magnetic field, from a temperature above the transition temperature to a measuring temperature in the spin glass state. This is the same procedure as the FC magnetization measurement (Figure 1). Therefore, at the measuring temperature, the system starts out with a magnetization equal to the FC magnetization (with the small deviation due to the weak logarithmic time-dependent decay of the FC magnetization) [15, 16]. In this magnetized state, at a constant temperature $T_m$, the sample is held for a time $t_w$. After this, the magnetic field is turned off, and magnetization is measured at small time intervals for a measuring time $t_m$. After the magnetic field is shut off, there is a rapid decrease in magnetization by an amount approximately equal to the ZFC magnetization at that temperature (with a small systematic difference due to the waiting time effect), and then, a slow decay occurs. This decay is the FC-TRM. From symmetry arguments, the final equilibrium magnetization, in the zero field, must be zero. Figure 2 displays the data observed in the FC-TRM measurement. The waiting time effect is clear in the shift of the curves, but there are other subtle differences between curves, which became clearer with further analysis.

Over most of the temperatures below the spin glass transition temperature, superposition appears to hold and can be described by Equation 1 [18]

$$M_{TRM}(t_w, t) = M_{FC}(0, t + t_w) - M_{ZFC}(t_w, t). \quad (1)$$

As mentioned previously, $M_{FC}(0, t + t_w)$ has a weak time dependence, but comparatively, it is small enough that its effect on the above equation can be ignored.

Superposition assumes that the removal of the magnetic field in the FC-TRM measurement is equivalent to adding a negative field to the sample in the FC state at time $t_w$. The implications of this are that (for reasonably small fields) the absolute value of the magnetic field does not matter, and only the change in magnetic field is important. This implies that the manifold of states into which the spin glass state freezes is effectively equivalent for small (<100 G) fields, including the zero magnetic field. Recently, it was found that the superposition principle breaks down close to $T_g$, and as the magnetic field increases, it may only be valid as $H \rightarrow 0$ [19].

An early attempt to analyze the entire decay curve was made using a stretched exponential function, Equation 2 [17].

$$M_{TRM}(t_w, t) = M_0 \lambda^{-\alpha} exp\left[-\left(\frac{t}{\tau_p}\right)^{1-n}\right]. \quad (2)$$

The power law was later added to describe the short time (<1 $s$) rapid decrease in magnetization [20]. $\lambda$ is a an effective time scale that, in the short time limit $t \ll t_w$, $\lambda \simeq t$, which is waiting time-independent. For that reason, this term is often called the stationary term [21]. Finally, regarding the structure of the entire TRM decay, there is a third time regime. It has been observed, using short waiting time and long measurement time scales, that the waiting time effect has a finite lifetime [22]. Using a fast cooling protocol [23], TRM decay measurements with short waiting times (7–100 s), measured over long times 10,000–100,000 s, show that the waiting time-dependent part of the total decay ends, and curves with different waiting times converge into a single waiting time-independent logarithmic decay. At low temperatures, this logarithmic term (for accessible waiting time) dominates the irreversibility, but the relative magnitude (log decay/waiting time decay) decreases as the transition temperature is approached [24]. The longer the waiting time, the further the decay, extending into the logarithmic term, strongly implying that the waiting time effect and the logarithmic term are related.

It was found that over most of the spin glass state that the stretching exponent n was a constant (see [25]; Figure 2). As $T_g$ was approached, this constant deviated toward n = 1. In order to fit this function, the time scale $\tau_0$ changed by approximately eight orders of magnitude (see [25]; Figure 3). The lack of a first-principles theory that predicts a stretched exponential has led to a decrease in the use

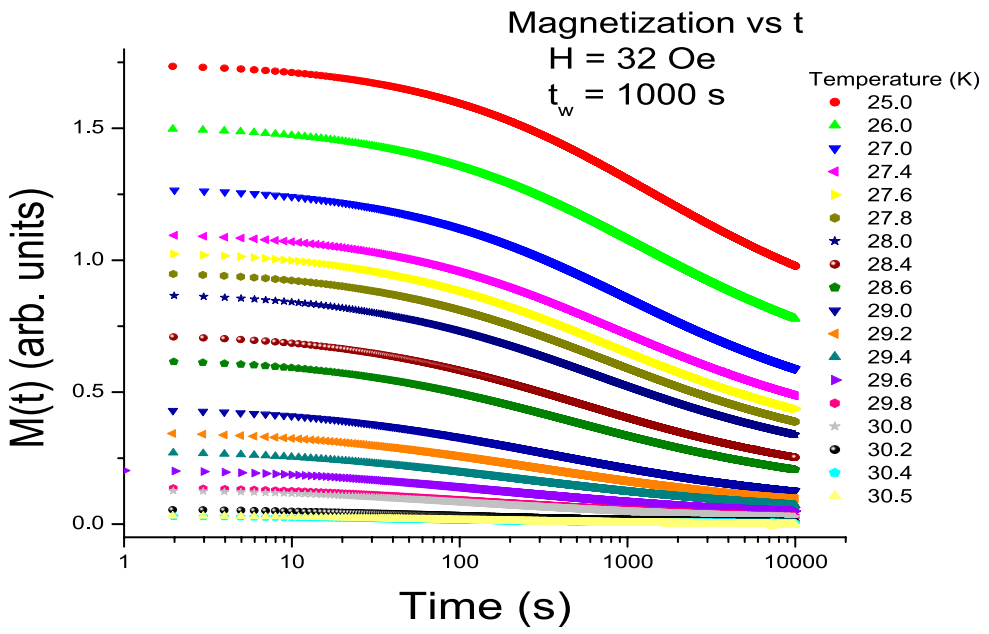


FIGURE 3
TRM waiting time effect for the $Cu_{0.94}Mn_{0.06}$ single-crystal sample for different temperatures. All measurements were made with a 32-Oe magnetic field and a waiting time of $t_w$ = 1000*s*.

of the function, although it is still used by some spin glass researchers.

A second analysis then evolved, where [26, 27] applied the phenomenological time scaling technique (first used by [28] to quantify the waiting time effect in polymers) to spin glasses. In this technique, all curves produced with different waiting times could be collapsed onto a single master curve by scaling the data with a reduced effective time scale defined by Equations 3, 4.

$$\xi = \lambda \; / \; t_w^{\mu}, \tag{3}$$

where

$$\lambda = \frac{t_w}{1-\mu}\left[\left(1+\frac{t}{t_w}\right)^{1-\mu} - 1\right], \quad \mu < 1. \tag{4}$$

In the limit $t \ll t_w$, $\xi$ reduces to $\frac{t}{t_w^{\mu}}$.

A new parameter $\mu$ is introduced. This proposes that all TRM decays, at a fixed temperature, with a wide range of waiting times can be effectively collapsed with a single parameter. This type of scaling is referred to as $\mu$-scaling. In [27] (Figure 2—inset), it can be observed that over most of the spin glass phase, $\mu$ is approximately constant. Sub-aging is observed over most of the spin glass phase with $\mu$ approximately equal to 0.9. From $0.8T_g \rightarrow 1.0T_g$, $\mu$ decreases. In a follow-up study, [29] found that at approximately $0.96T_g$, the decay curves could be collapsed at long measuring times or short measuring times but not both. This result suggests that $\mu$ scaling does not hold as the transition temperature is approached. Much of the impetus for the experimental work to follow comes from observations of the stretched exponential and $\mu$ scaling analysis and other deviations observed as the transition temperature is approached.

Perhaps, the most interesting aspect of the waiting time effect is that it appears to be effectively temperature-independent in the approximate temperature range $0.4T_g$–$0.8T_g$. Not only are the n values (from the stretched exponential) and $\mu$ values (from $\mu$ scaling) approximately constant in this region but the magnitude of the waiting time-dependent magnetization decay is also approximately constant over this temperature regime. This is rather amazing as the decays are fundamentally governed by thermally activated dynamics, which, in most cases, leads to Arrhenius behavior and very large temperature dependencies. A third method of analyzing the TRM data was put forth by [30]. They observed that on a logarithmic scale, the TRM decay displays an inflection point (see, for example, Figure 3). By plotting the logarithmic derivative Equation 5.

$$S(t) = -\frac{dM(t)}{dln(t)}, \tag{5}$$

the S(t) function displays a peak at a time equal to the time where the inflection point in the decay is observed. This time is called $t_w^{eff}$. Figure 4A displays the S(t) function for the 32-Oe magnetization data shown in Figure 3. The highest temperature data are shown in Figure 4B to show experimental resolution.

The S(t) function, as well as the associated characteristic time scale, $t_w^{eff}$ is a straightforward method of assigning a single parameter associated with the waiting time effect. In the temperature range $0.4T_g$–$0.8T_g$, this characteristic time scale is observed to occur at a time approximately equal to the input waiting time. The implication of this is that the decay reflects the time scale input during the waiting time. Actually, in the above mentioned temperature range, the S(t) function has a peak closer to $2t_w$, leading some researchers to use the total time $(t + t_w)$ as the correct time, where t is the measuring time. In this sense, the correct time is the total time spent at the measuring temperature. In this

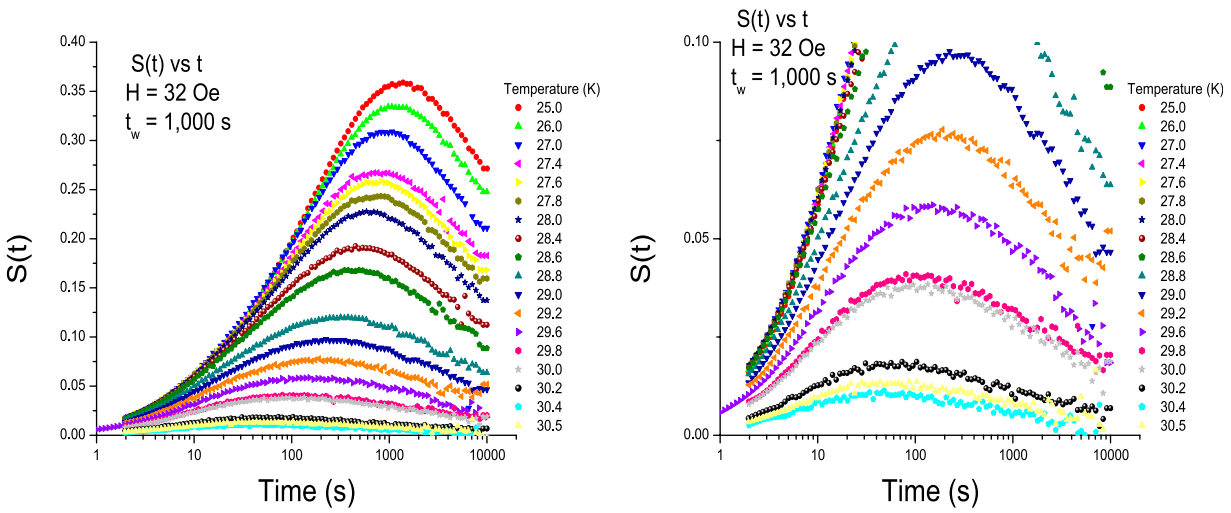


FIGURE 4
S(t) functions for the data given in Figure 3 as a function of temperature. All measurements were made with a 32-Oe magnetic field and a waiting time of $t_w$ = 1000s.

paper, we use the S(t) function to investigate time and spatial dependencies in the spin glass state near $T_g$, in particular focusing on the region T > $0.9T_g$.

[31] analyzed 2D and 3D numerical simulations of Ising spin glass models. They found that they could determine a spatially dependent coherence length scale using a 4-spin autocorrelation function, Equation 6.

$$G_T(r,t_w) = \frac{1}{N}\sum_{i=1}^{N}\frac{1}{t_w}\sum_{t=t_w}^{2t_w-1}\left[\langle S_i^a(t)S_{i+r}^a(t)S_i^b(t)S_{i+r}^b(t)\rangle\right]_{av}. \quad (6)$$

This spatial coherence length is observed to grow as a power law according to Equation 7.

$$\xi(t_w,T) = c_1\left(\frac{t_w}{\tau_0}\right)^{c_2(T/T_c)}, \quad (7)$$

where $\tau_o$ is a microscopic exchange time and $c_1$ and $c_2$ are constants.

This dynamic analysis was extended to CuMn(14%) thin films by [32], who found consistent results for three films with substantially different $\mathcal{L}$, using $c_1$ = 1.448 and $c_2$ = .104. They also associated the maximum barrier with the observed thin-film freezing temperatures $\Delta_{max} = k_b T_f(\mathcal{L})$ and found that Equation 7 substantially predicts the form of $T_f(\mathcal{L})$. In thin films, the FC/ZFC signatures look similar to bulk samples but at lower temperatures. We call the approximate freezing temperature in thin films $T_f$ to discriminate it from the bulk value $T_g$. In the above studies, it is assumed that $\xi$ grows isotropically until it reaches the thickness of the film. Slightly different results were found ($c_1$ = 0.87 and $c_2$ = 0.11) [33] using the freezing temperature associated with finite size effects in spin glass films [34].

Numerical analysis of the 4-spin correlation function showed that the power law growth (Equation 7) holds right up to the spin glass transition temperature, at which point the exponent $c_2(T/T_c)$ becomes a constant [2]. This is quite different from what we observed for the single-crystal sample in 16 Oe (Figure 5). Using

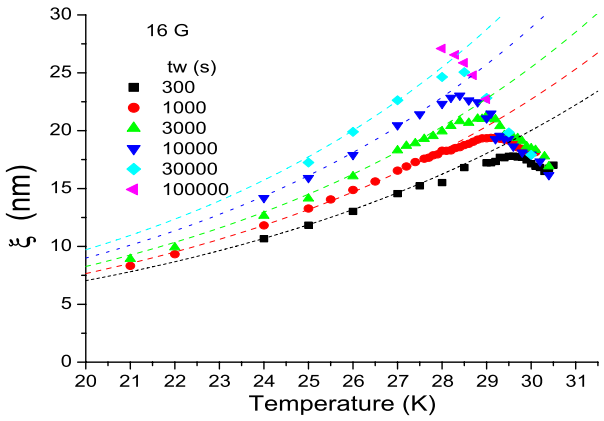


FIGURE 5
The plot is prepared by inserting $t_w^{eff}$ values from the 16-Oe S(t) data into $t_w$ in Equation 7. At low temperatures, a power law is observed, but as $T_g$ is approached, $\xi$ peaks and then decreases. The lines correspond to inserting $t_w$ in Equation 7, using $c_1$ and $c_2$ values from [33].

$t_w^{eff}$ in Equation 7 for $t_w$, it is observed that the calculated coherence length first grows as a power law [33] and then decreases as $T_g$ is approached.

Figure 6 shows the entire magnitude of the observed remanent magnetization for the single-crystal sample measured using a TRM protocol with a 16-Oe field. The solid symbols on this graph represent the remanent magnetization signal a few seconds after the magnetic field is shut off. This signal is comparable to the remanence defined by the difference in FC and ZFC magnetization. The open symbols are the corresponding measurement of the decay 10,000 s after the magnetic field was switched to H = 0 Oe. For the shorter waiting time (i.e., 1,000 s), the waiting time effect is almost over at 10,000 s, and the remaining magnetization (i.e., below the

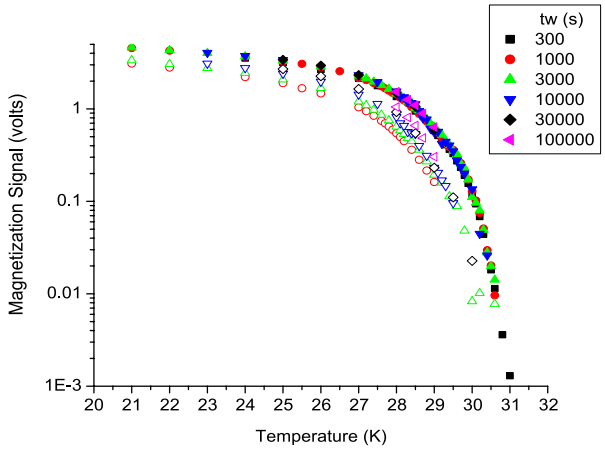


FIGURE 6
Magnitude of the observed remanent magnetization for the single-crystal sample cooled in a 16-Oe magnetic field. The solid symbols on this graph represent the remanent magnetization signal 12 s after the magnetic field is shut off. This signal is comparable to the remanence defined by the difference in the FC and ZFC magnetization. The open symbols are the corresponding measurement of the decay, 10,000 s after the magnetic field was switched to H = 0 Oe. For the shorter waiting time (i.e., 1,000 s), the waiting time effect is almost over at 10,000 s, and the remaining magnetization (i.e., below the open circles) decays logarithmically, as discussed previously.

open circles) decays logarithmically, as discussed previously. This decay happens on time scales much larger than the experimental time scales reported in this study.

Scaling theory and the underlying renormalization group theory have opened a path for understanding critical phenomena near phase transitions [35]. As the critical temperature of a phase transition is approached (either from high or low temperatures), the physics of the system is governed by the correlated growth of fluctuations and critical decreasing of fluctuation time scales. Near the thermodynamic critical point of a continuous magnetic phase transition, strong highly correlated magnetization fluctuations are expected that, in principle, can occur with any time and/or length scale [36]. For the discussion to follow, we plot the critical fluctuation time scale as a function of temperature, Figure 7A, and the critical correlation length scale, Figure 7B, as a function of temperature. In Figure 7A, we plot $\tau_c$ vs. T, Equation 8. The value for $\tau_{oc}$ corresponds to a transition temperature of 32.4 K ($\tau_{oc} = \frac{h}{k_B T_c} = 1.48x10^{-12}$ s).

$$\tau_c = \tau_{oc}\left|\frac{T - T_c}{T_c}\right|^{-z\nu} . \tag{8}$$

In Figure 7B, we plot $\xi_c$ vs. T, Equation 9, with $\xi_{oc} = 2.8x10^{-10}$ nm, where $\xi_{oc}$ is the mean nn Mn distance in $Cu_{0.94}Mn_{0.06}$.

$$\xi_c = \xi_{oc}\left|\frac{T - T_c}{T_c}\right|^{-\nu} . \tag{9}$$

These plots will be useful for understanding the theory proposed in Section 4.

## 2 Experimental methods

The challenge for TRM measurements close to, but below the transition temperature, is the need for extreme sensitivity. To begin with, the total remanent magnetization (and hence, the signal) rapidly decreases as the transition temperature is approached. This can be observed in Figure 6. In addition, the S(t) function is a derivative, significantly enhancing the noise observed in the magnetization decay. To probe close to the transition temperature, we build a dedicated, very high-sensitivity dual-DC SQUID magnetometer. The Indiana

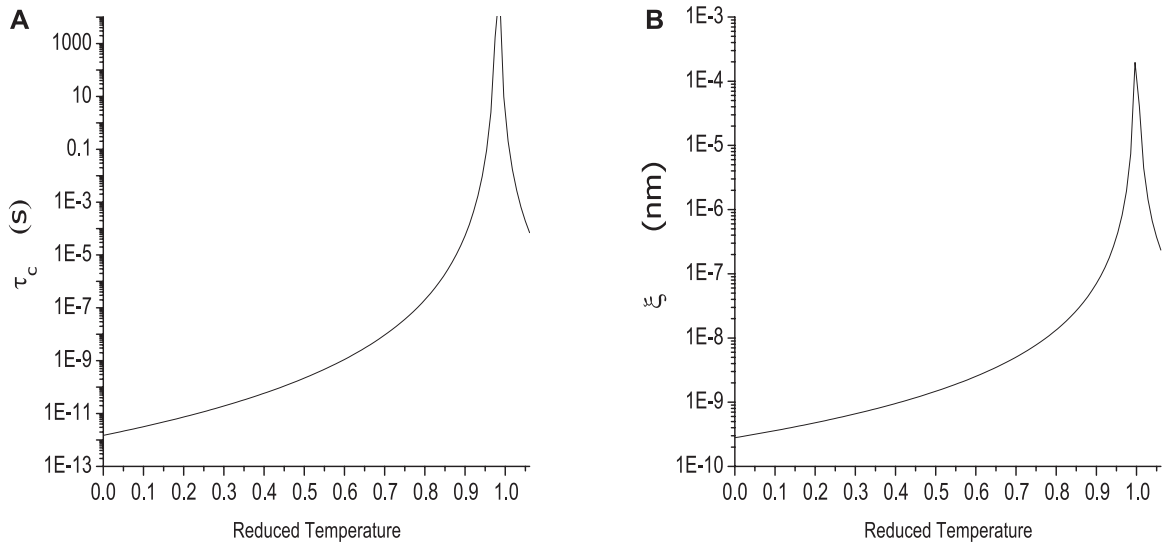


FIGURE 7
In **(A)** (top), we plot $\tau_c$ from Equation 8 with $\tau_{oc} = 1.48x10^{-12}$ s, using $T_c = 32.4$ *K*. In **(B)** (bottom), we plot $\xi_c$ from Equation 9 with $\xi_{oc} = 2.8x10^{-10}$ nm. These graphs are plotted on a reduced scale $(T/T_c)$.

University of Pennsylvania (IUP) magnetometer has two independent SQUID amplifiers. One measures the sample, and the other measures the ambient background. The pickup coils have nearly identical second-order gradiometer configurations and are displaced from each other by 10 cm. The pickup coils have a diameter of 1.1 cm. The resolution of the magnetometer at the baseline point is ±10 nano-emu. This is significantly better than the University of Texas Quantum Design DC SQUID magnetometer, which has a resolution of >±50 nano-emu. A comparison with the Quantum Design MPMS DC SQUID magnetometer is given in [37]. In addition we lowered the noise floor by a factor of five through enhanced pressure control of the helium bath. More details on the IUP magnetometer are given in [37].

The TRM measurements reported here are an analog measurement. The details are briefly discussed. In a magnetic field, the sample is brought from a high temperature, usually 5–6 K above $T_g$, down to the measuring temperature below $T_g$. The temperature reaches $T_m \pm 1mK$ within the first 100 s, so with significantly longer waiting times, we can ensure that the experiment is highly isothermal. The sample is held at the measuring temperature for a time $t_w$ before the magnetic field is cut. After the field is cut, we wait approximately 12 s (to ensure that the heaters used to reset the SQUID and pickup coils have cooled) and then start measuring. The first magnetization point measured is the value of $M_o$ plotted in Figure 6 (solid symbols). The DC SQUID continually measures the pickup coil signal, and a digital readout is taken at 1s intervals over the entire measurement. At the end of the measurement, we take a baseline measurement to put the TRM decays on an absolute scale. The baseline is measured in the following way. After the TRM decay is measured (in a zero magnetic field), the sample is raised in temperature to well over the transition temperature (40 K). In the paramagnetic state at zero field, the sample will have zero magnetic moment. The sample is then cooled back to the measuring temperature (in the zero magnetic field), the temperature is stabilized, and after 5 min, a baseline measurement is taken. This yields an absolute magnetization signal (zero magnetization). The data presented have this baseline signal subtracted from the TRM signal, providing an absolute magnetization scale. In this report, for example, in Figure 2, the magnetization scale reported as arb. units is actually volts, taken directly from the DC SQUID amplifier. As always, SQUIDS are susceptible to large jumps in the signal, which we call SQUID jumps. These look like step functions in the analog data and are generally much larger than the TRM signal and noise. They are therefore rather easy to remove post-processing. Having two SQUIDS allows us to observe which SQUID jumps are system-wide and which are confined to a particular SQUID.

To further enhance the stabilization of the system, measurements presented in this paper were made in two experimental sessions over which the magnetometer was kept cold. The data taken with a TRM field of 16 Oe were measured over a period of approximately 4 months in 2021, and the other magnetic field data presented were obtained in a 3-month session in 2022. Long sessions cold, enhanced the thermal stabilization of the equipment. The TRM measurements are isothermal measurements, so temperature control is very important. The sample, located at the end of a temperature-controlled $Al_2O_3$ rod, is centered in one of the pickup coils. Temperature control at the measuring temperature was stable to at least ≤±1 mK during the first month of a session and improved (after a month) to $< \pm 80\mu K$ over runs as long as $1x10^5 s$. Squid jumps effectively disappeared after the first month.

The bulk polycrystalline CuMn sample (Figure 1) was prepared by alloying high-purity Cu and Mn and then annealing at high temperature to randomize the Mn within the sample, followed by a rapid thermal quench to 77 K. For many years, it was believed within the spin glass experimental community that to correctly produce these types of metallic spin glasses, (i.e., a bulk CuMn sample), high-purity Cu and Mn must be alloyed and then annealed at high temperature (≈800 K for CuMn for up to 48 h). This was done to randomize Mn within the sample, followed by a rapid thermal quench (in our studies, to 77 K) to lock in the random disorder. This technique, however, produced small crystallites, and the effects of the crystallites on the time dependencies were unknown. In a previous study [37], we found that the time associated with the peak in the S(t) function ($tw_{eff}$) dramatically decreased above $0.9T_g$. It was conjectured that the correlation length may reach the polycrystalline size scale, and the dramatic decrease may be due to finite size effects [38]. In 2016, we began working with single crystals of CuMn in order to eliminate any effects due to crystallite sizes. Deborah Schlagle at Ames Laboratory produced three CuMn single-crystal boules of different Mn concentrations. Cu and Mn were arc-melted several times in an argon environment and cast in a copper mold. The ingot was then processed in a Bridgman furnace. X-ray fluorescence (XRF) and optical observation showed that the beginning of the growth is a single phase. Further details on the production and analysis of the sample, including X-ray diffraction, are presented elsewhere [32, 39]. To date, we found no differences in any of the spin glass signatures between the single-crystal samples (including FC-ZFC, FC-TRM, and ZFC-TRM, waiting time effect, and AC susceptibility) and polycrystalline samples, indicating that crystallite size effects in a polycrystalline spin glass sample have little or no effect and that the technique for producing the single crystals sufficiently randomizes the Mn.

## 3 Data and analysis

Previous studies on $Cu_{0.94}Mn_{0.06}$ single-crystal samples at 16 Oe found that the characteristic time scale ($t_w^{eff}$) associated with the peak of the S(t) function displayed a remarkable decrease as $T_g$ (31.5 K) is approached from temperatures below $T_g$ [33]. These data are shown in Figure 8B. In this study, we extend our measurements to other magnetic fields including 9.6, 16, 32, 64, and 96 Oe. Before we move on to discuss the effects of changing magnetic fields, let us review what we observed with 16 Oe. Like all waiting time effect measurements observed to date on CuMn spin glasses, we observe that below approximately 0.8 $T_g$, the peaks in the S(t) functions ($t_w^{eff}$) approach a value of ≈ $2t_w$. Above 0.8 $T_g$, we find a rapid decrease in both the remanent magnetization and the characteristic time scale $t_w^{eff}$ up to 0.96 $T_g$, where we lose the signal (Figures 3, 6). However, by approximately 29 K, the S(t) peak positions, for different waiting times, are indistinguishable, within the experimental

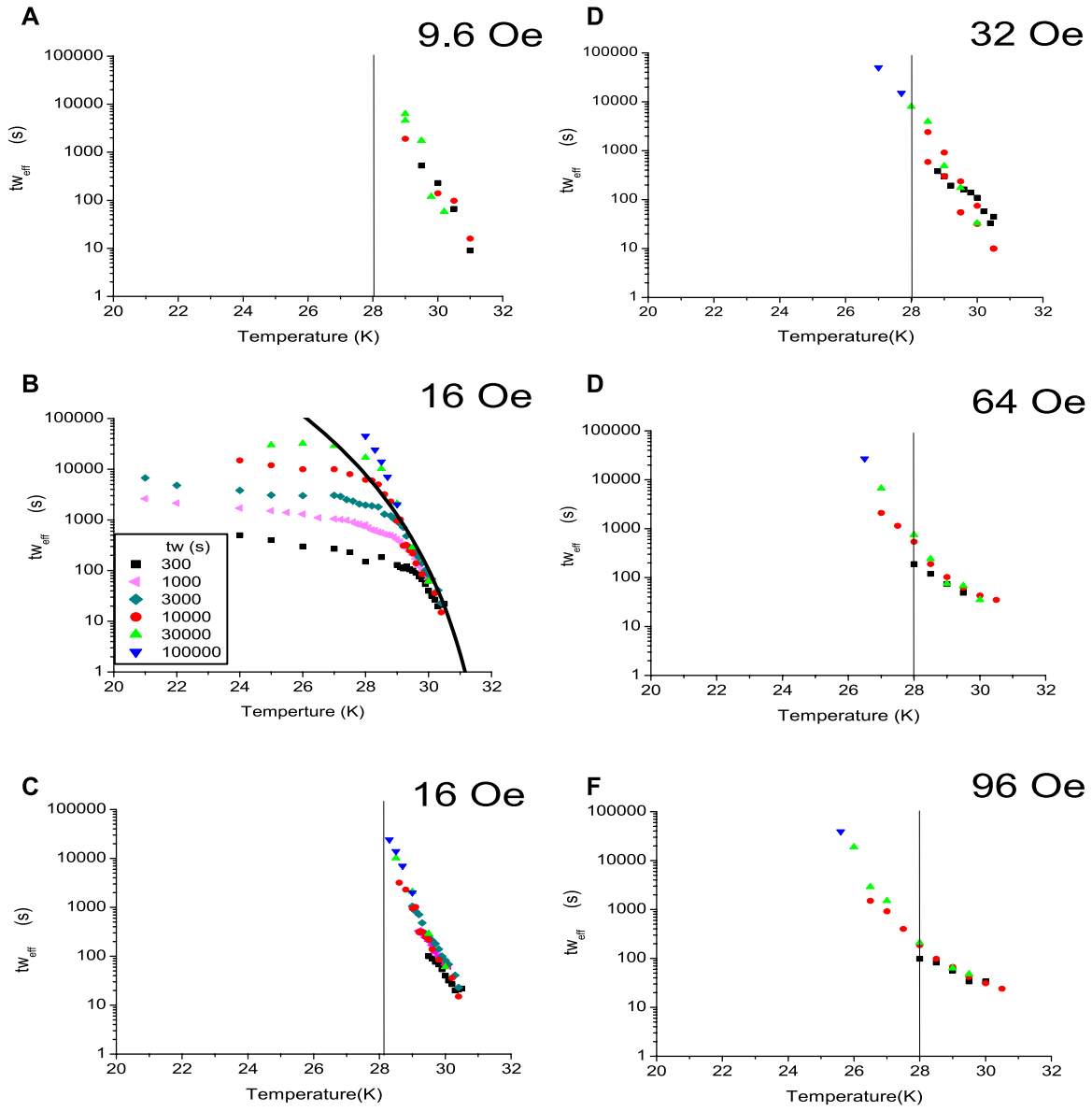


FIGURE 8
Plot of the crossover line for five different magnetic fields 9.6 Oe **(A)**, 16 Oe **(C)**, 32 Oe **(D)**, 64 Oe **(E)** and 96 Oe **(F)**. **(B)** is a plot of $t_w^{eff}$ vs. T for six different waiting times, over the entire temperature range plotted, with a TRM magnetic field of 16 Oe. **(C)** is the same data with the crossover line isolated. The same process was used on all other data covering the different magnetic fields. The vertical lines at 28 K are an aid for the eye. It can be observed that as the magnetic field increases, the crossover lines are further suppressed by the magnetic field. The solid line in **(B)** is Equation 18 with a 16-Oe field.

resolution. This result is extremely interesting as it appears to define a cut-off time scale. For waiting times less than this time scale, one observes waiting time-dependent decays, albeit with smaller $t_w^{eff}$ values, i.e., a suppressed waiting time effect. For waiting times larger than the cut-off time scale, the observed characteristic time scale was limited to the cut-off time scale, and therefore, no variation with waiting time is observed.

To begin the analysis of this effect, we first separated the waiting time-independent crossover line from the standard waiting time effect. This was accomplished by removing data associated with the break toward the standard waiting time effect. For example, both Figures 8B,C are plots of the same data (H = 16 Oe), with the waiting time-dependent data removed in Figure 8C. Unfortunately, the exact temperature limits on either side of the crossover line are somewhat subjective.

## 4 Discussion

A model has emerged for the waiting time effect within the spin glass state, and we apply this model to the critical region (near $T_g$). When the sample is cooled in a magnetic field to a measuring temperature within the spin glass state, the magnetization of the entire sample is $M_{fc}$. During the waiting time, there is a growth of coherent regions within the spin glass state, each with a magnetization of $M_{fc}$. Due to a "stiffening" of these coherent

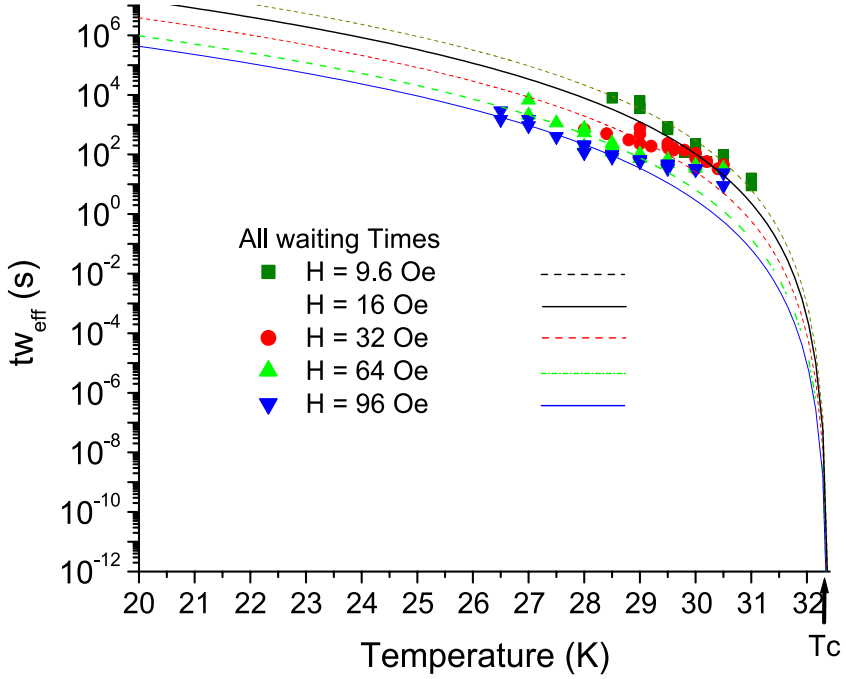


FIGURE 9
The crossover line data are plotted for four different magnetic fields. Plot of Equation 18 (lines) for five different fields. The 16-G data are fit to Equation 18 in Figure 8B.

regions during the waiting time, these regions are resistant to the change in the magnetic field that occurs after waiting time $t_w$ in the field cooled state and, therefore, decay slowly. As the temperature is increased toward the transition temperature, remanence rapidly decreases, and the effective time scales decrease.

From this point forward in the analysis, we use $T_c$ instead of $T_g$ to separate the experimental determination of the spin glass transition temperature $T_g$ (approximated from FC/ZFC measurements) from $T_c$, the phase transition fixed point. To understand the crossover line, we treat the energy associated with the waiting time effect as a small perturbation of the total free energy associated with the entire spin glass state below $T_c$. This is plausible as the total remanent magnetization in the temperature region of the crossover line (28 K–31 K) is only a few % of the total FC magnetization (Figure 1). Within the spin glass phase, during the waiting time in a magnetic field, there is a "stiffening" of at least a part of the spin glass during the waiting time. This "stiffening" contributes to the free energy and is associated with the maximum energy barrier, height, $\Delta(t_w)$, and growth during the waiting time. This energy barrier controls the decay of the waiting time-dependent magnetization through the Arrhenius law, Equation 10, [40, 41].

$$\delta f_{SG} = \Delta(t_w) = k_B T_m (lnt_w - ln\tau_o). \tag{10}$$

Since the sample is held at temperature $T_m$, we take $\tau_o = \frac{h}{k_B T_m}$ as the equilibrium fluctuation time scale.

It is clear that the suppression of the waiting time effect is already in effect at a lower temperature (below the crossover line), as observed in the reduction of the peak times $t_w^{eff}$ (from $2t_w$). Figure 8B shows that the suppression begins at a temperature at least as low as $0.8T_g$. We propose that this reduction of $t_w^{eff}$ is caused by the onset of significant critical fluctuations. This region is far away from the spin glass transition temperature, and therefore, critical fluctuations will be small (size scale) and of short duration having small yet noticeable effects on $t_w^{eff}$. As the crossover line is approached, critical fluctuations become larger and are of longer duration, increasing their effect on $t_w^{eff}$. The crossover line represents a crossover from a state that can maintain rigid spin glass clusters (up to the crossover time scale) to one dominated by large long-lived critical fluctuations that suppress the ordering associated with the waiting time.

In particular, at the crossover line, the small spin glass energy associated with the waiting time effect is

$$\delta f_{SG}(t_{co}) = \Delta(t_{co}) = k_B T_{co} (lnt_{co} - ln\tau_o). \tag{11}$$

We would expect the free energy perturbation to be a continuous function through the crossover region.

$$\delta f_{SG}(t_{co}) = \delta f_{critical}(t_{co}), \tag{12}$$

where $\delta f_{critical}(t_{co})$ is the free energy available, within the spin glass remanence, as the crossover line is crossed, and critical fluctuations dominate the system.

We expect that the magnetization decay in the critical region would be governed by the critical fluctuation time scale $\tau_c$, which exhibits a critical decrease as the transition temperature $T_c$ is approached.

$$\tau_c = \tau_{oc} \left| \frac{T - T_c}{T_c} \right|^{-z\nu}. \tag{13}$$

We propose an effective Arrhenius law in the critical region

$$\delta f_{critical}(t_{co}) = \Delta(t_{co}) = k_B T_{co} (lnA - ln\tau_c). \tag{14}$$

In this equation, we assume that $\tau_{oc}$ is governed by the fixed point at $T_c$ and, therefore, $\tau_{oc} = \frac{h}{k_B T_c}$. At this stage in the analysis, $A$ is an unknown parameter with units of time and will be used as a fitting parameter.

Substituting Equation (11) and (14) in Equation 12 leads to

$$\frac{t_{co}}{\tau_o} = \frac{A}{\tau_{oc}}. \tag{15}$$

Replacing $\tau_o$ and $\tau_{oc}$ with the expressions defined above leads to

$$t_{co} = \frac{AT_c}{T_{co}\left|\frac{T-T_c}{T_c}\right|^{-z\nu}} \quad . \tag{16}$$

Although this equation can be used to fit the data for $t_{co}$ vs. T with different $A$ values, we seek to understand the magnetic field effect on the crossover lines. It is clear from Figure 8 that the magnetic field suppresses $t_{co}$. We, therefore, write

$$t_{co} = \frac{AT_c}{g(H)T_{co}\left|\frac{T-T_c}{T_c}\right|^{-z\nu}} \quad , \tag{17}$$

where $g(H)$ is to its first order a monotonically increasing function. The first attempt to find $g(H)$ was to bring the magnetic field in by adding a Zeeman term in Equation 10 [42]. This was first used to probe the spin glass energy barrier landscape with a magnetic field. We find that adding this field dependence into Equation 10 and deriving through Equation 18 yield an expression for g(H) that is an exponential of $H^2$. With this field dependence, we cannot fit the data. Likewise, using the scaling ansatz for the critical region also brings an exponential of $H^{\frac{2}{\delta}}$ into Equation 16, and using an accepted value of $\frac{2}{\delta}$ = .216, we also cannot fit the data.

We do find, however, that the data fit to $g(H) = \alpha H^2$. With the substitution $A' = \frac{A}{\alpha}$, we fit our data to

$$t_{co} = \frac{A'T_c}{H^2 T_{co}}\left|\frac{T-T_c}{T_c}\right|^{z\nu} \quad . \tag{18}$$

Figure 9 is a plot of Equation 18 using $\tau_{oc} = \frac{h}{k_B T_c} = 1.48x10^{-12}$ s and ($z\nu = 7$) [10]. With two fitting parameters, $T_c = 32.4$ K ($1.03T_g$) and $A' = 3\ Oe^2 s$ $(3x10^{-8}\ T^2 s)$, we find that Equation 18 fits to the 9.6, 16, 32, 64, and 96-Oe crossover lines. We do not include the 16-Oe data in this plot, but we include the fit of Equation 18 with H = 16 Oe. We also plotted Equation 18 for H = 16 Oe in Figure 8B (the solid black line). It can be observed in Figure 8B that Equation 18 fits well above 29 K, but below 29 K, for $t_w$ = 100,000 s, the data, while suppressed ($t_w^{eff} \ll t_w$), are above the line. This suggests that critical fluctuations, while present and important, are not dominant below 29 K in 16 Oe.

The $H^2$ field dependence is strongly suggestive that the suppression of $\tau_{oc}$ by the magnetic field may be caused by the magnetic susceptibility (i.e., $g(H) \propto \chi_{SG}$). In particular, as $T_c$ is approached, it is expected that the nonlinear terms in the magnetization expansion diverge. The expansion of the susceptibility leads to [10, 43]

$$\chi_{SG} = \chi_1 + \chi_3 H^2 + \chi_5 H^4 + \chi_7 H^6 \ldots, \tag{19}$$

where the nonlinear terms $\chi_3$, $\chi_5$, $\chi_7$ etc., are expected to diverge as $T_c$ is approached. We analyzed the above data with Equation 19. However, with only five fields, polynomial fits to the $H^4$ and $H^6$ are problematic. Recently, we extended our measurements over the above temperature region with up to 11 different magnetic fields per temperature. It can also be observed in Figure 9 that as $T_c$ is approached, the higher-field data break off from Equation 18 and approach the lower-field data. This is also likely a nonlinear effect, and the analysis is forthcoming [44].

Finally, we discuss an observation made with respect to the field dependent data and some open questions. In Figure 8, it can be observed that as the magnetic field decreases, the crossover line becomes more vertical and shifts to higher temperatures. The line at 28 K is an aid to the eye. This clear difference implies that as $H \rightarrow 0\ G$, the crossover line may become vertical at the transition temperature. Does this imply that the coherence length of the ZFC-TRM can grow without bounds, even close to $T_c$? This shift also explains the breakdown of superposition between the FC-TRM and the ZFC-TRM [19]. In the ZFC-TRM, the spin glass is cooled in zero field and ages during the waiting time without the field-dependent suppression observed in the crossover line. The FC-TRM ages with the field-dependent suppression. The data and analysis in this paper strongly imply a phase transition at H = 0 Oe. In a magnetic field, the situation is not quite so clear. Does a limit on the coherence length, as observed in a magnetic field, imply a crossover transition in a magnetic field? Further understanding of the role of the coherence length and its intrinsic role in the spin glass state is warranted.

In summary, we measured the TRM decays for a range of magnetic fields and temperatures below the transition temperature. We find that on the approach to $T_c$, the waiting time effect is suppressed and reaches a cut-off time scale $t_{co}$. We mapped this suppression over five magnetic fields, from 9.6 to 96 Oe, and find that $t_{co}$ is a function of the magnetic field. We postulate that the free energy of this effect is a continuous function through $t_{co}$. Using the Arrhenius law as the governing mechanism for the decay of the TRM, we understand the cut-off in terms of critical dynamics. In a previous paper [33], lead by the apparent upward curvature of the crossover line, we fit the crossover line at 16 G to both a glass transition and a low temperature phase transition. In the Supplementary Material, we extend this analysis to the data for the magnetic fields reported in this paper.

## Data availability statement

The raw data supporting the conclusion of this article will be made available by the authors, without undue reservation.

## Author contributions

GK: conceptualization, data curation, formal analysis, funding acquisition, investigation, methodology, project administration, resources, software, supervision, validation, visualization, writing–original draft, and writing–review and editing. MB: data curation and writing–review and editing. RB: data curation and writing–review and editing. MH: data curation and writing–review

and editing. DT: data curation, investigation, and writing–review and editing.

## Funding

The author(s) declare that financial support was received for the research, authorship, and/or publication of this article. This work was supported by the US Department of Energy (USDOE), Office of Science, Basic Energy Sciences, under Award DE-SC0013599. The IUP Dual DC SQUID magnetometer was built under an NSF MRI, Award No. 0852643. Single-crystal growth was performed by Deborah Schlagel at the Ames Laboratory, which is supported by the Office of Science, Basic Energy Sciences, Materials Sciences and Engineering Division of the USDOE, under Contract No. DE-AC02-07CH11358.

## Acknowledgments

The authors thank R.L. Orbach, J. Meese, P. Young, E.D. Dahlberg, and J. Friedberg for useful discussions. The authors also thank GK for his help with the manuscript.

## Conflict of interest

The authors declare that the research was conducted in the absence of any commercial or financial relationships that could be construed as a potential conflict of interest.

## Publisher's note



## Supplementary material

The Supplementary Material for this article can be found online at: https://www.frontiersin.org/articles/10.3389/fphy.2024.1443298/full#supplementary-material

## References

1. Barahona F. On the computational complexity of ising spin glass models. *J Phys A: Math Gen* (2015) 15:3241–53. doi:10.1088/0305-4470/15/10/028

2. Fernandez LA, Martin-Mayor V. Testing statics-dynamics equivalence at the spin-glass transition in three dimensions. *Phys Rev B* (1982) 91:174202. doi:10.1103/PhysRevB.91.174202

3. Andriushchenko P, Kapitan D, Kapitan V. A new look at the spin glass problem from a deep learning perspective. *Entropy* (2022) 24:697. doi:10.3390/e24050697

4. King AD, Raymond J, Lanting T, Harris R, Zucca A, Altomare F, et al. Quantum critical dynamics in a 5,000-qubit programmable spin glass. *Nature* (2023) 617:61–6. doi:10.1038/s41586-023-05867-2

5. Tholence JL, Tournier R. Susceptibility and remanent magnetization of a spin glass. *Le J de Physique Colloques* (1974) 35:C4-229–35. doi:10.1051/jphyscol:1974442

6. Cannella V, Mydosh JA. Magnetic ordering in gold-iron alloys. *Phys Rev B* (1972) 6:4220–37. doi:10.1103/PhysRevB.6.4220

7. Mizoguchi T, McGuire TR, Kirkpatrick S, Gambino RJ. Measurement of the spin-glass order parameter in amorphous gd0.37 al0.63. *Phys Rev Lett* (1977) 38:89–92. doi:10.1103/PhysRevLett.38.89

8. Kinzel W. Remanent magnetization in spin-glasses. *Phys Rev B* (1979) 19:4595–607. doi:10.1103/PhysRevB.19.4595

9. Nagata S, Keesom PH, Harrison HR. Low-dc-field susceptibility of cu mn spin glass. *Phys Rev B* (1979) 19:1633–8. doi:10.1103/PhysRevB.19.1633

10. Levy LP, Ogielski AT. Nonlinear dynamic susceptibilities at the spin-glass transition of ag: Mn. *Phys Rev Lett* (1986) 57:3288–91. doi:10.1103/PhysRevLett.57.3288

11. Pradhan S, Harrison D, Kenning GG, Schlagel DSG. Investigation of experimental signatures of spin glass transition temperature. *Front Phys* (2024).

12. Sandlund L, Granberg P, Lundgren L, Nordblad P, Svedlindh P, Cowen JA, et al. Dynamics of cu-mn spin-glass films. *Phys Rev B* (1989) 40:869–72. doi:10.1103/PhysRevB.40.869

13. Kenning GG, Chu D, Orbach R. Irreversibility crossover in a cu: Mn spin glass in high magnetic fields: evidence for the gabay-toulouse transition. *Phys Rev Lett* (1991) 66:2923–6. doi:10.1103/PhysRevLett.66.2923

14. Lundgren L, Svedlindh P, Nordblad P, Beckman O. Dynamics of the relaxation-time spectrum in a cumn spin-glass. *Phys Rev Lett* (1983) 51:911–4. doi:10.1103/PhysRevLett.51.911

15. Djurberg C, Jonason K, Nordblad P. Magnetic relaxation phenomena in a cumn spin glass. *The Eur Phys J B-Condensed Matter Complex Syst* (1999) 10:15–21. doi:10.1007/s100510050824

16. Zhai Q, Orbach RL, Schlagel DL. Evidence for temperature chaos in spin glasses. *Phys Rev B* (2022) 105:014434. doi:10.1103/PhysRevB.105.014434

17. Chamberlin RV, Mozurkewich G, Orbach R. Time decay of the remanent magnetization in spin-glasses. *Phys Rev Lett* (1984) 52:867–70. doi:10.1103/PhysRevLett.52.867

18. Lundgren L, Nordblad P, Sandlund L. Memory behaviour of the spin glass relaxation. *Europhysics Lett* (1986) 1:529–34. doi:10.1209/0295-5075/1/10/007

19. Paga I, Zhai Q, Baity-Jesi M, Calore E, Cruz A, Cummings C, et al. Superposition principle and nonlinear response in spin glasses. *Phys Rev B* (2023) 107:214436. doi:10.1103/PhysRevB.107.214436

20. Bontemps N, Orbach R. Evidence for differing short-and long-time decay behavior in the dynamic response of the insulating spin-glass eu0.4 sr0.6 s. *Phys Rev B* (1988) 37:4708–13. doi:10.1103/PhysRevB.37.4708

21. Refregier P, Ocio M, Hammann J, Vincent E. Nonstationary spin glass dynamics from susceptibility and noise measurements. *J Appl Phys* (1988) 63:4343–5. doi:10.1063/1.340169

22. Kenning GG, Rodriguez GF, Orbach R. End of aging in a complex system. *Phys Rev Lett* (2006) 97:057201. doi:10.1103/PhysRevLett.97.057201

23. Rodriguez GF, Kenning GG, Orbach R. Effect of the thermal quench on aging in spin glasses. *Phys Rev B* (2013) 88:054302. doi:10.1103/physrevb.88.054302

24. Kenning GG, Bowen J, Sibani P, Rodriguez GF. Temperature dependence of effective fluctuation time scales in spin glasses. *Phys Rev B* (2010) 81:014424. doi:10.1103/PhysRevB.81.014424

25. Hoogerbeets R, Luo WL, Orbach R. Spin-glass response time in ag: Mn: exponential temperature dependence. *Phys Rev Lett* (1985) 55:111–3. doi:10.1103/PhysRevLett.55.111

26. Ocio JH M Alba M, Hammann J. Time scaling of the ageing process in spin-glasses: a study in csnifef. *J de Physique Lettres* (1985) 46:1101–7. doi:10.1051/jphyslet:0198500460230110100

27. Alba M, Hammann J, Ocio M, Refregier P, Bouchiat H. Spin–glass dynamics from magnetic noise, relaxation, and susceptibility measurements. *J Appl Phys* (1987) 61:3683–8. doi:10.1063/1.338661

28. Struik LC. *Physical aging in amorphous polymers and other materials*. Amsterdam: Elsevier (1978).

29. Rodriguez G. Ph.D. Thesis. Ph.D. thesis. Riverside, CA: University of California, Riverside (2004).

30. Nordblad P, Svedlindh P, Lundgren L, Sandlund L. Time decay of the remanent magnetization in a cumn spin glass. *Phys Rev B* (1986) 33:645–8. doi:10.1103/PhysRevB.33.645

31. Kisker J, Santen L, Schreckenberg M, Rieger H. Off-equilibrium dynamics in finite-dimensional spin-glass models. *Phys Rev B* (1996) 53:6418–28. doi:10.1103/PhysRevB.53.6418

32. Zhai Q, Harrison DC, Tennant D, Dahlberg ED, Kenning GG, Orbach RL. Glassy dynamics in cumn thin-film multilayers. *Phys Rev B* (2017) 95:054304. doi:10.1103/PhysRevB.95.054304

33. Kenning GG, Schlagel DL, Thompson V. Experimental determination of the critical spin-glass correlation length in single-crystal cumn. *Phys Rev B* (2020) 102:064427. doi:10.1103/PhysRevB.102.064427

34. Kenning GG, Bass J, Pratt JWP, Leslie-Pelecky D, Hoines L, Leach W, et al. Finite-size effects in cu-mn spin glasses. *Phys Rev B* (1990) 42:2393–415. doi:10.1103/physrevb.42.2393

35. Fisher ME. *Scaling, universality and renormalization group theory*. Berlin: Springer-Verlag (1983). p. 1.

36. Jin C, Tao Z, Kang K, Watanabe K, Taniguchi T, Mak KF, et al. Imaging and control of critical fluctuations in two-dimensional magnets. *Nat Mater* (2020) 19:1290–4. doi:10.1038/s41563-020-0706-8

37. Kenning GG, Tennant DM, Rost CM, da Silva FG, Walters BJ, Zhai Q, et al. End of aging as a probe of finite-size effects near the spin-glass transition temperature. *Phys Rev B* (2018) 98:104436. doi:10.1103/PhysRevB.98.104436

38. Tennant DM, Orbach RL. Collapse of the waiting time effect in a spin glass. *Phys Rev B* (2020) 101:174409. doi:10.1103/PhysRevB.101.174409

39. Zhai Q, Martin-Mayor V, Schlagel DL, Kenning GG, Orbach RL. Slowing down of spin glass correlation length growth: simulations meet experiments. *Phys Rev B* (2019) 100:094202. doi:10.1103/PhysRevB.100.094202

40. Lederman M, Orbach R, Hammann J, Ocio M, Vincent E. Dynamics in spin glasses. *Phys Rev B* (1991) 44:7403–12. doi:10.1103/physrevb.44.7403

41. Hammann J, Lederman M, Ocio M, Orbach R, Vincent E. Spin-glass dynamics: relation between theory and experiment: a beginning. *Physica A: Stat Mech its Appl* (1992) 185:278–294. doi:10.1016/0378-4371(92)90467-5

42. Joh YG, Orbach R, Wood GG, Hammann J, Vincent E. Extraction of the spin glass correlation length. *Phys Rev Lett* (1999) 82:438–41. doi:10.1103/PhysRevLett.82.438

43. He J, Orbach RL. Spin glass dynamics through the lens of the coherence length. *Front Phys* (2024) 12:1370278. doi:10.3389/fphy.2024.1370278

44. Kenning GG, Orbach RL. to be published (2024).

45. Garca-Coln LS, Del Castillo LF, Goldstein P. Theoretical basis for the vogel-fulcher-tammann equation. *Phys Rev B* (1989) 40:7040–4. doi:10.1103/PhysRevB.40.7040

frontiers | Frontiers in Physics

TYPE Review
PUBLISHED 20 September 2024
DOI 10.3389/fphy.2024.1466987



OPEN ACCESS

EDITED BY
Konrad Jerzy Kapcia,
Adam Mickiewicz University, Poland

REVIEWED BY
Francisco Welington Lima,
Federal University of Piauí, Brazil
Ekrem Aydiner,
Istanbul University, Türkiye

*CORRESPONDENCE
Stefan Boettcher,
sboettc@emory.edu

RECEIVED 18 July 2024
ACCEPTED 13 August 2024
PUBLISHED 20 September 2024

CITATION
Boettcher S (2024) Physics of the Edwards–Anderson spin glass in dimensions $d = 3, \ldots, 8$ from heuristic ground state optimization.
*Front. Phys.* 12:1466987.
doi: 10.3389/fphy.2024.1466987



# Physics of the Edwards–Anderson spin glass in dimensions $d = 3, \ldots, 8$ from heuristic ground state optimization

Stefan Boettcher*

Physics Department, Emory University, Atlanta, GA, United States

We present a collection of simulations of the Edwards–Anderson lattice spin glass at $T = 0$ to elucidate the nature of low-energy excitations over a range of dimensions that reach from physically realizable systems to the mean-field limit. Using heuristic methods, we sample the ground states of instances to determine their energies while eliciting excitations through manipulating boundary conditions. We exploit the universality of the phase diagram of bond-diluted lattices to make such a study in higher dimensions computationally feasible. As a result, we obtain a variety of accurate exponents for domain wall stiffness and finite-size corrections, which allow us to examine their dimensional behavior and their connection with predictions from mean-field theory. We also provide an experimentally testable prediction for the thermal-to-percolative crossover exponent in dilute lattice Ising spin glasses.

KEYWORDS

**Edwards–Anderson spin glass, critical dimension, domain wall excitations, ground-state energies, percolation, heuristic algorithms**

## 1 Introduction

Imagining physical systems in non-integer dimensions, such as through $\varepsilon$-expansion [1] or *dimensional regulation* [2], to name but two, has provided many important results for the understanding of physics in realistic dimensions. For example, the goal of the $\varepsilon$-expansion is to establish a connection between the (technically, infinite-dimensional) mean-field solution of a field theory and its real-space behavior. For a disordered system such as a spin glass [3–6], this playbook has proved rather difficult to follow theoretically [7–9]. In contrast, we endeavor to explore the transition between the often well-known mean-field properties and their modifications in real space using numerical means, free of any theoretical preconceptions. In this task, on top of the computationally extensive disorder averages, the complexity of spin glasses reveals itself through increasingly slower convergence in thermal simulations, while the deeper one pushes into the glassy regime. Going all the way to $T = 0$ then makes thermal explorations impossible and renders the problem of finding the ground-state NP-hard in general [10]. However, simulations at $T = 0$ also avail us considerable conceptual clarity and an entirely new suit of techniques, albeit for just a few, yet important, observables. Some equilibrium properties of spin glasses below $T_c$ can be obtained from merely determining ground-state energies, such as domain wall stiffness, finite-size corrections, and thermal–percolative crossover exponents. To keep systematic errors low while also creating enough statistics for the disorder average, we need to use fast but ultimately inexact heuristic methods to overcome NP-hardness. To reach a

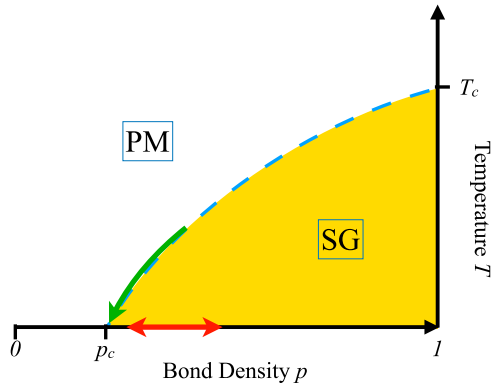


FIGURE 1
Phase diagram for bond-diluted spin glasses ($d > d_l$). The entire spin-glass (SG) phase for $T < T_c$ and $p > p_c$ has a universal positive domain wall exponent, $y > 0$. In our measurements, we therefore utilize an interval of bond densities at $T = 0$ (red arrow) where $p$ is sufficiently above the scaling window near $p_c$ (at finite system size) but small enough to asymptotically reach significant system sizes $L$. At $p = p_c$ and $T = T_c = 0$, we define the domain wall exponent for a spin glass on the percolating cluster as $y = y_P (<0)$. It allows us to extract the thermal–percolative crossover exponent $\phi$ that describes the behavior along the boundary $T_c(p) \sim (p - p_c)^\phi$ for $p \searrow p_c$ (green arrow). In the paramagnetic phase (PM) for $p < p_c$ or $T > T_c$, defect energies due to domain walls decay exponentially.

sensible scaling regime in system sizes, $N$, especially in higher dimensions, requires clever exploitation of the phase diagram of a spin glass. In this study, we discuss the results obtained from large-scale simulations conducted over several years and spread over a number of papers [11–15].[1]

To be specific, we simulate the Ising spin glass model due to Edwards and Anderson (EA) with the Hamiltonian [16].

$$H = -\sum_{<i,j>} J_{i,j}\,\sigma_i\,\sigma_j. \tag{1}$$

The dynamic variables are binary (Ising) spins $\sigma_i = \pm 1$ placed on a hypercubic lattice in the integer $d$ dimension with couplings between nearest neighbors $<i, j>$ via random bonds $J_{ij}$ drawn from some distribution $\mathcal{P}(J)$ of zero mean and unit variance. The lattices are periodic with base length $L$ in all directions, i.e., each such instance has $N = L^d$ spins. To relate real-world behavior in $d = 3$ (which is explored experimentally and theoretically in other articles in this collection) with mean-field behavior, which manifests itself above the upper critical dimension $d_u = 6$ [3], we found ground states of EA on lattices in $d = 3, \ldots, 8$. In each $d$, we need to simulate instances over a wide range of $L$ to extrapolate our results to the thermodynamic limit ($L \to \infty$). At each size $L$, we further need to measure a large number of instances with independently drawn random bonds for the disorder average inherent to obtain observables in spin glasses. Each instance entails approximating its ground state, which is an NP-hard combinatorial problem.

To sample ground-state of the Hamiltonian in Equation 1 at high throughput and with minimal systematic errors, heuristics can only be relied on for systems with not more than $N \approx 1000$ spins coupled together. This would appear to limit the "dynamic range" in size up to approximately $L = 10$ in $d = 3$ but limited to $L = 6$ in $d = 4$, and even to $L < 3$ in $d = 7$, definitely insufficient to extract any $L \to \infty$ limit. However, the phase diagram for a bond-diluted EA system (with $d \geq 3$ such that $T_c > 0$) shown in Figure 1 suggests that universal scaling behavior extends across the entire spin-glass (SG) phase down to the scaling window near the bond-percolation threshold $p_c$ for low enough $T$, i.e., most definitely for $T = 0$. Thus, our strategy is to find ground states for EA instances at bond density $p$ with sufficient dynamic ranges in $L$ for $p > p_c$ just above that scaling window to be within the SG phase, using *exact* reduction methods [12, 17] (see Supplementary Appendix SA) to remove a large number of spins, followed by heuristic optimization of remainder systems with $N_r \leq 1000$ [18, 19] (see Supplementary Appendix SB). These reduction methods recursively trace out all spins with fewer than four connected neighbors, at least, and are particularly effective near $p_c$ since each spin in the EA system has at most $2d$ potential neighbors while $p_c \sim 1/(2d)$ in large $d$ such that for $p$ just above $p_c$, lattices remain sparse, each spin being connected to barely more than one other spin, on average, albeit with large variations. For example, in $d = 8$ for $p = 0.0735 > p_c \approx 0.068$ and $L = 6$, an EA system with $N = 6^8 \approx 1.7 \times 10^6$ spins typically reduces to a remainder graph with $\langle N_r \rangle \approx 1000$ spins, each connected to 5.3 neighbors, on average, to be optimized heuristically.

## 2 Domain wall stiffness exponents

A quantity of fundamental importance for the modeling of amorphous magnetic materials through spin glasses [3, 20–23] is the domain wall or "stiffness" exponent $y$, often also labeled $\theta$. As Hook's law describes the response to increasing elastic energy imparted to a system for increasing displacement $L$ from its equilibrium position, the stiffness of a spin configuration describes the typical increase in magnetic energy $\Delta E$ due to an induced defect interface of a domain of size $L$. However, unlike uniform systems with a convex potential energy function over its configuration space (say, a parabola for the single degree of freedom in Hook's law, or a high-dimensional funnel for an Ising ferromagnet), an amorphous many-body system exhibits a function more reminiscent of a high-dimensional mountain landscape. Any defect-induced displacement of size $L$ in such a complicated energy landscape may move a system through numerous undulations in energy $\Delta E$. Averaging over many incarnations of such a system results in a typical energy scale

$$\sigma(\Delta E) \sim L^y \qquad (L \to \infty) \tag{2}$$

for the standard deviations of the domain wall energy $\Delta E$.

The importance of this exponent for small excitations in disordered spin systems has been discussed in many contexts [22, 24–28]. Spin systems with $y > 0$ provide resistance ("stiffness") against the spontaneous formation of defects at sufficiently low temperatures $T$, an indication that a phase transition $T_c > 0$ to an ordered state exists. For instance, in an Ising ferromagnet, the energy $\Delta E$ is always proportional to the size of the interface, i.e., $y = d - 1$, which is consistent with the fact that $T_c > 0$ only when $d > 1$. For $y < 0$, the state of a system is unstable with respect to defects, and

1 http://www.physics.emory.edu/faculty/boettcher

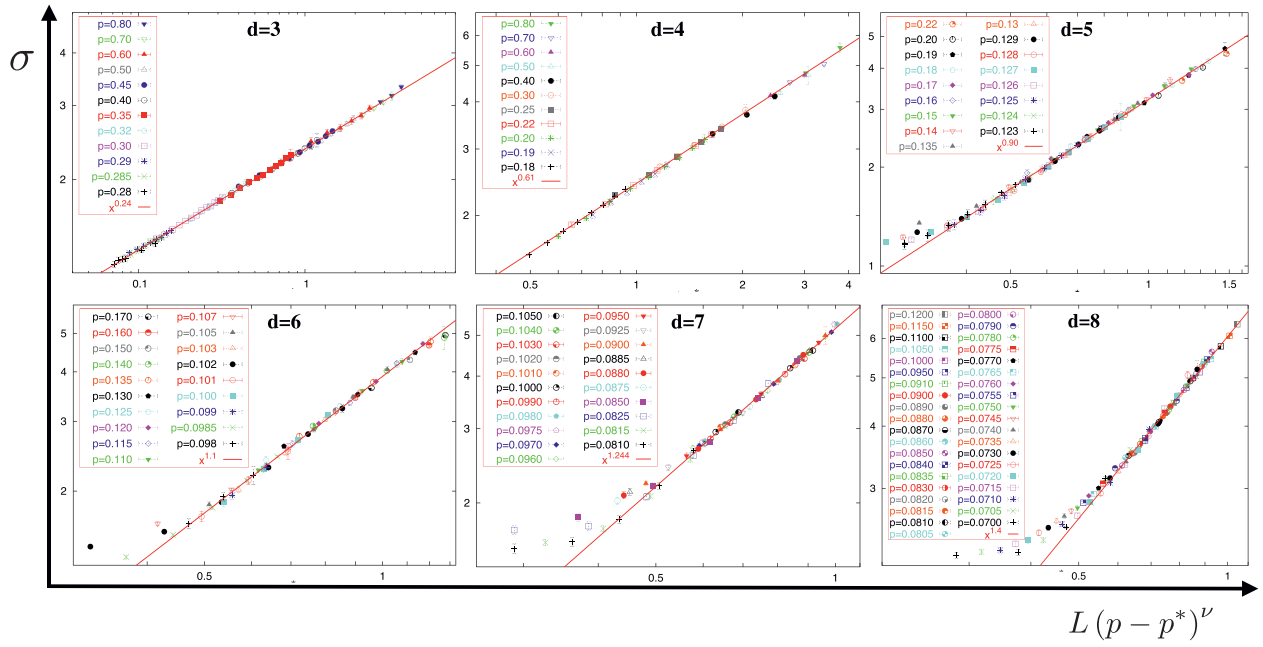


FIGURE 2
Data collapse for the domain wall scaling simulations of bond-diluted EA in $d = 3, \ldots, 8$ of $\sigma(L,p) \sim \mathcal{L}^y$ in the scaling variable $\mathcal{L} = L(p - p^*)^\nu$. For each $d$, datasets are created over a range in $p$ as listed in the respective legend, up to a size $L$ such that remainder graphs are typically $\langle N_r \rangle \approx 10^3$. The original data and the fitting parameters are listed in [11, 12]. The obtained domain wall scaling exponents $y_d$ are listed in Table 1. Note that for $d \leq 6$, transient data for smaller $\mathcal{L}$ have been omitted for clarity.

spontaneous fluctuations may proliferate, preventing any ordered state. Thus, determining the exact "lower critical dimension" $d_l$, where $y|_{d=d_l} = 0$, is of singular importance, and understanding the mechanism leading to $d_l$, however unnatural its value, provides clues to the origin of order [13, 29–33].

Instead of waiting for a thermal fluctuation to spontaneously induce a domain wall, it is expedient to directly impose domains of size $L$ through reversed boundary conditions on the system and measure the energy needed to determine $y$. To wit, in a system with periodic boundary conditions, we first obtain its ground state $E_0$ unaltered and obtain it again as $E_0'$ after reversing the signs on all bonds within a $(d-1)$-dimensional hyperplane, resulting in a complex domain of spins of size $\sim L$ that are reversed between both ground states such that $\Delta E = E_0 - E_0'$ is the energy due to the interface of that domain. Since $\Delta E$ is equally likely to be positive or negative, it is its deviation, $\sigma(\Delta E)$, which sets the energy scale in Equation 2. Notably, this problem places an even higher demand on the ground-state heuristic than described in the introduction. Here, the domain wall energy $\Delta E$ has a minute, sub-extensive difference between two almost identical, extensive energies, $E_0$ and $E_0'$, each of which is NP-hard to find. Thus, any systematic error would escalate rapidly with $N_r$, the size of the remainder graph.

As shown in Figure 2, using bond-diluted lattices for the EA system, in contrast, not only affords us a larger dynamic range in $L$ but also allows for an extended scaling regime due to the additional parameter of $p$ ranging over an entire interval. Instead of one set of data for increasing $L$ at a fixed $p$ (typically, $p = 1$ [34]) leading to the scaling in Equation 2, we can scale multiple independent sets for such a range of $p$ into a collective scaling variable, $\mathcal{L} = L(p - p^*)^\nu$, which collapses the data according to $\sigma(L,p) \sim \mathcal{L}^y$. Although the extension to an interval in $p$ makes simulations more laborious, it typically yields an extra order of magnitude in scaling compared to the prohibitive effort of confronting the NP-hard problem of reaching large $L$ at fixed $p$ alone. For instance, in $d = 3$ at $p = 1$, attainable sizes span $3 \leq L \leq 12$, at best, while we obtain a perfect data collapse for about $0.07 \leq \mathcal{L} \leq 3$ for $0.28 \leq p \leq 0.8$ (note that while $p^* \approx p_c$ and $\nu$ has some relation to the correlation-length exponent in percolation [see below], it is necessary to allow these to be a free parameter for the bimodal bonds used in these simulations, as was argued by [12]). The fitted values for $y$ for each $d$, as obtained from Figure 2, are listed in Table 1.

The values for $y$ are listed in Table 1 and plotted in Figure 4 as $1 - \frac{y}{d}$. That quantity has been obtained in the mean-field case by [35], yielding $1 - \frac{y}{d} = \frac{5}{6}$ above the upper critical dimension, $d \geq d_u = 6$. That value is clearly consistent with our high-dimensional data, providing a rare direct comparison between the mean field theory (RSB) and real-world spin glasses. As shown in Figure 4, the exponent varies continuously with dimension $d$ and allows for a simple cubic fit of the numerical data between $2 \leq d \leq 6$, weighted by the statistical errors [13]. The fit *independently* reproduces the exact known result *outside* the fitted domain at $d = 1$, $y = -1$, to less than 0.8% (not shown here). The fit has a zero at $d_l \approx 2.498$ and yields $y \approx 0.001$ at $d = \frac{5}{2}$; there is strong evidence that $d_l = 5/2$, which has also been suggested by theory [30, 33] and is consistent with the experiment [32].

In the following section, we consider some other uses of the domain wall excitations.

TABLE 1 Stiffness exponents for Edwards–Anderson spin glasses [11, 12] for dimensions $d = 2, \ldots, 8$ obtained numerically from domain wall excitations of ground states, as shown in Figure 2. The next column contains the measured values for finite-size corrections, denoted as $\omega$, from the fit of the data shown in Figure 3. The stiffness exponents $y_P$ obtained by [14] refer to EA at the bond–percolation threshold $p_c$, with values of $p_c$ obtained from [36] for $d = 3$ and [37] for $d \geq 4$. The correlation–length exponents $\nu$ for percolation are from [38] in $d = 3$ and from [39] for $d \geq 4$, where $\nu = 1/2$ is exactly above the upper critical dimension, $d \geq 6$.

| $d$ | $y$ | $1 - y/d$ | $\omega$ | $y_P$ | $1 - y_P/d$ | $p_c$ | $\nu$ | $\phi = -\nu y_P$ |
|---|---|---|---|---|---|---|---|---|
| 2 | −0.282(2) | 1.141(1) | | −0.993(3) | 1.497(2) | $\frac{1}{2}$ | $\frac{4}{3}$ | 1.323(4) |
| 3 | 0.24(1) | 0.920(4) | 0.915(4) | −1.289(6) | 1.429(3) | 0.2488126 | 0.87436(46) | 1.127(5) |
| 4 | 0.61(1) | 0.847(3) | 0.82(1) | −1.574(6) | 1.393(2) | 0.1601314 | 0.70(3) | 1.1(1) |
| 5 | 0.88(5) | 0.824(10) | 0.81(1) | −1.84(2) | 1.37(1) | 0.118172 | 0.571(3) | 1.05(2) |
| 6 | 1.1(1) | 0.82(2) | 0.82(2) | −2.01(4) | 1.34(1) | 0.0942019 | $\frac{1}{2}$ | 1.00(2) |
| 7 | 1.24(5) | 0.823(7) | 0.91(5) | −2.28(6) | 1.33(1) | 0.0786752 | $\frac{1}{2}$ | 1.14(3) |
| 8 | 1.2(1) | 0.85(2) | | | | | | |
| $\infty$ | $\sim \frac{d}{6}$ | $\frac{5}{6} = 0.8333$ | | | $\frac{4}{3} = 1.333$ | $\sim \frac{1}{2d}$ | $\frac{1}{2}$ | $\sim \frac{d}{6}$ (?) |

## 3 Ground-state finite-size correction exponents

Since simulations of statistical systems are bound to be conducted at system sizes $N$ typically quite far from the thermodynamic limit $N \to \infty$, it becomes essential to understand the corrections entailed by such limitations. This is especially pertinent for spin glasses beset with extra complexities such as NP-hardness at $T = 0$ (or, similarly, the lack of equilibration at low but finite $T$) or the additional burden of disorder averaging over many random samples severely limiting $N$. Only rarely do such corrections decay fast enough to reveal the thermodynamic behavior of an observable in a simulation at a single, "large enough" $N$. Instead, as already observed for the stiffness in Section 2, typically, sets of data need to be generated to glean the asymptotic behavior for large sizes. To extrapolate the value of an intensive observable (like the ground-state energy density), it is then necessary to have a handle on the nature of the finite-size corrections (FSCs) that have to be expected for the generated data [25, 40, 41]. However, FSCs are not only a technical necessity. Their behavior is often closely related to other physical properties in the thermodynamic limit via scaling relations [27]. They can also be instrumentalized, for instance, to assess the scalability of optimization heuristics [42, 43].

For the ground-state energy densities in the EA system, [27] argued that such FSCs should be due to locked-in domain walls of energy $\sim L^y$, which would lead to the scaling correction for the extensive energies of $E_L \sim e_\infty L^d + \Upsilon L^y$ for large $L$, defining $e_\infty$ as the $L \to \infty$ limit of the average ground-state energy density $e_L = \langle \frac{E_L}{L^d} \rangle$. This is consistent with Equation 2, where we purposefully created such a domain wall because the same system freed from that domain wall (or locked into another one) would have $E'_L \sim e_\infty L^d + \Upsilon' L^y$ and, thus, $\Delta E_L \sim \Delta\Upsilon L^y$. Dividing $E_L$ by system size, we obtain

$$e_L \sim e_\infty + \frac{A}{(L^d)^\omega}, \qquad (L \to \infty), \tag{3}$$

where the FSC exponent is conjectured to be

$$\omega = 1 - \frac{y}{d}. \tag{4}$$

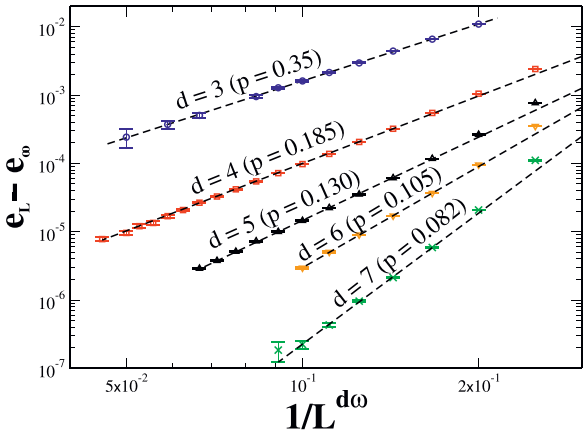


FIGURE 3
Plot of finite-size corrections to ground-state energies in bond-diluted lattice spin glasses (EA). For each dimension $d$, ground-state averages $e_L$ at increasing system sizes $L$ were obtained at a convenient bond density $p$. An asymptotic fit (dashed lines) of those data according to Equation 3 was obtained. The resulting values for the finite-size correction exponent $\omega$ are listed in Table 1 and plotted as shown in Figure 4, suggesting that Equation 4 holds.

Indeed, our direct evaluation of ground-state energy densities at some fixed bond density $p$ in dimensions $d = 3, \ldots, 7$, as shown in Figure 3, is convincingly in agreement with this picture for the dominant contributions to FSCs. However, that leaves us with somewhat of a conundrum when compared with mean-field simulations, where FSCs for the Sherrington–Kirkpatrick (SK) spin glass model [44–46] appear to yield $\omega \approx \frac{2}{3}$ for $d \to \infty$, which is not close to $1 - y/d \to \frac{5}{6}$ from RSB theory [35].

We conducted a corresponding ground-state study at the edge of the SG regime (see Figure 1) by choosing the percolation point $p = p_c$ exactly. Since the fractal percolation cluster cannot sustain an ordered state, we found that the stiffness exponent defined in Equation 2 is negative there, $y|_{p=p_c} = y_P < 0$. Numerical studies of ground states at $p_c$ (using Gaussian bonds $J_{ij}$ in this case) are computationally quite efficient since the fractals embedded in the lattice often reduce completely or so

substantially that heuristics produce little systemic error. Large lattice sizes $L$ can be achieved, limited only by rare large remainder graphs or the lack of memory needed to build the original, unreduced EA lattice. The values for $y_P$ thus obtained [14] are also listed in Table 1. Although the hypothesis for FSCs from Equation 4, $\omega = 1 - y_P/d$, leads to large values for $\omega$ when $y_P < 0$ and it becomes hard to test numerically, the corrections found are well consistent with the hypothesis [15]. In particular, it appears that $1 - y_P/d \to \frac{4}{3}$ for $d \geq d_u = 6$, which would be consistent with FSCs in percolating random graphs [47]. Although this provides an argument that Equation 4 should also hold in the mean-field limit for the EA system in the spin glass phase, the SK model might be a poor representation of that limit for the EA system. In the EA system, we first let $L \to \infty$ for a fixed number of neighbors $2dp$ before $d \to \infty$, while in the SK model, both system size and neighborhood diverge simultaneously. Unfortunately, sparse mean-field spin glasses on regular graphs ("Bethe lattices") appear to have FSCs with $\omega = \frac{2}{3}$ [48], but those results might depend, to some extent, on the structural details of the mean-field networks [45, 49, 50], and which structure most closely resembles a mean-field version of EA at $d \to \infty$ remains unclear.

## 4 Thermal–percolative crossover exponents

Having already determined the percolative stiffness exponents $y_P$ in the previous section, we can utilize it to make an interesting—and potentially experimentally testable—prediction about the behavior of the phase transition line, as shown in Figure 1. For diluted lattices at *variable* bond density $p \to p_c$, Equation 2 generalizes to [51, 52]

$$\sigma(\Delta E)_{L,p} \sim \mathcal{Y}(p) L^y f(L/\xi(p)). \tag{5}$$

Here, we assume that $\mathcal{Y}(p) \sim (p - p_c)^t \sim \xi^{-t/\nu}$ for the surface tension and $\xi(p) \sim (p - p_c)^{-\nu}$ is the conventional correlation length for percolation. The scaling function $f$ is defined to be constant for $L \gg \xi(p) \gg 1$, where percolation (and hence, $\xi$) plays no role, and we regain Equation 2 for $p > p_c$. For $\xi \gg L \gg 1$, Equation 5 requires $f(x) \sim x^\mu$ for $x \to 0$ to satisfy $\sigma \to 0$ with some power of $L$, needed to cancel the $\xi$ dependence at $p = p_c$. Thus, $\mu = -t/\nu$, and we obtain $y_P = y + \mu = y - t/\nu$ to mark the $L$ dependence of $\sigma$ at $p = p_c$, as mentioned before, which yields $t = \nu(y - y_P)$. Finally, at the crossover $\xi \sim L$, where the range $L$ of the excitations $\sigma(\Delta E)$ reaches the percolation length beyond which spin glass order ensues, Equation 5 provides

$$\sigma(\Delta E)_{\xi(p),p} \sim (p - p_c)^t \xi(p)^y f(1) \sim (p - p_c)^{-\nu y_P}. \tag{6}$$

Associating a temperature with the energy scale of the crossover in Equation 6 by $\sigma(\Delta E)_{\xi(p),p} \sim T_c$ (since, for $T > T_c$, thermal fluctuations destroy order at a length-scale $\ll \xi$) leads to

$$T_g(p) \sim (p - p_c)^\phi, \quad \text{with} \quad \phi = -\nu y_P, \tag{7}$$

defining [51] the "thermal–percolative crossover exponent" $\phi$. All data for $d = 2, \ldots, 7$ are listed in Table 1, and the results for $\phi$ are also shown in Figure 4. It appears that $\phi$ decreases with increasing $d$ for $d \leq d_u = 6$, has a minimum of $\phi = 1$ at $d_u = 6$, and increases as $\phi = d/6$ above $d_u$.

Of particular experimental interest is the result for $d = 3$, $y_P = -1.289(6)$, predicting $\phi = 1.127(5)$ with $\nu = 0.87436(46)$ [38]. This exponent provides a non-trivial, experimentally testable prediction derived from scaling arguments of equilibrium theory at low temperatures (since bond and site percolation are typically in the same universality class, it should make little difference whether an experiment varies the site concentration of atoms with dipolar spin or the bonds between them). Such tests are few as disordered materials by their very nature fall out of equilibrium when entering the glassy state. The phase boundary itself provides the perfect object for such a study. It can be approached by theory from below and by experiments from above where equilibration is possible. [53] already provided highly accurate results for the freezing temperature $T_M$ as a function of dilution $x$ for a doped, crystalline glass, $(La_{1-x}Gd_x)_{80}Au_{20}$, proposing a linear dependence, $T_M \sim x$. The tabulated data are equally well fitted using Equation 7 in that regime. [54] determined a phase diagram for $(Fe_xNi_{1-x})_{75}P_{16}B_6Al_4$, an amorphous alloy, for a wide range of temperatures $T$ and site concentrations $x$ but did not discuss its near-linear behavior at low $x$. A similar phase diagram for the insulator $CdCr_{2x}In_{2(1-x)}S_4$ is shown in Figure 1A of [55]. New experiments dedicated to the limit $x \searrow x_c$ should provide the results of sufficient accuracy to test our prediction for $\phi$.

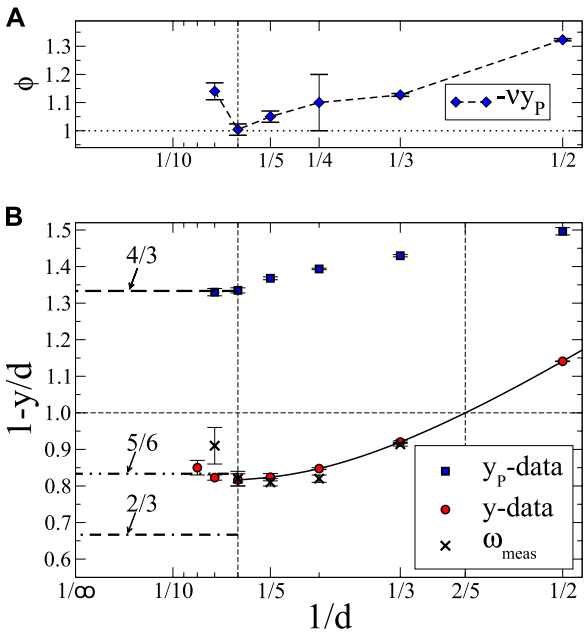


FIGURE 4
Plot summarizing the data for the exponents in Table 1, here plotted as a function of inverse dimension, $1/d$, to highlight the connection with the mean field limit for $d \geq d_u = 6$ (left vertical line). **(B)** refers to the stiffness exponents $y$ in the spin-glass regime (SG in Figure 1) or $y_P$ at $p_c$ and $T = 0$, each presented as $1 - y/d$. Included are also the measured FSC exponents $\omega$, which appear to be consistent with the conjecture in Equation 4. For stiffness, the $y$ data are quite consistent with $1 - y/d = 5/6$ predicted for $d \geq d_u$ [35] but not with the FSC $\omega_{SK} = 2/3$ found for SK [44]. The fit of this data (solid line) yields a lower critical dimension $d_l \approx \frac{5}{2}$, where $y = 0$ (right vertical line). At $p_c$, the $y_P$ data appear to approach a value of $\omega = 4/3$ expected for the FSCs of percolating random graphs. In **(A)**, $y_P$ is multiplied with the independent percolation exponent $\nu$to form the thermal–percolative crossover exponent $\phi$ that characterizes the behavior of the phase boundary near $p_c$ in Equation 7, see green arrows in Figure 1. It seems to show a minimum of $\phi \approx 1$ at $d = d_u = 6$.

## 5 Conclusions

We summarized a collection of simulation data pertaining to the lattice spin glass EA over a range of dimensions, providing a comprehensive description of low-energy excitations from experimentally accessible systems to the mean-field level, where exact results can be compared with. Putting all those results side-by-side paints a self-consistent picture of domain wall excitations, their role in the stability of the ordered glass state, and their role for finite-size corrections. Extending to the very physical concept of bond density made simulations in high dimensions feasible, added accuracy, and opened up the spin-glass phase diagram, which makes new observables experimentally accessible, such as the thermal–percolative crossover exponent.

Going forward, the methods developed here could be extended to study, say, ground-state entropy and their overlaps [56] or the fractal nature of domain walls [57, 58]. Our method might also inspire new ways of using dilution as a gadget to make simulations more efficient [59].

## Author contributions

SB: conceptualization, data curation, formal analysis, investigation, methodology, writing–original draft, and writing–review and editing.

## Funding

The author(s) declare that no financial support was received for the research, authorship, and/or publication of this article.

## Conflict of interest

The author declares that the research was conducted in the absence of any commercial or financial relationships that could be construed as a potential conflict of interest.

## Publisher's note

All claims expressed in this article are solely those of the authors and do not necessarily represent those of their affiliated organizations, or those of the publisher, the editors, and the reviewers. Any product that may be evaluated in this article, or claim that may be made by its manufacturer, is not guaranteed or endorsed by the publisher.

## Supplementary material

The Supplementary Material for this article can be found online at: https://www.frontiersin.org/articles/10.3389/fphy.2024.1466987/full#supplementary-material

## References

1. Wilson KG, Fisher ME. Critical exponents in 3.99 dimensions. *Phys Rev Lett* (1972) 28:240–3. doi:10.1103/physrevlett.28.240

2. t'Hooft G, Veltman MJG. Regularization and renormalization of gauge fields. *Nucl Phys B* (1972) 44:189–213. doi:10.1016/0550-3213(72)90279-9

3. Fischer KH, Hertz JA. *Spin glasses, Cambridge studies in magnetism*. Cambridge: Cambridge University Press (1991).

4. Mézard M, Parisi G, Virasoro MA. *Spin glass theory and beyond*. Singapore: World Scientific (1987).

5. Stein DL, Newman CM. *Spin glasses and complexity*. Princeton: Princeton University Press (2013).

6. Charbonneau P, Marinari E, Mezard M. Editors. *Spin glass theory and far beyond*. Singapore: World Scientific (2023).

7. de Dominicis C, Kondor I, Temesári T. Spin glasses and random fields. In: Young A, editor. *Series on directions in condensed matter physics: volume 12*. Singapore: World Scientific (1998).

8. Moore MA, Read N. Multicritical Point on the de Almeida–Thouless Line in Spin Glasses in d > 6 Dimensions. *Phys Rev Lett* (2018) 120:130602. doi:10.1103/physrevlett.120.130602

9. Moore MA. Droplet-scaling versus replica symmetry breaking debate in spin glasses revisited. *Phys Rev E* (2021) 103:062111. doi:10.1103/physreve.103.062111

10. Barahona F. On the computational complexity of Ising spin glass models. *J Phys A: Math Gen* (1982) 15:3241–53. doi:10.1088/0305-4470/15/10/028

11. Boettcher S. Stiffness exponents for lattice spin glasses in dimensions d = 3, . . . , 6. *The Eur Phys J B - Condensed Matter* (2004) 38:83–91. doi:10.1140/epjb/e2004-00102-5

12. Boettcher S. Low-temperature excitations of dilute lattice spin glasses. *Europhys Lett* (2004) 67:453–9. doi:10.1209/epl/i2004-10082-0

13. Boettcher S. Stiffness of the Edwards-Anderson model in all dimensions. *Phys Rev Lett* (2005) 95:197205. doi:10.1103/physrevlett.95.197205

14. Boettcher S, Marchetti E. Low-temperature phase boundary of dilute-lattice spin glasses. *Phys Rev B* (2008) 77:100405(R). doi:10.1103/physrevb.77.100405

15. Boettcher S, Falkner S. Finite-size corrections for ground states of Edwards-Anderson spin glasses. *EPL (Europhysics Letters)* (2012) 98:47005. doi:10.1209/0295-5075/98/47005

16. Edwards SF, Anderson PW. Theory of spin glasses. *J Phys F* (1975) 5:965–74. doi:10.1088/0305-4608/5/5/017

17. Boettcher S, Davidheiser J. Reduction of dilute Ising spin glasses. *Phys Rev B* (2008) 77:214432. doi:10.1103/physrevb.77.214432

18. Boettcher S, Percus AG. Optimization with extremal dynamics. *Phys Rev Lett* (2001) 86:5211–4. doi:10.1103/physrevlett.86.5211

19.In: Hartmann A, Rieger H, editors. *New optimization algorithms in physics*. Berlin: Wiley VCH (2004).

20. Southern BW, Young AP. Real space rescaling study of spin glass behaviour in three dimensions. *J Phys C: Solid State Phys* (1977) 10:2179–95. doi:10.1088/0022-3719/10/12/023

21. McMillan WL. Scaling theory of Ising spin glasses. *J Phys C: Solid State Phys* (1984) 17:3179–87. doi:10.1088/0022-3719/17/18/010

22. Fisher DS, Huse DA. Ordered phase of short-range Ising spin-glasses. *Phys Rev Lett* (1986) 56:1601–4. doi:10.1103/physrevlett.56.1601

23. Bray AJ, Moore MA. Heidelberg colloquium on glassy dynamics and optimization In: Van Hemmen L, Morgenstern I, editors. *Proceedings of a colloquium on spin glasses, optimization and neural networks held at the University of Heidelberg*. New York: Springer (1986). p. 121.

24. Krzakala F, Martin O. Spin and link overlaps in three-dimensional spin glasses. *Phys Rev Lett* (2000) 85:3013–6. doi:10.1103/physrevlett.85.3013

25. Palassini M, Young AP. Nature of the spin glass state. *Phys Rev Lett* (2000) 85:3017–20. doi:10.1103/physrevlett.85.3017

26. Palassini M, Liers F, Jünger M, Young AP. Interface energies in Ising spin glasses. *Phys Rev B* (2003) 68:064413. doi:10.1103/physrevb.68.064413

27. Bouchaud J-P, Krzakala F, Martin OC. Energy exponents and corrections to scaling in Ising spin glasses. *Phys Rev B* (2003) 68:224404. doi:10.1103/physrevb.68.224404

28. Aspelmeier T, Moore MA, Young AP. Interface energies in ising spin glasses. *Phys Rev Lett* (2003) 90:127202. doi:10.1103/physrevlett.90.127202

29. Bray AJ, Moore MA. Lower critical dimension of Ising spin glasses: a numerical study. *J Phys C: Solid State Phys* (1984) 17:L463–8. doi:10.1088/0022-3719/17/18/004

30. Franz S, Parisi G, Virasoro MA. Interfaces and lower critical dimension in a spin glass model. *J Phys (France)* (1994) 4:1657–67. doi:10.1051/jp1:1994213

31. Hartmann AK, Young AP. Lower critical dimension of Ising spin glasses. *Phys Rev B* (2001) 64:180404(R). doi:10.1103/physrevb.64.180404

32. Guchhait S, Orbach R. Direct dynamical evidence for the spin glass lower critical dimension 2 < dℓ < 3. *Phys Rev Lett* (2014) 112:126401. doi:10.1103/physrevlett.112.126401

33. Maiorano A, Parisi G. Support for the value 5/2 for the spin glass lower critical dimension at zero magnetic field. *Proc Natl Acad Sci U S A* (2018) 115:5129–34. doi:10.1073/pnas.1720832115

34. Hartmann AK. Ground-state clusters of two-three-and four-dimensional ± JIsing spin glasses. *Phys Rev E* (2000) 63:016106. doi:10.1103/physreve.63.016106

35. Parisi G, Rizzo T. Large deviations in the free energy of mean-field spin glasses. *Phys Rev Lett* (2008) 101:117205. doi:10.1103/physrevlett.101.117205

36. Lorenz CD, Ziff RM. Precise determination of the bond percolation thresholds and finite-size scaling corrections for the sc, fcc, and bcc lattices. *Phys Rev E* (1998) 57:230–6. doi:10.1103/physreve.57.230

37. Grassberger P. Critical percolation in high dimensions. *Phys Rev E* (2003) 67:036101. doi:10.1103/physreve.67.036101

38. Deng Y, Blöte HWJ. Monte Carlo study of the site-percolation model in two and three dimensions. *Phys Rev E* (2005) 72:016126. doi:10.1103/PhysRevE.72.016126

39. Hughes BD. *Random walks and random environments*. Oxford: Oxford University Press (1996).

40. Pal KF. The ground state of the cubic spin glass with short-range interactions of Gaussian distribution. *Physica A* (1996) 233:60–6. doi:10.1016/s0378-4371(96)00241-5

41. Young AP. *Finite-size scaling*. World Scientific (2024). p. 599–615.

42. Boettcher S. Analysis of the relation between quadratic unconstrained binary optimization and the spin-glass ground-state problem. *Phys Rev Res* (2019) 1:033142. doi:10.1103/physrevresearch.1.033142

43. Boettcher S. Deep reinforced learning heuristic tested on spin-glass ground states: the larger picture. *Nat Commun* (2023) 14:5658. doi:10.1038/s41467-023-41106-y

44. Boettcher S. Extremal optimization for Sherrington-Kirkpatrick spin glasses. *The Eur Phys J B* (2005) 46:501–5. doi:10.1140/epjb/e2005-00280-6

45. Boettcher S. Simulations of ground state fluctuations in mean-field Ising spin glasses. *J Stat Mech Theor Exp* (2010) 2010:P07002. doi:10.1088/1742-5468/2010/07/p07002

46. Aspelmeier T, Billoire A, Marinari E, Moore MA. Finite-size corrections in the Sherrington–Kirkpatrick model. *J Phys A: Math Theor* (2008) 41:324008. doi:10.1088/1751-8113/41/32/324008

47. Bollobas B. *Random graphs*. London: Academic Press (1985).

48. Boettcher S. Numerical results for ground states of spin glasses on Bethe lattices. *Eur Phys J B - Condensed Matter* (2003) 31:29–39. doi:10.1140/epjb/e2003-00005-y

49. Zdeborová L, Boettcher S. A conjecture on the maximum cut and bisection width in random regular graphs. *J Stat Mech Theor Exp* (2010) 2010:P02020. doi:10.1088/1742-5468/2010/02/p02020

50. Boettcher S. Ground state properties of the diluted Sherrington-Kirkpatrick spin glass. *Phys Rev Lett* (2020) 124:177202. doi:10.1103/physrevlett.124.177202

51. Banavar JR, Bray AJ, Feng S. Critical behavior of random spin systems at the percolation threshold. *Phys Rev Lett* (1987) 58:1463–6. doi:10.1103/physrevlett.58.1463

52. Bray AJ, Feng S. Percolation of order in frustrated systems: the dilute J spin glass. *Phys Rev B* (1987) 36:8456–60. doi:10.1103/physrevb.36.8456

53. Poon SJ, Durand J. Magnetic-cluster description of spin glasses in amorphous La-Gd-Au alloys. *Phys Rev B* (1978) 18:6253–64. doi:10.1103/physrevb.18.6253

54. Beckman O, Figueroa E, Gramm K, Lundgren L, Rao KV, Chen HS. Spin wave and scaling law Analysis of amorphous $(Fe_xNi_x)_{75}P_{16}B_6Al_3$by magnetization measurements. *Phys Scr* (1982) 25:726–30. doi:10.1088/0031-8949/25/6a/017

55. Vincent E. Ageing and the glass transition. In: Henkel M, Pleimling M, Sanctuary R, editors. *Ageing and the glass transition*. Heidelberg: Springer (2007). 716 of Springer Lecture Notes in Physics, condmat/063583.

56. Boettcher S. Reduction of spin glasses applied to the Migdal-Kadanoff hierarchical lattice. *Eur Phys J B - Condensed Matter* (2003) 33:439–45. doi:10.1140/epjb/e2003-00184-5

57. Wang W, Moore MA, Katzgraber HG. Fractal dimension of interfaces in Edwards-Anderson and long-range Ising spin glasses: determining the applicability of different theoretical descriptions. *Phys Rev Lett* (2017) 119:100602. doi:10.1103/physrevlett.119.100602

58. Vedula B, Moore MA, Sharma A. *Evidence that the AT transition disappears below six dimensions* (2024). doi:10.48550/arXiv.2402.03711

59. Jörg T, Ricci-Tersenghi F. Entropic effects in the very low temperature regime of diluted Ising spin glasses with discrete couplings. *Phys Rev Lett* (2008) 100:177203. doi:10.1103/physrevlett.100.177203

frontiers | Frontiers in Physics

TYPE Mini Review
PUBLISHED 18 October 2024
DOI 10.3389/fphy.2024.1431805



OPEN ACCESS

EDITED BY
Ralph Chamberlin,
Arizona State University, United States

REVIEWED BY
Sebastiano Pilati,
University of Camerino, Italy

*CORRESPONDENCE
David C. Harrison,
dcharrison@wisc.edu

RECEIVED 12 May 2024
ACCEPTED 30 August 2024
PUBLISHED 18 October 2024

CITATION
Harrison DC (2024) Electronic 1/*f* noise as a probe of dimensional effects on spin-glass dynamics.
*Front. Phys.* 12:1431805.
doi: 10.3389/fphy.2024.1431805



# Electronic 1/*f* noise as a probe of dimensional effects on spin-glass dynamics

David C. Harrison*

Department of Physics, University of Wisconsin-Madison, Madison, WI, United States

Over the past decade, spin-glass simulations have improved to the point that they now access time- and length-scales comparable to experiments at the mesoscale. A recent series of thin-film field-cooled/zero-field-cooled magnetization (FC/ZFC) experiments demonstrated activated spin dynamics, with a temperature-independent activation energy proportional to the logarithm of the film thickness and with coefficients in remarkable agreement with the simulation. These measurements require the application of small magnetic fields, which has been shown to affect the spin-glass energy landscape. Measurements of the 1/*f* noise in metallic spin-glasses have been previously shown to be a sensitive probe of the spin dynamics, and the measurements can be made without applying a magnetic field. In this mini-review, we review these techniques and discuss how transport measurements can fit into the current landscape of spin-glass measurements. We compare previous measurements to more recent measurements on similar films, made with ostensibly different cooling protocols, and compare both the previous and recent measurements to the magnetometry. The transport measurements—taken over a wider range of temperature than magnetometry—suggest that the maximum spin-glass energy barrier height is temperature-dependent, not fixed, possibly due to two-dimensional dynamics. We discuss this possibility, along with future measurements, which may be able to resolve this mystery.

KEYWORDS

**spin-glass, noise, dimensional crossover, 1/f, resistance fluctuations**

## Introduction

Spin-glasses are an archetypal complex system. The same rugged energy landscape characteristic to these frustrated magnets can describe polymers, structural glasses, the stock market, and even neural networks. Yet, despite the passage of more than 5 decades since their discovery, accompanied by intensive experimental and theoretical efforts, the underlying physics of the spin-glass state remains a mystery, with even the existence of a single ground state (in three dimensions) being an open question [1].

Experimentally, spin-glass systems are notoriously difficult to study. Spin-glasses are a magnetic system; however, absent the application of a magnetic field (either before or during a measurement), the magnetization will be 0. In order to directly probe the dynamics, an experimenter must apply a small magnetic field, which has been shown to alter the dynamics of the system, reducing the free-energy barriers due to the Zeeman interaction. Indeed, even small fields may fundamentally alter the nature of the system, with the "droplet" model [2, 3] predicting that the spin-glass state is destroyed by any field, no

matter how small, although this has proven difficult to distinguish experimentally from the mean-field prediction of a (de Almeida–Thouless) phase transition in a field [4].

Moreover, spin-glass systems rapidly fall out of equilibrium. Their dynamics are slow and exhibit memory: in general, the result of a measurement on a spin-glass will depend on the parameters (e.g., applied field and temperature) at the time of the measurement and on the values of those parameters at all previous time points since cooling into the spin-glass state, although this description is complicated by effects such as temperature chaos. For this reason, for an unambiguous comparison between simulation and experiment, a well-defined cooling protocol should be used.

In this mini-review, we discuss recent spin-glass magnetometry measurements, which have been interpreted through the spin-glass coherence length. The coherence length is defined using a four-spin correlation function, and it is physically the characteristic length-scale of the thermally equilibrated domains within a spin-glass sample. Well below the spin-glass transition temperature, the domains grow very slowly and the system is out-of-equilibrium. In experiments, one way to probe the coherence length is to fabricate devices where the coherence length can increase to the sample thickness. Then, the dynamics should change from three- to two-dimensional, and the apparent freezing temperature is reduced. In simulations, the ground state is never known and may not be unique, so to measure the coherence length, researchers look at the overlap between many replicas of the system [5]. Because the computing power has increased (and costs have decreased) dramatically over the past decades, the JANUS collaboration has been able to design and build an FPGA-based, ultra-parallelized processor optimized specifically for Monte Carlo simulations of spin-glasses [6]. These simulations provide access to the spin-glass coherence length, and for the first time, experiments and simulations on mesoscale systems are able to probe comparable time- and length-scales, allowing direct comparison between the two.

After the discussion of the state-of-the-art conventional measurements and simulation, we will move to the main topic of this review: electronic noise measurements. These measurements are an ideal complement to the more conventional measurements for measurements on mesoscale systems, where dimensional effects play a role. The techniques discussed here are not new, but they are of renewed importance due to the advances in simulation and recent measurements of the spin-glass coherence length.

## Magnetometry and spin-glass coherence length

When a spin-glass is quenched from above its glass temperature $T_g$ to a measurement temperature $T$ well below $T_g$, spin-glass correlations grow slowly in time and the system falls out of equilibrium. In order to describe this effect, Kisker et al. simulated Ising spin-glasses and measured a four-spin autocorrelation function [5]. In this way, the authors were able to define an effective coherence length, the fundamental length-scale describing the spatial extent of the spin-glass correlations after waiting time $t$,

$$\frac{\xi(t,T)}{a_0} = c_1\left(\frac{t}{\tau_0}\right)^{c_2 T/T_g}, \tag{1}$$

where $a_0$ is the average spacing between the magnetic dopants, $c_1$ is a prefactor of order unity, $\tau_0 \approx \hbar/k_B T_g$ is a characteristic timescale of microscopic magnetic fluctuations, and $c_2$ is a constant which can be determined experimentally [5]. On the experimental front, Joh *et al.* provided the first procedure for determining $\xi(t,T)$ experimentally [7]. One key insight is that after time $t$, the maximum free energy barrier, $\Delta_{max}$, surmounted will be given by

$$\Delta_{max}(t) \approx k_B T \ln\left(\frac{t}{\tau_0}\right), \tag{2}$$

according to the Arrhenius law.

Recently, variations on this approach have been employed on Ge:Mn [8, 9], single-crystal Cu:Mn [10–13], polycrystalline Cu:Mn [14], and Cu:Mn thin-films [15, 16]. Moreover, in the decades since the work by Kisker *et al.*, it has become possible to simulate spin-glasses on the same time- and length-scales probed experimentally [10, 11, 17–19]; the agreement between the dynamics of the coherence length extracted experimentally and from simulation has been remarkable [20].

In the Cu:Mn thin-film experiments (e.g., Refs. [15, 16]), the coherence length $\xi(t,T)$ increases in time according to Equation 1 until it reaches the film thickness $\mathcal{L}$, after which it can increase no further in the direction perpendicular to the plane of the film. Neglecting the effects of any in-plane increase in the coherence length on the energy barriers, according to Equation 1 and Equation 2, this will pin the maximum barrier height at

$$\frac{\Delta_{max}(\mathcal{L})}{k_B T_g} = \frac{1}{c_2}\left[\ln\left(\frac{\mathcal{L}}{a_0}\right) - \ln c_1\right]. \tag{3}$$

In the vicinity of $T_g$, the maximum barrier height will be fixed by the film thickness alone and independent of temperature. This implies that, at long times, the thermoremanent magnetization (TRM) and, equivalently, the irreversible magnetizaton (defined as the difference between the FC and ZFC magnetization) should be time-dependent, exhibiting an exponential decay, consistent with activated dynamics over a free energy barrier of height $\Delta_{max}(\mathcal{L})$. By the same argument, the apparent freezing temperature of a thin spin-glass film will depend on the measurement time $t$ according to

$$t \approx \tau_0 \exp\left[\frac{\Delta_{max}(\mathcal{L})}{k_B T_f}\right] \Leftrightarrow T_f \approx \frac{\Delta_{max}(\mathcal{L})}{k_B}\left[\ln\left(\frac{t}{\tau_0}\right)\right]^{-1}. \tag{4}$$

Using this approach, Zhai et al. was able to fit data for multiple film thicknesses (ranging from 4 nm to 20 nm), taken at multiple temperatures, to Equation 3 with $c_1 = 1.448$ and $c_2 = 0.104$ [15]. Using the Janus II supercomputer, Baity-Jesi et al. later measured an exponent in quantitative agreement with the $c_2$ from experiment [17], demonstrating the new synergy between experiment and simulation.

Applying a magnetic field will reduce the maximum barrier height, due to the Zeeman interaction. Here,

$$\Delta_{max}(H,\mathcal{L}) = \Delta_{max}(0,\mathcal{L}) - E_Z, \tag{5}$$

where the Zeeman energy is given by $E_Z = N_c\chi_{FC}H^2$, with $N_c$ the number of correlated spins, $\chi_{FC}$ the per-spin susceptibility, and $H$ the applied field. Repeating the measurements from Ref. [15] on the 20-nm film, over a range of applied fields, Zhai et al. was able to extract the number of spins in a correlated volume and determine that the correlated regions could not be spherical, but must instead be "pancake-like" (though possibly non-compact and fractal) [16]. Partially for this reason, most recent works have focused on single-crystal systems [10–13, 21], where—due to symmetry—the correlated regions will surely be spherical, to facilitate an understanding of the spin-glass state in the bulk.

Thin-film spin-glasses are of intrinsic interest, however from both an academic and practical perspective. For instance, the performance of SQUID-based superconducting circuits—including frequency-tunable qubits enabling fast quantum gates—is limited by anomalous $1/f$ magnetic flux noise at low temperatures, with the magnitude of order $\sim 1\mu\Phi_0/\mathrm{Hz}^{1/2}$ at 1 Hz, essentially independent of the geometry [22]. The weak dependence of the noise on the area of the SQUID loop points to a surface effect, and the most up-to-date work pinpoints adsorbed molecular oxygen as the origin [23]. This adsorbed oxygen—which freezes to the SQUID as it is cooled—appears to undergo a spin-glass transition at a temperature between 50 mK and 2 K, although the details are still not well-understood [22, 24, 25]. Certainly in such a system, dimensional effects play a role in the dynamics.

## Transport measurements in spin-glasses

While measurements of the field-cooled, zero-field-cooled, and thermoremanent magnetization, as well as measurements of the AC susceptibility, of mesoscale spin-glass devices have been tremendously successful, they are intrinsically limited due to magnetization being an extrinsic quantity: measurement signal-to-noise (SNR) always decreases with decreasing volume. These measurements require carefully designed systems and multi-layer samples, with many thin spin-glass layers separated by non-magnetic spacing layers [15, 16, 26–28]. Moreover, interesting spin-glass dynamics are the result of a rich energy landscape, consisting of many metastable states, and the application of even weak magnetic fields can alter this landscape [9, 16]. Finally, while this scheme works well for devices "small" in one dimension (thickness), it is difficult to imagine efficiently scaling the process to devices small in two or even three dimensions.

In the 1980s and 1990s, M.B. Weissman et al., demonstrated that transport measurements—specifically, measurements of either the fluctuations of the resistance of a mesoscale spin-glass device or measurements of the fluctuations in the fluctuations of the resistance—can provide similar and complementary information to the more conventional magnetometric probes [29–33]. Despite their non-ergodic nature, the fluctuation-dissipation theorem has been shown to apply to spin-glass dynamics, meaning that these noise measurements provide the same information as direct measurements of the AC susceptibility [34]. However, because resistance fluctuations are not an extrinsic property, going to smaller volumes does not degrade and can even improve the SNR. Additionally, noise measurements allow the spin-glass energy landscape to be probed without any perturbing magnetic field, eliminating any concern over whether the system is in the linear-response regime.

Transport measurements are a proven method of probing spin-glass dynamics. While the resistivity of a spin-glass shows no sharp signature near $T_g$, the magnitude of the resistance *fluctuations* does exhibit such a signature, increasing by more than an order of magnitude over a temperature range of approximately $0.2T_f$ [30, 31, 33]. For mesoscale dynamics, this can be an ideal probe because the SNR does not directly depend on the volume, which is by definition always small for a mesoscale device.

The observed noise is due to universal conductance fluctuations (UCFs). Here, elastic scattering off of the magnetic dopants dominates over inelastic scattering, and the noise is due to changes in the interference in the Feynman paths of the electrons due to the reorienting of the magnetic moments of the dopants (spins). The UCF theory does result in a temperature-dependent ($\propto T^2$) coupling between the magnetization and resistance fluctuations, that—along with an additional thermodynamic factor of $T$—must be divided out in our analysis [30, 31, 33].

Measurements of the $1/f^\gamma$ ($\gamma \approx 1$) noise are a relatively direct probe of the zero-field spin-glass energy landscape. Van der Ziel explains $1/f$ noise in terms of a collection of non-interacting two-level fluctuators (TLFs) with a distribution of energy barriers [35]. A single TLF produces a Lorentzian spectrum with a "knee" frequency given by the average switching rate (related to the energy barrier as $f = f_0 \exp[-E_B/kT]$ where $E_B$ is the barrier height and $f_0$ is the temperature-independent attempt frequency); the sum of many such spectra with a uniform distribution of energy barriers produces $1/f$ noise.

If the barrier distribution is not uniform, but weighted more heavily at higher (lower) energies, the spectral exponent will not be exactly $\gamma = 1$, but will be $\gamma < 1$ ($\gamma > 1$). Working within this model, Dutta and Horn noted that additionally, at a given temperature $T$ and for a given bandwidth ($f_{\min}$ to $f_{\max}$), an experiment probes the barrier distribution only within a small domain: $kT\ln(f_0/f_{\min}) < E_B < kT\ln(f_0/f_{\max})$ [36]. In other words, for a fixed bandwidth, reducing the temperature means probing the dynamics set by smaller barriers. Combining these two concepts, one can relate the measured spectral exponent $\gamma$ at a given frequency to the logarithmic derivative of the spectral density $S_M$ with respect to temperature, at that same frequency,

$$\gamma(f,T) = 1 - \frac{1}{\ln(f/f_0)}\left[\frac{d\ln S_M}{d\ln T} - 1\right]. \tag{6}$$

This is illustrated in Figure 1. The key assumption here is that the barrier heights are independent of temperature, i.e., that the dynamics are activated. If they are not, one can repeat this analysis, but allow $f_0$ to be a temperature-dependent free parameter rather than a physical attempt frequency. If the barriers are growing with decreasing temperature, but one performs the Dutta–Horn analysis assuming constant barriers, it will *appear* that the attempt frequency is very large, although this is not physical. To illustrate this, consider a toy model with barriers having a linear temperature dependence, $E_B \to E_{B0} - |\alpha|kT$. Inserting this into the Arrhenius law gives $f = f_0 \exp(|\alpha|)\exp[-E_{B0}/kT]$, which is equivalent to

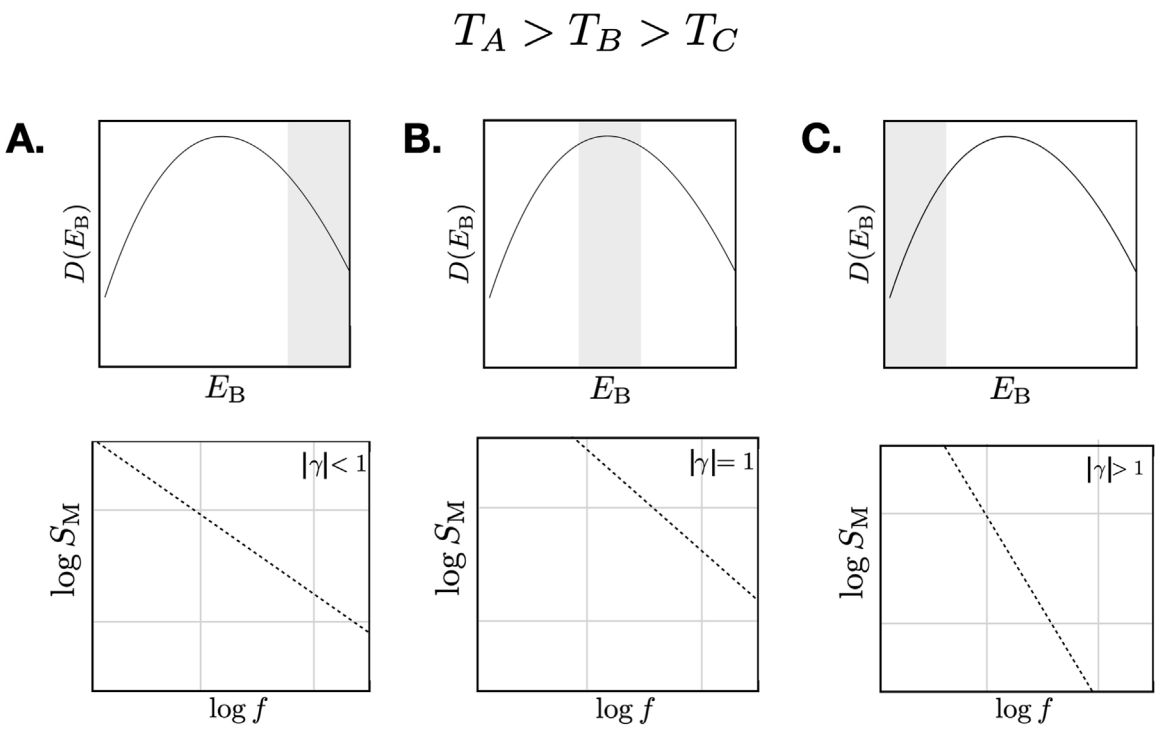


FIGURE 1
Dutta–Horn picture for a simple barrier distribution. **(A)** At high temperatures, a measurement will probe larger barriers. If the barrier distribution is weighted to lower energy, as shown, the spectral exponent will be smaller than unity. **(B)** At a lower temperature, the measurement will probe smaller barriers. Here, the experimental bandwidth is near the peak of the barrier distribution, which is approximately flat. The result is a spectral density with a spectral exponent near unity. The magnitude of the spectral density has also increased due to the larger density of barriers. **(C)** At a lower temperature still, the measurement will probe barriers below the peak. As the barrier distribution is now weighted to higher energy, the spectral exponent will be larger than unity, and because the barrier distribution is now smaller than at the peak, the magnitude of the noise has also decreased. Temperature-dependent barriers result in deviations from this picture.

$f_0 \rightarrow f_0 \exp(|\alpha|)$ and removing the temperature dependence from the barriers. Fenimore and Weissman suggested defining cooperativity from noise measurements, given by

$$c_N(f,T) \equiv -\frac{\partial \ln S_R}{\partial \ln T}(1-\gamma(f,T))^{-1}, \tag{7}$$

where we have converted from $S_M$ to the resistance spectral density $S_R$, taking into account the temperature-dependent factors. In the case of temperature-independent barriers, $c_N = \ln(f_0/f) \approx 30$ at all temperatures; the dynamics are activated. If, on the other hand, barriers are growing with decreasing temperature, then $c_N \gg 30$, indicating cooperative dynamics. This definition of cooperativity is analogous to the more traditional definition from magnetometry

$$c_M \equiv \frac{\partial \ln T_f}{\partial \ln f}, \tag{8}$$

but it is defined at all temperatures, including well away from $T_f$.

We again note that $S_M$ (derived from $S_R$) provides the same information as the imaginary part of the AC susceptibility, $\chi''$, according to the FDT [34]:

$$S_M(f,T) = \frac{k_B T}{f}\chi''(f,T). \tag{9}$$

## Discussion

First, we compare recent transport measurements in spin-glasses. The effect of the cooling protocol on spin-glass thin-film measurements is still an open question; it is possible that temperature chaos renders the details of the experimental temperature quench moot, while Ref. [37] suggests that it is critical to rapidly quench from well above the bulk $T_g$ to a measurement temperature $T$ between each measurement. To allow for unambiguous interpretation of the measurements, Harrison et al. employed this well-defined cooling protocol and reported noise measurements on Cu:Mn (13.5 at%) on films ranging in thickness from 10 nm to 80 nm [38]. For these measurements, the devices were patterned using electron-beam lithography to form a balanced bridge, as shown schematically in Figure 2A. Each arm measures 50 μm × 300 nm. The measurements are made with a lock-in amplifier. With this configuration, current fluctuations should affect each arm equally and cancel out, and the lock-in moves the signal away from the $1/f$ noise intrinsic to the electronics. The measured voltage fluctuations are then converted to resistance fluctuations, which can in turn be converted to magnetization fluctuations. In Figure 2B, we reproduce Figure 1 from Ref. [38], showing the change in both the shape and magnitude of the resistance spectral density as a function of temperature, while in

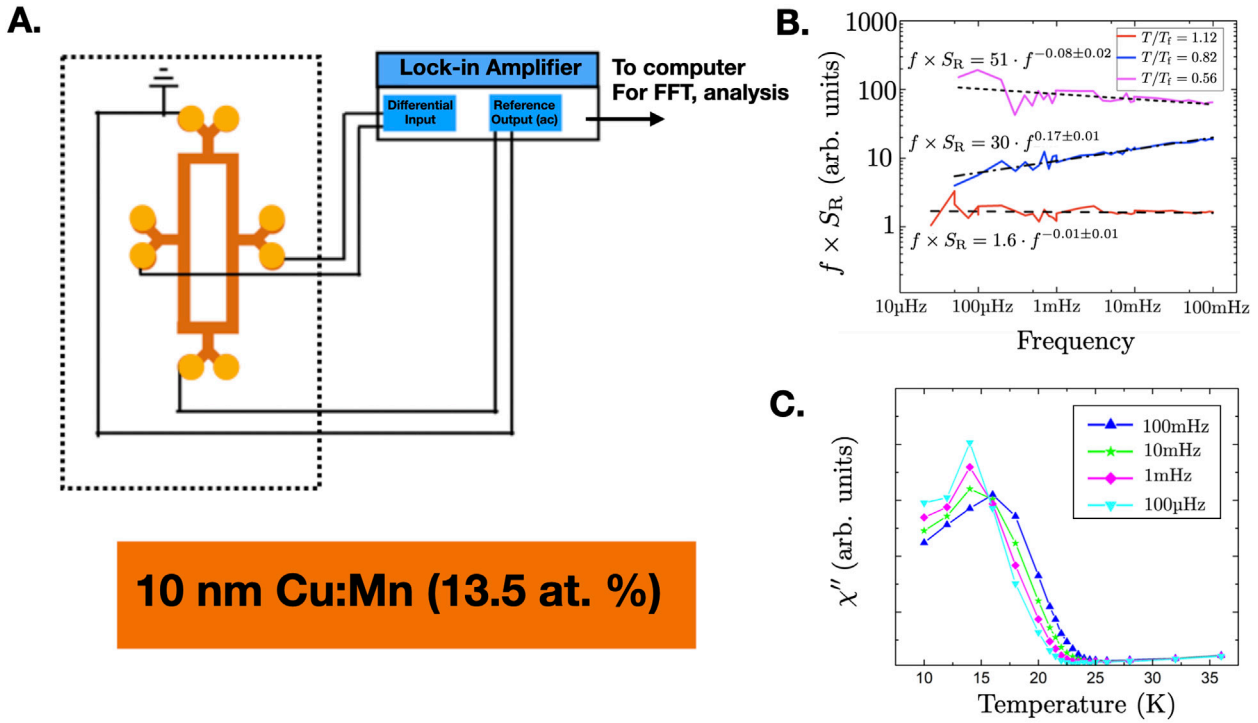


FIGURE 2
**(A)** Experimental setup for noise measurements; the dashed box denotes the inside of the cryostat. The spin-glass samples are patterned in a bridge configuration and measured with a lock-in technique. **(B)** $f \times S_R$ at three temperatures showing the strong dependence of both the spectral magnitude and exponent as a function of temperature. **(C)** Imaginary part of the AC susceptibility, $\chi''$ as computed from the noise measurement. The data are reproduced from Ref. [38].

Figure 2C, we reproduce Figure 2 from Ref. [38], showing the $\chi''$ computed from noise measurements. We first note the power of the transport technique here: as noted in Ref. [38], even a witness film 100 cm$^2$ in the area sputtered simultaneously with the thinnest transport film did not yield enough magnetic material for magnetization measurements in a commercial SQUID magnetometer.

The analysis by Zhai et al. in Refs. [15, 16] takes the maximum barrier height, which governs the dynamics of a spin-glass, to be fixed once the spin-glass coherence length reaches the film thickness. In other words, the continued increase (if any) in the coherence length in the plane of the sample is taken to have no effect on the maximum barrier height. At this point, the dynamics are activated over fixed (temperature-independent) barriers. As discussed earlier, this implies $c_N \approx 30$. While there is a marked reduction in the cooperativity with decreasing film thickness, the dynamics are always cooperative, never exhibiting simple thermal activation. This is in apparent contrast to the analysis in Refs. [15–17] (on the other hand, the recent measurements are roughly consistent with the earlier thin-film results—both transport and magnetometry from Refs. [27, 28, 31, 33]—suggesting that the cooling protocol does not play a key role, as it was not well-specified in the earlier work and was likely different). More measurements are needed to understand why this is the case. The most obvious explanation for temperature-dependent barrier heights is the growth of in-plane correlations; though it is not yet understood why these manifest more clearly here than in Ref. [15], we note that the transport measurements were all taken over a much broader temperature range than the magnetization measurements, which would have made this effect difficult to see in the latter case.

Fortunately, transport measurements offer a clear path in testing this physics. One possibility would be to fabricate samples small in two dimensions (e.g., 20-nm-wide wires) or in all three dimensions (e.g., 40-nm cubes). In order to get an acceptable SNR for the one-dimensional cubic devices, it would certainly be necessary to fabricate long chains with non-magnetic spacers, and it would be difficult to align and make good contact. However, while daunting, this is well within the limits of modern electron-beam lithography tools. With such devices, there would be only one length scale set by the film geometry, making it possible to rule out in-plane coherence length growth as the cause of temperature-dependent barriers. These measurements would leverage both advantages of transport techniques, which would enable the measurement of devices with such small volume while, and—because they do not rely on a Zeeman energy—would provide an independent confirmation of the previous measurements of in-plane correlation growth.

In addition, measurements of the second spectral density, i.e., the noise in the $1/f$ noise, in mesoscale devices has been shown to provide *different* information than that accessible from susceptibility measurements [30]. Again, these effects were

studied extensively by the Weissman group, but may be worth revisiting, employing the cooling protocol suggested by Ref. [37] and analyzing within the now-fully developed coherence length framework.

## Author contributions

DH: writing–original draft and writing–review and editing.

## Funding

The author(s) declare that no financial support was received for the research, authorship, and/or publication of this article.

## Conflict of interest

The author declares that the research was conducted in the absence of any commercial or financial relationships that could be construed as a potential conflict of interest.

## Publisher's note



## References

1. Newman CM, Stein DL. Ground-state stability and the nature of the spin glass phase. *Phys Rev E* (2022) 105:044132. doi:10.1103/physreve.105.044132

2. Fisher DS, Huse DA. Nonequilibrium dynamics of spin glasses. *Phys Rev B* (1988) 38:373–85. doi:10.1103/physrevb.38.373

3. Fisher DS, Huse DA. Equilibrium behavior of the spin-glass ordered phase. *Phys Rev B* (1988) 38:386–411. doi:10.1103/physrevb.38.386

4. de Almeida JR, Thouless DJ. Stability of the Sherrington-Kirkpatrick solution of a spin glass model. *J Phys A: Math Gen* (1978) 11 (5):983. doi:10.1088/0305-4470/11/5/028

5. Kisker J, Santen L, Schreckenberg M, Rieger H. Off-equilibrium dynamics in finite-dimensional spin-glass models. *Phys Rev B* (1996) 53:6418–28. doi:10.1103/physrevb.53.6418

6. Baity-Jesi M, Baños RA, Cruz A, Fernandez LA, Gil-Narvión J, Gordillo-Guerrero A, et al. *Comp Phys Comm* (2014) 185:550. doi:10.1016/j.cpc.2013.10.019

7. Joh YG, Orbach R, Wood GG, Hammann J, Vincent E. Extraction of the spin glass correlation length. *Phys Rev Lett* (1999) 82:438–41. doi:10.1103/physrevlett.82.438

8. Guchhait S, Orbach R. Direct dynamical evidence for the spin glass lower critical Dimension2<dℓ<3. *Phys Rev Lett* (2014) 112:126401. doi:10.1103/physrevlett.112.126401

9. Guchhait S, Orbach R. Magnetic field dependence of spin glass free energy barriers. *Phys Rev Lett* (2017) 118:157203. doi:10.1103/physrevlett.118.157203

10. Zhai Q, Paga I, Baity-Jesi M, Calore E, Cruz A, Fernandez LA, et al. *Phys Rev Lett* (2020) 125:237202. doi:10.1103/PhysRevLett.125.237202

11. Paga I, Zhai Q, Baity-Jesi M, Calore E, Cruz A, Cummings C, et al. *Phys Rev B* (2023) 107:214436. doi:10.1103/PhysRevB.107.214436

12. Zhai Q, Orbach RL, Schlagel DL. Evidence for temperature chaos in spin glasses. *Phys Rev B* (2022) 105:014434. doi:10.1103/physrevb.105.014434

13. Kenning GG, Schlagel DL, Thompson V. Experimental determination of the critical spin-glass correlation length in single-crystal CuMn. *Phys Rev B* (2020) 102:064427. doi:10.1103/physrevb.102.064427

14. Tennant DM, Orbach RL. Collapse of the waiting time effect in a spin glass. *Phys Rev B* (2020) 101:174409. doi:10.1103/physrevb.101.174409

15. Zhai Q, Harrison DC, Tennant D, Dahlberg ED, Kenning GG, Orbach RL, et al. *Phys Rev B* (2017) 95:054304. doi:10.1103/PhysRevB.95.054304

16. Zhai Q, Harrison DC, Orbach RL. Effect of magnetic fields on spin glass dynamics. *Phys Rev B* (2017) 96:054408. doi:10.1103/physrevb.96.054408

17. Baity-Jesi M, Calore E, Cruz A, Fernandez LA, Gil-Narvion JM, Gordillo-Guerrero A, et al. *Phys Rev Lett* (2018) 120:267203. doi:10.1103/PhysRevLett.120.267203

18. Fernandez LA, Marinari E, Martin-Mayor V, Parisi G, Ruiz-Lorenzo JJ. An experiment-oriented analysis of 2D spin-glass dynamics: a twelve time-decades scaling study. *J Phys A: Math Theor* (2019) 52:224002. doi:10.1088/1751-8121/ab1364

19. Fernandez LA, Marinari E, Martin-Mayor V, Paga I, Ruiz-Lorenzo JJ *Phys Rev B* (2019) 100:184412. doi:10.1103/PhysRevB.100.184412

20. He J, Orbach RL. Spin glass dynamics through the lens of the coherence length. *Front Phys* (2024) 12. doi:10.3389/fphy.2024.1370278

21. Zhai Q, Martin-Mayor V, Schlagel DL, Kenning GG, Orbach RL *Phys Rev B* (2019) 100:094202. doi:10.1103/PhysRevB.100.094202

22. Sendelbach S, Hover D, Kittel A, Mück M, Martinis JM, McDermott R. Magnetism in SQUIDs at millikelvin temperatures. *Phys Rev Lett* (2008) 100:227006. doi:10.1103/physrevlett.100.227006

23. Kumar P, Sendelbach S, Beck MA, Freeland JW, Wang Z, Wang H, et al. *Phys Rev App* (2016) 6:041001. doi:10.1103/PhysRevApplied.6.041001

24. Faoro L, Ioffe LB. Microscopic origin of low-frequency flux noise in josephson circuits. *Phys Rev Lett* (2008) 100:227005. doi:10.1103/physrevlett.100.227005

25. Sendelbach S, Hover D, Mück M, McDermott R. Complex inductance, excess noise, and surface magnetism in dc SQUIDs. *Phys Rev Lett* (2009) 103:117001. doi:10.1103/physrevlett.103.117001

26. Kenning G, Slaughter JM, Cowen JA. Finite-Size effects in a CuMn spin-glass. *Phys Rev Lett* (1987) 59:2596–9. doi:10.1103/physrevlett.59.2596

27. Granberg P, Nordblad P, Svedlindh P, Lundgren L, Stubi R, Kenning GG, et al. Dimensionality crossover in CuMn spin-glass films. *J Appl Phys* (1990) 67:5252–4. doi:10.1063/1.344627

28. Sandlund L, Granberg P, Lundgren L, Nordblad P, Svedlindh P, Cowen JA, et al. Dynamics of Cu-Mn spin-glass films. *Phys Rev B* (1989) 40:869–72. doi:10.1103/physrevb.40.869

29. Weissman MB, Israeloff NE, Alers GB *J Magn Magn Mater* (1992) 87:114. doi:10.1016/0304-8853(92)90336-M

30. Weissman MB. *Rev Mod Phys* (1993) 65:829–39. doi:10.1103/revmodphys.65.829

31. Israeloff NE, Weissman MB, Nieuwenhuys GJ, Kosiorowska J. Electrical noise from spin fluctuations in CuMn. *Phys Rev Lett* (1989) 63:794–7. doi:10.1103/physrevlett.63.794

32. Israeloff NE, Alers GB, Weissman MB. Spin-fluctuation statistics in*Cu*Mn. *Phys Rev B* (1991) 44:12613–6. doi:10.1103/physrevb.44.12613

33. Fenimore PW, Weissman MB. Resistance noise as a technique for measuring finite-size effects in single-layer Cu_Mn spin-glass films. *J Appl Phys* (1999) 85:8317–21. doi:10.1063/1.370676

34. Reim W, Koch RH, Malozemoff AP, Ketchen MP, Maletta H. Magnetic equilibrium noise in spin-glasses: Eu0.4Sr0.6S. *Phys Rev Lett* (1986) 57:905–8. doi:10.1103/PhysRevLett.57.905

35. Van der Ziel A. On the noise spectra of semi-conductor noise and of flicker effect. *Physica* (1950) 16:359–72. doi:10.1016/0031-8914(50)90078-4

36. Dutta P, Horn P. Low-frequency fluctuations in solids:1fnoise. *Rev Mod Phys* (1981) 53:497–516. doi:10.1103/revmodphys.53.497

37. Guchhait S, Kenning GG, Orbach RL, Rodriguez GF. Spin glass dynamics at the mesoscale. *Phys Rev B* (2015) 91:014434. doi:10.1103/physrevb.91.014434

38. Harrison DC, Dahlberg ED, Orbach RL *Phys Rev B* (2022) 105:014413. doi:10.1103/PhysRevB.105.014413

frontiers | Frontiers in Physics

TYPE Original Research
PUBLISHED 25 October 2024
DOI 10.3389/fphy.2024.1431810



OPEN ACCESS

EDITED BY
Federico Ricci-Tersenghi,
Sapienza University of Rome, Italy

REVIEWED BY
Pan Zhang,
Chinese Academy of Sciences (CAS), China
Alfredo Braunstein,
Polytechnic University of Turin, Italy

*CORRESPONDENCE
Stefanos Kourtis,
stefanos.kourtis@usherbrooke.ca

RECEIVED 13 May 2024
ACCEPTED 03 October 2024
PUBLISHED 25 October 2024

CITATION
Lanthier B, Côté J and Kourtis S (2024) Tensor networks for *p*-spin models .
*Front. Phys.* 12:1431810.
doi: 10.3389/fphy.2024.1431810



# Tensor networks for *p*-spin models

Benjamin Lanthier, Jeremy Côté and Stefanos Kourtis*

Institut quantique & Département de physique, Université de Sherbrooke, Sherbrooke, QC, Canada

We introduce a tensor network algorithm for the solution of *p*-spin models. We show that bond compression through rank-revealing decompositions performed during the tensor network contraction resolves logical redundancies in the system exactly and is thus lossless, yet leads to qualitative changes in runtime scaling in different regimes of the model. First, we find that bond compression emulates the so-called leaf-removal algorithm, solving the problem efficiently in the "easy" phase. Past a dynamical phase transition, we observe superpolynomial runtimes, reflecting the appearance of a core component. We then develop a graphical method to study the scaling of contraction for a minimal ensemble of core-only instances. We find subexponential scaling, improving on the exponential scaling that occurs without compression. Our results suggest that our tensor network algorithm subsumes the classical leaf removal algorithm and simplifies redundancies in the *p*-spin model through lossless compression, all without explicit knowledge of the problem's structure.

KEYWORDS

**spin glass (theory), tensor network algorithms, disordered magnetic systems, satisfiability (SAT), model counting**

## 1 Introduction

Spin glass physics appears in disciplines far-removed from its origin in condensed matter, including theoretical computer science [1], biology [2], and machine learning [3]. Spin glass models are generally easy to describe, yet hard to solve. One reason is that such models exhibit rugged energy landscapes [4], trapping optimization algorithms in local minima and leading to exponentially long run times.

A notable counterexample is the *p*-spin model [5], which is in fact easy to solve [6]. By mapping the model to a linear system of equations modulo 2, Gaussian elimination (GE) allows one to obtain the zero-temperature partition function of the model in polynomial time. While this model is a restricted version of a general spin glass model, its tractable analysis provides useful insights into the physics of spin glasses. Yet the *p*-spin model also exhibits rugged energy landscapes in certain regimes of the parameters, which is why it is a standard benchmark for classical [7–9] and quantum [10–15] optimization algorithms. In these regimes, simulated annealing fails or is inefficient for any $p > 2$ [13, 15], and the same is true for quantum annealing [11], even when no phase transition is encountered [15]. Boolean satisfiability and local solvers also struggle with these models [16–21].

In this work, we introduce a tensor network algorithm for solving *p*-spin models. A tensor network (TN) is a data structure that allows for compact representation of a given (weighted) graphical model, including (quantum) spin Hamiltonians and constraint satisfaction problems, and whose contraction amounts to a (weighted) count of the solutions to the model [22–26]. While exact TN contraction is computationally hard in general even for restricted graph classes, such as planar grids [27], techniques involving tensor compression can lead to accurate and efficient approximate estimation of classical

partition functions or quantum expectations in specific cases [28–30]. TN methods have also previously been used in mean-field studies of graphical models and disordered spin Hamiltonians [31, 32].

Here, we show that compressed TN contraction applied to the $p$-spin model automatically emulates previously discovered algorithms for the solution of the model in its different phases. In contrast to previous works, the compression we perform is exact, meaning that it only resolves and simplifies redundancies in the TN at each step without loss of information. We illustrate the above with an application to the 3-spin model, in which the average number of interactions per spin $\alpha$ controls transitions to different thermodynamic phases in the structure of the problem [5]. We find that compressed TN contraction automatically implements the leaf removal algorithm [5] and thus efficiently solves the problem when $\alpha < \alpha_d$, at which point a dynamical transition occurs. In contrast, compressed TN contraction scales superpolynomially when $\alpha > \alpha_d$ but improves substantially on the exponential scaling of TN contraction without compression. We further show that when $\alpha \in [2/3, 3/4]$, compressed TN contraction outperforms naive GE. Finally, by devising a graphical scheme that exactly captures the dynamics of compressed TN contraction in the special case of spins appearing in exactly two interaction terms, for which no leaf removal occurs, we show numerically that the TN method solves the problem in subexponential time.

# 2 Definitions

## 2.1 The $p$-spin model

We can write the $p$-spin model by specifying a bipartite graph $G = (U, V, E)$, where $U$ is the set of nodes representing the $n = |U|$ spins, $V$ is the set of nodes representing the $m = |V|$ interaction terms, and $E$ is the set of edges connecting spin nodes to interaction nodes. We can then write the Hamiltonian of the $p$-spin model as:

$$H = \frac{1}{2}\left[m - \sum_{v \in V} J_v \prod_{u \in N(v)} \sigma_u\right], \tag{1}$$

where $J_v \in \{-1, 1\}$ are the couplings for the interaction at node $v$, $\sigma_u \in \{-1, 1\}$ is the value of the spin at node $u$, and $N(v)$ is the set of $p$ neighbours for the interaction described by node $v$. The minimum energy is zero, and it occurs when every interaction satisfies $J_v = \prod_{u \in N(v)} \sigma_u$. In this paper, we are interested in counting the number of zero-energy configurations for a given ensemble of bipartite graphs, that is, evaluating the zero-temperature partition function of the model.

By letting $\sigma_u = (-1)^{x_u}$ and $J_v = (-1)^{b_v}$, we can rewrite the search for zero-energy configurations from Equation 1 as

$$A\vec{x} = \vec{b} \bmod 2, \tag{2}$$

where $A \in \{0, 1\}^{m \times n}$ is the biadjacency matrix of the graph $G$, with $A_{vu} = 1$ indicating $u \in N(v)$ and zero otherwise, $\vec{x} \in \{0, 1\}^n$ encodes the spin configuration, and $\vec{b} \in \{0, 1\}^m$ encodes the couplings. Finding the zero-energy configurations for Equation 1 is equivalent to solving the matrix Equation 2. Counting the number of configurations also involves manipulating Equation 2. With this form, we can then cast the problem into the language of Boolean satisfiability (SAT), which we detail below.

## 2.2 The #$p$-XORSAT problem

### 2.2.1 Definition

In its most general form, a SAT problem is the problem of deciding whether a logic formula built from a set of boolean variables $\{x\} = \{x_1, x_2, \ldots, x_n\}$ and the operators $\wedge$ (conjunction), $\vee$ (disjunction), and $\neg$ (negation) evaluates to true, i.e., is satisfiable [33]. The SAT problem is characterized by the conjunction of clauses, each comprising disjunctions of variables where the negation operator may be applied. The SAT problem is NP-complete, and the same is true for many of its variants.

The constraint stipulating that every clause must consist of exactly $p$ variables defines the $p$-SAT problem, which is also NP-complete. Counting the number of solutions that satisfy a given SAT problem, if any exist, defines the #SAT problem, which is even more challenging, falling under the #P-complete class. This property extends to #$p$-SAT problems for $p \geq 2$.

The variant of the #$p$-SAT problem that lets us count the number of zero-energy configurations of a given $p$-spin model is the #$p$-XORSAT problem, defined below.

The #$p$-XORSAT problem requires only a modification of the operators within the clauses from the standard $p$-SAT formulation. The disjunction is replaced by the exclusive-or (XOR) operator, which is mathematically represented by the summation modulo 2 operator ($\oplus$). Given $A$ and $\vec{b}$ as in Equation 2, we can define an instance $\phi$ of the $p$-XORSAT problem as:

$$\begin{aligned} \phi(\{x\}) &= \bigwedge_{i=1}^{m} c_i, \\ c_i &= 1 \oplus b_i \oplus A_i \cdot \vec{x}, \\ \vec{x} &= (x_1, x_2, \ldots, x_n) \in \{0, 1\}^n, \end{aligned} \tag{3}$$

where $A_i \in \{0, 1\}^n$ is the $i$-th row of $A$ and $b_i$ is the $i$-th component of $\vec{b}$, $A_i \cdot \vec{x}$ indicates the dot product between $A_i$ and $\vec{x}$ (modulo 2), and $c_i = 1$ implies the clause is satisfied ($b_i \oplus A_i \cdot \vec{x} = 0$).

When one generates $A$ by placing $p$ ones in each row uniformly at random with no repeated rows and uniformly chooses $\vec{b} \in \{0, 1\}^m$, the clause density $\alpha \equiv m/n$ characterizes much of the problem. In particular, $p$-XORSAT has two phase transitions [5]. The first occurs at $\alpha_d$, which indicates a dynamical transition in the structure of the solution space by dividing solutions into well-separated (in Hamming distance) clusters. The second occurs at the critical transition $\alpha_c$, where, with high probability, any instance becomes unsatisfiable (no solutions). This point signifies a similar phase transition even when $\vec{b} = 0$, meaning the configuration $\vec{x} = 0$ is always a solution [20]. For $p = 3$, the constants are $\alpha_d \approx 0.818$ and $\alpha_c \approx 0.918$ [5].

### 2.2.2 Gaussian elimination

Given a $p$-XORSAT instance $\phi(\{x\})$, as defined in Equation 3, we first translate it into the form of Equation 2. Then, we apply GE on the augmented matrix $[A|\vec{b}]$. If the system is inconsistent, there are no solutions. Otherwise, the solution count is:

$$\#\text{Solutions} = 2^{n - \text{rank}(A)}, \tag{4}$$

where all operations are modulo 2, as in applying GE. #$p$-XORSAT is thus in P since it can be solved using Equation 4 in at most $\mathcal{O}(n^3)$ time and $\mathcal{O}(n^2)$ memory.

In Ref. [34], the authors studied the time and memory requirements for solving Equation 2 for $p = 3$ using a "simple" version of GE. This version solves the linear equations in the order they appear in Equation 2 and with respect to a random variable. The authors showed that this simple algorithm will solve the problem in $\propto n$ time and memory when $\alpha \leq 2/3$, and in $\propto n^3$ time and $\propto n^2$ memory when $\alpha > 2/3$.

The authors also presented a "smart" version of GE, where one first looks for the variable appearing in the least number of equations left to be solved (ties broken arbitrarily), then solves for that variable and substitutes it into the remaining equations. They argued that this smarter version of GE will solve the problem in $\propto n$ time and memory when $\alpha < \alpha_d$, and in $\propto n^3$ time and $\propto n^2$ memory when $\alpha > \alpha_d$.

When one solves an equation that contains a variable which only appears in that equation, one can interpret the process graphically as a "leaf removal" algorithm [5]. We describe it below because it provides intuition as to why the "smart" version of GE is more efficient and will help explain the behaviour of our TN algorithm.

### 2.2.3 Leaf removal

Suppose we have an instance for $p = 3$ and the variable $x$ only appears in the linear equation $x \oplus y \oplus z = b$. No matter what values $y$ and $z$ take, it is always possible to choose $x$ to make the equation true. We can therefore solve this equation for $x$, and only fix it once we have solved the rest of the (fewer) linear equations. But removing this equation may now cause $y$ or $z$ to only appear in a single other equation, so we solve those equations for $y$ and $z$, and then what remains is an even smaller linear system. The process will continue until the remaining variables participate in at least two equations. In terms of the matrix $A$ in Equation 2, each column will have at least two 1s (Note that if a variable appears in no equations it is, in essence, not part of the problem and so we can ignore it and simply multiply the count by 2.)

This algorithm is called leaf removal [5], and it allows us to simplify the $p$-XORSAT problem. Graphically, the algorithm begins with the bipartite graph $G$ representing the problem, then iteratively finds variable nodes $u \in U$ such that $\deg(u) = 1$, and deletes the clause node $v \in N(u)$ and $v$'s associated edges. The algorithm continues until either no clause nodes remain (and therefore, no edges) or a "core" remains, a subgraph of $G$ where each variable node has degree at least two. One can then construct a solution to the original formula by working backwards from a solution to the formula corresponding to the core graph.

In Ref. [5], the authors showed that, for the ensemble where $p = 3$ and one picks each clause uniformly at random from the $\binom{n}{3}$ distinct tuples of variables, the leaf algorithm will succeed in reducing the corresponding graph to the empty graph when $\alpha < \alpha_d \approx 0.818$. Because at each step of the algorithm one can fix a variable node of degree 1 in order to remove a clause node, when no core remains the count will be $2^{n-m}$, where $m$ is the number of clauses (or variables we have fixed). When $\alpha > \alpha_d$, a core will remain, which means leaf removal is not enough to solve the entire problem. The value $\alpha_d$ indicates a dynamical transition in the problem, and it corresponds to a change in the structure of the set of solutions. The "smart" GE uses this principle to achieve a speedup over the standard version.

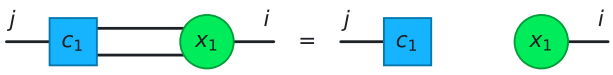


FIGURE 1
Graphical representation of the Hopf law. Clause nodes are blue squares, and variable nodes are green circles.

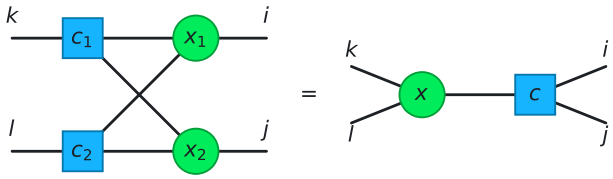


FIGURE 2
Graphical representation of the bialgebra law. Clause nodes are blue squares, and variable nodes are green circles.

We also note that when no core remains at the end of leaf removal, one can interpret the algorithm as finding a permutation of the rows and columns of the matrix $A$ such that one can transform $A$ into triangular form. Suppose the variable $x_i$ only appears in equation $j$. One would then permute the rows 1 and $j$ of $A$, as well as the columns 1 and $i$. Ignoring the first row and column of $A$, repeat the same procedure. Continuing in this way will yield a matrix $A'$ which is in triangular form and has the same rank as $A$. The triangular form of $A'$ implies that its rank is simply the number of rows, allowing one to calculate the number of solutions.

In the case of the $p$-XORSAT problem, this algorithm demonstrates that we can graphically identify and eliminate redundancy, reducing the problem's size by focusing on the remaining core. Graphically, this problem does not only exhibit this rank-1 variable redundancy; two more are explained in the following section.

### 2.2.4 Graphical simplifications

There exist graphical rules, such as the leaf removal explained in Section 2.2.3, that let us simplify a $p$-XORSAT problem. These will be used in Section 3.3, where we develop a complementary graphical method for TN contraction. Note that we will study the case where $\vec{b} = 0$ for simplicity. Then, we have the following examples of simplifications.

The first example is the Hopf law [35], where a clause involves the same variable multiple times. In this case, since $i \oplus i = 0$ for boolean indices, when there are $t$ occurrences of a variable in a clause, only $t \bmod 2$ of them are necessary and the rest are redundant. In Figure 1, we show an example for $t = 2$.

The second example is the bialgebra law [35], where a set of clause nodes are all connected to a set of variable nodes. An example for two clauses and two variables is shown in Figure 2. These structures simplify to a single clause and single variable, as shown in Figure 2.

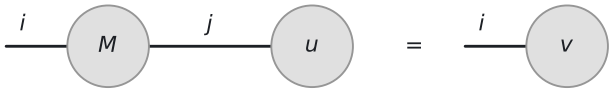


FIGURE 3
Matrix-vector multiplication in TN format.

These simplifications correspond to eliminating redundancies in the problem. Resolving these redundancies can be exploited to solve the problem faster.

## 2.3 Tensor networks

TNs are a data structure that encodes a list of tensor multiplications. Intuitively, one can imagine a TN as a graph where each node represents a tensor, and edges represent the common axes along which one multiplies two tensors[1]. By contracting together neighboring nodes—multiplying the corresponding tensors together—one can sometimes efficiently compute a variety of quantities, making it a useful numerical method. Originally developed to efficiently evaluate quantum expectation values and partition functions of many-body systems, this tool now has applicability in many domains, including quantum circuit simulation [36] and machine learning [37]. As shown in [22], this tool can also be used for $p$-SAT problems.

For our work, contracting all of the tensors in the network together will yield the number of solutions to Equation 2. Below, we review the main ideas for TN methods that are relevant for us and determine the performance of our algorithm. These elements are: how to perform contractions, the importance of contraction ordering, and how to locally optimize the sizes of the tensors (which affect the memory requirements). We then describe our TN algorithm for the #$p$-XORSAT problem in Section 3.1.

### 2.3.1 Contraction

A single tensor is a multidimensional array of values. Graphically, the number of axes (or rank) of the tensor is the degree of the corresponding node, and the size of the tensor is the number of elements (the product of the dimensions of the axes). The size of the TN is then the sum of all the tensor sizes. For any TN algorithm, one must keep track of the size of the TN to ensure the memory requirements do not exceed one's computational limits. In particular, one must consider how contracting tensors together changes the TN's size.

A simple example of contraction is the matrix-vector multiplication, which is represented graphically in Figure 3.Here, the vector $\vec{u}$ (a rank-1 tensor) is represented by a node with a single edge connected to it and the matrix $M$ (a rank-2 tensor) is also a node, but with two edges. The matrix-vector multiplication shown in Figure 3 can also be written as the following summation:

$$\sum_j M_{ij} u_j = v_i. \tag{5}$$

In general, one can write the contraction of a TN by this summation over all the common (shared) axes. We will sometimes call tensors with common axes adjacent, in reference to a TN's graphical depiction.

When contracting tensors where each axis has the same dimension, we can graphically determine the resulting size by looking at the degree of the new node. In Figure 3, the resulting tensor has rank 1, which is the same as $\vec{u}$'s rank. However, the resulting tensor size can be much larger than the original tensors. Suppose we contract tensors of rank $d_1$ and $d_2$ which share a single common axis and each axis has dimension 2, then the size of the resulting tensor will be $2^{d_1+d_2-2}$ and thus scales exponentially in tensor ranks.

### 2.3.2 Contraction order

Though we can carry out the contraction of a TN in any order, the size of the TN in intermediate steps of the contraction can vary widely. Ideally, a contraction will choose an order that limits the memory required to store the TN during all steps of the contraction, making it feasible. Given a contraction order, we can define the contraction width $W$ of the TN [38] in two equivalent ways:

$$W = \begin{cases} \max_{v \in P} \deg(v) & \text{(graphical)}, \\ \max_{T \in \mathcal{T}} \log_2 s(T) & \text{(tensors)}. \end{cases} \tag{6}$$

For the graphical representation, $P$ is the set of nodes representing the tensors present at any stage of the contraction. In the tensor representation, $\mathcal{T}$ is the set of all tensors that are present at any stage of the contraction, and $s(T)$ is the size (number of elements) of the tensor $T$. Note that $W$ depends on the TN and the contraction order. Then, up to a prefactor [38], $2^W$ captures the memory requirements for the entire contraction. We use the contraction width as a proxy to runtime because it defines the largest tensor that one must manipulate during the contraction using multilinear operations, which take polynomial time in the size of that tensor [38]. Finding such orderings is an optimization problem and algorithms exist to find optimized contraction ordering according to the TN structure. While finding the optimal contraction order is easy in some cases, for example, a square lattice, it is much more complex in others, such as random networks [30]. In general, the computational demands of a TN contraction grow exponentially with the number of tensors in both time and memory. Even so, a method called bond compression allows us to further optimize the contraction by accepting a little error. We review this method below, and we explain in Section 2.2.4 how we use bond compression in a novel way.

### 2.3.3 Bond compression

Bond compression involves, in its simplest form, performing a contraction-decomposition operation on adjacent tensors within the TN. The term "bond" refers to the common index between tensors. The decomposition step primarily uses rank-revealing methods such as QR or singular value decomposition (SVD). Of these, the SVD plays a central role in TN algorithms. By setting a threshold value for singular values, either absolute or relative, we retain only the

1 Though this does not factor into our work, it is also possible to have "free" edges with only one end connected to a node, indicating an axis in which no tensor multiplication occurs.

singular values above the threshold and corresponding singular vectors, thereby approximating subsequent contractions. This approach facilitates the contraction of larger TNs by reducing the contraction width during the process. However, in general, this comes at the expense of approximating the final result.

We implement bond compression as follows. Given two adjacent tensors $T_A$ and $T_B$ in the network, we transform them into the approximate tensors $\tilde{T}_A$ and $\tilde{T}_B$ as

$$\begin{aligned} T_A T_B &= Q_A R_A R_B Q_B \\ &= Q_A R_{AB} Q_B \\ &= Q_A \left(U \Sigma V^\dagger\right) Q_B \\ &\approx Q_A \left(\tilde{U} \tilde{\Sigma} \tilde{V}^\dagger\right) Q_B \\ &= \left(Q_A \tilde{U} \tilde{\Sigma}^{\frac{1}{2}}\right)\left(\tilde{\Sigma}^{\frac{1}{2}} \tilde{V}^\dagger Q_B\right) \\ &= \tilde{T}_A \tilde{T}_B. \end{aligned} \tag{7}$$

The first equality comes after applying a QR decomposition to the tensors. Since the QR decomposition operates solely on matrices, we first need to reshape those tensors into matrices before decomposing them. Concretely, if we have a tensor $T$ that has indices $(i_1, i_2, \ldots, i_k)$ and we want to apply the QR on the index $i_3$, then the reshaping would give a matrix with indices $(\prod_{j\neq 3} i_j, i_3)$ (where the product signifies grouping the indices into a composite index). This matrix allows for the direct application of the QR decomposition on the desired dimension. The second equality comes from multiplying the matrices $R_A$ and $R_B$ to get the matrix $R_{AB}$. The third equality comes after performing the SVD on $R_{AB}$. Then, the threshold is applied, reducing the sizes of the singular values matrix, of $U$ and of $V$ and possibly approximating the result. The following equality comes from splitting this diagonal singular values matrix into two equal ones. The final equality comes from multiplying the matrices together in each parenthesis to get two new tensors with a "compressed" bond between them. This schedule optimizes the bond compression since the contraction between two tensors of possibly high dimensions is avoided.

# 3 Methodology

## 3.1 Tensor networks for $p$-XORSAT

As shown in Ref. [22], we can map any $p$-XORSAT instance as a TN. Contracting it will yield the number of solutions to the problem. As with the $p$-spin model in Section 2.1, we can define a $p$-XORSAT instance by a bipartite graph $G = (U, V, E)$ and a vector $\vec{b}$ of parities. Then, to each node $u \in U$ we will assign a "variable" (or COPY) tensor, which has the form:

$$T^{\mathrm{COPY}\{u\}}_{i_1 i_2 \ldots i_d} = \begin{cases} 1, & \text{if } i_1 = i_2 = \ldots = i_d, \\ 0, & \text{else,} \end{cases} \tag{8}$$

where the indices $i_1 i_2 \ldots i_d$ are boolean and $d = \deg(u)$. For each node $v \in V$, we will assign a "clause" (or XOR) tensor of the form:

$$T^{\mathrm{XOR}\{v\}}_{i_1 i_2 \ldots i_p} = \begin{cases} 1, & \text{if } i_1 \oplus i_2 \oplus \ldots \oplus i_p = b_v \\ 0, & \text{else} \end{cases}, \tag{9}$$

where the indices are also boolean, $p = \deg(v)$ and $b_v$ is the parity associated to clause $v$. Finally, the edges $E$ indicate which indices are common between different tensors in the TN and need to be summed over. Obtaining the solution count for the problem involves writing a summation over all of the common indices, yielding an expression similar (but much more involved for larger TNs) to Equation 5. In Figure 4, we give an example of a 3-XORSAT instance with $n = |U| = 5$ and $m = |V| = 3$ where the green circles represent tensors built following Equation 8 and the blue squares represent tensors built following Equation 9.

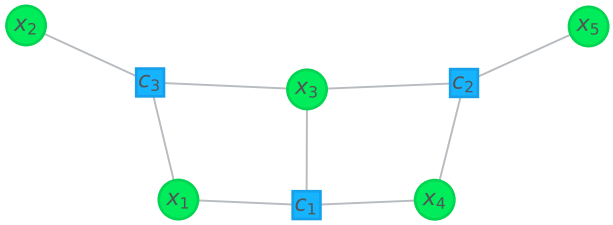


FIGURE 4
An example of a TN representing a 3-XORSAT instance with $n = 5$ (green circles), $m = 3$ (blue squares).

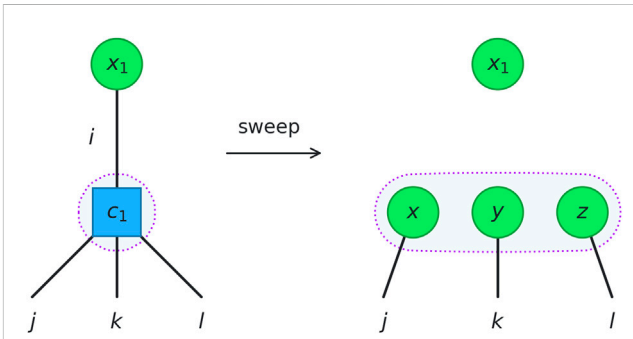


FIGURE 5
Applying bond compression on a rank-1 variable tensor (green circular node labelled $x_1$ on the left) connected to a rank-4 clause tensor (blue square node labelled $c_1$ on the left). The result is a scalar and a rank-3 tensor that is equivalent to the tensor product of three rank-1 variable tensors.

As explained in Section 2.3.2, we can evaluate the contraction width $W$ of those TNs by extracting the highest tensor rank reached during its contraction.

## 3.2 Eliminating redundancies through bond compression

There are several possible simplifications for a $p$-XORSAT problem that occur during the intermediate steps of the TN contraction. By recognizing these simplifications, we can reduce the size of the TN and therefore the time and memory requirements for its contraction. We will focus on the case where $\vec{b} = \vec{0}$, so all parities are even.

We will use bond compression to contract and decompose all adjacent tensors in the TN, a process commonly called a sweep, which is standard practice in TN methods. However, we will not

remove any nonzero singular values in the decomposition. If the tensors are full-rank, this is useless; the tensors remain unchanged after performing bond compression. On the other hand, TNs representing $p$-XORSAT problems often contain redundancy (see Section 2.2.4), which results in singular values that are zero to numerical accuracy. Therefore, performing bond compression and removing null singular values allows us to reduce the tensor sizes while keeping the resulting contraction exact.

An interesting fact with this method is that applying bond compression to the bond between a rank-1 variable tensor and a rank-$d$ clause tensor will effectively remove the bond, leading to a scalar (rank-0 tensor) and a rank-$(d-1)$ tensor. This rank-$(d-1)$ tensor will be composed of only ones (with a prefactor), which is equivalent to the tensor product of $d-1$ rank-1 variable tensors. We illustrate an example of this in Figure 5. The following sweep step will then remove those $d-1$ bonds (because they connect to a rank-1 variable, or COPY, tensor). This means the algorithm effectively removes the clause tensor and all its bonds, which is equivalent to one step in the leaf removal algorithm. This process could cascade through the entire TN, potentially eliminating all its bonds or resulting in a leafless core, giving the same outcome as the leaf removal algorithm. Therefore, bond compression sweeps automatically implement the leaf removal algorithm.

The contraction width will be the figure of merit for the performance of this algorithm because of its relation with the maximum intermediate tensor size (see Equation 6).

## 3.3 Graphical contraction

When $\alpha < \alpha_d$, leaf removal is likely to completely simplify the graph encoding the problem (Section 2.2.3). Translated to TN contraction, the bond compression shown in Figure 5 would be enough to dramatically simplify the TN contraction. This allows us to scale our simulations to large system sizes. However, when $\alpha > \alpha_d$, a core will likely remain. In this case, the remaining TN to contract comprises a core, and this will change the scaling of resources. In particular, the presence of a core will increase the contraction width (and therefore the memory requirements) much more quickly than when $\alpha < \alpha_d$. This limits our ability to test the performance of our algorithm on large instances in this regime.

To bypass this bottleneck and provide further scaling evidence, we develop a graphical algorithm that allows us to study the contraction width throughout a contraction by only studying the connectivity of the instance's graph. As discussed in Section 2.3.1, this is always possible for any exact contraction of a TN, since one simply needs to keep track of the tensor ranks at each step of the contraction (regardless of the tensors' contents). However, because we seek to study the performance of our TN algorithm that detects simplifications through bond compression, we must also encode the graphical patterns that will lead to simplifications. We will make use of the graphical simplifications discussed in Section 2.2.4, as well as more discussed in Section 3 of Ref. [35].

The graphical algorithm works as follows. Starting from a graph $G$ encoding the instance, each node will always represent either a variable or a clause, and by default we will assign each node to a distinct "cluster". The algorithm "contracts" two nodes by assigning them to the same cluster. One can think of the cluster as a contracted tensor. Then, whenever the algorithm performs a "sweep", it will search for any possible simplifications between clusters involving variable and clause nodes. If the algorithm finds any, it will perform the simplifications by removing edges in the problem[2]. The algorithm alternates between sweeping and contracting until every node in the graph belongs to the same cluster, in which case it terminates. It uses the same contraction ordering as in our TN algorithm. In graphical contraction, the goal is to obtain the sizes of intermediate tensors encountered in the contraction, not the values of the tensors themselves. Therefore, the graphical algorithm will not produce a solution count, just a contraction width. We also note that a degree-2 variable tensor is, in its tensor representation, equal to a $2 \times 2$ identity matrix (see Equation 8). Knowing that, we can replace any degree-2 variable nodes in a cluster by edges.

The rank of an intermediate tensor is the number of outgoing edges from a cluster, and its size is:

$$\text{size}_{cluster} = 2^{\#\text{outgoing edges}}. \tag{10}$$

Taking the maximum number of outgoing edges over all contraction steps and clusters directly yields the contraction width.

We now interpret the sweeping method as implementing graphical simplifications. Recall that the TN contraction is a sum over all the boolean indices of the tensors and only the indices which satisfy the logic of the TN will contribute 1 to the sum (and 0 otherwise), yielding the solution count to the problem. Therefore, any simplifications from bond compression must correspond to redundancy in specifying the logic of the TN. Suppose the algorithm is compressing the bonds between tensors $T_A$ and $T_B$. For concreteness, suppose there are $k$ bonds. The algorithm will first transform the $k$ bonds of dimension 2 into a single bond of dimension $2^k$. Then, the algorithm will compress that bond according to Equation 7, yielding new tensors $\tilde{T}_A$ and $\tilde{T}_B$ such that their shared bond is minimized due to the SVD. We observe that the new shared bond has dimension $2^{k'}$ for $k' \leq k$, and $k'$ corresponds to the minimum number of bits needed to preserve the logic of contracting $T_A$ and $T_B$. Note that we can interpret a single bond of dimension $2^{k'}$ as $k'$ bonds of dimension 2, which is how we display our graphical simplifications.

For example, in the leaf removal algorithm, compressing the bond of a rank-1 variable tensor $T^{\text{COPY}}$ with a rank-4 clause tensor $T^{\text{XOR}}$ will yield a shared "bond" of dimension $2^0$, due to redundancy in the representation of contracting those two tensors. This dimension 1 "bond" signifies that the contraction of those tensors will be a tensor product that reduces to an element wise multiplication of tensor $\tilde{T}^{\text{XOR}}$ with the scalar value of $\tilde{T}^{\text{COPY}}$. Similarly, we show below that there are several known logical simplifications present between tensors in these TNs which minimize the number of bits needed to preserve the contraction, implying the QR/SVD will find them. We observe as much in our experiments, which led us to developing our graphical algorithm.

The algorithm must detect and simplify any tensor that our TN algorithm would simplify. For the (2,3)-biregular graph ensemble ($\alpha = 2/3$ leaf-free instances) we consider, only a

2 The algorithm can also remove edges within a cluster, if it is part of the simplification (see Figure 7).

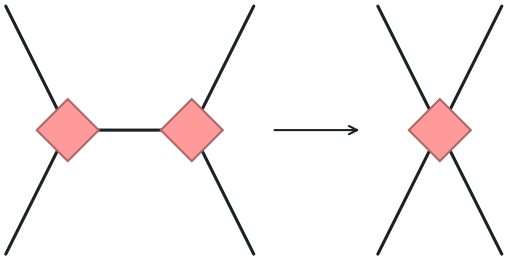

FIGURE 6
The fusion rule on two nodes that are in the same cluster, identified as red here. Nodes of diamond shape represent nodes that could be either of type clause or of type variable.

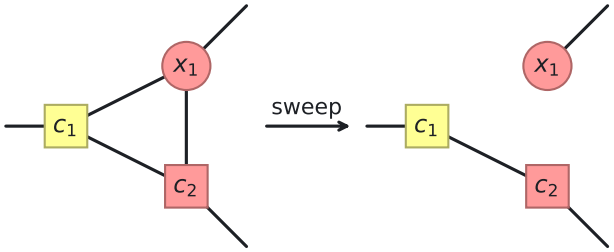


FIGURE 7
One of the two possible cases of the triangle simplification. Node $c_1$ is in one cluster (yellow), and nodes $(c_2, x_1)$ are in the other (red). There are initially two shared edges between the clusters. After the sweep, edges $c_1x_1$ and $c_2x_1$ disappear, resulting in only one shared edge remaining between the two clusters.


FIGURE 8
The multiple edges between nodes of the same type simplification. The nodes are in different clusters (yellow and red), and initially share multiple edges. After a sweep, only one edge is needed to represent the same tensor structure.

subset of the possible $p$-XORSAT simplifications are present. Following the examples in Ref. [35], our graphical algorithm detects the following possible simplifications (we assume $\vec{b} = \vec{0}$ for simplicity):

- Fusion rule,
- Generalized Hopf law,
- Triangle simplification,
- Multiple edges between nodes of the same type,
- Scalar decomposition.

The fusion rule says that neighboring clause nodes in the same cluster can be contracted together to form a bigger clause node, and the same is true for variable nodes. In this case, we actually replace the two nodes with a single node representing them. Their corresponding tensor representations would then be exactly those of a clause or variable tensor of larger rank. This rule is schematically shown in Figure 6. One can also apply the same rule for nodes of the same type which share multiple edges. However, for clause nodes, there will be an overall numerical factor of $2^{\#\text{shared edges}-1}$ in the entries of the tensor, corresponding to the summation over shared indices. Since we are only concerned with the size of the tensors, this coefficient is not relevant.

The generalized Hopf law ensures that if a clause node and a variable node share $t$ edges and the degree of each is greater than $t$, a sweep will leave $t$ mod 2 edges between them (as discussed in Section 2.2.4).

The triangle simplification is an implementation of the Hopf law between two clusters that, between them, contain a "triangle" of nodes. Those triangles contain two nodes of one type (clause or variable) and one of the other. Because we always contract nodes of the same type within a cluster using the fusion rule, a triangle simplification can only occur when the nodes of the same type are in different clusters. When we sweep between these clusters, applying the fusion rule and then a basic Hopf law will remove edges, as shown in Figure 7.

The simplification of multiple edges between nodes of the same type is a variant of the fusion rule. Consider the example in Figure 8. If the nodes are in different clusters, sweeping would not contract the nodes, but would simplify all the edges except one in the same way as a the fusion rule (ignoring once again an overall factor).

Finally, the scalar decomposition occurs when there are two nodes of the same type and at least one shares all its edges with the other. A sweep will merge the two nodes, and then only factor out a scalar (degree-0 node) in the decomposition to return to two tensors. However, the sweep will remove all edges between the tensors.

We now argue that these simplifications are sufficient to characterize any possible simplification present in the (2,3)-biregular graph ensemble. Each variable node has degree 2, so the bialgebra law and any higher-order generalizations cannot occur because they require variable nodes of degree at least 3. Because we replace any degree-2 variable node in a cluster by an edge and the fusion rule combines clause nodes within a cluster, most clusters will be a single clause node of some degree. Our rules above capture simplifications between such clusters. The one exception is that variable nodes are their own clusters at the start of the algorithm before being contracted with other nodes. In this case, the simplifications given by Figure 7 may apply. Therefore, our set of graphical rules should be sufficient to capture all possible simplifications in this ensemble. We also provide evidence of this claim in Section 4.2.

## 3.4 Numerical experiments and tools

### 3.4.1 Generation of random instances

To generate our instances at a given $\alpha$ and $n$, we choose $m = \alpha n$ tuples[3] of $p$ variables uniformly at random without replacement

3 Note that we choose $m, n$, and $\alpha$ such that $m$ and $n$ are integers.

from $\{x\}$, the set of variables defined in Section 2.2. This means that each variable tensor's rank $d$ conforms to the following Poisson distribution:

$$\mathcal{P}(\text{rank}(x_i) = d) = \frac{(p\alpha)^d}{d!} e^{-p\alpha}.$$

This rank is defined as the number of times that a variable is present in the problem. In the language of Equation 2, we randomly place $p$ ones in each row of $A$ and the rank of the variable $x_i$ corresponds to the number of ones in column $i$. For our numerical experiments, we set $p = 3$. We also exclusively focus on the case $\vec{b} = \vec{0}$ (the unfrustrated version of the $p$-spin model). We do so because in the regime $\alpha < \alpha_c$ that we study, the problem will contain at least one solution for any given $\vec{b}$ (with high probability in the limit of large problem size), which allows us to redefine the problem such that $\vec{b} = \vec{0}$ [5, 34] and the solution count remains the same.

### 3.4.2 Generation of leaf-free instances

Since we are mainly concerned with the scaling of resources for instances which contain a core, we choose a minimal ensemble with this property. We will study the ensemble of connected 3-regular graphs on $m$ clause nodes generated uniformly at random using the `Degree_Sequence` function in `igraph` with the Viger-Latapy method [39]. To create a 3-XORSAT instance, we place a variable node along each edge of the regular graph. This ensures the variable nodes all have degree two, and the clause nodes have degree three. Therefore, the ensemble of instances is for $\alpha = 2/3$. Note that this is below $\alpha_d$, but the method of construction explicitly ensures a core.

### 3.4.3 Implementation of contraction methods

For TN contractions, we use `quimb`, a Python package for manipulating TNs [40]. For the graphical method, we use `igraph`, an efficient network analysis library [41], in order to work with node attributes on the graph directly. Those attributes let us define the node types (clause and variable) and the nodes' clusters.

The TN contraction order, as discussed in Section 2.3.2, determines the contraction width. Without applying our sweeping method, one can track this quantity without actually performing the tensor contraction. One must simply keep track of the ranks of the tensors at any point in the contraction, noting as in Section 2.3.1 that combining two tensors yields a new tensor of known rank. We use `cotengra`, a Python package for TN contractions, to track this quantity [38]. In order to track this quantity when sweeps are applied, we use `quimb` in order to read the tensors' sizes during the contraction and calculate the contraction width using Equation 6.

For random TNs such as ours, there exist multiple heuristic algorithms for finding contraction orderings [30, 38] which lower the contraction width and are practically useful for carrying out computations. For the results in Section 4, we determine the ordering using a community detection algorithm based on the edge betweenness centrality [42] (`EBC`) of the network. This algorithm is implemented as `community_edge_betweenness` in the Python package `igraph` [41]. We use the `EBC` algorithm because it looks for communities in the graph, thus contracting dense sections first. This is useful in random TNs because it minimizes the chances of having to work with huge tensors quickly, which could result in a tensor of large rank (and therefore, large contraction width). This algorithm is also deterministic, ensuring reproducibility of the contraction orderings. Furthermore, in Section 4.2, we compare the results obtained using this contraction ordering with two others: `KaHyPar` [43, 44] and `greedy`, both from the Python package `cotengra`.

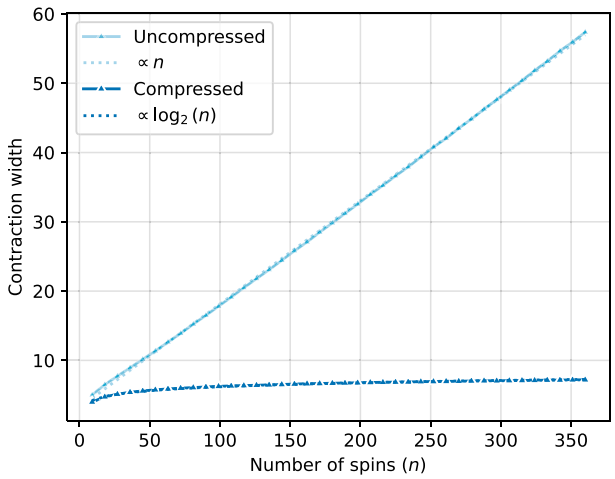


FIGURE 9
Average contraction width for $\alpha = 2/3$ without (light) and with (dark) compression.

Even with these better contraction orderings, exactly contracting these random TNs without bond compression will generally result in an exponential growth in $n$ of time and memory (see Section 4). However, we will show that by manipulating the TN after each contraction using the algorithm defined in Section 3.4.4, we can alter the scaling of resources for a range of parameter values in the problem.

### 3.4.4 Sweeping method

To ensure lossless compression in bond sweeping, we set the relative threshold for zero singular values to be $10^{-12}$. We sweep the TN in arbitrary order until the tensor sizes converge. During a sweep, we compress all the bonds using the `compress_all` method implemented in `quimb`, which uses the compression schedule described in Equation 7. We perform sweeps before each contraction, potentially finding simplifications (see Section 2.2.4) in the structure of the TN during each step of the full contraction.

## 4 Results

### 4.1 Numerical contraction for random instances

Numerical TN contractions were performed on an AMD EPYC 7F72 @ 3.2 GHz processor, with a maximum allocated RAM of 1 TB. Each point in the figures of this section corresponds to the median contraction width or contraction runtime over $10^4$ instances for a given number of spins $n$, except for Figure 9 which shows the average scaling of the contraction width. The contraction width determines, to leading order, the contraction runtime. As is common in random

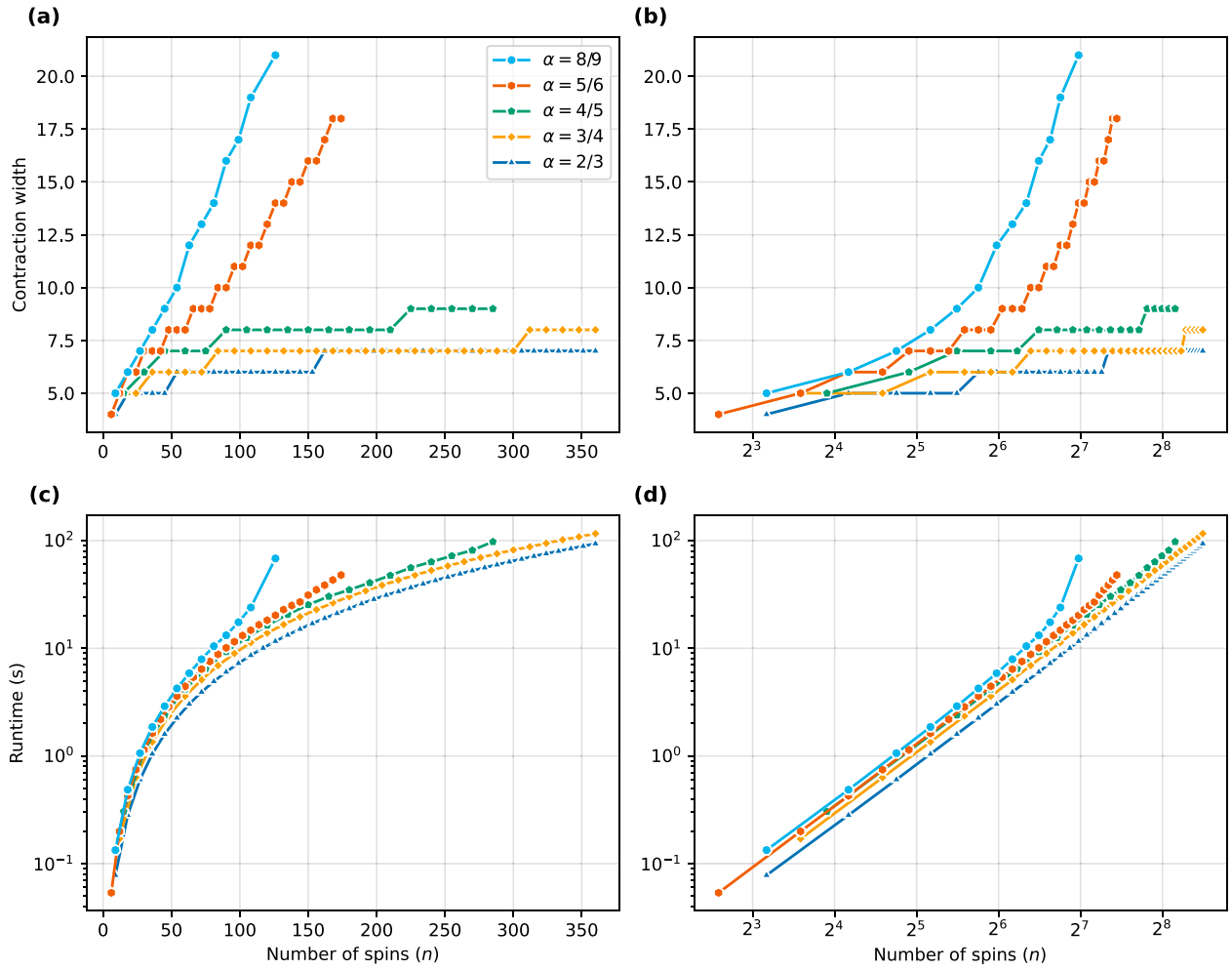


FIGURE 10
Scaling of the contraction width and runtime of compressed TN contraction for the 3-spin model. **(A)** The median contraction width. **(B)** The same data as in **(A)**, but on a logarithmic horizontal scale to accentuate the curves which follow a logarithmic scale (which can be fitted with straight lines). **(C)** Our algorithm's compressed contraction median runtime. This panel shows the exponential scaling by straight lines. **(D)** The same data as in **(C)**, but shown on a horizontal logarithmic scale to accentuate the curves which follow polynomial scaling (straight lines).

graph ensembles for spin-glass models or Boolean variable graphical models, the instance samples contains outliers that are much harder to solve than the typical instance.

In Figure 9, we show the average contraction width with and without compression (sweeping) for $\alpha = 2/3$. Without compression, the scaling of the average contraction width is linear, indicating exponential growth of tensor sizes. By contrast, compression changes the scaling to one that is well described by a logarithmic curve, indicating polynomially growing tensor sizes and hence contraction runtimes.

We studied larger values of $\alpha$ and we show in Figure 10 how the scaling of both the median contraction width and median contraction runtime evolve as $\alpha$ increases. For the largest system sizes, out of $10^4$ instances, a few outliers require times beyond any reasonable timeout we have tried, as expected. We therefore cannot report unbiased runtime averages for these sizes. However, when plotted against system size, the data for the average and median of the contraction width are comparable (likewise for the contraction runtime). Note that we observe that the average contraction width is a smoother function of system size than the median contraction width; though we show the median contraction width in Figure 10, we use the average contraction width data to extract a scaling. We do the same for the contraction runtime. In this case, the curves in the bottom of Figure 10 are already smooth.

The results in Figure 10A highlight linear scaling of the curves for $\alpha = 5/6$ and $\alpha = 8/9$ while Figure 10B clearly shows the logarithmic nature of the curves for $\alpha = 2/3$ and $\alpha = 3/4$. For $\alpha = 4/5$, this median scaling seems to be of logarithmic nature in Figure 10B, but analysing the average shows that it actually starts to "peel-off" from logarithmic scaling.

The logarithmic scaling for $\alpha = 2/3$ and $\alpha = 3/4$ is mainly due to the TN algorithm automatically implementing leaf removal, since $\alpha < \alpha_d$. Indeed, this leads to a high probability that the initial sweeps will remove all the edges in the TN even before the first contraction, leaving only scalars to be multiplied. For $\alpha = 5/6$ and $\alpha = 8/9$, values that are greater than $\alpha_d$, we find that the algorithm is less efficient due to a core that remains after the initial sweeps. Those cores lead to actual tensor contractions instead of scalar multiplications, so the

TABLE 1 Performance comparison between optimized compressed TN contraction and GE.

| Methods | $\alpha$ | Memory | Time |
|---|---|---|---|
| Standard GE | 2/3 | $\propto n$ | $\propto n$ |
| Standard GE | 3/4 | $\propto n^2$ | $\propto n^3$ |
| Smart GE | $< \alpha_d$ | $\propto n$ | $\propto n$ |
| Compressed TN | 2/3 | $\propto n^{1.030}$ | $\propto n^{1.226}$ |
| Compressed TN | 3/4 | $\propto n^{1.112}$ | $\propto n^{1.420}$ |

instances with $\alpha = 5/6$ and $\alpha = 8/9$ become harder to compute, hence the contraction widths' polynomial scaling. As we noted, since $\alpha = 4/5$ is close to $\alpha_d$, there is a probability of a core remaining for our finite system sizes, so the algorithm starts becoming less efficient here too. Sweeping still removes all the edges in the TN in most cases, but less so than with $\alpha = 3/4$, thus the "peel-off" starting at $\alpha = 4/5$.

In Figure 10C, we see the scaling of the median contraction runtime (in seconds) with a logarithmic vertical axis and the same data is shown with a logarithmic horizontal axis in Figure 10D. Accordingly with the contraction width scaling, we find polynomial curves for $\alpha = 2/3$ ($\propto n^{1.928}$) and $\alpha = 3/4$ ($\propto n^{1.902}$). For smaller $n$, we see that the time scaling for all the curves follow a polynomial scaling. This is due to the small finite size of the TN, since it changes for bigger TNs, or for larger $n$. The "peel-off" phenomenon is thus also observed at the end of the curves for $\alpha \in \{4/5, 5/6, 8/9\}$, becoming more pronounced with increasing $\alpha$. This means that the scaling transitions from polynomial to superpolynomial, like the conclusion on memory usage in Figure 10B.

At $\alpha = 2/3$ and 3/4, the compressed TN algorithm exhibits performance between those of the standard and "smart" GE methods (see Table 1). For these values of the $\alpha$ parameter, the contraction runtime can be further improved by removing bonds of dimension 1 after each contraction step. Indeed, when a bond is completely compressed by our algorithm, a dimension 1 bond remains between the two neighboring tensors. These dimension 1 bonds do not affect memory scaling, yet the sweeping algorithm will continue trying to compress them, even though they cannot be further compressed. Eliminating those "useless" bonds results in improved polynomial contraction runtimes for $\alpha = 2/3$ and 3/4, as shown in Table 1, since the subsequent sweeps will not try to compress those bonds anymore. In this same table, the memory is defined as the maximum size of the whole TN—the sum of all its tensors' sizes—reached during its contraction with the sweeping method applied.

## 4.2 Graphical contraction for leaf-free instances

For the leaf-free ensemble, each point in the figures has been averaged over 200 random leaf-free instances. With the graphical method, the contraction widths are extracted from the number of clusters' outgoing edges during the TN contraction, as explained in Section 3.3 (see Equation 10). All the results for the contraction width obtained with this graphical method are shown in Figures 11, 12.

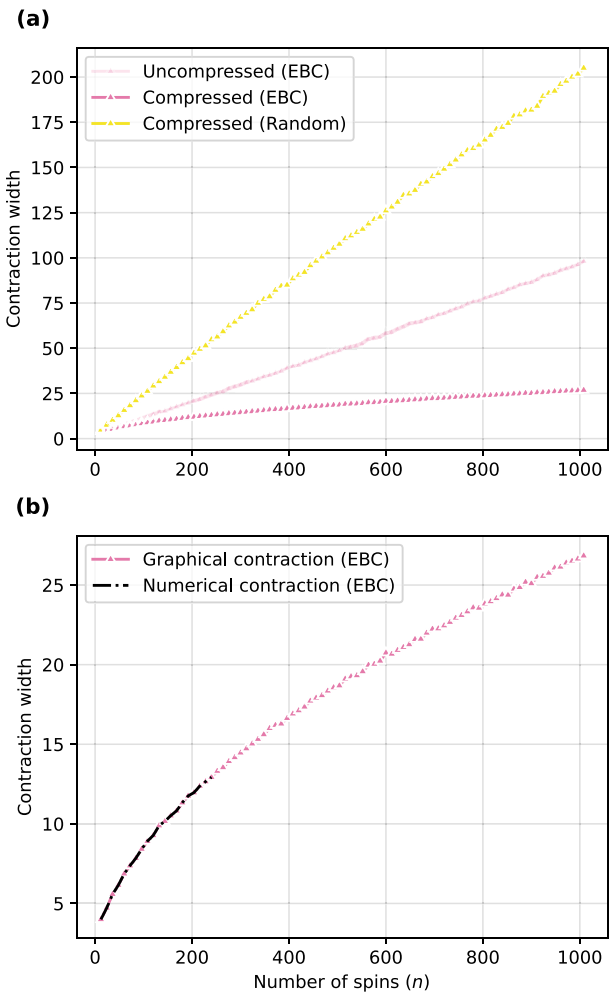


FIGURE 11
**(A)** Scaling of the average contraction width for instances in the (2,3)-biregular graph ensemble ($\alpha = 2/3$ leaf-free instances) using the EBC contraction ordering with and without sweeping, and using the Random contraction ordering with sweeping. We obtained all results using graphical contractions. **(B)** Comparison of the scaling of the average contraction width (with the EBC contraction ordering) obtained using graphical contractions and obtained using the numerical contractions with sweeps applied.

Now having the possibility to study larger TNs without being limited by the memory, we can compare the contraction width of the algorithm on different contraction orderings. In Figure 11A, we compare two of them: EBC and Random. The Random method chooses the next tensors to be contracted completely randomly. It can thus only be usefully studied with this graphical method because it quickly scales to astronomical contraction widths, as seen in Figure 11A.

From Figure 11A, we see that a good contraction ordering is an important factor for the success of the sweeping method during the contraction of a given TN that models a $p$-XORSAT problem. Two known methods for random tensor networks have also been used in order to compare the results obtained from the EBC method, as shown in Figure 12.

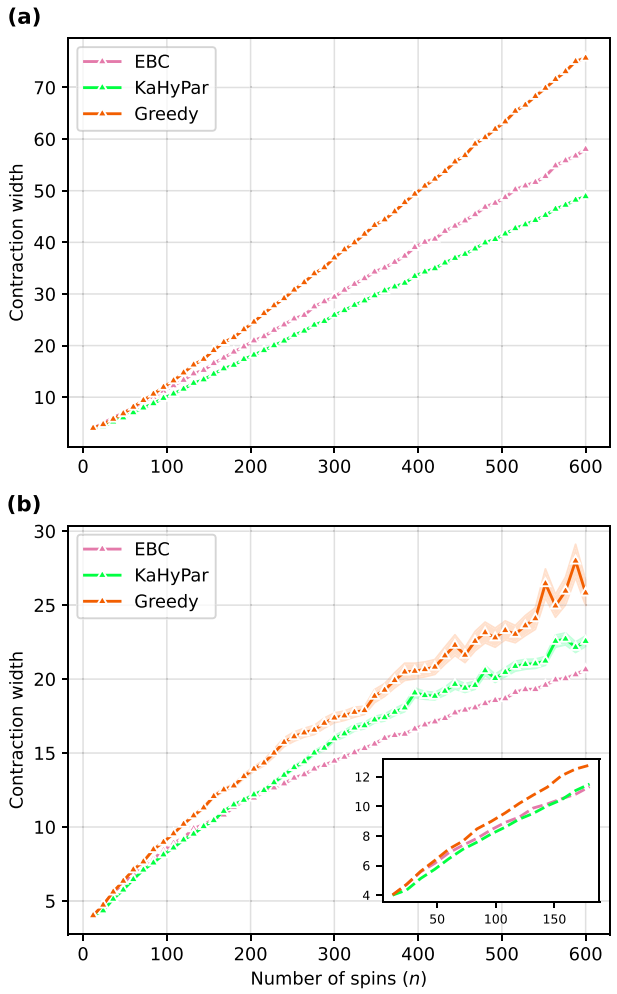


FIGURE 12
All the results were obtained using graphical contractions. **(A)** Scaling of the average contraction width for instances in the (2,3)-biregular graph ensemble ($\alpha = 2/3$ leaf-free instances) using the `EBC`, `KaHyPar` and `greedy` contraction orderings without sweeping. **(B)** Comparison of the average contraction width for the same ensemble using the same three contraction orderings, but with sweeps applied.

The results demonstrate that the sweeping method finds enough simplifications for instances in the (2,3)-biregular graph ensemble so that the scaling of the average contraction width changes from linear to sublinear for the `EBC`, `KaHyPar` and `greedy` contraction orderings. From those results, after $n \approx 150$, we see that the `EBC` method is most efficient in finding those simplifications of the three, followed by `KaHyPar` and then `greedy`. The precise functional form of the scaling is nontrivial and we have not been able to determine a sufficiently accurate fitting function. This means that the sweeping method goes beyond the efficacy of the leaf removal in the TN representation of the 3-spin model.

Note that the (2,3)-biregular graph ensemble we consider offers a simplification of the corresponding $p$-XORSAT problem which allows leaf removal—and by extension, our TN algorithm—to work efficiently in polynomial time. Suppose $A$ is the $m \times n$ matrix encoding the problem. By definition of the ensemble, each column of $A$ has exactly two 1s. Therefore, the rows of $A$ satisfy $A_1 + A_2 + \cdots + A_m = 0 \bmod 2$, indicating the rows are linearly dependent. In other words, we can remove some row $A_i$ from the problem without changing the solution space and count. In terms of the graph, one can remove the corresponding clause node encoding $A_i$ because it is made redundant by the other clauses. However, removing a clause node allows leaf removal to begin since the variable nodes that were connected to that removed clause node will now be degree-1. Leaf removal will then succeed in solving the problem and producing an empty core, implying both leaf removal and our TN algorithm are efficient for this ensemble if we first remove a single redundant clause.

We have verified that the graphical contraction method of Section 3.3 yields tensor sizes identical to those found via numerical contraction at each contraction step by comparing the two methods for 100 random instances with $n = 81$ (for the `EBC` and `Random` contraction orderings). Moreover, all contraction widths for the 200 random instances used to get the results in Figure 11B with sizes up to $n = 240$ are identical to those obtained with numerical contraction (for the `EBC` contraction ordering).

## 5 Conclusion

In this work, we have applied compressed TN contraction to the $p$-spin model. Focusing on $p = 3$, we have shown that lossless compression sweeps over the bonds of the network emulate the leaf removal algorithm, meaning that the TN method is efficient (i.e., polynomial-time) below the dynamical transition at $\alpha_d \approx 0.818$. Above the dynamical transition, the appearance of a leafless core adversely affects the performance of the TN algorithm, which is now superpolynomial-time. Nevertheless, by focusing on the restricted ensemble of biregular instances where every spin participates in exactly two interactions, we find that compressed contraction can be done in subexponential time. This speedup over the anticipated exponential scaling depends crucially on the choice of contraction path. We note that, unlike some previous TN techniques applied to spin-glass models [45], our methods are exact and can be made to suffer no loss of precision for the case of XOR constraints. Indeed, we observe that the local singular values during each sweeping step correspond to either positive or fractional powers of two if they are distributed properly after having applied the SVD. This means that we either have those values or zero/numerical zero singular values. A similar observation has been made for Clifford circuits, essentially parity circuits, where stabilizer states possess flat entanglement spectra [46–48]. To our knowledge, this is the first general-purpose numerical method for spin-model partition function and model counting computations that achieves this performance for $p$-spin models without invoking GE as a subroutine. Furthermore, we believe that this is the first nontrivial case of a spin model defined on random sparse graphs (that are not trees) where compressed TN contraction solves the model exactly, yet leads to an exponential-to-subexponential speedup over direct TN contraction.

## Data availability statement

The raw data supporting the conclusions of this article will be made available by the authors, without undue reservation.

## Author contributions

BL: Conceptualization, Data curation, Formal Analysis, Investigation, Methodology, Software, Validation, Visualization, Writing–original draft, Writing–review and editing. JC: Conceptualization, Formal Analysis, Investigation, Methodology, Supervision, Validation, Writing–original draft, Writing–review and editing. SK: Conceptualization, Formal Analysis, Funding acquisition, Methodology, Project administration, Resources, Software, Supervision, Writing–original draft, Writing–review and editing.

## Funding

The author(s) declare that financial support was received for the research, authorship, and/or publication of this article. This work was supported by the Ministère de l'Économie, de l'Innovation et de l'Énergie du Québec through its Research Chair in Quantum Computing, an NSERC Discovery grant, and the Canada First Research Excellence Fund. This work made use of the compute infrastructure of Calcul Québec and the Digital Research Alliance of Canada.

## Conflict of interest

The authors declare that the research was conducted in the absence of any commercial or financial relationships that could be construed as a potential conflict of interest.

## Publisher's note

All claims expressed in this article are solely those of the authors and do not necessarily represent those of their affiliated organizations, or those of the publisher, the editors and the reviewers. Any product that may be evaluated in this article, or claim that may be made by its manufacturer, is not guaranteed or endorsed by the publisher.

## References

1. Kirkpatrick S, Toulouse G. Configuration space analysis of travelling salesman problems. *J Phys France* (1985) 46:1277–92. doi:10.1051/jphys:019850046080127700

2. Bryngelson JD, Wolynes PG. Spin glasses and the statistical mechanics of protein folding. *Proc Natl Acad Sci* (1987) 84:7524–8. doi:10.1073/pnas.84.21.7524

3. Venkataraman G, Athithan G. Spin glass, the travelling salesman problem, neural networks and all that. *Pramana* (1991) 36:1–77. doi:10.1007/BF02846491

4. Stein DL, Newman CM. *Spin glasses and complexity*. Princeton University Press (2013). doi:10.23943/princeton/9780691147338.001.0001

5. Mézard M, Ricci-Tersenghi F, Zecchina R. Two solutions to diluted p-spin models and XORSAT problems. *J Stat Phys* (2003) 111:505–33. doi:10.1023/A:1022886412117

6. Ricci-Tersenghi F. Being glassy without being hard to solve. *Science* (2010) 330:1639–40. doi:10.1126/science.1189804

7. Bernaschi M, Bisson M, Fatica M, Marinari E, Martin-Mayor V, Parisi G, et al. How we are leading a 3-xorsat challenge: from the energy landscape to the algorithm and its efficient implementation on gpus(a). *Europhysics Lett* (2021) 133:60005. doi:10.1209/0295-5075/133/60005

8. Kanao T, Goto H. Simulated bifurcation for higher-order cost functions. *Appl Phys Express* (2022) 16:014501. doi:10.35848/1882-0786/acaba9

9. Aadit NA, Nikhar S, Kannan S, Chowdhury S, Camsari KY. All-to-all reconfigurability with sparse Ising machines: the XORSAT challenge with p-bits (2023). doi:10.1088/arXiv:2312.08748

10. Jörg T, Krzakala F, Semerjian G, Zamponi F. First-order transitions and the performance of quantum algorithms in random optimization problems. *Phys Rev Lett* (2010) 104:207206. doi:10.1103/PhysRevLett.104.207206

11. Farhi E, Gosset D, Hen I, Sandvik AW, Shor P, Young AP, et al. Performance of the quantum adiabatic algorithm on random instances of two optimization problems on regular hypergraphs. *Phys Rev A* (2012) 86:052334. doi:10.1103/PhysRevA.86.052334

12. Hen I. Equation planting: a tool for benchmarking ising machines. *Phys Rev Appl* (2019) 12:011003. doi:10.1103/PhysRevApplied.12.011003

13. Bellitti M, Ricci-Tersenghi F, Scardicchio A. Entropic barriers as a reason for hardness in both classical and quantum algorithms. *Phys Rev Res* (2021) 3:043015. doi:10.1103/PhysRevResearch.3.043015

14. Kowalsky M, Albash T, Hen I, Lidar DA. 3-regular three-xorsat planted solutions benchmark of classical and quantum heuristic optimizers. *Quan Sci Technology* (2022) 7:025008. doi:10.1088/2058-9565/ac4d1b

15. Patil P, Kourtis S, Chamon C, Mucciolo ER, Ruckenstein AE. Obstacles to quantum annealing in a planar embedding of XORSAT. *Phys Rev B* (2019) 100:054435. doi:10.1103/PhysRevB.100.054435

16. Haanpää H, Järvisalo M, Kaski P, Niemelä I. Hard satisfiable clause sets for benchmarking equivalence reasoning techniques. *J Satisfiability, Boolean Model Comput* (2006) 2:27–46. doi:10.3233/SAT190015

17. Järvisalo M. Further investigations into regular xorsat. In: *Aaai* (2006). p. 1873–4.

18. Jia H, Moore C, Selman B. From spin glasses to hard satisfiable formulas. In: Hoos HH, Mitchell DG, editors. *Theory and applications of satisfiability testing*. Berlin, Heidelberg: Springer Berlin Heidelberg (2005). p. 199–210.

19. Barthel W, Hartmann AK, Leone M, Ricci-Tersenghi F, Weigt M, Zecchina R. Hiding solutions in random satisfiability problems: a statistical mechanics approach. *Phys Rev Lett* (2002) 88:188701. doi:10.1103/PhysRevLett.88.188701

20. Ricci-Tersenghi F, Weigt M, Zecchina R. Simplest random**K**-satisfiability problem. *Phys Rev E* (2001) 63:026702. doi:10.1103/PhysRevE.63.026702

21. Guidetti M, Young AP. Complexity of several constraint-satisfaction problems using the heuristic classical algorithm walksat. *Phys Rev E* (2011) 84:011102. doi:10.1103/PhysRevE.84.011102

22. Garcia-Saez A, Latorre JI An exact tensor network for the 3SAT problem. (2011).

23. Biamonte JD, Morton J, Turner J. Tensor network contractions for# sat. *J Stat Phys* (2015) 160:1389–404. doi:10.1007/s10955-015-1276-z

24. Kourtis S, Chamon C, Mucciolo ER, Ruckenstein AE. Fast counting with tensor networks. *Scipost Phys* (2019) 7:060. doi:10.21468/SciPostPhys.7.5.060

25. Meichanetzidis K, Kourtis S. Evaluating the jones polynomial with tensor networks. *Phys Rev E* (2019) 100:033303. doi:10.1103/PhysRevE.100.033303

26. de Beaudrap N, Kissinger A, Meichanetzidis K. Tensor network rewriting strategies for satisfiability and counting. *EPTCS* (2021) 340:46–59. doi:10.4204/eptcs.340.3

27. Schuch N, Wolf MM, Verstraete F, Cirac JI. Computational complexity of projected entangled pair states. *Phys Rev Lett* (2007) 98:140506. doi:10.1103/PhysRevLett.98.140506

28. Evenbly G, Vidal G. Tensor network renormalization. *Phys Rev Lett* (2015) 115:180405. doi:10.1103/PhysRevLett.115.180405

29. Evenbly G. Algorithms for tensor network renormalization. *Phys Rev B* (2017) 95:045117. doi:10.1103/PhysRevB.95.045117

30. Gray J, Chan GK-L. Hyperoptimized approximate contraction of tensor networks with arbitrary geometry. *Phys Rev X* (2024) 14:011009. doi:10.1103/PhysRevX.14.011009

31. Alkabetz R, Arad I. Tensor networks contraction and the belief propagation algorithm. *Phys Rev Res* (2021) 3:023073. doi:10.1103/PhysRevResearch.3.023073

32. Pancotti N, Gray J. One-step replica symmetry breaking in the language of tensor networks. (2023).

33. Garey MR, Johnson DS. *Computers and intractability: a guide to the theory of NP-completeness*. San Francisco, CA: W. H. Freeman (1979).

34. Braunstein A, Leone M, Ricci-Tersenghi F, Zecchina R. Complexity transitions in global algorithms for sparse linear systems over finite fields. *J Phys A: Math Gen* (2002) 35:7559–74. doi:10.1088/0305-4470/35/35/301

35. Denny SJ, Biamonte JD, Jaksch D, Clark SR. Algebraically contractible topological tensor network states. *J Phys A: Math Theor* (2011) 45:015309. doi:10.1088/1751-8113/45/1/015309

36. Seitz P, Medina I, Cruz E, Huang Q, Mendl CB. Simulating quantum circuits using tree tensor networks. *Quantum* (2023) 7:964. doi:10.22331/q-2023-03-30-964

37. Wang M, Pan Y, Xu Z, Yang X, Li G, Cichocki A. Tensor networks meet neural networks: a survey and future perspectives. *arXiv preprint arXiv:2302.09019* (2023). doi:10.48550/arXiv.2302.09019

38. Gray J, Kourtis S. Hyper-optimized tensor network contraction. *Quantum* (2021) 5:410. doi:10.22331/q-2021-03-15-410

39. Viger F, Latapy M. Efficient and simple generation of random simple connected graphs with prescribed degree sequence. *J Complex Networks* (2015) 4:15–37. doi:10.1093/comnet/cnv013

40. Gray J. quimb: a python package for quantum information and many-body calculations. *J Open Source Softw* (2018) 3:819. doi:10.21105/joss.00819

41. Csardi G, Nepusz T. The igraph software package for complex network research. *InterJournal Complex Syst* (2006) 1695.

42. Girvan M, Newman MEJ. Community structure in social and biological networks. *Proc Natl Acad Sci* (2002) 99:7821–6. doi:10.1073/pnas.122653799

43. Schlag S, Henne V, Heuer T, Meyerhenke H, Sanders P, Schulz C. (????). *¡italic¿k¡/italic¿-way Hypergraph Partitioning via ¡italic¿n¡/italic¿-Level Recursive Bisection* 53–67. doi:10.1137/1.9781611974317.5

44. Akhremtsev Y, Heuer T, Sanders P, Schlag S. Engineering a direct ¡italic¿k¡/italic¿-way Hypergraph Partitioning Algorithm. In: 2017 Proceedings of the Ninteenth Workshop on Algorithm Engineering and Experiments (ALENEX), 28–42 (2017). doi:10.1137/1.9781611974768.3

45. Zhu Z, Katzgraber HG. Do tensor renormalization group methods work for frustrated spin systems? *arXiv preprint arXiv:1903.07721* (2019). doi:10.48550/arXiv.1903.07721

46. Fattal D, Cubitt TS, Yamamoto Y, Bravyi S, Chuang IL. Entanglement in the stabilizer formalism. *arXiv* (2004). doi:10.48550/arXiv.quant-ph/0406168

47. Hamma A, Ionicioiu R, Zanardi P. Bipartite entanglement and entropic boundary law in lattice spin systems. *Phys Rev A* (2005) 71:022315. doi:10.1103/PhysRevA.71.022315

48. Zhou S, Yang Z-C, Hamma A, Chamon C. Single T gate in a Clifford circuit drives transition to universal entanglement spectrum statistics. *Scipost Phys* (2020) 9:087. doi:10.21468/SciPostPhys.9.6.087

frontiers | Frontiers in Physics

TYPE Mini Review
PUBLISHED 05 November 2024
DOI 10.3389/fphy.2024.1488275



OPEN ACCESS

EDITED BY
Ralph Chamberlin,
Arizona State University, United States

REVIEWED BY
Aakansha,
Banasthali University, India

*CORRESPONDENCE
Raymond L. Orbach,
orbach@utexas.edu

RECEIVED 29 August 2024
ACCEPTED 07 October 2024
PUBLISHED 05 November 2024

CITATION
Zhai Q and Orbach RL (2024) Toward understanding the dimensional crossover of canonical spin-glass thin films.
*Front. Phys.* 12:1488275.
doi: 10.3389/fphy.2024.1488275



# Toward understanding the dimensional crossover of canonical spin-glass thin films

Qiang Zhai[1] and Raymond L. Orbach[2]*

[1]MOE Key Laboratory for Nonequilibrium Synthesis and Modulation of Condensed Matter, School of Physics, Xi'an Jiaotong University, Xi'an, Shaanxi, China, [2]Texas Materials Institute, The University of Texas at Austin, Austin, TX, United States

Spin-glass thin films exhibit many features different from the bulk. The freezing temperatures of spin-glass films are suppressed for reduced thickness and follow the Kenning relation. The dynamics are altered near the vacuum interface. These phenomena are closely related to the lower critical dimension of spin glasses, the spin-glass correlation length, and the dimensional crossover from $d = 3$ to $d = 2$. In this article, we review the experimental facts and theoretical perspectives for spin-glass thin films. We focus on canonical spin-glass systems with the Ruderman–Kittel–Kasuya–Yosida (RKKY) interaction between magnetic impurities in a nonmagnetic host. Open questions to be addressed are emphasized.

KEYWORDS

**spin glasses, dimensional crossover, freezing temperature, correlation length, interfacial effects**

## 1 Introduction

Spin glasses [1] with random spin orientations yet strong correlations have motivated theoretical developments [2] to understand their emergent complexities and continue to spur new findings in complex systems [3]. After more than half a century of intensive efforts to uncover the physics of spin-glass dynamics, controversies remain. A consensus regarding the density of ground states and the stability of the spin-glass phase [4, 5] in an external field is still lacking.

Finite-size effects of spin glasses, first reported by the pioneering work of Kenning, Slaughter, and Cowen [6], offer a new route to uncover some of their mysteries. A surge of research interest in spin-glass thin films focuses on the dimensional crossover from $d = 3$ to $d = 2$ [7–14]. In this work, we review the experimental discoveries and theoretical developments for metallic canonical spin-glass thin films. The freezing temperature, $T_f$, one of the most studied quantities of thin films, is first introduced. The correlation length offers a unique lens through which to understand dimensional crossover. Simulations to extract the growth laws governing correlation lengths are introduced. We also examine the impact of the interface on the spin-freezing process. We conclude the paper with open questions and remarks.

## 2 The freezing temperature and dimensional crossover: experiments

The freezing temperature $T_f$ [6, 7] of spin glasses is different from the critical temperature $T_c$. Approaching $T_c$ from above in a bulk sample, a continuous symmetry

breaking in the phase space commences and signifies a phase transition. In thin film magnetometry measurements, $T_f$ is defined as the temperature below which the zero-field-cooled (ZFC) magnetization, $M_{ZFC}(T,t)$, differs from the reference field-cooled magnetization $M_{FC}(T,t)$ (in some literature, $T_f$ is defined as the peak of $M_{ZFC}(T,t)$; the difference between the two is small in a small enough magnetic field).

The time dependence of $M_{ZFC}(T,t)$ naturally leads to the time dependence of $T_f(t)$. When cooled from the paramagnetic phase to the working temperature $T$, $M_{ZFC}(T,t)$ exhibits a sudden jump after the field is switched on, and gradually increases toward $M_{FC}(T,t)$. $T_f(t)$ is, therefore, the highest temperature below which nonequilibrium dynamics set in for a fixed observation time $t$. In a domain growth model, the length scale sets the relaxation time. Consequently, the equality of relaxation time and observation time gives rise to the observed freezing temperature.

The technical difficulty of extracting $T_f$ is the very weak magnetic signal of a thin film with dilute magnetic spins dispersed in a nonmagnetic host. To circumvent this issue, Kenning et al. [6] have used multilayers of CuMn thin films, separated by layers of either pure Cu or Si, to decouple the direct contact between the CuMn thin films. They found that $T_f$ decreases monotonically as the CuMn film thickness is reduced. The data were originally fitted to the finite-size scaling form of Equation 1

$$T_c - T_f(L) \sim L^{-1/\nu_3}, \tag{1}$$

as proposed in the real-space droplet (domain) model, where $L$ is the film thickness. The droplet model assumes the existence of two ground states of the spin-glass phase, related by time-reversal symmetry. The finite-temperature properties are governed by low-lying excitations of droplets of typical size $\ell$. In response to Kenning's results, a new scaling ansatz for the free energy of the droplet in $d = 2$ was proposed, Equation 2,

$$F_\ell \sim \gamma \ell^{\theta_2}. \tag{2}$$

Because $\theta_2 < 0$, the spin-glass phase is unstable in $d = 2$, and long-range order is destroyed. Fisher and Huse [15] predicted that in the critical region,

$$\frac{T_c - T_f(L,t)}{T_c} \sim L^{-1/\nu_3}\left[\ln\left(t/L^{z_3}\right)\right]^{\left[\left(\psi_3+\nu_2\psi_2\theta_3\right)\nu_3\right]^{-1}}. \tag{3}$$

Equation 3 is difficult to test experimentally, as an accurate estimation of $T_c$ is difficult. In addition, the error bars of the many exponents in Equation 3 contribute to the uncertainty of $T_c$.

An alternative interpretation of the freezing temperature was given in [12]:

$$\frac{T_f(L,t)}{T_g}\ln(t) \propto \ln(L/a_0), \tag{4}$$

where $a_0$ is the average spacing between the magnetic impurities, $t$ is the experimental time scale, and $T_g$ is the freezing temperature for the bulk sample. Equation 4 is referred to as the Kenning relation.

Figure 1 exhibits data for $T_f/T_g$ plotted against film thickness from [12,16], and [17]. It is assumed that the equilibrium correlation length perpendicular to the film plane, $\xi_\perp$, has saturated at the film thickness $L$ at the time $t$, indicative of a dimensional crossover.

Because the lower critical dimension $d_l$ of spin glass is between 2 and 3 (exactly 2.5 for Edwards–Anderson spin glass [18]), the critical temperature is zero after a dimensional crossover from $d = 3$ to $d = 2$. The energy barrier height that governs the relaxation time was found to only depend on $L$ in a temperature range of 1 K at $T \approx 0.9T_f$ up to film thickness of 20 nm [12]. Equation 4 indicates that $T_f$ shifts to lower $T$ with slower cooling rates, or longer $t$, which is qualitatively consistent with experimental observations (e.g., Figure 1).

Additional support for the dimensional crossover of spin-glass thin films was obtained through polarized neutron reflectometry (PNR) [19, 20]. An asymmetry parameter $A$, defined as

$$A = (R^+ - R^-)/(R^+ + R^-), \tag{5}$$

was measured for AuFe thin films, where $R^+$ and $R^-$ are the reflectivities for the spin-up neutrons and spin-down neutrons, respectively. By fitting Equation 5 with a Parratt recursion formalism, the average magnetic moment for Fe atoms was obtained, as reproduced in Figure 2. In the high-temperature regime, $\overline{\mu_{Fe}}$ can be described by the Brillouin function, $B(J,x)$, where $J$ is the angular momentum, and $x = \mu B/k_BT$ with $\mu$ being the magnetic moment of impurities.

Below 50 K, $\overline{\mu_{Fe}}$ deviates from $B(J,x)$, in a range of 0.5–1.3 $\mu_B$ for $L \geq 5$ nm. Exceptions are for $L = 2$ nm and $L = 1$ nm, which follow a paramagnetic line down to 2 K. In particular, for the 1 nm film, the measured magnetic moment 4.2 $\mu_B$ is very close to the value for non-interacting Fe atoms.

These measurements were performed in a very high magnetic field of 6 T. In large fields, the measured moment should correspond to a quasi-equilibrium spin-glass phase. Therefore, at large observation times and for ultra-thin film, Equation 4 implies a $T_f \approx 0$, consistent with the measurements. In addition, the freezing of the magnetic moment for the thicker films implies the existence of a spin-glass phase up to 6 T.

According to calculations based on an Ising model, an A-T line [21] exists for the $H - T$ phase diagram of spin glasses, while the droplet picture predicts that the spin-glass phase vanishes in a magnetic field. However, equilibrium states are difficult to access in laboratory experiments, leaving a lack of consensus on the nature of the spin-glass phase in the presence of a magnetic field [21, 22].

## 3 Correlation length growth and dimensional crossover: simulations

It has been shown through Monte Carlo (MC) simulations and finite-size scaling [23–27] that the correlation length $\xi$ diverges at a finite temperature for a 3D-Ising Edwards–Anderson (EA) model with either Gaussian or bimodal interactions. Similar conclusions were reached for the 3D-Heisenberg spin glass [28, 29] with the aid of a much larger sample size. The 2D-Ising (Heisenberg) spin glass only exhibits a phase transition at $T = 0$, as shown by free energy calculations

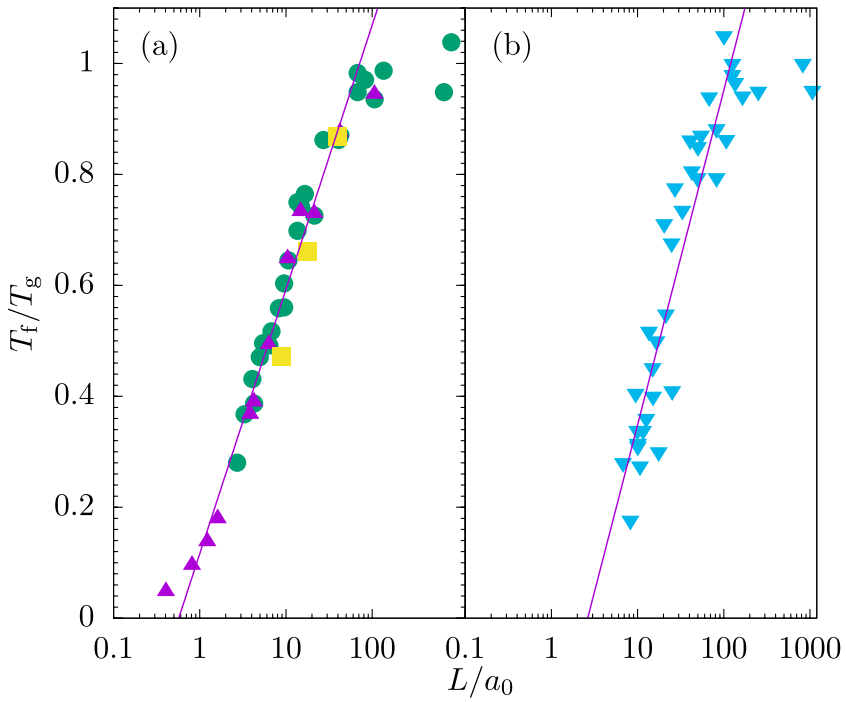


FIGURE 1
$T_f$ collapses using Equation 4 for $L/a_0 \leq 100$. **(A)** Measurements of $T_f$ for CuMn/Cu multilayer samples. The circle symbols represent data from [16], squares represent data taken from [12], and triangles indicate data taken from [17]. **(B)** $T_f$ of CuMn multilayer films with a 7-nm Si interlayer.

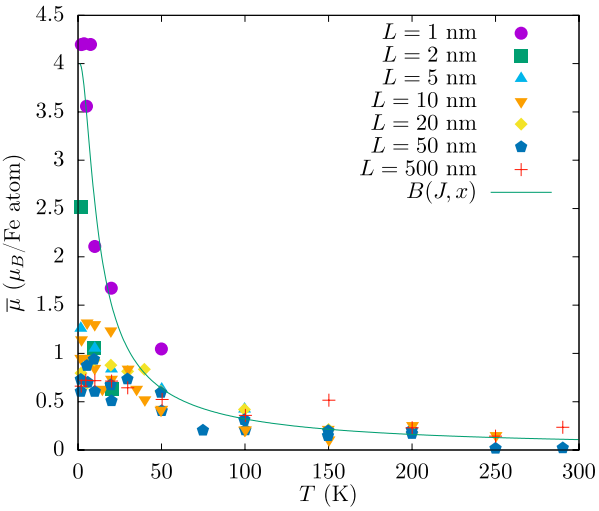


FIGURE 2
Averaged magnetic moment per Fe atom for AuFe films of different thickness $L$. A paramagnetic behavior is exhibited when $L$ is reduced below 2 nm. Figure created based on the data of [19, 20].

[30] and MC simulations [31]. These findings imply that there must be a crossover of the spin-glass dynamics when the size of the system is reduced gradually by one dimension. Simulations are usually limited by sample size and time scales, but compared to experiments, they enjoy enhanced spatial resolutions and gain immediate access to spin configurations. They thus provide a unique route to understand dimensional crossover. In particular, they have been able to directly extract $\xi$.

Of particular interest is the aging dynamics of $\xi$ when the spin-glass phase evolves from nonequilibrium towards equilibrium. In practice, simulations suddenly quench the sample from the paramagnetic state (infinite temperature) to a temperature comparable to experiments. Rieger et al. [32, 33] performed MC simulations on an Ising EA model with Gaussian interactions. In order to understand the aging phenomena observed in experiments, the autocorrelation function is introduced, defined by

$$C(t, t_w) = \frac{1}{N}\overline{\langle \sum_i S_i(t + t_w) S_i(t_w) \rangle}, \tag{6}$$

where $t_w$ is the duration in which the sample remains at $T$ after quench, and the averages are taken over thermal fluctuation and quenched disorder. For $t_w \gg \tau_{eq}$, $C(t, t_w)$ is stationary and only depends on $t$ in Equation 6. For $t_w \ll \tau_{eq}$ and $t > t_w$, a power law of Equation 7 is found,

$$C(t, t_w) \propto t^{-\zeta(T)}. \tag{7}$$

$C(t, t_w)$ for different $t_w$ obeys the simple scaling form,

$$\bar{c}\left(t/\tau(t_w)\right), \tag{8}$$

where $\tau(t_w) = t_w$ if $t_w \ll \tau_{eq}$. This is not consistent with activated dynamics,

$$\xi(t_w) \propto (\log t_w)^{1/\psi}, \tag{9}$$

which leads to a logarithmic scaling. The spatial correlation is calculated through Equation 10,

$$G(r,t_w)=\frac{1}{t_w}\sum_{t=t_w+1}^{2t_w}\overline{\langle S_0(t)S_r(t)\rangle^2}, \tag{10}$$

and the correlation length at $t_w$ is given by Equation 11,

$$\xi(t_w)=2\int_0^\infty drG(r,t_w). \tag{11}$$

The growth of $\xi$ can be fitted with the activated dynamics of Equation 9 or a power-law dynamics,

$$\xi(t_w)\propto t_w^{\alpha(T)}. \tag{12}$$

However, Equation 12 naturally leads to the scaling form of Equation 8 when assuming $C(t,t_w)\propto[\xi(t_w)/\xi(t)]^\lambda$, where $\lambda=\zeta(T)/\alpha(T)$. The power-law growth of $\xi$ was later verified by Joh et al. [34].

A twelve-time-decade MC simulation of the Ising EA model was carried out by Fernandez et al. [13]. They clarified growth dynamics for $\xi$ and reinforced the evidence for the scaling function of Equation 8. They found that, Equation 13,

$$\frac{\xi(t_w)}{\xi_{eq}}=\mathcal{G}\left(t_w/\tau(T)\right)+\mathcal{O}\left[(\xi(t_w))^{-\omega},\left(\xi_{eq}\right)^{-\omega}\right], \tag{13}$$

where $\omega$ is the corrections-to-scaling exponent, $\tau(T)\propto\exp(B/T^{1+\epsilon})$, and $\epsilon$ is a small number. This verified that the energy barrier height inferred from aging dynamics is physical [12].

The first MC simulation for dimensional crossover in a thin film geometry, comparable to experiments, was carried out by Victor Martin-Mayor and his coworkers [14]. The protocol used in this simulation closely resembled that of experiments: The sample was quenched to a working temperature, and the complete growth process (from nonequilibrium to equilibrium) of the correlation length was monitored. The correlation length is related to the autocorrelation function of Equation 14,

$$C_4(T,\boldsymbol{r},t)=\overline{\langle q^{(a,b)}(\boldsymbol{x},t)q^{(a,b)}(\boldsymbol{x}+\boldsymbol{r},t)\rangle}_T, \tag{14}$$

where $q^{(a,b)}(\boldsymbol{x},t)$ is the overlap between spin configuration $\sigma^{(a)}(\boldsymbol{x},t)$ and $\sigma^{(b)}(\boldsymbol{x},t)$ in replicas (a) and (b).

The estimator for the correlation length is given by Equation 15

$$\begin{aligned}\xi_\parallel(T,t)&=\int_0^\infty drr^2C_4(T,\boldsymbol{r},t)\Big/\int_0^\infty drrC_4(T,\boldsymbol{r},t),\\ \xi_\perp(T,t)&=\int_0^\infty drr^2C_4^\perp(T,\boldsymbol{r},t)\Big/\int_0^\infty drrC_4^\perp(T,\boldsymbol{r},t).\end{aligned} \tag{15}$$

Again, they found a power-law growth of the correlation length $\xi\propto t^{1/z}$.

Four time regimes were identified, with different $z$ for $\xi_\parallel(T,t)$. In the first, $\xi_\parallel(T,t)$ grows with the aging rate $z_{d=3}$. Upon saturation of $\xi_\perp$ close to the film thickness $h$, the growth of $\xi_\parallel$ gradually speeds up in the second time regime. The aging rate of $\xi_\parallel$ in the third regime finally matches $z_{d=2}$, smaller than $z_{d=3}$ (faster dynamics). Finally, in the fourth regime, $\xi_\parallel$ reaches to its equilibrium value $\xi_\parallel^{eq}$.

Further analysis leads to a scaling function,

$$\frac{\xi_\parallel(t,T,L)}{\xi_{d=3}(t)}=\mathcal{F}\left[\xi_{d=3}(t,T)/L\right], \tag{16}$$

where $\xi_{d=3}(t)$ is the correlation length of a 3D sample. The invariance of Equation 16 allows a Kananoff–Wilson block spin transformation of the simulation results. These, in turn, lead to the mapping of the temperature of the film $T$ to an effective temperature in $d=2$ (a true monolayer film),

$$\xi_\parallel^{eq}(T,L)=L\,\xi_{d=2}^{eq}\left(T_{d=2}^{eff}\right). \tag{17}$$

The mapping given by Equation 17 is remarkable in that an effective temperature can allow for treating the $3D$ spin-glass problem exactly in $2D$. For example, for $T\approx0.9T_c$, $T_{d=2}^{eff}\approx1.04T$. As the correction is negligible, the analyses of CuMn thin films in [12–14] are adequate.

## 4 Interfacial effects on spin freezing

Much of our understanding of dimensional crossover in thin films arises from multilayers of spin-glass films separated by non-magnetic metallic or insulating layers. It is natural to ask whether the interface between the spin-glass layers and the decoupling layers leads to artificial or unwanted effects. For example, as illustrated in Figure 1, the $T_f$ of the same CuMn film decoupled by Si is lower than films decoupled by Cu [16]. The RKKY interaction, responsible for spin-glass behavior in metallic spin glasses, is mediated by the conduction electrons. This long-range interaction is sharply cut off at the CuMn/Si boundary but falls off slowly at the CuMn/Cu boundary [35], perhaps accounting for the difference. A quantitative analysis is lacking.

The first systematic study to address the effects of the decoupling layers was conducted by Granberg et al. [9]. They varied the thickness of Cu layers, $L_i$, to explore the freezing process of CuMn/Cu multilayers. We identify the $T_f$ from Figure 1 of [9] in order to display the time dependence of $T_f$ in Figure 3. The reduction of $T_f$ follows a logarithmic time dependence given by Equation 4. The rates of reduction, $dT_f/d\log(t)$ for different $L_i$ are displayed in Figure 4. The rate decreases with decreasing thickness of the decoupling layer until it reaches its $d=3$ value.

An explanation for the behaviors exhibited in Figures 3, 4 was given in [12]. For a given observation time, the inequality of Equation 18,

$$c_1a_0\left(\frac{t}{\tau_0}\right)^{c_2T/T_g}\le\xi_{eq}(T), \tag{18}$$

holds for $T\le T_f$ in $d=3$, where $\xi_{eq}(T)$ is the equilibrium correlation length obtained in the FC state. The growth of the correlation length for the ZFC protocol obeys the growth law on the left of Equation 18. For spin-glass films fully decoupled from one another, $\xi_\perp(t)$ is bounded by $L$ regardless of $T$. $\xi_\parallel(t)$ grows faster than $\xi_\perp(t)$ [14]. Then, any films with $L\le\xi_{d=3}^{eq}(T)$ should be much more sensitive to the variation of the observation time scale. Between the $d=3$ and the fully decoupled layer limit, crosstalk occurs among the neighboring layers, leading to an intermediate sensitivity to the variation of observation time $t$.

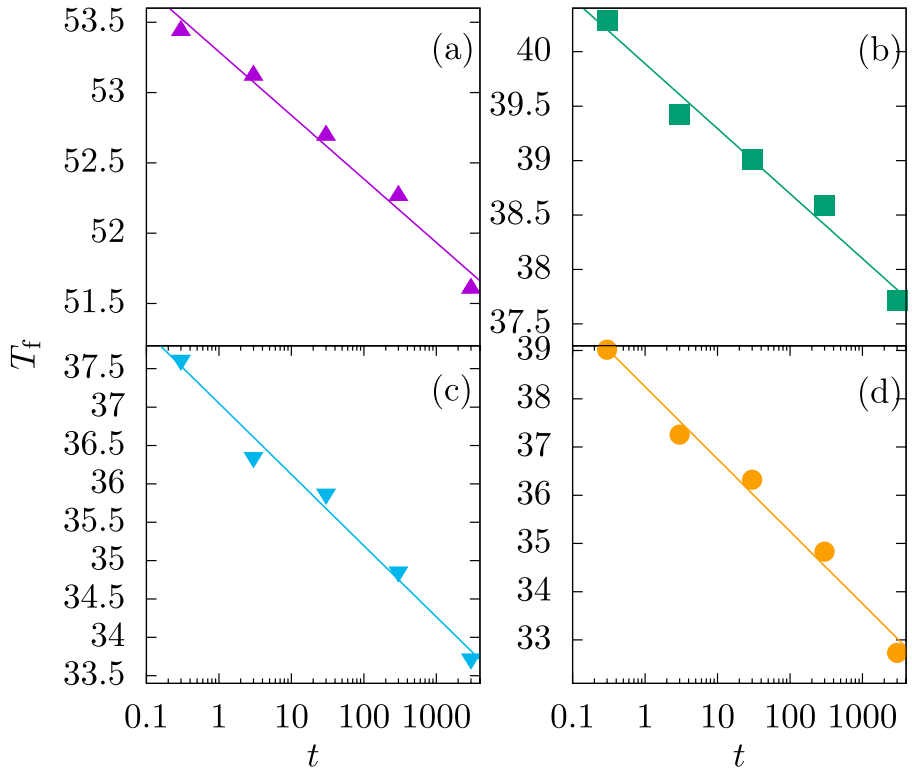


FIGURE 3
The freezing temperature decreases logarithmically with observation time $t$ for CuMn/Cu multilayer thin films with interlayer thickness of **(A)** $L_i$ = 1 nm, **(B)** $L_i$ = 7 nm, **(C)** $L_i$ = 15 nm, and **(D)** $L_i$ = 120 nm.

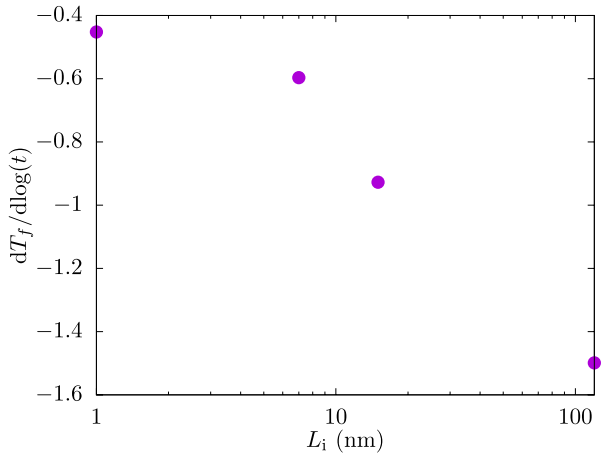


FIGURE 4
Changing rate of freezing temperature $T_f$ versus the interlayer thickness $L_i$.

A direct probe of the surface dynamics has been carried out by depth-dependent muon-spin-relaxation ($\mu$SR) studies [36]. The $\mu$SR is a powerful technique to probe local spin orientations [37–39]. In the experimental setup, the polarized $\mu^+$ beam is stopped by the sample, and the decay positron emitted from $\mu^+$ is counted. The backward (EB) and forward (EF) counting rates are given by Equation 19,

$$N_{EF}(t) = N_F \exp(-t/\tau_u)[1 + G_z(t)],$$
$$N_{EB}(t) = N_F \exp(-t/\tau_u)[1 - G_z(t)], \quad (19)$$

where $\tau_\mu$ is the lifetime of $\mu^+$, and $G_z(t)$ is the muon-spin-relaxation function. $G_z(t) = 1$ for completely polarized spins, and $G_z(t) = 0$ for completely depolarized spins. The depolarization process can be inferred from the asymmetric time evolution of $N_{EF}(t)$ and $N_{EB}(t)$.

The muons are assumed to take random interstitial sites in the sample and do not diffuse in the lattice. For a CuMn (1 at%) sample, the atomic dipolar field (~100 G) from the Mn impurity dominates compared to the average RKKY field (~10 G) and the Cu nuclear dipolar field (~4 G). For an ordered translational invariant magnetic phase (e.g., a ferromagnet), the muon spin will precess with a single frequency in the local dipolar field. In the case of spin glasses, the randomness of the local dipolar field leads to a rapid depolarization of the polarized muons.

Taking into account the static random local fields and their fluctuation, a stochastic theory of muon-spin-relaxation for $G_z(t)$ was formulated by Uemura et al. [39]:

$$G_z(t) = \frac{1}{3}\exp\left[-\left(4a_d^2 t/\nu\right)^{1/2}\right] + \frac{2}{3}\left[1 - \frac{a_s^2 t^2}{\left(4a_d^2 t/\nu + a_s^2 t^2\right)^{1/2}}\right]\exp\left[-\left(4a_d^2 t/\nu + a_s^2 t^2\right)^{1/2}\right], \quad (20)$$

where $a_s = \sqrt{q_{EA}}a$ and $a_d = \sqrt{1 - q_{EA}}a$ with $a$ are the average amplitude of random fields. It was assumed that, Equation 21,

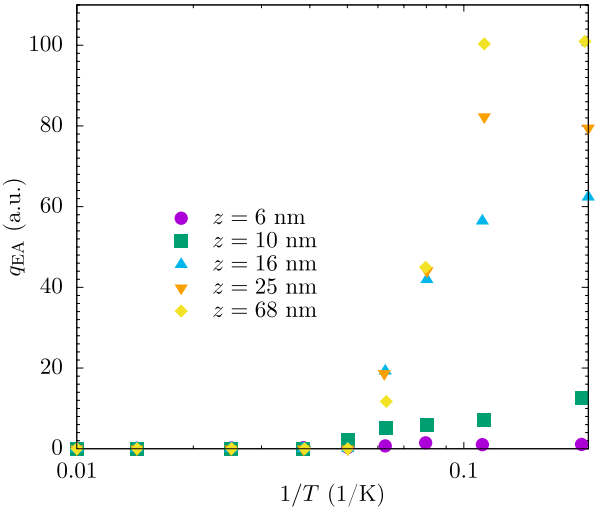


FIGURE 5
Self-overlap parameter, $q_{EA}$, plotted against $1/T$ at different depths of $z$ from the vacuum interface for a 220-nm-thick AuFe film.

$$\overline{\langle S(t)S(0)\rangle} = (1 - q_{EA})\exp(-\nu t) + q_{EA}, \tag{21}$$

where the brackets represent thermal averages, and the bar indicates spatial averages. Each spin $S$ has a preferred static component $\sqrt{q_{EA}}S$ below $T_g$, and a dynamic component $(1 - \sqrt{q_{EA}})S$ with a fluctuating rate $\nu$.

Therefore, the order parameter $q_{EA}$ [40] can be obtained by fitting Equation 20 to the experimental data. Figure 5 reproduced the extracted values of $q_{EA}$ at different depth $z$ of a 220-nm-thick AuFe film by [36]. At the low-temperature regime, $q_{EA}$ attains a finite value, signifying the onset of spin freezing. The dynamical fluctuations of spins are significantly reduced with increasing distance from the surface. This suggests an inhomogeneous freezing gradient along the direction of the film thickness because of the vacuum interface. It is likely that the RKKY interaction between magnetic impurities is modified by the vacuum interface. However, again, a treatment to quantify this effect is lacking.

Recent $1/f$ noise measurements [41, 42], covering a much larger temperature window (inaccessible in magnetometry measurements) for a larger collection of film thicknesses, suggest that the maximum barrier height is temperature dependent for thicker films. Although this appears to conflict with the magnetometry measurements [12] at first glance, the $1/f$ noise is sensitive to the length scales associated with the electronic mean free path, which are much shorter than the range of the RKKY interaction. This may be the reason behind the discrepancy between the two experimental processes.

## 5 Conclusion

We have examined the evidence for dimensional crossover from $d = 3$ to $d = 2$ of spin-glass thin films. The results from the magnetometry and the PNR measurements are consistent with the Kenning relation, Equation 4. The correlation length serves as a caliber to quantify $T_f$. The $\log(t)$ dependence of $T_f$ originates from the power-law growth of the correlation length, as detailed in large-scale simulations.

Although much has been understood concerning the dynamics of thin film spin-glasses, in our opinion, a few questions remain to be addressed:

(1) In the low-temperature regime of the spin-glass phase, the dynamics become too slow to be probed by magnetometry and simulations. The validity of the Kenning relation remains to be tested with novel experimental protocols or data analyses.
(2) Both the vacuum and Si interfaces alter the spin-freezing process. It remains unknown how the interface affects the spin correlations. A theoretical treatment of the interfacial effects would not only contribute to a deeper understanding of spin-glass physics but also would benefit devices utilizing junctions between spin-glasses and other magnetic ordering materials [43, 44].

## Author contributions

QZ: writing–original draft and writing–review and editing. RO: writing–original draft and writing–review and editing.

## Funding

The author(s) declare that financial support was received for the research, authorship, and/or publication of this article. QZ was supported by China Postdoc Fund Grant No. 2022M722548, Shaanxi NSF Grant No. 2023-JC-QN-0018, and Central University Basis Research Fund Grant No. xzy012023044. RO was supported by the U.S. Department of Energy, Office of Science, Basic Energy Sciences, Division of Materials Science and Engineering, under Award No. DE-SC0013599.

## Conflict of interest

The authors declare that the research was conducted in the absence of any commercial or financial relationships that could be construed as a potential conflict of interest.

## Publisher's note

# References


1. Cannella V, Mydosh JA. Magnetic ordering in gold-iron alloys. *Phys Rev B* (1972) 6: 4220–37. doi:10.1103/PhysRevB.6.4220

2. Mézard M, Parisi G, Virasoro MA. *Spin glass theory and beyond: an introduction to the replica method and its applications*, 9. World Scientific Publishing Company (1987).

3. Charbonneau P, Marinari E, Parisi G, Ricci-tersenghi F, Sicuro G, Zamponi F, et al. Spin glass theory and far beyond: replica symmetry breaking after 40 years. *World Scientific* (2023). doi:10.1142/13341

4. Mézard M, Parisi G, Sourlas N, Toulouse G, Virasoro M. Nature of the spin-glass phase. *Phys Rev Lett* (1984) 52:1156–9. doi:10.1103/PhysRevLett.52.1156

5. Fisher DS, Huse DA. Ordered phase of short-range ising spin-glasses. *Phys Rev Lett* (1986) 56:1601–4. doi:10.1103/PhysRevLett.56.1601

6. Kenning GG, Slaughter JM, Cowen JA. Finite-size effects in a cumn spin-glass. *Phys Rev Lett* (1987) 59:2596–9. doi:10.1103/PhysRevLett.59.2596

7. Sandlund L, Granberg P, Lundgren L, Nordblad P, Svedlindh P, Cowen JA, et al. Dynamics of cu-mn spin-glass films. *Phys Rev B* (1989) 40:869–72. doi:10.1103/PhysRevB.40.869

8. Granberg P, Nordblad P, Svedlindh P, Lundgren L, Stubi R, Kenning G, et al. Dimensionality crossover in cumn spin-glass films. *J Appl Phys* (1990) 67:5252–4. doi:10.1063/1.344627

9. Granberg P, Mattsson J, Nordblad P, Lundgren L, Stubi R, Bass J, et al. Dynamics of coupled two-dimensional cu(mn) spin-glass films. *Phys Rev B* (1991) 44:4410–4. doi:10.1103/PhysRevB.44.4410

10. Wood G. The spin glass correlation length and the crossover from three to two dimensions. *J magnetism Magn Mater* (2010) 322:1775–8. doi:10.1016/j.jmmm.2009.12.028

11. Guchhait S, Orbach R. Direct dynamical evidence for the spin glass lower critical dimension $2 \leq dl \leq 3$. *Phys Rev Lett* (2014) 112:126401. doi:10.1103/PhysRevLett.112.126401

12. Zhai Q, Harrison DC, Tennant D, Dahlberg ED, Kenning GG, Orbach RL. Glassy dynamics in cumn thin-film multilayers. *Phys Rev B* (2017) 95:054304. doi:10.1103/PhysRevB.95.054304

13. Fernandez LA, Marinari E, Martin-Mayor V, Parisi G, Ruiz-Lorenzo JJ. An experiment-oriented analysis of 2d spin-glass dynamics: a twelve time-decades scaling study. *J Phys A: Math Theor* (2019) 52:224002. doi:10.1088/1751-8121/ab1364

14. Fernandez LA, Marinari E, Martin-Mayor V, Paga I, Ruiz-Lorenzo JJ. Dimensional crossover in the aging dynamics of spin glasses in a film geometry. *Phys Rev B* (2019) 100:184412. doi:10.1103/PhysRevB.100.184412

15. Fisher DS, Huse DA. Static and dynamic behavior of spin-glass films. *Phys Rev B* (1987) 36:8937–40. doi:10.1103/PhysRevB.36.8937

16. Kenning GG, Bass J, Pratt WP, Leslie-Pelecky D, Hoines L, Leach W, et al. Finite-size effects in cu-mn spin glasses. *Phys Rev B* (1990) 42:2393–415. doi:10.1103/PhysRevB.42.2393

17. Hoines L, Stubi R, Loloee R, Cowen JA, Bass J. How thin a spin glass is still a spin glass? *Phys Rev Lett* (1991) 66:1224–7. doi:10.1103/PhysRevLett.66.1224

18. Boettcher S. Stiffness of the edwards-anderson model in all dimensions. *Phys Rev Lett* (2005) 95:197205. doi:10.1103/PhysRevLett.95.197205

19. Saoudi M, Fritzsche H, Nieuwenhuys GJ, Hesselberth MBS. Size effect in the spin glass magnetization of thin aufe films as studied by polarized neutron reflectometry. *Phys Rev Lett* (2008) 100:057204. doi:10.1103/PhysRevLett.100.057204

20. Fritzsche H, van der Knaap JM, Hesselberth MBS, Nieuwenhuys GJ. Loss of spin glass behavior in ultrathin aufe films. *Phys Rev B* (2010) 81:132402. doi:10.1103/PhysRevB.81.132402

21. de Almeida J, Thouless D. Stability of the sherrington-kirkpatrick solution of a spin glass model. *J Phys A: Math Gen* (1978) 11:983–90. doi:10.1088/0305-4470/11/5/028

22. Young AP, Katzgraber HG. Absence of an almeida-thouless line in three-dimensional spin glasses. *Phys Rev Lett* (2004) 93:207203. doi:10.1103/PhysRevLett.93.207203

23. Palassini M, Caracciolo S. Universal finite-size scaling functions in the 3d ising spin glass. *Phys Rev Lett* (1999) 82:5128–31. doi:10.1103/PhysRevLett.82.5128

24. Ballesteros HG, Cruz A, Fernández LA, Martín-Mayor V, Pech J, Ruiz-Lorenzo JJ, et al. Critical behavior of the three-dimensional ising spin glass. *Phys Rev B* (2000) 62: 14237–45. doi:10.1103/PhysRevB.62.14237

25. Katzgraber HG, Körner M, Young AP. Universality in three-dimensional ising spin glasses: a Monte Carlo study. *Phys Rev B* (2006) 73:224432. doi:10.1103/PhysRevB.73.224432

26. Hasenbusch M, Pelissetto A, Vicari E. Critical behavior of three-dimensional ising spin glass models. *Phys Rev B* (2008) 78:214205. doi:10.1103/PhysRevB.78.214205

27. Baity-Jesi M, Baños RA, Cruz A, Fernandez LA, Gil-Narvion JM, Gordillo-Guerrero A, et al. Critical parameters of the three-dimensional ising spin glass. *Phys Rev B* (2013) 88:224416. doi:10.1103/PhysRevB.88.224416

28. Fernandez LA, Martin-Mayor V, Perez-Gaviro S, Tarancon A, Young AP. Phase transition in the three dimensional heisenberg spin glass: finite-size scaling analysis. *Phys Rev B* (2009) 80:024422. doi:10.1103/PhysRevB.80.024422

29. Baity-Jesi M, Fernández LA, Martín-Mayor V, Sanz JM. Phase transition in three-dimensional heisenberg spin glasses with strong random anisotropies through a multi-gpu parallelization. *Phys Rev B* (2014) 89:014202. doi:10.1103/PhysRevB.89.014202

30. Morgenstern I, Binder K. Magnetic correlations in two-dimensional spin-glasses. *Phys Rev B* (1980) 22:288–303. doi:10.1103/PhysRevB.22.288

31. Kawamura H, Yonehara H. Ordering of the heisenberg spin glass in two dimensions. *J Phys A: Math Gen* (2003) 36:10867–80. doi:10.1088/0305-4470/36/43/013

32. Rieger H, Steckemetz B, Schreckenberg M. Aging and domain growth in the two-dimensional ising spin glass model. *Europhysics Lett* (1994) 27:485–90. doi:10.1209/0295-5075/27/6/013

33. Rieger H, Schehr G, Paul R. Growing length scales during aging in 2d disordered systems. *Prog Theor Phys Suppl* (2005) 157:111–9. doi:10.1143/ptps.157.111

34. Joh Y, Orbach R, Wood G, Hammann J, Vincent E. Extraction of the spin glass correlation length. *Phys Rev Lett* (1999) 82:438–41. doi:10.1103/physrevlett.82.438

35. Kasuya T. s–d and s–f interaction and rare earth metals. Magnetism, 2. Academic Press New York (1966). 215–94.

36. Morenzoni E, Luetkens H, Prokscha T, Suter A, Vongtragool S, Galli F, et al. Depth-dependent spin dynamics of canonical spin-glass films: a low-energy muon-spin-rotation study. *Phys Rev Lett* (2008) 100:147205. doi:10.1103/PhysRevLett.100.147205

37. Uemura YJ, Yamazaki T, Hayano RS, Nakai R, Huang CY. Zero-field spin relaxation of $\mu^+$ as a probe of the spin dynamics of AuFe and CuMn spin-glasses. *Phys Rev Lett* (1980) 45:583–7. doi:10.1103/PhysRevLett.45.583

38. Heffner R, Leon M, Schillaci M, MacLaughlin D, Dodds S. Muon spin relaxation studies of the spin glass agmn. *J Appl Phys* (1982) 53:2174–8. doi:10.1063/1.330771

39. Uemura YJ, Yamazaki T, Harshman DR, Senba M, Ansaldo EJ. Muon-spin relaxation in aufe and cumn spin glasses. *Phys Rev B* (1985) 31:546–63. doi:10.1103/PhysRevB.31.546

40. Edwards SF, Anderson PW. Theory of spin glasses. *J Phys F: Metal Phys* (1975) 5: 965–74. doi:10.1088/0305-4608/5/5/017

41. Harrison DC, Dahlberg ED, Orbach RL. Effect of anisotropy on 1/f noise measurements of cumn spin glasses. *Phys Rev B* (2019) 100:064411. doi:10.1103/PhysRevB.100.064411

42. Harrison DC, Dahlberg ED, Orbach RL. Extraction of the spin-glass free-energy landscape from 1/f noise measurements. *Phys Rev B* (2022) 105:014413. doi:10.1103/PhysRevB.105.014413

43. Ali M, Adie P, Marrows CH, Greig D, Hickey BJ, Stamps RL. Exchange bias using a spin glass. *Nat Mater* (2007) 6:70–5. doi:10.1038/nmat1809

44. Usadel KD, Nowak U. Exchange bias for a ferromagnetic film coupled to a spin glass. *Phys Rev B* (2009) 80:014418. doi:10.1103/PhysRevB.80.014418

frontiers | Frontiers in Physics

TYPE Original Research
PUBLISHED 14 November 2024
DOI 10.3389/fphy.2024.1473378



OPEN ACCESS

EDITED BY
Stefan Boettcher,
Emory University, United States

REVIEWED BY
Alberto Fachechi,
University of Salento, Italy
Tommaso Rizzo,
National Research Council (CNR), Italy

*CORRESPONDENCE
D. L. Stein,
daniel.stein@nyu.edu

RECEIVED 30 July 2024
ACCEPTED 24 October 2024
PUBLISHED 14 November 2024

CITATION
Newman CM and Stein DL (2024) Critical droplets and replica symmetry breaking. *Front. Phys.* 12:1473378. doi: 10.3389/fphy.2024.1473378



# Critical droplets and replica symmetry breaking

C. M. Newman[1,2] and D. L. Stein[3,4,5]*

[1]Courant Institute of Mathematical Sciences, New York University, New York, NY, United States, [2]NYU-ECNU Institute of Mathematical Sciences at NYU Shanghai, Shanghai, China, [3]Department of Physics and Courant Institute of Mathematical Sciences, New York University, New York, NY, United States, [4]NYU-ECNU Institutes of Physics and Mathematical Sciences at NYU Shanghai, Shanghai, China, [5]Santa Fe Institute, Santa Fe, NM, United States

We show that the notion of critical droplets is central to an understanding of the nature of ground states in the Edwards–Anderson–Ising model of a spin glass in arbitrary dimensions. Given a specific ground state, we suppose that the coupling value for a given edge is varied with all other couplings held fixed. Beyond some specific value of the coupling, a droplet will flip, leading to a new ground state; we refer to this as the critical droplet for that edge and ground state. We show that the distribution of sizes and energies over all edges for a specific ground state can be used to determine which of the leading scenarios for the spin glass phase is correct. In particular, the existence of low-energy interfaces between incongruent ground states, as predicted by replica symmetry breaking, is equivalent to the presence of critical droplets, whose boundaries comprise a positive fraction of edges in the infinite lattice.

KEYWORDS

**spin glasses, ground states, critical droplets, replica symmetry breaking, ground-state interfaces**

## 1 Introduction

The nature of the low-temperature phase of the Edwards–Anderson (EA) Hamiltonian [1] in finite dimensions

$$\mathcal{H}_J = -\sum_{<x,y>} J_{xy}\sigma_x\sigma_y \tag{1}$$

remains unresolved. Here, $\sigma_x = \pm 1$ is the Ising spin at site $x$, and $\langle x,y\rangle$ denotes a nearest-neighbor edge in the edge set $\mathbb{E}^d$ of the $d$-dimensional cubic lattice $\mathbb{Z}^d$. The couplings $J_{xy}$ are taken to be independent, identically distributed continuous random variables chosen from a distribution $\nu(dJ_{xy})$, with random variable $J_{xy}$ assigned to the edge $\langle x,y\rangle$. Our requirements on $\nu$ are that it be supported on the entire real line, distributed symmetrically about 0, and has finite variance; e.g., a Gaussian with mean 0 and variance 1. We denote a particular realization of the couplings by $J$.

There are, at present, four scenarios for the spin glass phase that are consistent both with numerical results and, as far as is currently known, mathematically consistent: replica symmetry breaking (RSB) [2–12], droplet-scaling [13–17], trivial–non-trivial spin overlap (TNT) [18, 19], and chaotic pairs [10, 20–22]. One of the central open questions in spin glass theory is which (if any) of these scenarios is correct and for which dimensions and temperatures.

The differences among the four scenarios at positive temperature are described elsewhere [12, 23, 24]; here, we are concerned with their different predictions at zero temperature, i.e., for the ground-state structure of the EA Hamiltonian. Of the four, two (RSB and chaotic pairs) predict the existence of many ground states, and the other two (droplet-scaling and TNT) predict the existence of only a single pair [17, 25, 26]. Although important, these differences are less fundamental than the nature of the *interfaces* that separate their ground states from their lowest-lying long-wavelength excitations. The presence or absence of multiplicity of ground states follows as a consequence of the nature of these excitations.

In this paper, we focus on the nature of low-energy long-wavelength excitations above the ground state and how they relate to ground state stability, with a view toward distinguishing different predictions of the four scenarios. Aside from elucidating the different (and potentially testable) predictions of these scenarios, determining the stability properties of the ground state is crucial in determining the low-temperature properties of the spin glass phase, including central questions such as multiplicity of pure states and the presence or absence of an Almeida-Thouless (AT) line [27]. We begin by defining the parameters of the study.

A finite volume $\Lambda_L$ was chosen corresponding to a cube of side $L$ centered at the origin. A finite-volume ground state $\sigma_L$ is the lowest-energy spin configuration in $\Lambda_L$, which is subject to a specified boundary condition. An infinite-volume ground state $\sigma$ is a spin configuration on all of $\mathbb{Z}^d$, which is defined by the condition that its energy cannot be lowered by flipping any *finite* subset of spins. ($\sigma$ is always defined with respect to a specific $J$, but we suppress its dependence for notational convenience.) The condition for $\sigma$ to be a ground state is then

$$E_S = \sum_{\langle x,y\rangle \in S} J_{xy}\sigma_x\sigma_y \; > 0, \tag{2}$$

where $S$ is any closed surface (or contour in two dimensions) in the dual lattice. The surface $S$ encloses a connected set of spins (a "droplet"), and $\langle x,y\rangle \in S$ is the set of edges connecting spins in the interior of $S$ to spins outside $S$. The inequality in Equation 2 is strict because, by the continuity of $\nu(dJ_{xy})$, there is zero probability of any closed surface having exactly zero energy in $\sigma$. The condition in Equation 2 must also hold for finite-volume ground states for any closed surface completely inside $\Lambda_L$. It is then not hard to show that an alternative (and equivalent) definition, which we also use sometimes, is that an infinite-volume ground state is any convergent limit of an infinite sequence of finite-volume ground states. Given the spin-flip symmetry of the Hamiltonian, a ground state, whether of finite or infinite volume, generated by a spin-symmetric boundary condition, such as free or periodic, will appear as one part of a globally spin-reversed pair; we therefore refer generally to ground state pairs (GSPs) rather than individual ground states.

## 2 Interfaces and critical droplets

An interface between two infinite-volume spin configurations $\alpha$ and $\beta$ comprises the set of edges whose associated couplings are satisfied in $\alpha$ and unsatisfied in $\beta$, or *vice versa*; they separate regions in which the spins in $\alpha$ agree with those in $\beta$ from regions in which their spins disagree. An interface may consist of a single connected component or multiple disjoint ones, but (again using the continuity of the coupling distribution) if $\alpha$ and $\beta$ are ground states, any such connected component must be infinite in extent.

Interfaces can be characterized by their geometry and energy. They can either be "space-filling," meaning they comprise a positive density of all edges in $\mathbb{E}^d$, or zero-density, in which the dimensionality of the interface is strictly less than the dimension $d$. Ground states are called *incongruent* if they differ by a space-filling interface [28, 29].

Interfaces can also differ by how their energies scale with volume. The energy might diverge (though not monotonically) as one examines interfaces contained within increasingly larger volumes, or it might remain $O(1)$, independent of the volume considered. We will denote the former as a "high-energy interface" and the latter as a "low-energy interface."

An excitation above the ground state is any spin configuration obtained by overturning one or more spins in the ground state (while leaving an infinite subset of spins in the original ground state intact); therefore, an interface is the boundary of an excitation. We are primarily interested in excitations consisting of overturning droplets of large, or possibly infinite, size; because an interface is the boundary of such an excitation, the energy of the excitation is simply twice the interface energy. An excitation above a ground state may itself be a new ground state (this would require the excitation to involve overturning an infinite number of spins such that Equation 2 remains satisfied). Indeed, as proven elsewhere [9], an excitation having a space-filling interface with the original ground state may generate a new ground state entirely.

With this in mind, we present the four low-temperature spin glass scenarios in Table 1, which illustrates their various relationships (and clarifies why we consider these four scenarios together).

As shown elsewhere [9], the existence of space-filling interfaces in the first row scenarios (RSB and chaotic pairs) implies the presence of multiple GSPs, whereas droplet-scaling and TNT both predict a single GSP [9, 25, 26, 28, 29].

Remarks on Table 1. The droplet-scaling scenario predicts a broad distribution of (free) energies for a minimal energy compact droplet of diameter $O(L)$, with a characteristic energy growing as $L^\theta$ with $\theta > 0$ in dimensions where a low-temperature spin glass phase is present. The distribution is such that there exist droplets of $O(1)$ energy on large length scales, but these appear with a probability falling off as $L^{-\theta}$ as $L \to \infty$. In contrast, both the RSB and TNT scenarios require droplets with $O(1)$ energy to appear with positive probability bounded away from 0 on all length scales. Thus, the droplet-scaling scenario is shown in the second column of Table 1.

We now focus on the concepts of flexibility and critical droplets, which were introduced by Newman et al. [30, 31] and whose properties were described extensively in [24] (see also [26, 32]). Here, we only summarize their main features. We first provide some definitions (all with respect to some fixed coupling realization $J$):

**Definition 2.1:** (Newman et al. [24]) Consider the GSP $\sigma_L$ for the EA Hamiltonian (Equation 1) on a finite-volume $\Lambda_L$ with boundary conditions chosen independently of $J$ (for specificity, we always use periodic boundary conditions (PBCs) in this paper). Choose an edge $b_{xy} = \langle x,y\rangle$ with $x,y \in \Lambda_L$, and consider all closed

TABLE 1 Four scenarios described in the text for the low-temperature phase of the EA model, categorized in terms of interface geometry (rows) and energetics (columns). The column headings describe the energy scaling along the interface of the minimal long-wavelength excitations above the ground state predicted by each. Adapted from Figure 1 of [23].

| | Low-energy | High-energy |
|---|---|---|
| Space-filling | RSB | Chaotic pairs |
| Zero-density | TNT | Droplet-scaling |

surfaces in the dual-edge lattice $\mathbb{E}_L^*$, which includes the dual edge $b_{xy}^*$. From Equation 2 and the continuity of the couplings, these all have distinct positive energies. There then exists a closed-surface $\partial D(b_{xy}, \sigma_L)$, passing through $b_{xy}^*$, with *least* energy in $\sigma_L$. We call $\partial D(b_{xy}, \sigma_L)$ the *critical droplet boundary* of $b_{xy}$ in $\sigma_L$ and the set of spins $D(b_{xy}, \sigma_L)$ enclosed by $\partial D(b_{xy}, \sigma_L)$ the *critical droplet* of $b_{xy}$ in $\sigma_L$.

Remarks. Critical droplets are defined with respect to edges rather than associated couplings to avoid confusion, given that we often vary the coupling value associated with specific edges, while the edges themselves are fixed, geometric objects.

We define the energy $E\left(D\left(b_{xy}, \sigma_L\right)\right)$ of the critical droplet of $b_{xy}$ in $\sigma_L$ to be the energy of its boundary as given by Equation 2:

$$E\left(D\left(b_{xy}, \sigma_L\right)\right) = \sum_{<x,y> \in \partial D\left(b_{xy}, \sigma_L\right)} J_{xy}\sigma_x\sigma_y. \tag{3}$$

**Definition 2.2:** (Newman et al. [24]) The *critical value* of the coupling $J_{xy}$ associated with $b_{xy}$ in $\sigma_L$ is the value of $J_{xy}$, where $E\left(D(b_{xy}, \sigma_L)\right) = 0$, while all other couplings in $J$ are held fixed.

We next define the *flexibility* $f(J_{xy}, \sigma_L)$:

**Definition 2.3:** (Newman et al. [24]) Let $J_{xy}$ be the value of the coupling assigned to the edge $b_{xy}$ in coupling realization $J$ and $J_c(b_{xy}, \sigma_L)$ be the critical value of $b_{xy}$ in $\sigma_L$. We define the flexibility $f(b_{xy}, \sigma_L)$ of $b_{xy}$ in $\sigma_L$ to be $f(b_{xy}, \sigma_L) = |J_{xy} - J_c(b_{xy})|$.

Remarks. The critical value $J_c$ of an edge $b_{xy}$ with coupling value $J_{xy}$ is determined by all couplings in $J$, *except* $J_{xy}$. Because couplings are chosen independently from $\nu(dJ_{xy})$, it follows that the value $J_{xy}$ is *independent* of $J_c$. Therefore, given the continuity of $\nu(dJ_{xy})$, there is zero probability in a ground state that any coupling has exactly zero flexibility.

It follows from the definitions above and Equation 3 that

$$f\left(b_{xy}, \sigma_L\right) = E\left(D\left(b_{xy}, \sigma_L\right)\right).$$

Therefore, couplings which share the same critical droplet have the same (strictly positive) flexibility.

A rigorous definition of critical droplets and flexibilities within infinite-volume ground states requires use of the excitation metastate, whose definition and properties are presented in [26, 30, 31, 33]. Here, we simply note that finite-volume critical droplets and their associated flexibilities converge with their properties preserved in the infinite-volume limit, for reasons presented in [24]. This result would be trivial if all critical droplets in infinite-volume ground states were finite. However, it could also be that critical droplets can be infinite in extent in one or more directions, in which case metastates can be used to define such unbounded critical droplets which enclose an infinite subset of spins: they are the infinite-volume limits of critical droplets in finite-volume ground states.

## 3 Classification of critical droplets

In [24], critical droplets in infinite-volume ground states were classified according to the size of their boundary $\partial D(b_{xy}, \sigma)$, which is the relevant factor in associating the presence of a given type of critical droplet with one of the scenarios in Table 1. We simplify the nomenclature used in that paper by focusing on three different kinds of critical droplets. Let $|\partial D(b_{xy}, \sigma)|$ denote the number of edges in the critical droplet boundary. A *finite* critical droplet is one in which $|\partial D(b_{xy}, \sigma)| < \infty$; in two and more dimensions, this implies that the critical droplet $D(b_{xy}, \sigma)$ itself consists of a finite set of spins and thus can be completely contained within some finite volume. (A $1D$ chain is an exception: here, the critical droplet boundary of any edge consists of that edge alone, but the associated critical droplet consists of a semi-infinite chain of spins.) If these are the only type of critical droplets present, then the distribution of their sizes becomes important in answering fundamental questions involving edge disorder chaos and ground-state structure [26]. It is not hard to show that in any dimension, an EA ground state must contain at least a positive density of edges with finite critical droplets (whereas in $1D$, this is the case for *all* edges).

There are two kinds of critical droplets with $|\partial D(b_{xy}, \sigma)| = \infty$. The first class includes those with infinite boundary $\partial D(b_{xy}, \sigma)$ having a lower dimensionality than the space dimension $d$; that is, the critical droplet boundary is infinite but zero-density in $\mathbb{E}^d$. We refer to these as zero – density critical droplets (ZDCDs). (a finite critical droplet boundary also has zero density in $\mathbb{E}^d$, but we reserve the term "ZDCD" to apply only to critical droplets with an infinite boundary.)

Finally, there is the possibility that there exist infinite number of critical droplets whose boundary has dimension $d$, i.e., $\partial D(b_{xy}, \sigma)$ comprises a positive density of edges in $\mathbb{E}^d$. We refer to these as *space-filling* critical droplets (SFCDs). These critical droplets have boundaries that pass within a distance $O(1)$ of any site in $\mathbb{Z}^d$; i.e., the closest distance from any site in $\mathbb{Z}^d$ to $\partial D(b_{xy}, \sigma)$ is essentially independent of the location of the site.

Because our ground states are chosen from the zero-temperature PBC metastate (denoted $\kappa_J$), we can adapt a result from [25, 34, 35], which is described below:

**Theorem 3.1:** Let $\sigma$ denote an infinite-volume spin configuration. Then, for almost every $(J, \sigma)$ pair at zero temperature (which restricts the set of $\sigma$s to ground states corresponding to particular coupling realizations $J$), and for any type of critical droplet (finite, zero-density, or positive-density), either a positive density of edges in $\sigma$ has a critical droplet of that type or else no edges do.

The method of proof of this theorem is essentially identical to that used in [25, 35] and so will be omitted here. The conclusion is that there is zero probability that a ground state $\sigma$ chosen from $\kappa_J$ has a (finite or infinite) set of edges with zero density in $\mathbb{E}^d$ and has SFCDs (or finite critical droplets or ZDCDs).

# 4 Critical droplets and replica symmetry breaking

In [24], it was shown that there is a close connection between critical droplets and the four scenarios shown in Table 1. However, the results obtained were incomplete for the most prominent of the four scenarios, namely, replica symmetry breaking. In particular, it was proven there that the existence of SFCDs was a sufficient condition for some pairs of incongruent ground states to be separated by space-filling low-energy interfaces, hereafter referred to simply as "RSB interfaces" in accordance with Table 1. However, they were not shown to be necessary. This paper aimed to complete the correspondence between critical droplets and spin glass scenarios by demonstrating that the presence of SFCDs is not only sufficient but also a necessary condition for RSB interfaces to be present.

## 4.1 Sufficient condition

We first discuss the sufficient condition, which was derived in [24] as Theorem 8.2.

**Theorem 4.1:** (Newman et al. [24]). If a GSP $\sigma$ chosen from $\kappa_J$ has a positive fraction of edges with SFCDs, then $\sigma$ will have an RSB interface with one or more other GSPs in $\kappa_J$.

We reproduce the proof from reference [24] below.

Proof. In each finite-volume $\Lambda_L$, an arbitrary edge was chosen uniformly at random within $\mathbb{E}_L$ (the edge set restricted to $\Lambda_L$), and the excited-state $\tau_L$ generated by flipping its critical droplet was considered (with $J$ remaining fixed).

By assumption, the procedure defined above has a positive probability of generating a positive-density critical droplet, in which case the size of the interface boundary between $\tau_L$ and $\sigma_L$ scales as $L^d$. By the usual compactness arguments, the set of interfaces between the $\tau_L$s and $\sigma_L$s will converge to limiting space-filling interfaces between $\sigma$ and $\tau$, the infinite-volume spin configurations to which $\sigma_L$ and $\tau_L$ converge along one or more subsequences of $\Lambda_L$s. By construction, the energy of the interface in any volume is twice the flexibility of the chosen edge and must decrease with $L$, so in the infinite-volume limit, the energy of the generated interface between $\tau$ and $\sigma$ remains $O(1)$ in any finite-volume subset of $\mathbb{Z}^d$.

Using this procedure, one such edge $b_1$ was chosen in $\mathbb{E}_L$, which has an SFCD in $\sigma_L$. By definition, the critical droplet is the lowest-energy droplet generated by changing an edge's coupling value past its critical value. Then, Equation 2 is satisfied in $\tau_L$ for all closed contours or surfaces, *except* those passing through $b_1$. Next, a fixed cube (a "window") centered at the origin whose edge $w$ satisfies $1 \ll w \ll L$ was considered. Because $b_1$ is chosen uniformly at random within $\Lambda_L$, it will move outside any fixed window with probability approaching one as $L \to \infty$; therefore, Equation 2 will be satisfied within any fixed window for $\tau$ itself. Consequently, $\tau$ is also an infinite-volume GSP of the Hamiltonian (Equation 1) with a positive-density low-energy interface with $\sigma$. ⋄

## 4.2 Necessary condition

In [24], it was shown that a necessary condition for the existence of RSB interfaces was the presence of at least one of two kinds of edges. The first of these consists of edges having SFCDs, and the second includes edges without SFCDs, but which lie in the critical droplet boundary of a positive density (in $\mathbb{E}^d$) of other edges. Next, we show that the second kind of edge is not needed and the presence of SFCDs is by itself a necessary condition. To do this, we use the concept of a metastate; an extensive introduction and review can be found in [12]. Here, we simply note that a metastate is a probability measure on the thermodynamic states of the system. Two different constructions can be found in [20, 36]. Without reference to various constructions, a metastate satisfies three properties: first, it is supported solely on the thermodynamic states of a given Hamiltonian generated through an infinite sequence of volumes with prespecified boundary conditions (such as periodic, free, or fixed). Second, it satisfies the property of coupling covariance, meaning that the set of thermodynamic states in the support of the metastate does not change when any finite set of couplings are varied. That is, correlations in the thermodynamic states may change, but every thermodynamic state in the metastate is mapped continuously to a new one as the couplings vary; no thermodynamic states flow into or out of the metastate under a finite change in couplings. Third, the metastate satisfies translation covariance, that is, a uniform lattice shift does not affect the metastate properties.

Using the properties of metastates, Arguin et al. [37] proved the following result for the EA Ising model:

**Theorem 4.2:** [37]. An edge correlation function $\langle \sigma_x \sigma_y \rangle$, which differs with positive probability in two distinct metastates $\kappa_1$ and $\kappa_2$ was assumed. A thermodynamic state $\Gamma_1$ with the support of $\kappa_1$ and similarly a thermodynamic state $\Gamma_2$ with the support of$\kappa_2$ was chosen. $F_L(\Gamma_1, \Gamma_2)$ denoted the free energy difference between $\Gamma_1$ and $\Gamma_2$ within the restricted volume $\Lambda_L \in \mathbb{Z}^d$. Then, there is a constant $c > 0$ such that the variance of $F_L(\Gamma, \Gamma')$ with respect to varying the couplings inside $\Lambda_L$ satisfies

$$\mathrm{Var}\left(F_L(\Gamma, \Gamma')\right) \geq c|\Lambda_L|. \tag{4}$$

In [34, 35], the authors extended these ideas to a new kind of metastate called the *restricted metastate*. The idea behind restricted metastates is to start with a conventional metastate, which was constructed using an infinite sequence of volumes with PBCs ($\kappa_J$). Next, a pure state (call it $\omega$) randomly from $\kappa_J$ was chosen, and then only those pure states in $\kappa_J$ whose edge overlap falls within a narrow prespecified range were retained. The edge overlap between two Gibbs states $\alpha$ and $\alpha'$ is defined to be

$$q^{(e)}_{\alpha\alpha'} = \lim_{L\to\infty} \frac{1}{d|\Lambda_L|} \sum_{\langle xy \rangle \in E_L} \langle \sigma_x \sigma_y \rangle_\alpha \langle \sigma_x \sigma_y \rangle_{\alpha'}. \tag{5}$$

where $E_L$ denotes the edge set within $\Lambda_L$. This will generate a non-trivial metastate if $\kappa_J$ contains multiple "incongruent" pure states as predicted by RSB, i.e., pairs of pure states whose edge overlap is strictly smaller than their self-overlap. By choosing different prespecified overlaps, one can construct different restricted metastates that satisfy the conditions of Theorem 4.2, leading to the conclusion that the variance of free energy fluctuations increases linearly with the volume considered.

However, this can be done (so far) only at positive temperature because of the requirement of coupling covariance. It was shown in [35] (Lemma 4.1) that at positive temperature $q^{(e)}_{\alpha\alpha'}$ was invariant

with respect to a finite change in couplings. However, it is not necessarily the case that this is true for ground states because of the possibility of the existence of SFCDs. But it is also clear from Equation 5 that if SFCDs do not exist, then any finite change in couplings can affect only a zero density of edge correlations $\sigma_x\sigma_y$ (with $x$ and $y$ nearest neighbors) in either $\alpha$ or $\alpha'$, now understood to refer to infinite-volume ground states. In this case, $q^{(e)}_{\alpha\alpha'}$ again remains invariant under any finite change in couplings, coupling covariance is satisfied, and Theorem 4.2 can now be applied.

Now if RSB interfaces exist, then there must be ground states in the support of $\kappa_J$, which are mutually incongruent. Moreover, the magnitude of the energy of an interface (as measured from either $\alpha$ or $\alpha'$) in $\Lambda_L$ equals half the energy difference between $\alpha$ and $\alpha'$ inside $\Lambda_L$. But, as shown in Equation 4, the interface energy between $\alpha$ and $\alpha'$—or any other pair of ground states chosen from $\kappa_J$—scales with $L$ (typically as $L^{d/2}$); see also Proposition 6.1 in [36]. The conclusion is that no pair of ground states in the support of $\kappa_J$ can differ by an RSB interface if SFCDs exist. We have therefore proved the main new result of this paper:

**Theorem 4.3:** If ground states in the support of the PBC metastate $\kappa_J$ have no edges with SFCDs, then RSB interfaces between two ground states are absent in the metastate.

Following the discussion in Section 12 of [35], we also have the following corollary:

**Corollary 4.4:** If ground states in the support of the two-dimensional zero-temperature PBC metastate $\kappa_J$ have no edges with SFCDs, then the metastate is supported on a single pair of spin-reversed ground states.

## 5 Discussion

Replica symmetry breaking predicts that there exist space-filling, low-energy interfaces between ground states in three and higher dimensions. We have shown that this prediction is equivalent to the presence of SFCDs for a positive density of edges in $\mathbb{E}^d$ in a typical ground state; that is, the presence of SFCDs is both a necessary and sufficient condition for the appearance of RSB interfaces. A stronger conclusion can be drawn in two dimensions, where ground state multiplicity relies on SFCDs: if they are absent, the zero-temperature PBC metastate $\kappa_J$ is supported on a single pair of spin-reversed ground states.

Where does this leave the other three scenarios appearing in Table 1? Like RSB, the chaotic pair scenario also predicts the appearance of multiple incongruent ground states separated by space-filling interfaces, but unlike RSB, the interface energy in chaotic pairs scales with $L$. To address this scenario, we require the following quantities, introduced in [24]. Let $K^*(b,\sigma)$ denote the number of edges in $\mathbb{E}^d$ whose critical droplet boundaries in ground-state $\sigma$ pass through the edge $b$. Then, for $k = 1,2,3,\ldots$, $P(k,\sigma)$ is defined to be the fraction of edges $b \in \mathbb{E}^d$ such that $K^*(b,\sigma) = k$, and let

$$E_\sigma[K^*] = \sum_{k=1}^{\infty} k\, P(k,\sigma). \tag{6}$$

That is, $E_\sigma[K^*]$ is the average number of edges whose critical droplet boundaries a typical edge belongs to in the GSP $\sigma$. Using results from this paper, Equation 6, and [24], we conclude that if SFCDs are absent and (a positive fraction of) ground states in $\kappa_J$ are characterized by $E_\sigma[K^*] = \infty$, then the chaotic pair scenario should hold.

It follows that neither RSB nor chaotic pairs will hold if $E_\sigma[K^*] < \infty$, which follows if $P(k,\sigma)$ falls off faster than $k^{-(2+\varepsilon)}$ for any $\varepsilon > 0$ as $k \to \infty$. If this is the case, then $\kappa_J$ is supported on a single pair of spin-reversed ground states and either droplet-scaling or TNT should hold.

## Data availability statement

The original contributions presented in the study are included in the article/Supplementary Material; further inquiries can be directed to the corresponding author.

## Author contributions

CN: conceptualization, formal analysis, investigation, validation, writing–original draft, and writing–review and editing. DS: conceptualization, formal analysis, investigation, validation, writing–original draft, and writing–review and editing.

## Funding

The author(s) declare no that financial support was received for the research, authorship, and/or publication of this article.

## Acknowledgments

The authors thank the two reviewers for their comments on an earlier version, which helped clarify parts of this paper.

## Conflict of interest

The authors declare that the research was conducted in the absence of any commercial or financial relationships that could be construed as a potential conflict of interest.

## Publisher's note

# References


1. Edwards S, Anderson PW. Theory of spin glasses. *J Phys F* (1975) 5:965–74. doi:10.1088/0305-4608/5/5/017

2. Parisi G. Infinite number of order parameters for spin-glasses. *Phys Rev Lett* (1979) 43:1754–6. doi:10.1103/physrevlett.43.1754

3. Parisi G. Order parameter for spin-glasses. *Phys Rev Lett* (1983) 50:1946–8. doi:10.1103/physrevlett.50.1946

4. Mézard M, Parisi G, Sourlas N, Toulouse G, Virasoro M. Nature of the spin-glass phase. *Phys Rev Lett* (1984) 52:1156–9. doi:10.1103/physrevlett.52.1156

5. Mézard M, Parisi G, Sourlas N, Toulouse G, Virasoro M. Replica symmetry breaking and the nature of the spin glass phase. *J Phys (Paris)* (1984) 45:843–54. doi:10.1051/jphys:01984004505084300

6. Mézard M, Parisi G, Virasoro MA, editors. *Spin glass theory and beyond*. Singapore: World Scientific (1987).

7. Marinari E, Parisi G, Ruiz-Lorenzo JJ, Ritort F. Numerical evidence for spontaneously broken replica symmetry in 3D spin glasses. *Phys Rev Lett* (1996) 76:843–6. doi:10.1103/physrevlett.76.843

8. Marinari E, Parisi G, Ricci-Tersenghi F, Ruiz-Lorenzo JJ, Zuliani F. *J Stat Phys* (2000) 98:973–1074. doi:10.1023/a:1018607809852

9. Newman CM, Stein DL. *J Stat Phys* (2002) 106:213–44. doi:10.1023/a:1013128314054

10. Newman CM, Stein DL. Ordering and broken symmetry in short-ranged spin glasses. *Cond Mat* (2003) 15:R1319–64. doi:10.1088/0953-8984/15/32/202

11. Read N. Short-range Ising spin glasses: the metastate interpretation of replica symmetry breaking. *Phys Rev E* (2014) 90:032142. doi:10.1103/physreve.90.032142

12. Newman CM, Read N, Stein DL In: P Charbonneau, E Marinari, M Mézard, G Parisi, F Ricci-Tersenghi, G Sicuro, et al. editors *Spin glass theory and far beyond: replica symmetry breaking after 40 years*. Singapore: World Scientific (2023). p. 697–718.

13. McMillan WL. Scaling theory of Ising spin glasses. *J Phys C* (1984) 17:3179–87. doi:10.1088/0022-3719/17/18/010

14. Bray AJ, Moore MA. Critical behavior of the three-dimensional Ising spin glass. *Phys Rev B* (1985) 31:631–3. doi:10.1103/physrevb.31.631

15. Bray AJ, Moore MA. Chaotic nature of the spin-glass phase. *Phys Rev Lett* (1987) 58:57–60. doi:10.1103/physrevlett.58.57

16. Fisher DS, Huse DA. Ordered phase of short-range ising spin-glasses. *Phys Rev Lett* (1986) 56:1601–4. doi:10.1103/physrevlett.56.1601

17. Fisher DS, Huse DA. Equilibrium behavior of the spin-glass ordered phase. *Phys Rev B* (1988) 38:386–411. doi:10.1103/physrevb.38.386

18. Marinari E, Parisi G. Effects of changing the boundary conditions on the ground state of Ising spin glasses. *Phys Rev B* (2000) 62:11677–85. doi:10.1103/physrevb.62.11677

19. Palassini M, Young AP. Nature of the spin glass state. *Phys Rev Lett* (2000) 85:3017–20. doi:10.1103/physrevlett.85.3017

20. Newman CM, Stein DL. Spatial inhomogeneity and thermodynamic chaos. *Phys Rev Lett* (1996) 76:4821–4. doi:10.1103/physrevlett.76.4821

21. Newman CM, Stein DL. Metastate approach to thermodynamic chaos. *Phys Rev E* (1997) 55:5194–211. doi:10.1103/physreve.55.5194

22. Newman CM, Stein DL. *Mathematics of spin glasses and neural networks*. Boston: Birkhauser (1998). p. 243–87.

23. Newman CM, Stein DL. *Ann. Henri poincaré, suppl. 1 4* (2003). p. S497.

24. Newman CM, Stein DL. Ground-state stability and the nature of the spin glass phase. *Phys Rev E* (2022) 105:044132. doi:10.1103/physreve.105.044132

25. Newman CM, Stein DL. Interfaces and the question of regional congruence in spin glasses. *Phys Rev Lett* (2001) 87:077201. doi:10.1103/physrevlett.87.077201

26. Arguin L-P, Newman CM, Stein DL. A relation between disorder chaos and incongruent states in spin glasses on $Z^d$. *Commun Math Phys* (2019) 367:1019–43. doi:10.1007/s00220-019-03418-3

27. de Almeida JRL, Thouless DJ. Stability of the Sherrington-Kirkpatrick solution of a spin glass model. *J Phys A* (1978) 11:983–90. doi:10.1088/0305-4470/11/5/028

28. Huse DA, Fisher DS. Pure states in spin glasses. *J Phys A* (1987) 20:L997–L1003. doi:10.1088/0305-4470/20/15/012

29. Fisher DS, Huse DA. Absence of many states in realistic spin glasses. *J Phys A* (1987) 20:L1005–10. doi:10.1088/0305-4470/20/15/013

30. Newman CM, Stein DL. Nature of ground state incongruence in two-dimensional spin glasses. *Phys Rev Lett* (2000) 84:3966–9. doi:10.1103/physrevlett.84.3966

31. Newman CM, Stein DL. *Commun Math Phys* (2001) 224:205–18. doi:10.1007/pl00005586

32. Arguin L-P, Newman CM, Stein DL. In: *In and out of equilibrium 3: celebrating vladas sidoravicius* ME Vares, R Fernandez, LR Fontes, CM Newman, editors. Cham: Birkhäuser (2021). p. 17–25.

33. Arguin L-P, Damron M, Newman CM, Stein DL. Uniqueness of ground states for short-range spin glasses in the half-plane. *Commun Math Phys* (2010) 300:641–57. doi:10.1007/s00220-010-1130-8

34. Newman CM, Stein DL. Overlap structure and free energy fluctuations in short-range spin glasses. *J Phys A : Math Theor* (2024) 57:11LT01. doi:10.1088/1751-8121/ad2b87

35. Newman CM, Stein DL, (2024), arXiv:2407.17506.

36. Aizenman M, Wehr J. Rounding effects of quenched randomness on first-order phase transitions. *Commun Math Phys* (1990) 130:489–528. doi:10.1007/bf02096933

37. Arguin L-P, Newman CM, Stein DL, Wehr J. Fluctuation bounds for interface free energies in spin glasses. *J Stat Phys* (2014) 156:221–38. doi:10.1007/s10955-014-1009-8

frontiers | Frontiers in Physics

TYPE Review
PUBLISHED 03 December 2024
DOI 10.3389/fphy.2024.1447018



OPEN ACCESS

EDITED BY
Ralph Chamberlin,
Arizona State University, United States

REVIEWED BY
Ekrem Aydiner,
Istanbul University, Türkiye
Petra Jönsson,
Uppsala University, Sweden

*CORRESPONDENCE
Jennifer Sari Freedberg,
freed114@umn.edu

RECEIVED 10 June 2024
ACCEPTED 07 November 2024
PUBLISHED 03 December 2024

CITATION
Freedberg J and Dahlberg ED (2024) A brief review of spin glass magnetometry techniques.
*Front. Phys.* 12:1447018.
doi: 10.3389/fphy.2024.1447018



# A brief review of spin glass magnetometry techniques

Jennifer Freedberg* and E. Dan Dahlberg

University of Minnesota Twin Cities, School of Physics and Astronomy, Minneapolis, MN, United States

Spin glasses are inherently dynamical. Taken properly, measurements of these materials can capture their dynamics and provide a wealth of insight into the physics of the spin glass state. In this methods review, two magnetometry methods are directly compared—ac and dc. Because these measurements are taken differently, the resulting data of each method will contain different information about spin glass behavior. This review will specifically focus on how the out-of-equilibrium effects of aging, rejuvenation, and memory manifest in each of these techniques, and how to construct protocols to measure these effects. We then describe the physical significance of each type of measurement and how to interpret their results. Finally, we explicitly detail which applications are most appropriate for which method. This will help the reader select the most helpful technique to carry out their own future experiments.

KEYWORDS

**spin glass, dc magnetometry, ac magnetometry, nonequilibrium, dynamics**

## 1 Introduction

Broadly speaking, spin glass magnetometry measurements come in two "flavors," ac susceptibility, and dc magnetization. Due to the fact that spin glasses are out-of-equilibrium, it is crucial to understand how a prototypical ac and dc measurement differ from each other so that the dynamical behavior measured can be better understood. The purpose of this review is to provide insight for both types of measurements and when they are most appropriately used. This will be accomplished by introducing an ac protocol which exhibits the phenomena of aging, rejuvenation, and memory, and then briefly describing them. Analogous dc protocols will then be discussed.

Since the typical ac susceptibility measurement more easily lends itself to temperature sweeps than the typical dc measurement, this discussion will be framed from an ac perspective. The purpose of this review is to discuss spin glass magnetometry techniques, and so the focus will be on exemplifying the out-of-equilibrium dynamics seen in dc and ac experiments. Then, where it is necessary, we will point out how various pictures of spin glass behavior can be used to explain these observations.

Before introducing protocols with out-of-equilibrium effects, however, it is instructive to first show spin glass measurements without dynamics in both dc and ac settings. In a dc experiment, one can find the dynamical freezing temperature, $T_f$ by measuring the so-called "onset of irreversibility," shown in Figure 1. This is the point where a field cooled (FC) and a zero field cooled ZFC curve begin to

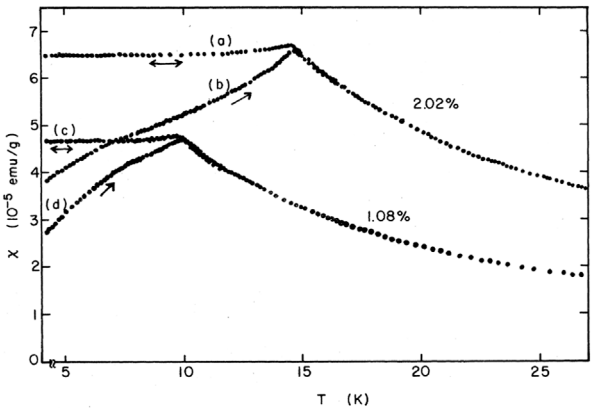


FIGURE 1
Field-cooled [(a) and (c)]/zero-field-cooled curves [(b) and (d)] as a function of temperature for 1.08 and 2.02 at% Mn. All measurements used an applied field of 5.90 Oe. This figure was reprinted with permission from [1].

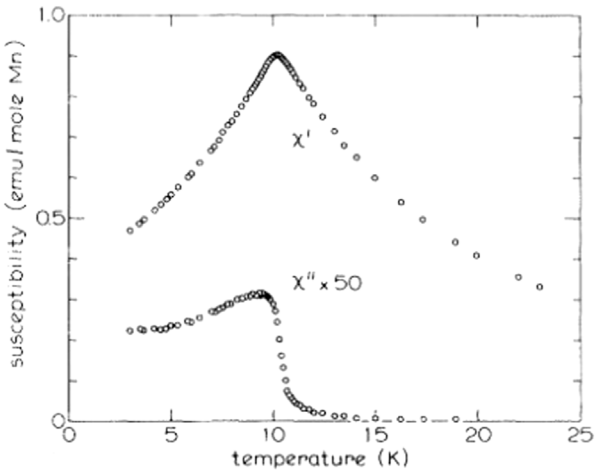


FIGURE 2
Real part of the ac susceptibility (top) and imaginary part of the ac susceptibility (bottom) as a function of temperature. The magnitude of the ac field is 0.1Oe and the measuring frequency is 234Hz. These measurements were carried out on a sample of AgMn2.98at.%. This figure was reprinted with permission from [4].

differ. This difference was experimentally measured for the first time in [1] and reproduced in Figure 1.

In a FC protocol, the spin glass is always in the presence of a field. We now consider a temperature sweep from above to below the glass transition temperature, $T_g$. Above $T_g$, the system is paramagnetic, and thus the magnetization will first increase until $T = T_g$. At this temperature, the spins will begin to freeze and stay roughly constant to the lowest temperatures measured. This FC magnetization is usually thought of as static, though in reality, it varies slightly as illustrated in [2,3]. It is then compared to a ZFC curve, which is brought to the (experimentally selected) base temperature in zero field, and then raised above $T_g$ in an applied field. This magnetization increases with temperature until $T_g$, where the spins then unfreeze. At this point, since there is no longer any frozen-in order, the system will behave exactly the same way as the FC curve.

A typical ac susceptibility measurement is shown in Figure 2. As the temperature is swept (typically from above to below the transition), the real part of the magnetic susceptibility, $\chi'$ has a cusp and the imaginary part, $\chi''$ has an inflection point. Above $T_g$, the system is a paramagnet, so there is no dissipation ($\chi'' = 0$) and the real part of the susceptibility behaves like a Curie-Weiss law. At the transition, the dissipation increases sharply as the spin glass freezes, and the in-phase response begins to decrease as spin glass order sets in. Despite the fact that $\chi''$ is typically a few orders of magnitude smaller than $\chi'$, most experimentalists studying ac susceptibility analyze $\chi''$ because the size of the out-of-equlibrium effects observed are relatively larger than in $\chi'$.

Under the application of any magnetic field, spin glasses exhibit crossover behavior, known in theory as the de Almeida-Thouless line [5]. Experimentally, the effect of an applied magnetic field is clearly demonstrated by the experiments in [6, 7]. This means that any measured transition temperature will always be a freezing temperature and not the true glass temperature, $T_g$. However, this effect can be reduced if the experimentalist selects the lowest field possible for their sample to still obtain conclusive results. For example, the applied field in Figure 1 is 5.90Oe and the amplitude of the ac field in Figure 2 is 0.1Oe. However, it is important to emphasize that experimental parameters such as applied field and cooling rate are known to change the dynamical freezing temperature [4, 8]. To properly determine the glass temperature $T_g$ as opposed to the dynamical freezing temperature $T_f$, one must conduct a scaling analysis as discussed in [4, 8].

Now, we return to measuring the dynamical effects observed in spin glasses. Due to the fact spin glass measurements are very protocol-dependent, it is imperative to have a control protocol for comparison. In a prototypical ac measurement, the sample starts above $T_g$ and is then lowered at a finite rate until some chosen base temperature is reached, for example, as shown in Figure 2. When comparing directly to protocols with aging, rejuvenation, and memory, this is called the "reference curve". To demonstrate the differences between these protocols, the temperature profile as a function of time is displayed on the left panel of Figure 3, and the resulting susceptibility is displayed on the right panel of Figure 3. In this figure, the reference curve is denoted by the teal dashed line. In a dc experiment which has multiple waiting temperatures, the measurement is compared to individual protocols which only wait at one temperature. In this case, the reference protocol is called either the "isothermal" or "native" aging curve, as can be seen in [9, 10], respectively.

## 2 Aging

A spin glass has a rugged energy landscape, meaning it possesses a large range of barrier heights corresponding to a wide range of relaxational timescales. Because the spin glass is seen to be dynamical on laboratory timescales, the barriers are expected to

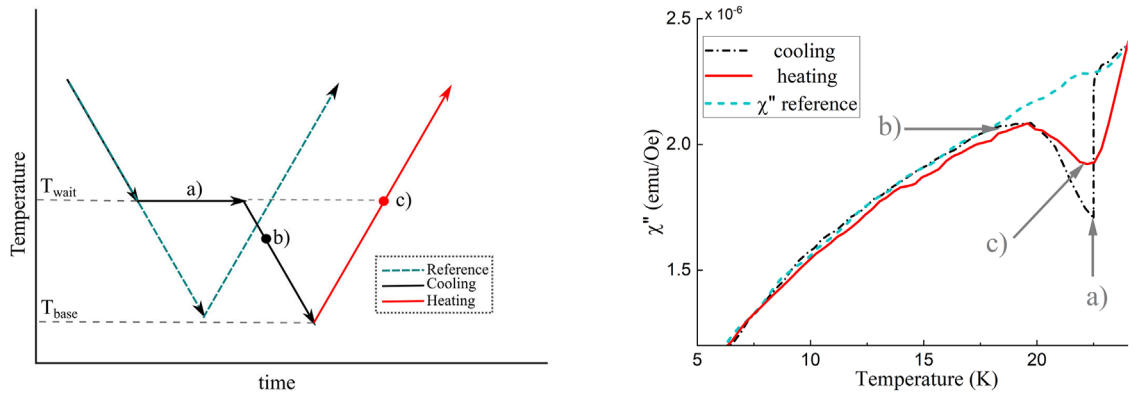


FIGURE 3
A simple waiting time protocol which exhibits aging, rejuvenation, and memory shown on the left and the resulting susceptibility shown on the right. The reference curve is shown as the dotted teal line in both cases. On both sides, the label a) corresponds to the aging, b) to rejuvenation, and c) to memory, which will be discussed later in this Review. This figure is adapted from [12].

have a height that gives rise to experimentally confirmed timescales of at least up to weeks[1].

The process of hopping over barriers will induce relaxation as the system reduces its energy in a process known as "aging". If measured in a lab, this exploration manifests as a decrease in the magnetic susceptibility, which is then attributed to the growth of the spin glass order [13, 14]. Regardless of the mechanism used to describe this growth, the community generally agrees that it grows with time spent in the spin glass state, and that this growth is very slow [13, 15, 16].

Within both the Droplet [17] and Hierarchical [18] models, aging is associated with thermal activation processes whose energy barriers are determined by the spatial size of emerging spin glass order. The larger this length scale, the higher the energy barrier. The spin glass order grows from flipping spins, which thereby induces changes to the overall magnetization [15, 19–21].

## 2.1 Measurements

Aging is the most easily measurable quantity in both ac and dc experiments. In this subsection, these methods will be juxtaposed to highlight the uses of each technique. While the measurements themselves differ based on whether or not ac or dc methods are used, there is some overarching commonality. During aging protocols, the system is brought to a waiting temperature $T_w$ and allowed to sit at this temperature for some waiting time $t_w$. As discussed above, this will give the spin glass time to explore the energy landscape.

### 2.1.1 Ac protocols

Once the reference measurement has been taken, we proceed to investigate the out-of-equilibrium effects. We begin the experiment in the same way, except instead of cooling at a continuous rate to the base temperature, cooling is stopped at an intermediate temperature, as shown by the label a) in Figure 3.

In this part of the protocol, the ac susceptibility, defined as $\chi \equiv \chi' - i\chi''$, relaxes over time in both the in-phase, $\chi'$, and out-of-phase, $\chi''$, components. This relaxation marks a departure from the reference curve, and thereby establishes the spin glass as an out-of-equilibrium system. This is the most standard type of aging experiment in ac susceptibility measurements and is depicted by the vertical drop on the right side and the flat line on the left side of Figure 3. This relaxation as a function of time is shown in Figure 4.

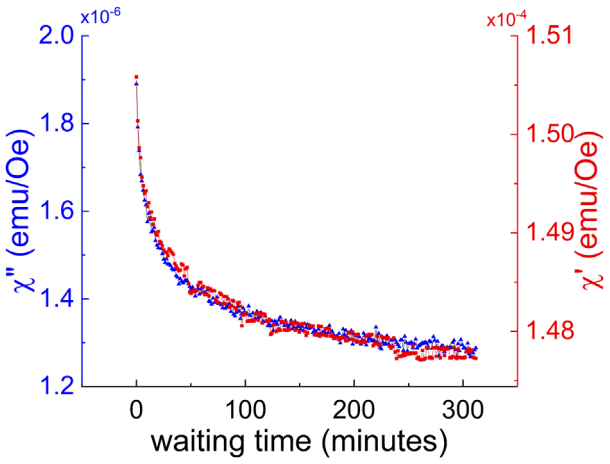


FIGURE 4
Aging as a function of time for both $\chi''$ (left) and $\chi'$ (right) in a single crystal of CuMn 7.92 at.%. The two curves are overlaid on each other and plotted on linear axes to highlight that the relaxations in either susceptibility have nearly identical form. However, by looking at the axis scale, it becomes clear that the relative change in $\chi''$ is larger than that in $\chi'$. Thus, almost all ac studies only report on $\chi''$, since the effects are stronger. The measuring field is 10 Oe with a frequency of 1 Hz. The sample is quenched to the waiting temperature $T/T_g = 0.72$, or $T = 30$ K and then aged for 200 min.

1 The longest experiment we are aware of was an unpublished result from our group at the beginning of COVID-19 lockdown taken by David C. Harrison. Even after a month of continuous measurement, aging was still seen.

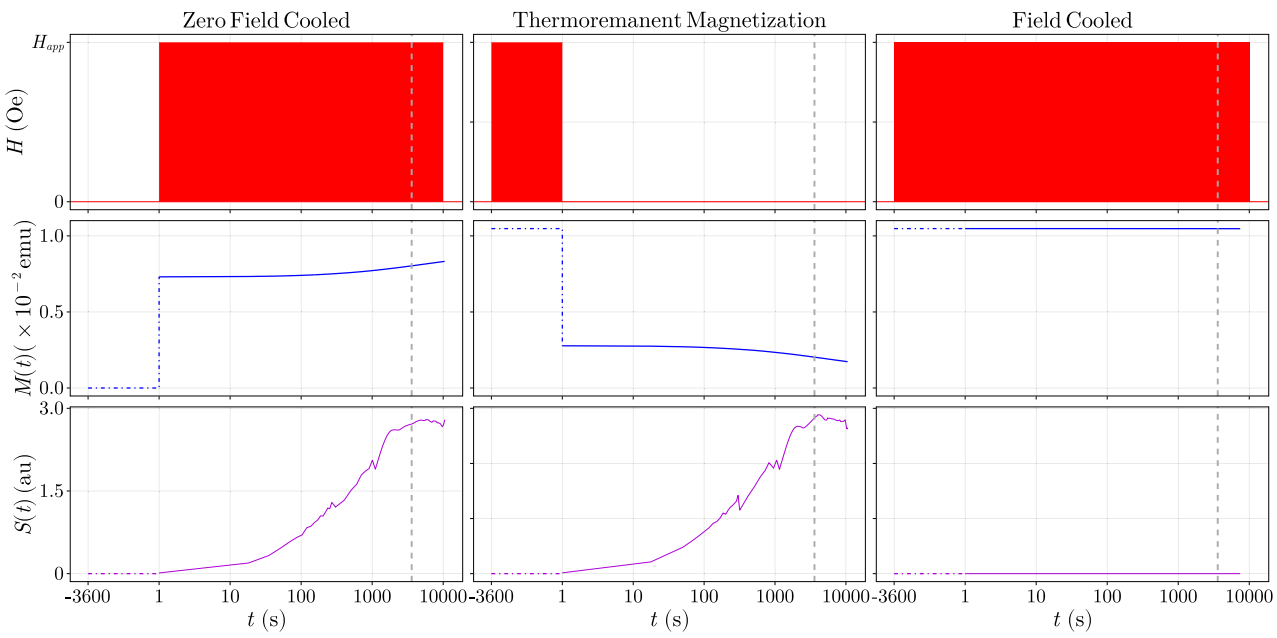


FIGURE 5
The three most common dc magnetization measurements are shown. In each protocol, an example set of data is plotted. From left to right columns, zero field cooled (ZFC), thermoremanent magnetization (TRM), and field cooled (FC). The top row indicates the external magnetic field applied as a function of time, the middle row is the magnetization as a function of time, and the bottom row is the resulting $S(t) \equiv \frac{\partial M}{\partial(\log t)}$ curve as a function of time. The positive $x$–axis is plotted on a log scale, with the time before the measurement starts (the waiting time) is plotted on a linear scale. The measurements during the waiting time are displayed to illustrate what the magnetization or $S(t)$ curves are expected to look like during this time and are denoted by the dot-dash lines. The key feature of the $S(t)$ curves is the presence of the peak $\sim t_w$. The waiting time is denoted by the vertical grey dashed lines in all nine panels of the figure. As can be seen, in both the left and center columns, the peak in $S(t)$ curves falls roughly on this dotted line. Note that in the center column, the $S(t) \to S(t) \times -1$ for visual clarity. In the rightmost column, the field cooled magnetization is shown. This figure can be found in [12]. This figure was made in the Julia programming [41] language using the Makie package for plotting [42].

By definition, ac susceptibility measurements are sensitive to the dynamic *magnetic* response of the system–that is, the measured signal is related to the number of spins responding to the ac field. In a spin glass, as the spin-glass-order grows (and more spins become frozen), the system becomes less responsive to the applied field. Thus, during an aging experiment, we measure the growth of the spin glass order through the decay of the magnetic fluctuations.

### 2.1.2 dc protocols

Measurements which utilize dc magnetometry, compared to the protocol shown in Figure 3, are most frequently taken only at a fixed temperature. A typical dc protocol has two parts–an aging portion and a measurement portion. The field can either start off, as is the case in zero -field-cooled (ZFC) measurements, or on, as is the case in thermoremanent magnetization (TRM). A schematic of these protocols is shown in Figure 5. The main difference between the two is *when* the field is applied: for a ZFC measurement, the applied magnetic field is held at 0Oe from above the glass temperature to the target temperature and then aged at that temperature. When the aging is completed, the field is applied. For the TRM measurement, the applied magnetic field is kept at some selected finite value from above the glass temperature and then maintained until the aging portion is complete, and then the applied field is removed.

There are other, more nuanced protocols, detailed in [22] which explore the effect on the spin glass order *when* a magnetic field is turned on in a variant of a TRM protocol (*i.e.*, before or after settling at the waiting temperature). For readers who are interested in learning about the history of TRM measurements in the development of the field, [23] in this collection has a comprehensive overview. However, for brevity, these will not be discussed here.

To emphasize–dc measurements have two parts, and only the first is traditionally called "aging." In Figure 5, this is denoted by the dot-dashed lines at negative times. However, when people discuss ac experiments, typically *any* time in the spin glass state is called aging. This is a subtle difference in naming conventions between the two sets of experiments which is not typically discussed.

To process dc magnetization data, the logarithmic derivative of the resulting magnetization is plotted as a function of time (traditionally on a log scale). This curve is known as $S(t) \equiv \mathrm{d}M/\mathrm{d}\log(t)$, first measured by Lundgren, Svedlindh, and Beckman [24]. It is observed that the relaxation of the magnetization displays an inflection point at approximately the waiting time ($t_w$), so $S(t)$ will be peaked at this value. The value of the peak, $t_w^{eff}$, and the width of the $S(t)$ curve are determined by many factors, such as waiting time, external magnetic field, and temperature. As a rule, $t_w^{eff}$ is interpreted as containing information about the barrier distribution. Below, we investigate why this is.

To illustrate this, we consider a TRM (ZFC) protocol. In the aging stage of the experiment, the waiting time determines the average barrier surmounted and thus the average size of a spin glass order. After aging, once the magnetic field is removed (applied), the spin glass begins to relax to zero (the FC value for

the) magnetization. If the spin glass energy landscape is made up of a distribution of Arrhenius-like barriers, then the change in magnetization as a function of time will contain information about the distribution of energy barriers of the system. If this function is peaked, the peak position will be related to the most probable barrier in the distribution [24, 25].

We then can ask why the aging portion of the experiment causes a peak in the $S(t)$. As discussed above, during aging, the spin glass order grows to some typical size. Thus, the peak in $S(t)$, a function which is a measure of the relaxation rate, will occur on the order of the typical size of spin glass order [25].

# 3 Rejuvenation

Aging occurs when the sample stays below the transition temperature for some fixed amount of time, as shown in Figures 4, 5. Of all the spin glass phenomena, it is the best understood. Rejuvenation occurs as the temperature is changed (traditionally decreased) after an aging protocol. Remarkably, as is observed in both ac and dc experiments, after some sufficient temperature difference, $\delta T$, the spin glass loses any knowledge of its aging history, and behaves afterwards as though it had never aged in the first place (see Figure 3).

Rejuvenation can occur with either positive or negative temperature shifts, and has been studied, for example, in Refs. [4, 9]. While there are differences in how rejuvenation manifests, the re-initialization of the aging process is common to both positive and negative temperature shifts. However, this Review will focus on the overall protocol, rather than the specific results obtained in each case.

In the following subsections, we investigate how rejuvenation appears in experiments, and their implications. Additionally, we briefly mention one possible mechanism for rejuvenation and reference experiments and simulations which test this model.

## 3.1 Measurements

### 3.1.1 Ac protocols

After an aging process is completed at $T_{w1}$ for $t_{w1}$, the temperature is then changed again. In Figure 3, the temperature is then decreased from $T_{w1}$. In this case, naïvely, we might expect the susceptibility to decrease with decreasing temperature, since the thermal energy (and therefore thermal fluctuations allowing us to explore the energy landscape) decreases with decreasing temperature. Indeed, this is seen in the reference curve. However, for procedures where the temperature is lowered following aging, the susceptibility *rises* back to the reference curve as if no aging occurred at all. This is known as rejuvenation. After some change in temperature, $\delta T$, the reference curve and the curve with aging and rejuvenation become the same. This effect is shown in Figure 3 in the range where $\chi''$ is increasing back to the reference curve upon cooling after aging.

In the case of a positive temperature shift (e.g., the temperature is *raised* following aging), it is traditionally more common to quench rather than heat continuously, as done in [9].

### 3.1.2 Dc protocols

From the description of aging using dc methods, it should be clear that it is difficult to develop dc protocols which study multi-temperature effects. Due to the fact that temperature sweeps in TRM or ZFC dc protocols face this challenge, there are generally two paths utilized[2].

The first way to observe rejuvenation in dc measurements is using the FC magnetization and observing differences in decays over time, as done in [2,3]. This technique is similar to ac protocols, since for this type of experiment, there is no aging time before the measurement starts. In this case, the system is quenched to the first waiting temperature $T_{w1}$ for time $t_{w1}$, then changed to the second waiting temperature $T_{w2}$ for $t_{w2}$. If, upon shifting the temperature, he aging process "restarts," rejuvenation is said to occur. Otherwise, the aging is said to be "cumulative," or "accumulative" [2, 3].

The second way to observe rejuvenation in a dc protocol is to measure $M(t, T_{w1}, T_{w2})$ from ZFC or TRM protocols and construct an $S(t)$ curve using a temperature-step protocol, as described in [3, 9, 27]. In this case, the system is quenched to the first waiting temperature $T_{w1}$ for time $t_{w1}$, then brought to a second measuring temperature $T_{w2}$ and immediately applying (or turning off) the field and measuring the ZFC (TRM) curve.

If rejuvenation has occurred, the character of the resulting $S(t)$ curve will be different than the isothermal $S(t)$ curves at the measuring temperature. The specific details of how exactly the $S(t)$ curve evolve are complicated, but very well characterized in [4, 9]. To summarize their findings briefly: if aging is cumulative, then the peak in $S(t)$ will occur at slightly larger $t_{w_{eff}}$ than that of the isothermal aging curve, corresponding to the fact that the aging at $t_{w1}$ corresponded to the growth of spin glass order at the measuring temperature. If the aging is not cumulative, then the peak in $S(t)$ will occur at smaller values of $t_{w_{eff}}$.

Note that even if the aging is not cumulative, there tend to be long "tails" in the $S(t)$ curve, meaning that, despite the fact the sample has rejuvenated, the system still contains some knowledge of its aging at $T_{w1}$. This hints at the last dynamical effect which will be discussed in this Review: memory.

It is important to note here that there is a major discrepancy seen between rejuvenation in ac and dc measurements. In ac measurements, rejuvenation appears in the susceptibility, whereas in dc measurements, rejuvenation appears in the character of $S(t)$. Both have been associated with temperature chaos [2, 10, 28, 29]. However, in ac experiments, rejuvenation tends to takes place over a few kelvin (as in Figure 3, and [9, 29]), while dc experiments measure ranges of ~0.5K, as seen in [2,3]. The reason behind this discrepancy is not well-understood.

# 4 Memory

The final step in the experiment shown in Figure 3 is to raise the temperature from the base temperature back to its starting point (both chosen by the experimentalist). In the past, it was

2 It is possible to design a protocol in other ways, such as described by the simulations in [26], but this Review will focus on the most commonly utilized protocols.

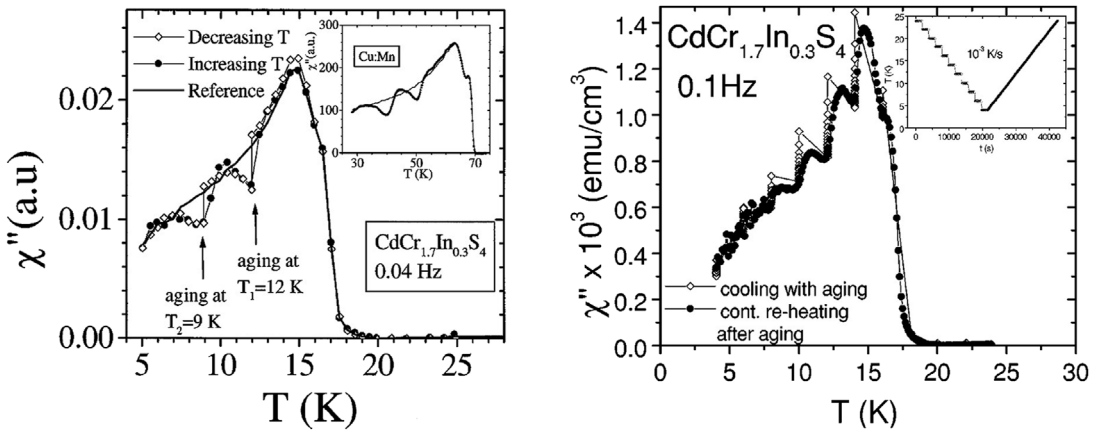


FIGURE 6
Left: the original memory experiment with two waiting temperatures (12 K and 9 K). Despite waiting at the low temperature for 40 h, the memory is still apparently perfect. The inset shows the reference (line) and heating (scatter) curves in the canonical spin glass, copper manganese. Right: A series of multiple aging steps upon cooling, leading to perfect memory upon continuous heating. The inset shows the temperature profile as a function of time. Both figures use the same insulating spin glass (although the ac frequencies are slightly different). The left figure is taken from [29] and the right figure is taken from [30].

often the case that the heating rate differed from the cooling rate such as in [30]. While commonplace, it has been recently found that the relaxational dynamics markedly changes as a function of cooling rate [31], and therefore the most controlled experiments would be where all temperature changes occur at the same rate.

Like the protocols outlined for rejuvenation, $T_{w2}$ need not be lower than $T_{w1}$. Examples of both cases are shown in [4, 9]. However, the following discussion will not focus on the specific results obtained in each case. Instead, in the following subsection, we detail how memory manifests in both ac and dc experiments, and what the signatures of these measurements tells us about the spin glass state.

## 4.1 Measurements

### 4.1.1 Ac protocols

Following the canonical protocols described in Figures 2, 6, the temperature is increased from the base temperature at a constant rate. After the temperature rises beyond the aging temperature, the spin glass has an apparent memory of its previous cooling history. Since the ac susceptibility is related to the magnitude of magnetic fluctuations, a decrease in the susceptibility relative to the reference curve indicates that the spin glass is becoming more frozen relative to the reference curve as it approaches and surpasses the waiting temperature upon heating.

A few remarkable examples of the memory effect is in Figure 6, where despite either the many temperature steps or an extremely long waiting time, memory is clearly retained upon heating. This is in contrast to the data shown in Figure 3 where, despite only aging for an hour, significant memory loss is seen. Across the literature, it can be seen that memory is often incomplete in metallic spin glasses [11, 32], but is often almost perfect in insulating spin glasses [29, 30].

### 4.1.2 Dc protocols

In a dc protocol investigating the memory effect, one completes a temperature cycling protocol. The first part of the experiment is the same as described in Section. 3.1.2. Now however, instead of simply turning on (or off) the field at the second temperature, the sample is aged again for $t_{w2}$ at $T_{w2}$. In the final step of the experiment, the sample is heated back to $T_{w1}$ and the field is applied (or removed). Because of the aging at $T_{w2}$, the $S(t)$ curve will now have two peaks. The location of these peaks can yield important information about the glassy dynamics.

In this case, it becomes clear why dc experiments need a control protocol. The control measurement is just an isothermal aging experiment for $t_{w1}$ at $T_{w1}$ or for $t_{w2}$ at $T_{w2}$, and so the $S(t)$ curves obtained from these two sets of measurements can be directly compared. One can see that if $t_{weff}$ from temperature cycling is smaller than the isothermal $t_{weff}$ for $T_{w1}$, then memory is reduced, as seen in metallic spin glasses in [9].

The double peak in the $S(t)$ curve is interesting in its own right as well. It indicates that there are two different typical length scales present in dc experiments where $T_{w1}$ and $T_{w2}$ are sufficiently separated. This has been interpreted to mean that the growth of spin glass order between the two temperatures are independent of each other. One of the proposed mechanisms to explain this is called "temperature chaos." In their 1978 paper, Bray and Moore find that a sufficiently large change in temperature will destabilize the energy landscape and cause the breakup of spin glass order [33]. While this explanation has evolved since its inception, the core idea–that the metastable state at one temperature need not be metastable at a different temperature–remains the same. Recent experiments and simulations have sought to characterize the exact nature of temperature chaos to see if this explanation can account for rejuvenation, including [2, 3, 9, 10, 30, 32, 34, 35].

The results of the ac and dc experiments, taken together, indicate that the spin glass order developed at the first waiting time somehow is preserved, despite rejuvenation. Since its discovery [29], there have

been many studies which have investigated this effect such as Refs. [9, 11, 30, 32, 35–38] to name just a few. While the details differ, a common explanation centers around the following description: as the temperature increases again, the larger regions of spin glass order which were previously frozen-in at the lower temperatures "unfreeze" and become active once more [9, 11, 30, 36, 38].

# 5 Pros and cons of each technique

The essence of spin-glass magnetometry is that the out-of-equilibrium dynamics are characterized by a dependence on two timescales. In ac experiments, these timescales are the ac frequency and the waiting time as shown in Figure 3. In dc experiments, meanwhile, the two times are the waiting time and the measuring time. Their impacts are measured using a protocol that constructs an $S(t)$ curve as shown in Figure 5. Because of the differences in how the measurements are taken, some applications are best suited for an ac measurement, while others are better suited for a dc measurement.

In spin glass research, ac susceptibility is a better tool to measure the effect of changing temperatures. In dc measurements which produce $S(t)$ curves, one cannot construct a protocol undergoing a continuous temperature sweep, because recording the magnetization is always the second step in the measurement. In either case, while temperature cycling protocols can be constructed which provide meaningful insight about the spin glass state, it is inherently more challenging in dc measurements than in ac measurements. Because of this, it is much easier to study rejuvenation and memory using ac susceptibility. Additionally, it is virtually impossible to determine the effect the cooling rate has on the evolution of the spin glass state in dc magnetometry, while this measurement is very straightforward using ac susceptibility.

On the other hand, dc magnetometry is better suited to study aging than ac susceptibility. This is because much of the dynamics in dc measurements can be wrapped up in a single physically significant number – $t_w^{eff}$. It is thus relatively simpler to characterize the many factors which affect the value of $t_w^{eff}$ such as waiting temperature, waiting time, and magnetic field. Additionally, the value of $t_w^{eff}$ is robust against experimental realities such as the change in signal which comes from simply needing to reload a sample. As such, characterizing the behavior $t_w^{eff}$ more straightforwardly allows for comparisons between quantities which are accessible in theory and simulations. This is to be contrasted with ac susceptibility measurements, where it is not as clear if a single parameter exists which captures the behavior of an aging system. Because of this, it is more difficult to quantitatively compare between ac aging curves via simulations or theory, especially since the absolute magnitude of the susceptibility depends on experimental conditions.

## 5.1 Experimental considerations

There are a few experimental parameters which are important to discuss. In ac experiments, the ac frequency must be sufficiently low to ensure that the dynamical relaxational effects are still visible. However, because the time it takes to acquire a single data point increases as frequency decreases, the experimentalist must determine the lowest reasonable frequency within their own logistical constraints. The effect of ac frequency on resulting spin glass measurements is examined in another submission to this collection [39].

The results in [7, 22], and [40] show that the time it takes to turn the magnetic field on or off affect the $S(t)$ curve like a waiting time effect would. If the time it takes to turn on the field is slow, this would introduce, in effect, a second waiting time in the experiment. Indeed, differences in the resulting character of the $S(t)$ measurements persist, even at very long waiting times. On the other hand, dc measurements taken in a constant field (FC) will not have these artifacts and thus can be performed in a standard magnetometer.

Likewise, both ac and dc experiments are affected by the fact that temperatures cannot change instantaneously, even when cooling at the fastest rate the instrument can. This also can act like another waiting time, as seen in [7, 22], and [31].

One final note: while the spin glass community at large treats ac and dc measurements as equivalent in the limit of zero frequency, this is hard to verify in practice because the types of experiments are typically conducted very differently from each other. As discussed in [31], there are large discrepancies between certain dc and ac results which indicate that the physics relating the two is not as straightforward as is typically assumed.

# Author contributions

JF: Writing–original draft, Writing–review and editing. ED: Writing–review and editing.

# Funding

The author(s) declare that financial support was received for the research, authorship, and/or publication of this article. This work was supported by the U.S. Department of Energy, Office of Basic Energy Sciences, Division of Materials Science and Engineering, under Award No. DE-SC0013599.

# Acknowledgments

The authors thank the Editors for this collection, and especially to Greg Kenning for many helpful discussions. In addition, the authors appreciate discussions with Samaresh Guchait and Ray Orbach. Finally, the authors would like to thank W. Joe Meese for his help, especially during the writing of this manuscript.

# Conflict of interest

The authors declare that the research was conducted in the absence of any commercial or financial relationships that could be construed as a potential conflict of interest.

## Publisher's note



## References

1. Nagata S, Keesom PH, Harrison HR. Low-dc-field susceptibility of CuMn spin glass. *Phys Rev B* (1979) 19:1633–8. doi:10.1103/physrevb.19.1633

2. Zhai Q, Orbach RL, Schlagel DL. Evidence for temperature chaos in spin glasses. *Phys Rev B* (2022) 105:014434. doi:10.1103/physrevb.105.014434

3. Djurberg C, Jonason K, Nordblad P. Magnetic relaxation phenomena in a cumn spin glass. *Eur Phys J B-Condensed Matter Complex Syst* (1999) 10:15–21. doi:10.1007/s100510050824

4. Mulder CAM, van Duyneveldt AJ, Mydosh JA. Frequency and field dependence of the ac susceptibility of the AuMn spin-glass. *Phys Rev B* (1982) 25:515–8. doi:10.1103/physrevb.25.515

5. de Almeida JRL, Thouless DJ. Stability of the sherrington-kirkpatrick solution of a spin glass model. *J Phys A: Math Gen* (1978) 11(5):983–90. doi:10.1088/0305-4470/11/5/028

6. Mattsson J, Jonsson T, Nordblad P, Aruga Katori H, Ito A. No phase transition in a magnetic field in the ising spin glass $fe_{0.5}$ $mn_{0.5}$ $tio_3$. *Phys Rev Lett* (1995) 74:4305–8. doi:10.1103/physrevlett.74.4305

7. Lefloch F, Hammann J, Ocio M, Vincent E. Spin glasses in a magnetic field: phase diagram and dynamics. *Physica B: Condensed Matter* (1994) 203(1):63–74. doi:10.1016/0921-4526(94)90278-x

8. Mulder CAM, van Duyneveldt AJ, Mydosh JA. Susceptibility of the CuMn spin-glass: frequency and field dependences. *Phys Rev B* (1981) 23:1384–96. doi:10.1103/physrevb.23.1384

9. Jönsson PE, Mathieu R, Nordblad P, Yoshino H, Aruga Katori H, Ito A. Nonequilibrium dynamics of spin glasses: examination of the ghost domain scenario. *Phys Rev B* (2004) 70:174402. doi:10.1103/physrevb.70.174402

10. Baity-Jesi M, Calore E, Cruz A, Fernandez LA, Gil-Narvion JM, Gonzalez-Adalid Pemartin I, et al. Temperature chaos is present in off-equilibrium spin-glass dynamics. *Nat Commun Phys* (2021) 4(1):74. doi:10.1038/s42005-021-00565-9

11. Freedberg J, Joe Meese W, He J, Schlagel DL, Dan Dahlberg E, Orbach RL. On the nature of memory and rejuvenation in glassy systems, 2023.

12. Freedberg J. *Protocol dependence of spatially inhomogeneous magnetic systems*. Conservancy University of Minnesota (2024).

13. Kisker J, Santen L, Schreckenberg M, Rieger H. Off-equilibrium dynamics in finite-dimensional spin-glass models. *Phys Rev B* (1996) 53:6418–28. doi:10.1103/physrevb.53.6418

14. Baity-Jesi M, Calore E, Cruz A, Fernandez LA, Gil-Narvion JM, Gordillo-Guerrero A, et al. Aging rate of spin glasses from simulations matches experiments. *Phys Rev Lett* (2018) 120:267203. doi:10.1103/physrevlett.120.267203

15. Lundgren L, Svedlindh P, Beckman O. Anomalous time dependence of the susceptibility in a Cu(Mn) spin glass. *J Magn Magn Mater* (1983) 31–34:1349–50. doi:10.1016/0304-8853(83)90922-8

16. Vincent E. Ageing, rejuvenation and memory: the example of spin glasses. In: M Henkel, M Pleimling, R Sanctuary, editors. *Ageing and the glass transition, number 716 in lecture notes in physics*. Springer (2007).

17. Fisher DS, Huse DA. Nonequilibrium dynamics of spin glasses. *Phys Rev B* (1988) 38:373–85. doi:10.1103/physrevb.38.373

18. Mézard M, Parisi G, Sourlas N, Toulouse G, Virasoro M. Replica symmetry breaking and the nature of the spin glass phase. *J de Physique* (1984) 45(5):843–54. doi:10.1051/jphys:01984004505084300

19. Ocio M, Alba M, Hammann J. Time scaling of the ageing process in spin-glasses: a study in csnifef 6. *J de Physique Lettres* (1985) 46(23):1101–7. doi:10.1051/jphyslet:0198500460230110100

20. Chamberlin RV. Time decay of the thermoremanent magnetization in spin-glasses as a function of the time spent in the field-cooled state. *Phys Rev B* (1984) 30:5393–5. doi:10.1103/physrevb.30.5393

21. Weissman MB, Israeloff NE, Alers GB. Spin-glass fluctuation statistics: mesoscopic experiments in Mn. *J magnetism Magn Mater* (1992) 114(1-2):87–130. doi:10.1016/0304-8853(92)90336-m

22. Zotev VS, Rodriguez GF, Kenning GG, Orbach R, Vincent E, Hammann J. Role of initial conditions in spin-glass aging experiments. *Phys Rev B* (2003) 67:184422. doi:10.1103/physrevb.67.184422

23. Kenning GG, Brandt M, Brake R, Hepler M, Tennant D. Observation of critical scaling in spin glasses below $t_c$ using the thermoremanent magnetization. *Front Phys* (2024) 12. This reference will be furnished when the manuscript has been posted. doi:10.3389/fphy.2024.1443298

24. Lundgren L, Svedlindh P, Beckman O. Experimental indications for a critical relaxation time in spin-glasses. *Phys Rev B* (1982) 26:3990–3. doi:10.1103/physrevb.26.3990

25. Joh YG, Orbach R, Wood GG, Hammann J, Vincent E. Extraction of the spin glass correlation length. *Phys Rev Lett* (1999) 82:438–41. doi:10.1103/physrevlett.82.438

26. Baity-Jesi M, Calore E, Cruz A, Fernandez LA, Gil-Narvion JM, Gonzalez-Adalid Pemartin I, et al. Memory and rejuvenation effects in spin glasses are governed by more than one length scale. *Nat Phys* (2023) 19:978–85. doi:10.1038/s41567-023-02014-6

27. Leif Ec Lundgren . Non-equilibrium dynamics in spin glasses. In: *AIP conference proceedings*, 256. American Institute of Physics (1992). p. 407–16.

28. Miyashita S, Vincent E. A microscopic mechanism for rejuvenation and memory effects in spin glasses. *Eur Phys J B* (2001) 22:203–11. doi:10.1007/s100510170128

29. Jonason K, Vincent E, Hammann J, Bouchaud JP, Nordblad P. Memory and chaos effects in spin glasses. *Phys Rev Lett* (1998) 81:3243–6. doi:10.1103/physrevlett.81.3243

30. Jean-Philippe B, Vincent D, Hammann J, Vincent E. Separation of time and length scales in spin glasses: temperature as a microscope. *Phys Rev B* (2001) 65:024439. doi:10.1103/physrevb.65.024439

31. Freedberg J, Schlagel DL, Orbach RL, Dan Dahlberg E. Investigating the interplay between aging and rejuvenation in spin glasses. (2024).

32. Jönsson PE, Yoshino H, Nordblad P. Symmetrical temperature-chaos effect with positive and negative temperature shifts in a spin glass. *Phys Rev Lett* (2002) 89:097201. doi:10.1103/physrevlett.89.097201

33. Bray AJ, Moore MA. Replica-symmetry breaking in spin-glass theories. *Phys Rev Lett* (1978) 41:1068–72. doi:10.1103/physrevlett.41.1068

34. Berthier L, Young AP. Temperature cycles in the heisenberg spin glass. *Phys Rev B* (2005) 71:214429. doi:10.1103/physrevb.71.214429

35. Sasaki M, Dupuis V, Bouchaud J-P, Vincent E. Deviations from perfect memory in spin glass temperature cycling experiments. *Eur Phys J B* (2002) 29:469–79. doi:10.1140/epjb/e2002-00327-2

36. Paga I, He J, Baity-Jesi M, Calore E, Cruz A, Fernandez LA, et al. Quantifying memory in spin glass. *Unpublished, reference be added by Publ*, 2023. doi:10.48550/arXiv.2307.02224

37. Dupuis V, Bert F, Bouchaud J-P, Hammann J, Ladieu F, Parker D, et al. Aging, rejuvenation and memory phenomena in spin glasses. *Pramana J Phys* (2005) 64:1109–19. doi:10.1007/bf02704172

38. Jonason K, Nordblad P, Vincent E, Hammann J, Bouchaud J-P. Memory interference effects in spin glasses. *Eur Phys J B* (2000) 13(99):99–105. doi:10.1007/s100510050014

39. Pradhan S, Harrison D, Kenning G, Schlagel DL, Guchait S. Investigation of experimental signatures of spin glass transition temperature. *Front Phys* (2024) Remaining information will be furnished once this manuscript is published. doi:10.3389/fphy.2024.1482907

40. Jean-Philippe Bouchaud. Weak ergodicity breaking and aging in disordered systems. *J de Physique* (1992) 2(9):1705–13. doi:10.1051/jp1:1992238

41. Bezanson J, Edelman A. Julia: A fresh approach to numerical computing. *SIAM Review* (2017) 59 (1), 65–98. doi:10.1137/141000671

42. Simon D, Julius K. Flexible high-performance data visualization for Juli. *J Open Source Software* (2021) 6 (65), 3349. doi:10.21105/joss.03349

frontiers | Frontiers in Physics

TYPE Original Research
PUBLISHED 13 December 2024
DOI 10.3389/fphy.2024.1482907



OPEN ACCESS

EDITED BY
Stefan Boettcher,
Emory University, United States

REVIEWED BY
Clodoaldo Irineu Levartoski de Araujo,
Universidade Federal de Viçosa, Brazil
Daniel Barci,
Rio de Janeiro State University, Brazil

*CORRESPONDENCE
Sahil Pradhan,
sahil.pradhan@bison.howard.edu

RECEIVED 19 August 2024
ACCEPTED 30 October 2024
PUBLISHED 13 December 2024

CITATION
Pradhan S, Harrison D, Kenning G, Schlagel DL and Guchhait S (2024) Investigation of experimental signatures of spin glass transition temperature.
*Front. Phys.* 12:1482907.
doi: 10.3389/fphy.2024.1482907



# Investigation of experimental signatures of spin glass transition temperature

Sahil Pradhan[1]*, David Harrison[2], Gregory Kenning[3], Deborah L. Schlagel[4] and Samaresh Guchhait[1]

[1]Department of Physics and Astronomy, Howard University, Washington, DC, United States, [2]School of Physics and Astronomy, The University of Minnesota, Minneapolis, MN, United States, [3]Department of Physics, Indiana University of Pennsylvania, Indiana, PA, United States, [4]Division of Materials Science and Engineering, Ames Laboratory, Ames, IA, United States

We present a series of temperature and field-dependent magnetization studies of large single-crystal spin glass samples, focusing on both field-cooled (FC) and zero-field-cooled (ZFC) magnetization studies, as well as ac susceptibility measurements. Using the above experimental techniques we aim to understand the nature of spin glass transition in presence of a field, a key factor in understanding the properties of these systems. Building on previous studies that have explored magnetic signatures indicative of spin glass transitions, our research employs a systematic approach to refine the identification of this transition temperature. Through static and dynamic measurements, we aim to shed light on the open issues regarding the key markers of spin glass transitions, enhancing our understanding of these complex systems.

KEYWORDS

**disorder magnetic systems, complex systems, spin glass transition, glass transition temperature, field-cooled magnetization, zero-field-cooled magnetization, AC susceptibility**

## 1 Introduction

Over the years experimentalists have used a series of techniques to "determine" the spin glass phase transition temperature $T_g$. This value is then often used (usually as an energy scale) in theoretical explanations of various effects within the spin glass phase, such as aging. If these techniques actually determined the phase transition temperature $T_c$, then one might expect the measured $T_g$ to be the same for all of these techniques and the values to have similar behavior, for example, as a function of magnetic field. This manuscript provides the first comparative analysis of these techniques.

AC and DC magnetic susceptibility measurements under varying conditions are important for understanding the properties of spin glasses. Early seminal work by Cannella and Mydosh [1] highlighted the critical importance of ac susceptibility studies in exploring the magnetic properties of gold-iron alloys, particularly noting the presence of a susceptibility cusp indicative of a possible phase transition in this system. With further exploration, it was found that this characteristic curve exhibited a time-dependent behavior, adding a dynamic complexity to the magnetic response of such materials [2]. Moreover, the "static" magnetization measurements, specifically field-cooled (FC) and zero-field-cooled (ZFC) magnetization studies, have been important

in characterizing spin glass behavior. These methods, discussed extensively by Kenning et al. [3, 4], serve as fundamental techniques to determine the onset of spin glass ordering. The FC and ZFC magnetization measurements were first performed by T. Mizoguchi et al. [5] and later adopted by other researchers working on other spin glasses, such as Cu:Mn [6] and Au:Fe [7, 8]. Subtracting the ZFC magnetization from the FC magnetization shows the onset of irreversible behavior. This is an indication of non-equilibrium state of the spin glass phase. The bifurcation temperature of the FC and ZFC magnetization curves is magnetic field dependent, and pinpoints the temperature at which the magnetic irreversibility begins. In this manuscript, we'll call this temperature $T_g^{irr}(H)$.

Lévy [9] found, in a Ag:Mn spin glass, that at low frequencies ($\leq$ 0.1 Hz) the peak is not time-dependent. They interpreted this as a finite size effect caused by the critical correlation length reaching the sample size. They measured the non-linear susceptibility, revealing critical behavior and extrapolated singularities at the spin glass phase transition temperature $T_c$. This work reveals how higher-order non-linear susceptibilities, like $\chi_3$, $\chi_5$, and $\chi_7$, diverge at $T_c$ when approached from the high temperature side. Further research by Levy and Ogielski [10] provides strong experimental evidence of phase transition in Ag:Mn, characterizing the power-law divergences of nonlinear susceptibilities, and their critical scaling in the vicinity of $T_c$. However, the relationship between this divergence at $T_c$, the well-documented susceptibility cusp, and the various other transition temperatures identified through FC and ZFC measurements remains poorly explored and understood. More recently, measurements on the same single crystal sample discussed in this paper, report critical scaling, with a transition temperature $T_c = 32.4$ K [4]. In this paper, we consider $T_c$ as the actual phase transition temperature.

Experimentally, both ac and "static" or dc measurement techniques (i.e., FC and ZFC magnetizations), have been used as a rough estimate of the transition temperature. Kenning et al. [11], working on a poly-crystalline $Cu_{0.94}$ $Mn_{0.06}$ sample, defined the onset of irreversibility as the difference between field-cooled and zero-field-cooled magnetization. For this sample, they determined $T_g^{irr}(H \to 0) = 31.5$ K. Coincidentally the single crystal $Cu_{0.94}$ $Mn_{0.06}$ sample used in this study was also found to have $T_g^{irr}(H \to 0) \approx 31.5$ K, so we can directly compare these samples with each other. Other researchers have taken the peak of the ZFC magnetization [12] or the peak in the FC magnetization [13] as the spin glass transition temperature [12]. We label this transition temperature as $T_g^{ZFC}$ and $T_g^{FC}$, respectively. The peak in the ac susceptibility has also been used as a transition temperature [1]. We'll call this temperature $T_g^{ac}$.

In this paper, we conduct a systematic examination of these techniques. We'll evaluate the relationship of these transition temperatures with each other, and their relationship to the critical transition temperature $T_c$. We assess whether these different indicators of transition temperature are consistent with each other or they differ. Previous studies used poly-crystalline samples for these experiments. Due to the long timescales associated with the spin glass phase, all measurement techniques below the spin glass phase transition temperature measure non-equilibrium phenomena. In this study, we use a single crystal $Cu_{0.94}$ $Mn_{0.06}$ sample, and a comparative study will allow us to explore the role of finite size effects in determining the transition temperature [14–16].

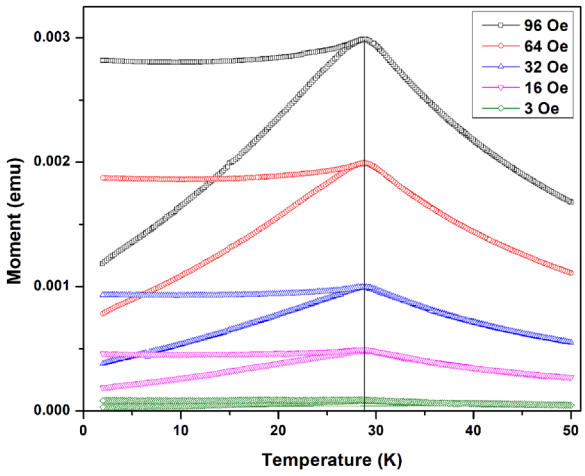


FIGURE 1
Temperature dependent FC and ZFC magnetization curves of a single crystal $Cu_{0.94}$ $Mn_{0.06}$ sample for different constant DC magnetic fields between 3 and 96 Oe. This data show the peak temperature (vertical line) of ZFC magnetization does not change with applied field, but the onset of irreversibility temperature changes. These measurements are performed at Howard University.

One issue with comparing metallic spin glasses is that the transition temperature is strongly sensitive to the concentration of the magnetic constituent. For example, Vier et al. found that in Cu:Mn the transition temperature (determined by the peak in the DC FC-magnetization) increases by 4–5 K for every % increase in Mn [13]. Therefore comparisons are difficult unless one is working on the same sample. In this study, we are comparing the results of different techniques used to measure the glass transition temperature. If all of these techniques actually define the glass transition temperature then we might expect that all of these measurements would imply the same transition temperatures and this transition temperature would have similar properties as a function of magnetic field. In this study, we chose a Cu:Mn (6%) single crystal sample for our measurements. Cu:Mn is the most studied spin glass and often termed the canonical spin glass. We expect the results found in this paper to not only extend to other concentrations of Cu:Mn but also to hold for other metallic spin glasses such as Ag:Mn and Au:Fe. While further experiments will test this hypothesis, this comparison is a starting point for analysis.

## 2 Experimental methods

All samples used in this study are cut from a single crystal $Cu_{0.94}$ $Mn_{0.06}$ boule, grown by the Bridgman method at the Materials Preparation Center (MPC) of Ames Laboratory [17]. Measurements performed at the University of Minnesota (UM) used a Quantum Design MPMS-5S DC SQUID magnetometer. In performing both the FC and ZFC measurements, the MPMS-5S took sequential temperature points every 110 s. This is similar to measurements of the polycrystalline $Cu_{0.94}$ $Mn_{0.06}$ spin glass taken on the SHE model 90 RF SQUID magnetometer in Ref. [11]. Howard University (HU) measurements were taken with a Quantum Design 9 T PPMS

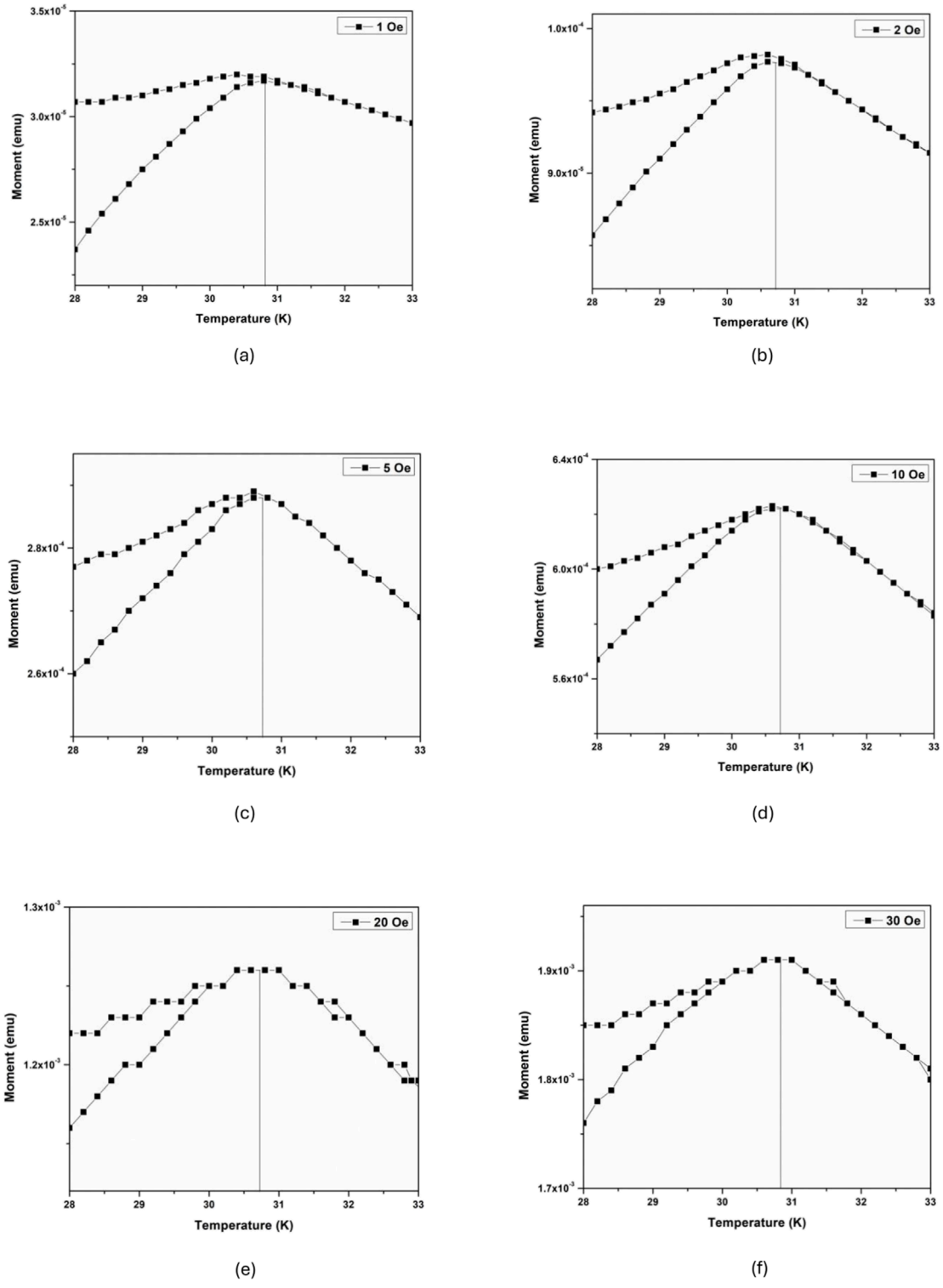


FIGURE 2
Field-cooled and zero-field-cooled magnetization plots vs. temperature for different fields: **(A)** 1, **(B)** 2, **(C)** 5, **(D)** 10, **(E)** 20, and **(F)** 30 Oe. This data indicate that the ZFC magnetization peak temperature does not shift with applied magnetic field, but the irreversibility onset temperature lowers with increasing field. The data was taken using a MPMS-5S SQUID Magnetometer at the University of Minnesota.

Dynacool vibrating sample magnetometer (VSM). The sample at Howard University had a weight of ~ 134.68 mg and approximate dimensions of 2 mm × 2 mm × 3 mm. The PPMS experimental procedure began by cooling the sample down to 2 K in the absence of any external magnetic field from a temperature well above the glass transition temperature. Subsequently, a magnetic field ($H$)

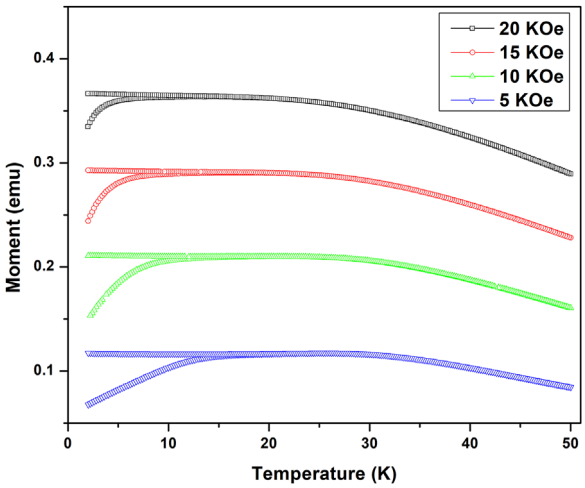


FIGURE 3
The field-cooled (FC) and zero-field-cooled (ZFC) curves as a function of temperature for higher fields (5, 10, 15, and 20 kOe). These measurements were performed at Howard University.

is applied, and sample magnetization at different temperature is measured while temperature is incrementally increased by 0.2 K, reaching a maximum of 50 K. These measurements define the zero-field cooled magnetization ($M_{ZFC}$). Following this, the temperature is lowered down to 2 K while maintaining the same magnetic field, and measurements are taken at the same temperatures. These measurements are defined as the field-cooled magnetization ($M_{FC}$). For both the described processes, the temperature was gradually adjusted at a rate of 0.5 K/min using a no-overshoot approach. At each measurement point, the system was allowed to stabilize for 20 s before recording data for 10 s. The same procedure was repeated for different fields between 3 and 20,000 Oe. For the University of Minnesota experiments, the sample was initially cooled to 20 K in absence of any magnetic field. After temperature stabilization, a magnetic field was applied. The temperature was then increased in stages. First, it was raised to 28 K with 2 K increments. Following this, the temperature increment is reduced to 0.2 K per step, continuing until it reached 33 K. Finally, from 34 K onwards, the temperature was again increased in 2 K increments up to 50 K. Only low fields (1, 2, 5, 10, 20, and 30 Oe) measurements were made with the MPMS-5S SQUID magnetometer at the University of Minnesota.

## 3 Results

Figure 1 shows FC and ZFC magnetization curves of $Cu_{0.94}Mn_{0.06}$ single crystal sample for various fields between 3 and 96 Oe. We note that the temperatures associated with the peak in the ZFC curves, do not change with the magnetic field. In Figure 1, it is clear that all the ZFC curve peaks align with the vertical straight line, which is positioned at 28.8 K. This observation suggests that the ZFC peak is independent of the external magnetic field. However, the onset of irreversibility, which is defined as the bifurcation point between $M_{FC}$ and $M_{ZFC}$ curves, changes with the applied field. Figures 2A–F displays low-field FC and ZFC magnetization curves measured at the University of Minnesota using a MPMS-5S SQUID magnetometer. The two important features that we observed in Figure 1 can also be seen in the University of Minnesota data, i.e., (a) the peak of the ZFC remains constant and (b) as the magnetic field increases, the irreversibility onset temperature decreases. For the sample measured at Howard University, the peak of the ZFC curve occurs at a slightly lower temperature, 28.8 K than the peak of the ZFC curve of the sample measured at the University of Minnesota which occurs at approximately 30.7 K. We believe this difference may be due to differences in the temperature control systems of the two different magnetometers used to measure the data. Because of this, the data obtained at Howard University is re-scaled so that it's consistent with the University of Minnesota studies and the studies of Kenning et al. [4]. Figure 3 shows the temperature dependent FC and ZFC plots in higher magnetic fields. We observe that the cusp in the $M_{ZFC}$ becomes less pronounced and levels off as the magnetic field increases. With increasing magnetic field we observe that the onset of irreversibilty moves towards the lower temperature side consistent with observations reported earlier [11].

The difference between field-cooled magnetization and zero-field-cooled magnetization defines the irreversible magnetization ($M_{irr} = M_{FC} - M_{ZFC}$). The irreversibility onset temperature has been used as the spin glass transition temperature [11]. In contrast to the behavior of the peak in the ZFC curve, this irreversibility onset temperature shows a downward shift with increasing magnetic field strength. This phenomenon has been interpreted as the de Almeida-Thouless (AT) line. The Mean Field Theory predicts a magnetic field dependent phase transition that scales with the magnetic field as $T_c(0) - T_c(H) \approx H^{\frac{2}{3}}$, the de Almeida-Thouless (AT) line [11, 18]. Figures 4A–F and Figures 5A, B shows the $M_{FC} - M_{ZFC}$ vs. temperature plots for different fields. A closer inspection of Figure 4 shows that for low magnetic fields there are two distinct regions: 1) a high temperatures paramagnetic region without any irreversibility, and 2) a low temperature region with irreversibility. This suggests that at low fields ( < 100 Oe) the system behaves like an Ising-like spin glass just below the transition temperature where it exhibits only one single transition [19], which is an indication of longitudinal freezing [20].

Figure 5 shows the same study for high magnetic fields ( > 500 Oe). There are three distinct regions in temperature-dependent irreversible magnetization plots: 1) a high temperatures paramagnetic region with no irreversibility, 2) the onset of a low-temperature weak irreversibility just below the transition, and 3) the onset of a stronger irreversibility at even lower temperature. The existence of these three regions have been reported before in Ref. [11]. The onset temperature of weak irreversibility, $T_w$, is determined by fitting a straight line to the weak irreversible magnetization right below the transition temperature. Subsequently, the temperature at which the irreversible magnetization first departed from weak irreversibility as temperature decreased further from $T_w$ was recognized as the onset of strong irreversibility, denoted as $T_s$. These two transitions are shown in Figures 4, 5, although Figures 4A–F show only weak irreversibility transition. The onset temperature of the weak irreversibility transition in high field has been associated with the Gabay-Toulouse transition for Heisenberg spin glass [20, 21], where the transverse components of the spin freeze out [22]. Moreover, the onset temperature of the strong irreversibility has

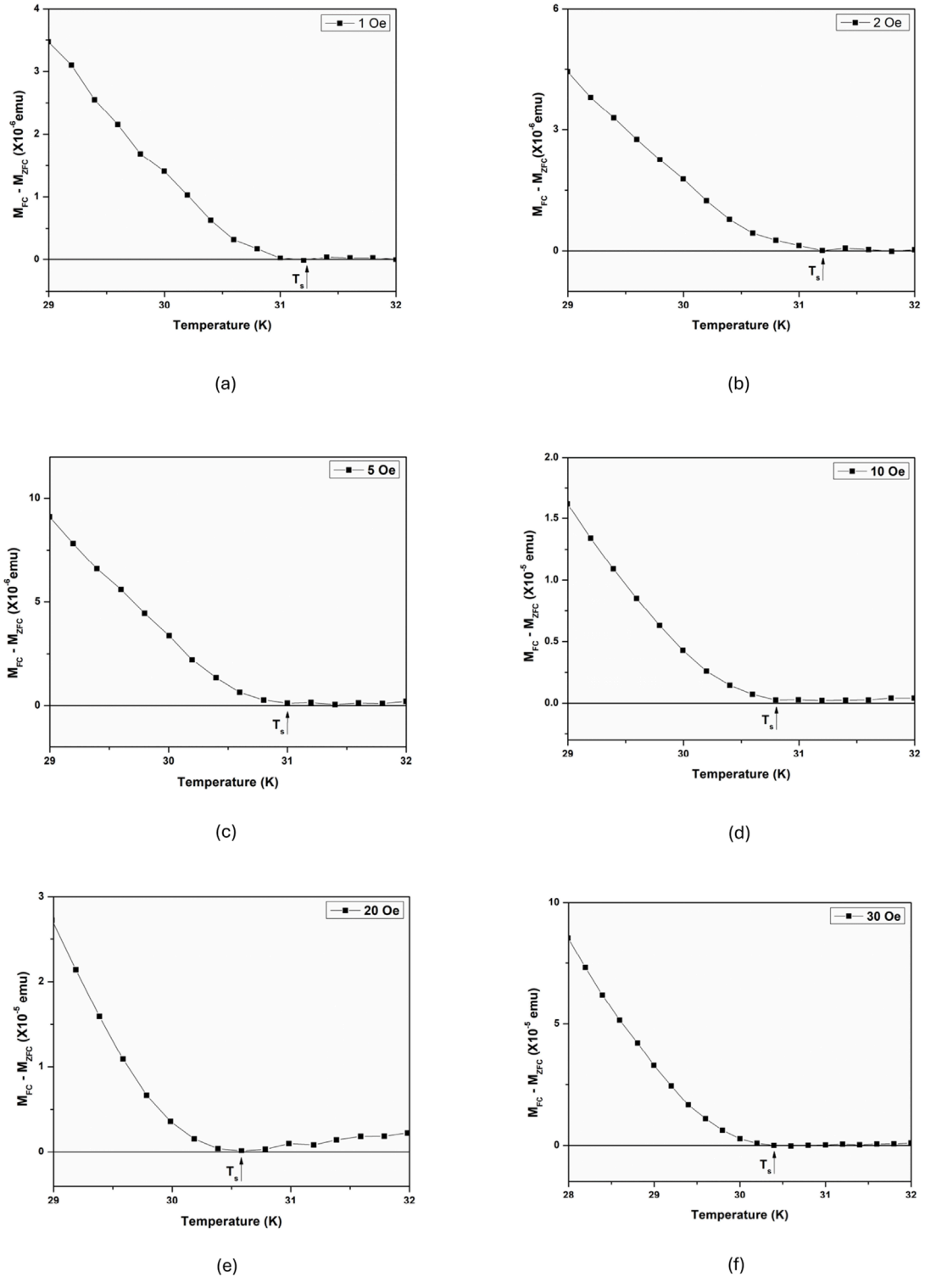


FIGURE 4
Plot of $M_{FC} - M_{ZFC}$ vs. temperature for a dc field of **(A)** 1 Oe, **(B)** 2 Oe, **(C)** 5 Oe, **(D)** 10 Oe, **(E)** 20 Oe, and **(F)** 30 Oe.

been associated with the de Almeida-Thouless transition [18] where the longitudinal components of the spin also freeze out. However, for the low fields, we only observe a single transition, consistent with the previous report [11].

The temperature and field-dependent ac magnetic susceptibility ($\chi'$) studies conducted on the $Cu_{0.94}$ $Mn_{0.06}$ crystal provide further insights into the material's spin glass properties. Figures 6A, B illustrate the real part of ac magnetic susceptibility plotted against

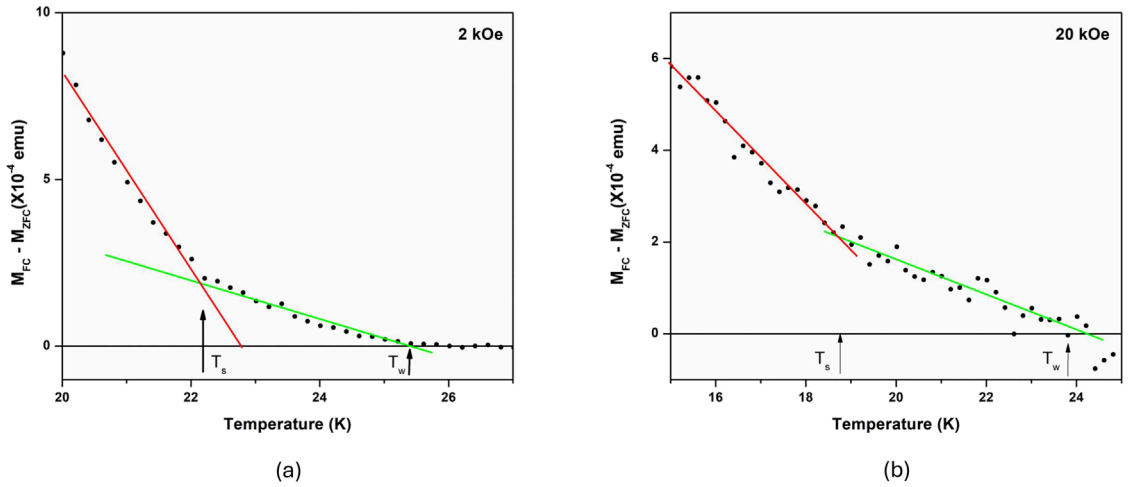


FIGURE 5
**(A)** A plot of $M_{FC} - M_{ZFC}$ vs. temperature for an external field of **(A)** 2 kOe measured at a temperature increment of 0.2 K, and **(B)** 20 kOe measured at a temperature increment of 0.2 K. These data show presence of two transitions below the paramagnetic phase. These measurements are performed at Howard University.

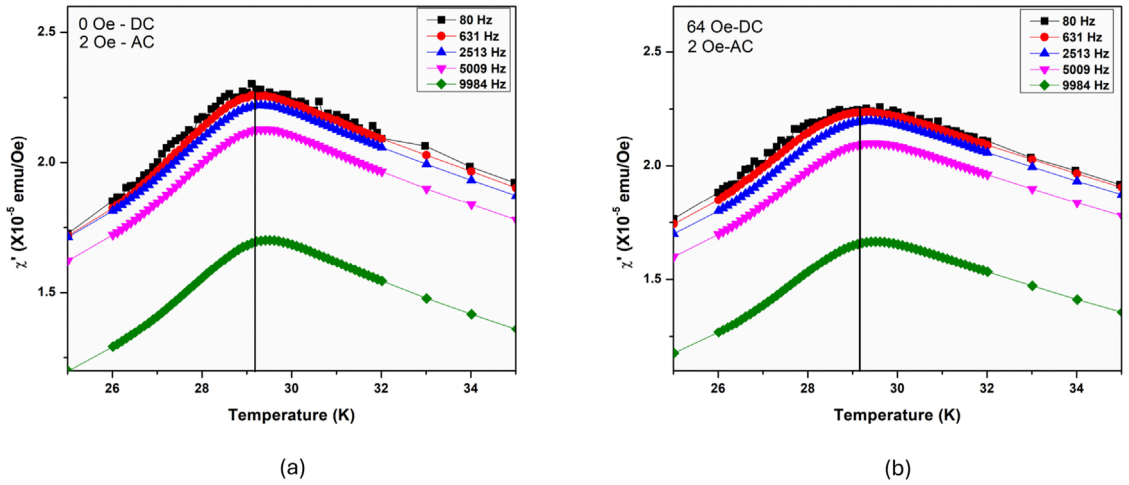


FIGURE 6
Real part of susceptibility ($\chi'$) vs. temperature for different frequencies at constant **(A)** 0 Oe DC field, and **(B)** 64 Oe DC field.

temperature across a range of frequencies from 80 to 10,000 Hz. The shape of $\chi'$ mirrors the ZFC (DC) magnetization presented in Figure 1 (which is considered a low frequency measurement). This equivalence arises because the frequency of the ac measurement corresponds to the inverse of the duration spent at each temperature step during the ZFC heating process [23]. One prominent observation from these figures is the shifting of the cusp of the real part of susceptibility towards lower temperatures as the frequency decreases. Also, there is a corresponding reduction in the intensity of the peaks. This drop in $\chi'$ amplitude with increasing frequency is likely due to the skin depth effects [24] which will be explored further.

To further explore the spin glass behavior of the $Cu_{0.94}Mn_{0.06}$ sample, ac magnetic susceptibility measurements were made in a constant magnetic field, with magnetic fields ranging from 0 to 64 Oe. Figure 7 shows the corresponding plots obtained from these experiments. Remarkably, despite the variation in static magnetic field strength, the peak of the susceptibility curve remains unchanged. Extrapolating the time dependence of the ac susceptibility, we find that the peak temperature of the ac susceptibility crosses the peak temperature of both the FC and ZFC peaks between 0.16 and 1 Hz (shaded region in Figure 7). This is very near the frequency region where Lévy [9] observe that the ac susceptibility peak no longer shifts (or shifts much more slowly) as a function of decreasing frequency. This observation aligns with the behavior observed in the ZFC and FC magnetization, where the peak position remains constant irrespective of the applied magnetic field (for low fields).

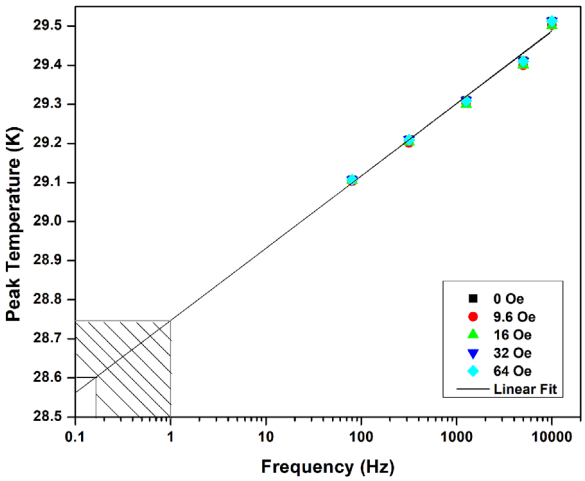


FIGURE 7
Peak temperature of ac susceptibility ($\chi'$) curves for different frequencies and fields. The shaded region indicates the range where the peak temperature of $\chi'$ intersects the peak temperatures of both the FC and ZFC curves.

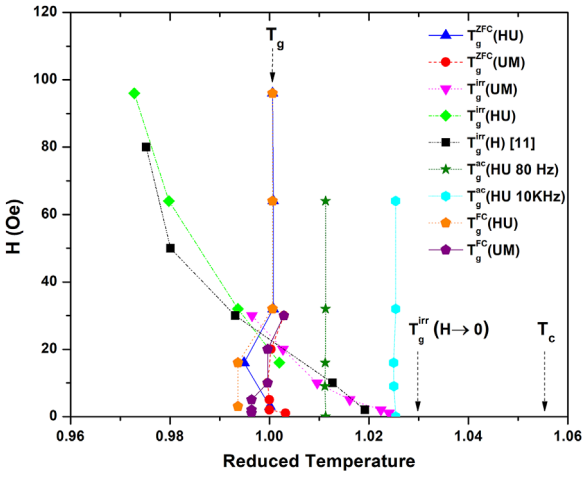


FIGURE 8
A comparison of different datasets plotted against the reduced temperature. $T_g^{ZFC}$ (HU), $T_g^{FC}$ (HU) corresponds to the peak of the ZFC curves and FC curves and $T_g^{irr}$ (HU) corresponds to the onset of irreversibility in Figure 1. $T_g^{ZFC}$ (UM), $T_g^{FC}$ (UM) [from Figure 2] and $T_g^{irr}$ (UM) [from Figure 4] correspond to the peak temperature of ZFC, FC, and the onset temperature of irreversibility, respectively. $T_g^{ac}$ (HU 80 Hz) and $T_g^{ac}$ (HU 10 KHz) [from Figures 6A, B] is the peak of the $\chi'$ curve. $T_g^{irr}(H)$ refers to the onset temperature of irreversibility in Ref. [11]. Here, the reduced temperature = $T/T_g^{ZFC}$, where T is the measurement temperature and $T_g^{ZFC}$ is the peak of the respective ZFC magnetization curve [12].

Figure 8 is a plot of the magnetic field ($H$) vs. various transition temperatures for several different types of experimental studies. For a better comparison of all these studies, we have plotted these transition temperatures: $T_g^{FC}$, $T_g^{ZFC}$, $T_g^{ac}$, and $T_g^{irr}$, as a function of the reduced temperature (defined as $T/T_g^{ZFC}$), where $T_g^{ZFC}$ is the peak temperature of respective ZFC magnetization. All the data has been plotted with respect to the reduced temperature. This temperature normalization is important because now we can compare all the results obtained from different experiments. The results are quite interesting. Except the irreversibility onset temperature, all other transition temperatures in Figure 8 are magnetic field independent.

## 4 Discussion

The comparison of different techniques for determining $T_g$ depicts some interesting results in Figure 8. First, the peaks in the FC magnetization and peaks in the ZFC magnetization (within error limits) occur at the same temperature. Second, they (and the ac susceptibility) are magnetic field independent in the measurement range between 1 and 100 Oe. Third, the time dependence of the peak in the ac susceptibility extrapolates to the "static" $T_g$ determined by the FC and ZFC peaks. All three of these methods suggest a single magnetic field independent temperature which we will call $T_g$.

The question remains, "Is the $T_g$ as defined above, the critical phase transition temperature $T_c$"? Probably the strongest evidence for $T_g = T_c$ is the previously described study of the non-linear susceptibility by Lévy [9]. While the spin glass phase transition temperature may occur at the above defined $T_g$, there are some issues which argue for a slightly higher value of $T_c$.

First, in low magnetic fields, the onset of irreversibility (the difference between the FC and ZFC magnetizations) begins at a temperature above $T_g$ and then as the magnetic field is increased, the onset of irreversibility shifts through $T_g$ to lower temperatures (Figure 8). This effect is highly reproducible with three examples in this paper (including single crystal and polycrystalline samples), and has been observed in other types of spin glasses such as the chromium thiospinel compound $CdCr_{1.7}$ $In_{0.3}$ $S_4$ [25]. In higher magnetic fields (i.e., $H > 10$ Oe) the peaks in the FC and ZFC magnetizations overlap looking effectively reversible. Reversibility in spin glasses is generally observed above the phase transition temperature in the paramagnetic state. While it is possible that the irreversibility above $T_g$ (low magnetic fields) is due to the growth of spin glass correlations in the paramagnetic phase, as a function of magnetic field, the onset of irreversibility seamlessly transitions through $T_g$. If $T_g$ is the phase transition temperature, a discontinuity or change in the irreversible magnetization might be expected at that temperature.

A second issue with the above definition of $T_g$ is following. The Mean Field theory predicts an AT line which shows that the transition temperature is dependent on the magnetic field. The peaks in the FC and ZFC are independent of the magnetic field whereas the onset of irreversibility decreases as the magnetic field increases in a manner consistent with an AT line [11]. It is however unclear in the theory how large this shift should be, over the magnetic field range that we are exploring. It is possible that this is a very small shift and unobservable in the range we are exploring leading to no observation of a field dependence.

Finally, on the same samples, Ref. [4] observes a continuous decrease in the timescale $t_w^{eff}$ associated with aging in the spin glass phase, right up to and at, the above defined temperature $T_g$. Aging is observed in the spin glass remnant magnetization and is associated

with the spin glass phase. Above $T_g$, both the magnetization signal and $t_w^{eff}$ move outside the window of their experimental resolution and time scale. The continuous decease in both the magnetization and $t_w^{eff}$ implies that aging will continue above $T_g$. In Ref. [11] an argument is made for a phase transition temperature of $T_c = 1.055\,T_g$.

## 5 Summary

In summary, we conducted a thorough investigation involving static measurements, (FC and ZFC) magnetization measurements, and dynamic measurements, (ac susceptibility) on a single crystal $Cu_{0.94}$ $Mn_{0.06}$ sample. We observe that the peak of the FC and ZFC magnetizations remains constant as a function of magnetic field at least for the low fields, while the onset of irreversibility moves down to lower temperatures with increasing magnetic field and intersects the position of the ZFC peak. We also note that the peak of the $\chi'$ (80 Hz) remains constant as a function of fields at ~0.963 $T_c$, which corroborates the stability of the ZFC curve's peak.

## Data availability statement

The raw data supporting the conclusions of this article will be made available by the authors, without undue reservation.

## Author contributions

SP: Data curation, Formal Analysis, Investigation, Methodology, Writing–original draft, Writing–review and editing. DH: Methodology, Writing–review and editing. GK: Funding acquisition, Investigation, Methodology, Project administration, Supervision, Writing–review and editing, Conceptualization, Writing–original draft. DS: Methodology, Writing–review and editing. SG: Conceptualization, Funding acquisition, Investigation, Supervision, Writing–review and editing, Writing–original draft.

## Funding

The author(s) declare that financial support was received for the research, authorship, and/or publication of this article. This work is supported by the NSF Award No. DMR-2018579. This work was supported in part by the U.S. Department of Energy, Office of Science, Office of Basic Energy Sciences, Division of Materials Science and Engineering, under Award No. DE-SC0013599. Part of the research was performed at the Ames National Laboratory, which is operated for the U.S. DOE by Iowa State University under Contract No. DE-AC02-07CH11358. Part of this work was performed at the Institute for Rock Magnetism (IRM) at the University of Minnesota. The IRM is a US National Multi-user Facility supported through the Instrumentation and Facilities program of the National Science Foundation, Earth Sciences Division, award NSF-EAR 2153786, and by funding from the University of Minnesota.

## Acknowledgments

We sincerely thank Raymond L. Orbach and E. Dan Dahlberg for their insightful conversations, which greatly contributed to this work.

## Conflict of interest

The authors declare that the research was conducted in the absence of any commercial or financial relationships that could be construed as a potential conflict of interest.

## Publisher's note



## References

1. Cannella V, Mydosh JA. Magnetic ordering in gold-iron alloys. *Phys Rev B* (1972) 6:4220–37. doi:10.1103/physrevb.6.4220

2. Mulder C, Van Duyneveldt A, Mydosh J. Susceptibility of the cu mn spin-glass: frequency and field dependences. *Phys Rev B* (1981) 23:1384–96. doi:10.1103/physrevb.23.1384

3. Kenning G, Chu D, Alavi B, Hammann J, Orbach R. Magnetic-field dependence of tg in bulk cu: Mn and cu: Mn/cu multilayer systems. *J Appl Phys* (1991) 69:5240–2. doi:10.1063/1.348091

4. Kenning GG, Brandt M, Brake R, Hepler M, Tennant D. Observation of critical scaling in spin glasses below tc using thermoremanent magnetization. *Front Phys* (2024) 12:1443298. doi:10.3389/fphy.2024.1443298

5. Mizoguchi T, McGuire T, Kirkpatrick S, Gambino R. Measurement of the spin-glass order parameter in amorphous gd0.37al0.63. *Phys Rev Lett* (1977) 38:89–92. doi:10.1103/physrevlett.38.89

6. Nagata S, Keesom P, Harrison H. Low-dc-field susceptibility of cu mn spin glass. *Phys Rev B* (1979) 19:1633–8. doi:10.1103/physrevb.19.1633

7. Kinzel W. Remanent magnetization in spin-glasses. *Phys Rev B* (1979) 19:4595–607. doi:10.1103/physrevb.19.4595

8. Senoussi S, Elkhatouri D. Field and temperature behaviour of the zero field cooled and the field cooled magnetization of au22fe18. *J Magnetism Magn Mater* (1986) 54:153–4. doi:10.1016/0304-8853(86)90528-7

9. Lévy LP. Critical dynamics of metallic spin glasses. *Phys Rev B* (1988) 38:4963–73. doi:10.1103/physrevb.38.4963

10. Levy LP, Ogielski AT. Nonlinear dynamic susceptibilities at the spin-glass transition of ag: Mn. *Phys Rev Lett* (1986) 57:3288–91. doi:10.1103/physrevlett.57.3288

11. Kenning G, Chu D, Orbach R. Irreversibility crossover in a cu: Mn spin glass in high magnetic fields: evidence for the gabay-toulouse transition. *Phys Rev Lett* (1991) 66:2923–6. doi:10.1103/physrevlett.66.2923

12. Sandlund L, Granberg P, Lundgren L, Nordblad P, Svedlindh P, Cowen J, et al. Dynamics of cu-mn spin-glass films. *Phys Rev B* (1989) 40:869–72. doi:10.1103/physrevb.40.869

13. Vier D, Schultz S. Evidence for multiple mechanisms contributing to the transition temperature in metallic spin-glasses. *Phys Rev Lett* (1985) 54:150–3. doi:10.1103/physrevlett.54.150

14. Guchhait S, Kenning GG, Orbach RL, Rodriguez GF. Spin glass dynamics at the mesoscale. *Phys Rev B* (2015) 91:014434. doi:10.1103/physrevb.91.014434

15. Zhai Q, Harrison DC, Tennant D, Dahlberg ED, Kenning GG, Orbach RL. Glassy dynamics in cumn thin-film multilayers. *Phys Rev B* (2017) 95:054304. doi:10.1103/physrevb.95.054304

16. Kenning GG, Tennant DM, Rost CM, da Silva FG, Walters BJ, Zhai Q, et al. End of aging as a probe of finite-size effects near the spin-glass transition temperature. *Phys Rev B* (2018) 98:104436. doi:10.1103/physrevb.98.104436

17. Zhai Q, Martin-Mayor V, Schlagel DL, Kenning GG, Orbach RL. Slowing down of spin glass correlation length growth: simulations meet experiments. *Phys Rev B* (2019) 100:094202. doi:10.1103/physrevb.100.094202

18. de Almeida JR, Thouless DJ. Stability of the sherrington-kirkpatrick solution of a spin glass model. *J Phys A: Math Gen* (1978) 11:983–90. doi:10.1088/0305-4470/11/5/028

19. Kotliar G, Sompolinsky H. Phase transition in a dzyaloshinsky-moriya spin-glass. *Phys Rev Lett* (1984) 53:1751–4. doi:10.1103/physrevlett.53.1751

20. Gabay M, Toulouse G. Coexistence of spin-glass and ferromagnetic orderings. *Phys Rev Lett* (1981) 47:201–4. doi:10.1103/physrevlett.47.201

21. Cragg DM, Sherrington D, Gabay M. Instabilities of an m-vector spin-glass in a field. *Phys Rev Lett* (1982) 49:158–61. doi:10.1103/physrevlett.49.158

22. Petit DCI, Fruchter L, Campbell IA. Ordering in heisenberg spin glasses. *Phys Rev Lett* (2002) 88:207206. doi:10.1103/physrevlett.88.207206

23. Vincent E. Spin glass experiments. In: T Chakraborty, editor. *Encyclopedia of condensed matter physics*. 2nd edn. Oxford: Academic Press (2024). p. 371–87.

24. Jackson JD. *Classical electrodynamics*. 3rd edn. New York: Wiley (1998).

25. Lefloch F, Hammann J, Ocio M, Vincent E. Spin glasses in a magnetic field: phase diagram and dynamics. *Physica B: Condensed Matter* (1994) 203:63–74. doi:10.1016/0921-4526(94)90278-x

frontiers | Frontiers in Physics

TYPE Original Research
PUBLISHED 13 February 2025
DOI 10.3389/fphy.2024.1507250



OPEN ACCESS

EDITED BY
Federico Ricci-Tersenghi,
Sapienza University of Rome, Italy

REVIEWED BY
Victor Martin-Mayor,
Universidad Complutense de Madrid, Spain
Alexander Hartmann,
University of Oldenburg, Germany

*CORRESPONDENCE
Koji Hukushima,
k-hukushima@g.ecc.u-tokyo.ac.jp

RECEIVED 07 October 2024
ACCEPTED 17 December 2024
PUBLISHED 13 February 2025

CITATION
Hukushima K and Krauth W (2025) Damage spreading and coupling in spin glasses and hard spheres.
*Front. Phys.* 12:1507250.
doi: 10.3389/fphy.2024.1507250



# Damage spreading and coupling in spin glasses and hard spheres

Koji Hukushima[1]* and Werner Krauth[2,3,4]

[1]Graduate School of Arts and Sciences, The University of Tokyo, Tokyo, Japan, [2]Laboratoire de Physique de l'Ecole normale supérieure, ENS, Université PSL, CNRS, Sorbonne Université, Université Paris Cité, Paris, France, [3]Rudolf Peierls Centre for Theoretical Physics, Clarendon Laboratory, University of Oxford, Oxford, United Kingdom, [4]Simons Center for Computational Physical Chemistry, New York University, New York, NY, United States

We study the connection between damage spreading, a phenomenon long discussed in the physics literature, and the coupling of Markov chains, a technique used to bound the mixing time. We discuss in parallel the Edwards–Anderson spin-glass model and the hard-disk system, focusing on how coupling provides bounds on the extension of the paramagnetic and liquid phases. We also work out the connection between path coupling and damage spreading. Numerically, the scaling analysis of the mean coupling time determines a critical point between fast and slow couplings. The exact relationship between fast coupling and disordered phases has not been established rigorously, but we suggest that it will ultimately enhance our understanding of phase behavior in disordered systems.

KEYWORDS

**spin glasses, hard-sphere model, Markov chains, coupling times, damage spreading, thermodynamic phase transitions, dynamic phase transitions**

## 1 Introduction

Monte Carlo simulations based on Markov chains [36, 37] play an important role in the study of complex systems in physics and other sciences. In a given sample space, Markov chains perform random walks that, in their large-time steady state, visit configurations according to a prescribed stationary distribution (often the Boltzmann distribution). At early times, in contrast, after its start from a given initial configuration, each Markov chain samples different time-dependent distributions. The characterization of convergence (that is, of the mixing timescale [39] for approaching the stationary distribution) is of greatest importance as, by definition, convergence is required for sampling from the prescribed distribution and for estimating mean values of observables (pressure, specific heat, and internal energy) as running averages. Moreover, the mixing timescale by itself carries important information on the sampling problem. In a physics context, the sudden slowdown of mixing and relaxation times (without reference to any observable) often indicates a phase transition. Well-known examples are the slowdown of the Glauber dynamics at the paramagnetic–ferromagnetic transition in the Ising model [22, 41], as well as the glass transition, which is defined through the slowdown of relaxation processes (although it is not of thermodynamic origin). The spin-glass transition is believed to be signaled by a stark increase in the relaxation times at low temperatures [23]. In addition, in certain local Monte Carlo algorithms for particle systems, fast mixing (in a way that we will discuss later) is only possible in the liquid phase [32], so a statement about thermodynamic phases is obtained from an analysis of mixing times without invoking

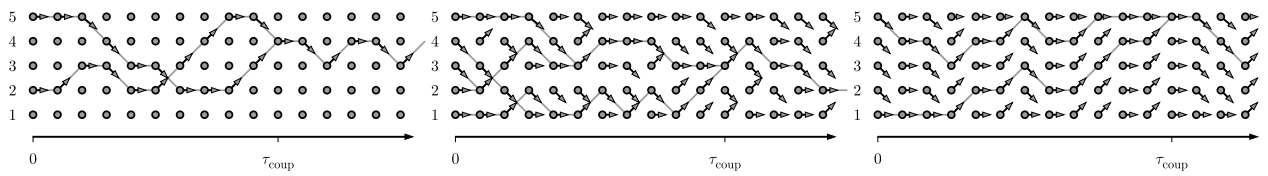


FIGURE 1
Coupling for the random walk on a path graph (arrows point into the three directions with equal probabilities, and those leaving the graph are replaced by straight arrows). *Left*: Classic coupling: the two random walks advance independently until they merge at $\tau_{\text{coup}}$. *Middle*: A random-map implementation of the classic coupling (independent arrows). *Right*: A random-share, monotone coupling, where at a given time, all configurations are updated with the same random number. Trajectories cannot cross.

observables. However, establishing mixing and relaxation times can be an arduous task, both in practice and in theory.

As convergence sets in, samples and empirical mean values (running averages) become independent of initial configurations. Much stronger than mere independence, samples can actually become identical for two (or more) different initial configurations. This phenomenon, called coupling, is a focus of the present article. A coupling is a bivariate stochastic process that starts from two far-away initial configurations at time $t = 0$, say, $x_0$ and $y_0$, under the condition that the projected evolution of $x_t$ and of $y_t$, taken separately, realize a Markov chain with its transition matrix $P$. When the evolutions of the two trajectories meet at the coupling time $\tau_{\text{coup}}$, with $x_{\tau_{\text{coup}}} = y_{\tau_{\text{coup}}}$, they are glued together for all later times (see the lhs of Figure 1). Couplings of a given Markov chain can take many different forms, but for all of them, the coupling time provides an upper bound for the mixing time. This property has been used for almost a century to prove theorems on Markov chains [20], as cited in Ref. [28]. Among many other developments, a more recent version of coupling, known as "coupling from the past" [48], has allowed for the perfect sampling of the stationary distribution without any error, completely sidestepping the estimation of mixing-time scales.

The path-coupling approach [13] attempts to bound the *global* coupling time through an analysis that is *local* in both time and space. The two far-away initial configurations are imagined as end points of a "path" of many configurations. Configurations that are connected on the path are neighbors in the sample space with respect to a given metric. For the one-dimensional random walk, the metric may correspond to the Euclidean distance (see the lhs of Figure 1). For Ising systems, the metric could be the Hamming distance: neighboring configurations differ by only one spin. Similarly, for low-density systems of $N$ hard spheres, neighboring configurations differ in only one sphere, which can be arbitrarily far away in the two configurations, while the other $N-1$ spheres coincide. It is often possible to deduce upper limits for the coupling time from the contraction rates for the individual path links. Path coupling was foreshadowed in the physics literature in a phenomenon termed "damage spreading" [53], which also studied such neighboring configurations under coupled-Markov-chain dynamics, a special type of coupling for Glauber dynamics. In the Ising model, for the same dynamics, the damage was found to disappear rapidly throughout the paramagnetic phase, a phenomenon later understood through the concept of "monotone coupling." In the Ising spin-glass model, the damage was found to disappear above a finite temperature in the paramagnetic phase, even in two spatial dimensions, where the spin-glass transition temperature is believed to vanish. Attempts to directly connect the damage spreading with a thermodynamics process, such as a percolation transition, were finally unsuccessful. In other words, the connection between damage spreading, path coupling, and thermodynamics is that "fast" path coupling implies fast coupling, which implies fast mixing. Fast mixing, in turn, very often implies, in a physics context, that the thermodynamic phase is trivial. This can lead to non-trivial rigorous bounds on the extension of the paramagnetic phase for spin models [22] or the liquid phase for particle systems [32].

This article presents a unified description of coupling and damage spreading, using spin-glass and hard-sphere models as examples. In Section 2, we provide common definitions, discuss theoretical foundations, and explore the connection between coupling and mixing, as well as the relationship between the aforementioned path coupling and damage spreading. We also introduce the scaling approach to phase transitions that we later apply to the coupling phenomenon. Section 3 is dedicated to spin glasses. We discuss rigorous results and the generally accepted theoretical framework for the spin-glass model introduced by Edwards and Anderson. Additionally, we explore path coupling and damage spreading for this model. We further apply the scaling analysis to its mean coupling time, which suggests a phase transition between fast and slow couplings. Section 4 addresses the hard-sphere model, for which we can generally transpose all the theoretical approaches of Section 3. The conclusions of our work are presented in Section 5.

## 2 Theoretical foundations

In this section, we discuss some fundamentals of Markov chains and first concentrate on the connection between the convergence of a Markov chain expressed through its mixing time and any of its couplings (Section 2.1). The special case of "monotone" coupling, which we also address, has important consequences for the ferromagnetic Ising model, although it does not apply to spin-glass models or to hard spheres in more than one dimension [49]. We then discuss damage spreading in terms of path coupling (Section 2.2). We will discuss the intimate relationship between a global view on coupling and a purely local view, which only surveys configurations that differ minimally. We finally discuss in Section 2.3 the scaling

approach to coupling that later will be shown to apply both to spin glasses and to hard spheres.

## 2.1 Mixing, coupling, and monotone coupling

We consider a Markov chain with samples $x_t$ at time $t = 0, 1, \ldots$ in a sample space $\Omega$. In our case, its transition matrix $P$ implements the heat-bath algorithm [17, 26, 27] (in other words, Glauber dynamics) for the Edwards–Anderson model or a version of the Metropolis algorithm [43] for hard spheres. We define the element $P(x,x')$ as the conditional probability to move from configuration $x$ at time $t$ to configuration $x'$ at time $t+1$. With an initial configuration $x_0$, the distribution $\pi^{\{t=0\}}$ is a delta function centered at $x_0$. The distribution evolves over time as $\pi^{\{t+1\}}(x') = \sum_x \pi^{\{t\}}(x) P(x,x')$ for each time step $t$. The approach to equilibrium is quantified by the mixing time, which is the time it takes for $\pi^{\{t\}}$ (which depends on the choice of $x_0$) to approach the stationary distribution $\pi^{\{t\to\infty\}} = \pi$:

$$\tau_{\text{mix}}(\epsilon) = \min_t \left\{ \underbrace{\max_{x_0 \in \Omega} \left\| \pi^{\{t\}} - \pi \right\|_{\text{TV}}}_{d(t)} < \epsilon \right\}. \tag{1}$$

Here, $\|\cdots\|_{\text{TV}}$ denotes the total variation distance [39], that is, one half of the absolute difference between $\pi^{\{t\}}$ and $\pi$ over all the sample space, and $\epsilon$ is an arbitrary positive parameter that must be taken smaller than $\frac{1}{2}$. In Equation 1, the "max" refers to the worst initial choice for the approach of $\pi^{\{t\}}$ (which depends on $x_0$) to $\pi$, and this allows one to define the distance $d(t)$ between $\pi^{\{t\}}$ and $\pi$, without explicit reference to the starting distribution $\pi^{\{t=0\}}$. The mixing time is a non-asymptotic time scale [2] that describes the initial approach of $\pi^{\{t\}}$ toward the equilibrium distribution $\pi$ on a finite distance scale $\epsilon$. It comes with an exponential bound, valid from $\tau_{\text{mix}}$ up to $t \to \infty$, while the asymptotic approach toward equilibrium, described by the (absolute) inverse gap of the transition matrix, can be much faster [39].

For a given transition matrix $P$ of a Markov chain on a sample space $\Omega$, a coupling is defined as a bivariate stochastic process with a configuration $(x_t, y_t)$ at time $t$ on the sample space $\Omega \times \Omega$, such that

$$\mathbb{P}\left[x_{t+1} = x' \mid (x_t, y_t) = (x,y)\right] = P(x,x'),$$

$$\mathbb{P}\left[y_{t+1} = y' \mid (x_t, y_t) = (x,y)\right] = P(y,y').$$

The bivariate process that updates the two copies $x$ and $y$ need not be Markovian [28] at a difference of its two projections. Non-Markovian couplings are theoretically important but have not been used yet in applications. Markovian couplings are described by a transition matrix $P^{\text{coup}}[(\cdot),(\cdot)]$ on the sample space $\Omega \times \Omega$ that satisfies

$$\sum_{y'} P^{\text{coup}}[(x,y),(x',y')] = P(x,x'),$$

$$\sum_{x'} P^{\text{coup}}[(x,y),(x',y')] = P(y,y'),$$

so that the transition matrix of the coupled Markov chain, which acts on two copies of the sample space $\Omega$, when projected on either copy, returns the original transition matrix.

Couplings can take a variety of forms. The "classic" coupling performs two statistically independent Markov chains until, by accident, they couple, from when on they are glued together:

$$P^{\text{coup}}[(x,y),(x',y')] = \begin{cases} P(x,x')P(y,y') & \text{if } x \neq y, \\ P(x,x') & \text{if } x = y,\ x' = y', \\ 0 & \text{if } x = y,\ x' \neq y', \end{cases} \tag{2}$$

(see the lhs of Figure 1). At the coupling time $\tau_{\text{coup}}$, the trajectories first meet:

$$\tau_{\text{coup}} = \min_t \{x_t = y_t\}.$$

Transition matrices, as the ones in Equation 2, are implemented in Monte Carlo algorithms with the use of random elements, that is, one or several random numbers for selecting a particle or a spin, for choosing a move, and for accepting or rejecting it, etc. For example, the move from $x$ at time $t$ may produce an outcome $x'$ that depends on the realization of the random element, but when this element is specified, as $\Upsilon_t(x)$, it becomes a function called a random map $\{t\} \times \Omega \to \Omega: x \to x' = \phi[x, \Upsilon_t(x)]$. The random map $\phi[x, \Upsilon_t(x)]$ implementing this move must satisfy

$$\mathbb{P}\{\phi[x, \Upsilon_t(x)] = x'\} = P(x,x'),$$

as it must reproduce the transition matrix $P$. A random map $\phi$ (also called a "grand" coupling [39]) specifies a coupling, and it automatically implements a "gluing" operation, as two Markov chains that meet at a position $x$ at time $t$ encounter the same random element. For the classic coupling of Equation 2, the randomness at time $t$ is a vector $\boldsymbol{\Upsilon}_t = \{\Upsilon_t(x): x \in \Omega\}$ of i.i.d random variables, that is of random numbers drawn from the same distribution (see center of Figure 1). For the "random-share" coupling, one uses, at time $t$, the same random element for all configurations $x \in \Omega$: $\boldsymbol{\Upsilon}_t = \{\Upsilon_t, \ldots, \Upsilon_t\}$. In other words, all configurations are updated with the same random numbers. Many other couplings exist, and it is only important that the projection onto a single copy produces a valid Markov chain. While every random map corresponds to a coupling, it appears that not all couplings (for example, the path couplings in Ref. [32]) can be expressed as random maps.

The connection between mixing times and coupling times is as follows ([39], corollary 5.3):

$$d(t) \leq \max_{x_0, y_0 \in \Omega} \mathbb{P}_{x_0,y_0}\left\{\tau_{\text{coup}} > t\right\}, \tag{3}$$

where $d(t)$ is the distance entering the definition of the mixing time in Equation 1. From our previous discussion, it is evident that for random walks on large graphs, the classic coupling time can be much larger than the mixing time simply because the two Markov chains must hit the same configuration at the same time. In contrast, the random-share coupling time is of the same order as the mixing time for many random walks. In the problems at the focus of this article, we will witness different regimes, as a function of external parameters, that are separated by a phase transition. In this context, it is of great interest that an optimal coupling [28] realizes the coupling at time $t$ and at position $x_t$ of two Markov chains that have started at time $t = 0$ at configurations $x_0$ and $y_0$ with the minimum of the probabilities to go from $x_0$ or from $y_0$ to $x_t$. The optimal coupling

is non-Markovian and virtually impossible to construct in practice, but it demonstrates that the bound of Equation 3 can be saturated.

A special class of couplings for which the inequality of Equation 3 can be tight (up to logarithms) requires the concept of monotonicity. In monotone couplings, there exists a partial ordering "$\preceq$" of configurations so that $x_t \preceq y_t$ implies $x_{t+1} \preceq y_{t+1}$. In terms of the random map, $x \preceq y$ implies $\phi(x, \Upsilon) \preceq \phi(y, \Upsilon)$. No partial ordering exists for the random walk on the path graph with a classic coupling, and trajectories of Markov chains may cross (see the lhs of Figure 1). In contrast, for the random-share coupling of the one-dimensional random walk (which is a grand coupling), the ordering is complete. For a monotone grand coupling, with $l$ the length of the longest "chain" in the partially ordered subset, the mean coupling time $\tau_{\text{coup}}$ satisfies

$$\left\langle \tau_{\text{coup}} \right\rangle < 2\tau_{\text{mix}}\,(1/e)\,(1+\log\, l)\,. \tag{4}$$

With Equation 3, there are thus upper and lower bounds for the monotone coupling time in terms of the mixing time, and the two agree up to a logarithm. For a monotone coupling with extremal elements, one must only survey their evolution, which will bracket all other configurations (see the rhs of Figure 1). Full surveys are possible in other cases [15], but the upper bound in Equation 4 is then often lost.

## 2.2 Path coupling and damage spreading

We can consider families of Markov chains that correspond to physical systems with size $N$, which may represent the number of sites, spins, or particles. As $N$ increases and approaches infinity, under suitable conditions, such as constant temperature for spin systems or constant density for particle systems, the behavior of these systems can be studied. We may refer to "fast" coupling if the mean coupling time $\left\langle \tau_{\text{coup}} \right\rangle$ scales not slower than a power of the system size $N$ (in later sections, we will use an $N$ log $N$ scaling).

As mentioned in the introduction, we may imagine the worst-case initial configurations $x_0$ and $y_0$ as the end points of a path of configurations, with adjacent elements on the path being neighbors, with respect to some metric. Under some conditions, it is often possible to show that any pair of neighboring configurations come in expectation even closer after one step of the Markov chain, and this establishes that the distance between $x_1$ and $y_1$ contracts, and similarly for later times, leading to a proof of fast coupling [13].

The path-coupling analysis that is local in sample space and in time yet valid uniformly for any pair of neighboring configurations yields a rigorous global fast-coupling bound. We will discuss the limiting temperature $T_{\text{path}}$ for spin glasses and limiting density $\eta_{\text{path}}$ for hard-sphere systems for which the uniform contraction allows one to prove fast coupling. However, the path-coupling approach is quite conservative. Numerical evidence [4] indicates fast coupling down to a temperature $T_{\text{coup}}$ that is lower than $T_{\text{path}}$, and up to a density $\eta_{\text{coup}}$ that is higher than $\eta_{\text{path}}$. However, only $T_{\text{path}}$ and $\eta_{\text{path}}$ are known analytically. In the models that we study, the coupling is either exponential (and thus "slow") or "fast."

The path-coupling analysis provides a justification for "damage spreading," which has been extensively studied for spin systems in the physics literature, with the random-share coupling. As in path coupling, two neighboring initial configurations $x_0$ and $y_0$ were chosen and were followed for very large times. The explicit relationship between the time to couple and the time to mix is lost, but the mean coupling time starting from neighboring initial configurations is again exponential below $T_{\text{coup}}$ and $\sim N \log N$ or faster above. The connection between coupling and damage spreading was made in [4].

## 2.3 From rigorous to non-rigorous approaches to coupling, scaling approach results

The coupling time in Equation 3 that allows bounding the mixing time follows the worst-case pair of starting configurations, $x_0$ and $y_0$. For monotone coupling, these configurations are given by the two extremal elements, but in general, this requires a survey of the entire sample space. For the Glauber dynamics of spin glasses with the random-share coupling, the patch algorithm [15] rigorously surveys the $|\Omega| \sim 10^{600}$ configurations on a $64 \times 64$ lattice, and the same algorithm also applies to hard-sphere models, where it allows one to establish the grand-coupling time [4, 16]. It was found, however, that a few hundred random initial configurations contained worst-case pairs with high probability. Such a partial-survey approximation is easy to set up in practice.

We use the partial-survey approximation to evaluate the mean coupling time $\left\langle \tau_{\text{coup}} \right\rangle$ for spin-glass and hard-sphere systems. Here, a systematic numerical approach, inspired by the finite-size scaling analysis of second-order phase transitions, is discussed for distinguishing between fast and slow couplings. In this context, fixing the system size $N$ corresponds to limiting the worst-case pair distance between initial configurations, and the scaling behavior is analyzed as $N$ grows by varying $N$. Suppose we obtain $\left\langle \tau_{\text{coup}} \right\rangle (N, \beta)$ numerically as a function of the system size $N$ and the model parameter $\beta$, which represents the inverse temperature in the case of spin-glass systems. For hard-sphere systems, this parameter may also be the density $\eta$. In the fast-coupling regime, the size dependence of $\left\langle \tau_{\text{coup}} \right\rangle$ exhibits $N \log N$ behavior at high temperatures, while in the slow-coupling regime, it increases exponentially at low temperatures. This phenomenon can be viewed as a dynamical phase transition, with the two behaviors changing at a certain critical temperature $\beta_{\text{coup}}$.

Assuming that, as $\beta$ approaches $\beta_{\text{coup}}$, $N^*(\beta)$ provides a diverging scale that controls the coupling behavior, the scaling form is postulated to hold in the vicinity of $\beta_{\text{coup}}$, expressed as

$$\left\langle \tau_{\text{coup}} \right\rangle (N, \beta) = N^{\phi} f(N/N^*(\beta)) \quad \text{with} \quad N^*(\beta) = |\beta_{\text{coup}} - \beta|^{-\omega}, \tag{5}$$

where $\phi$ and $\omega$ are positive parameters associated with the dynamical transition, and $f$ is a universal scaling function. The two behaviors of fast and slow couplings are represented in the asymptotic form of this scaling function $f(x)$, with $x = N|\beta_{\text{coup}} - \beta|^{\omega}$:

$$f(x) = \begin{cases} x^{1-\phi} \log\, x & \text{as } x \to \infty \text{ for } \beta_{\text{coup}} > \beta, \\ \exp(ax) & \text{as } x \to \infty \text{ for } \beta_{\text{coup}} < \beta, \end{cases}$$

with a positive constant $a$. The value of the scaling function $f(0)$ at $\beta = \beta_{\text{coup}}$ is constant, and the parameter $\phi$ can be identified

as the exponent of the power-law divergence of $\tau_{\text{coup}}$ at $\beta_{\text{coup}}$. In the case of a ferromagnetic Ising model with monotone coupling, where the coupling time and the mixing time coincide, these parameters characterize the universality class of the corresponding ferromagnetic phase transition and are related to the dynamical exponent $z$ and the correlation length exponent $\nu$ through the dimensionality $d$. For example, in the case of the mean-field ferromagnetic Ising model, it has been rigorously shown that $\phi = 3/2$ [19], which is consistent with $z = 2$. However, in general, the singularity at $\beta_{\text{coup}}$ in this coupling time is not directly associated with an order parameter of the physical system.

## 3 Coupling in spin glasses

This section examines the coupling in the Edwards–Anderson model [23] of spin glasses, focusing on the dynamical properties of its Glauber dynamics. We first review known exact results on the thermodynamics of the model in finite dimensions (Section 3.1), followed by an analysis of path coupling and numerical calculations (Section 3.2). Finally, we discuss the physical significance of these findings (Section 3.3).

The Edwards–Anderson model describes $N$ Ising spins $\boldsymbol{\sigma} = \{\sigma_0, \ldots, \sigma_{N-1}\}$ with $\sigma_k = \pm 1$ on a $d$-dimensional hypercubic lattice with periodic boundary conditions and even side length $L$. The stationary weight $\pi(\boldsymbol{\sigma})$ of each configuration is given through its energy $E(\boldsymbol{\sigma})$ as follows:

$$\pi(\boldsymbol{\sigma}) = \exp\left[-\beta E(\boldsymbol{\sigma})\right] \quad E(\boldsymbol{\sigma}) = -\sum_{\langle ij \rangle} J_{ij}\sigma_i\sigma_j,$$

where $\langle ij \rangle$ denotes the sum over nearest-neighbor pairs of spins. For each spin-glass sample, the interactions $J_{ij} = J_{ji} \in \{-1, +1\}$ are quenched (that is, fixed). The ensemble average is obtained by taking the $J_{ij}$ as i.i.d., with $J_{ij} = +1$ or $J_{ij} = -1$ with equal probability. In our statements about mixing and coupling, this ensemble average is understood.

We consider two versions of the heat-bath algorithm, namely, random updates and parallel updates. For the random updates, at each time step, starting from a configuration $\boldsymbol{\sigma}(t) = \{\sigma_0, \ldots, \sigma_{N-1}\}$, one random spin $\sigma_k$ among the $N = L^d$ spins is sampled. At time $t+1$, the configurations $\boldsymbol{\sigma}^+ = \{\sigma_0, \ldots, \sigma_{k-1}, +1, \sigma_{k+1}, \ldots, \sigma_{N-1}\}$ and $\boldsymbol{\sigma}^- = \{\sigma_0, \ldots, \sigma_{k-1}, -1, \sigma_{k+1}, \ldots, \sigma_{N-1}\}$ are chosen with probability $\pi(\boldsymbol{\sigma}^+)/[\pi(\boldsymbol{\sigma}^+) + \pi(\boldsymbol{\sigma}^-)]$ and $\pi(\boldsymbol{\sigma}^-)/[\pi(\boldsymbol{\sigma}^+) + \pi(\boldsymbol{\sigma}^-)]$, respectively. These probabilities can be written as $\pi^+(h_k)$ and $1 - \pi^+(h_k)$, through the local field $h_k = \sum_{j \in \text{nbr}(k)} J_{kj}\sigma_j$, with the sum over the neighboring sites $j$ of site $k$. For parallel updates, on a bipartite lattice, as the hypercubic lattice with even $L$, the energy couples spins on different sub-lattices. In one Monte Carlo cycle, all the spins are first updated on one sublattice, followed by those on the other sublattice. For simplicity, we count time in terms of "Monte Carlo cycles," that is, $N$ updates, for the random update case also.

The classic coupling of Equation 2, applied to the heat-bath algorithm with the random updates, randomly chooses two spins $\sigma_k$ and $\tau_k$ in order to independently update the configurations $\boldsymbol{\sigma}_t$ and $\boldsymbol{\tau}_t$, until they meet. In terms of random maps, this requires $2 \times 2^N$ random numbers at each time $t$, one to choose the spin, and one to update it, which is not practical. It is evident that at all temperatures, including infinite temperature, the coupling time is exponential in $N$, as the trajectories must accidentally meet.

For the random-share coupling, the heat-bath algorithm for the random update uses a source of randomness $\boldsymbol{\Upsilon}_t$ given by:

$$\boldsymbol{\Upsilon}_t = \{k, \Upsilon\} = \{\underbrace{\texttt{nran}(0, N-1)}_{\text{lattice site } k}, \underbrace{\texttt{ran}(0,1)}_{\text{heat–bath}}\}. \tag{6}$$

In short, the randomness $\boldsymbol{\Upsilon}_t$ samples the lattice site $k$ to be updated, as well as the random number used for the heat-bath update. The random-maps function $\phi$ is then defined for a given spin configuration $\boldsymbol{\sigma}$ and the randomness $\boldsymbol{\Upsilon}_t$ as follows:

$$\phi(\boldsymbol{\sigma}, \boldsymbol{\Upsilon}_t)\!:\!\sigma_k(t+1) = \begin{cases} 1 & \text{if } \Upsilon < \pi^+\left(h_k(\boldsymbol{\sigma})\right) = \left[1 + \mathrm{e}^{-2\beta h_k(\boldsymbol{\sigma})}\right]^{-1}, \\ -1 & \text{else}, \end{cases} \tag{7}$$

where the local field is $h_k = \sum_{j \in \text{nbr}(k)} J_{kj}\sigma_j$. We note that $\sigma_k(t+1)$ does not depend on $\sigma_k(t)$.

For the parallel update on a bipartite lattice, the randomness $\boldsymbol{\Upsilon}_t$ is given by

$$\boldsymbol{\Upsilon}_t = \{\Upsilon^0, \Upsilon^1, \ldots, \Upsilon^{N-1}\} = \{\underbrace{\texttt{ran}(0,1)}_{\text{site } 0}, \underbrace{\texttt{ran}(0,1)}_{\text{site } 1}, \ldots, \underbrace{\texttt{ran}(0,1)}_{\text{site } N-1}\}.$$

The update is performed in two half steps on the two sub-lattices, as described earlier. The coupling corresponding to Equation 7 is monotone only for the ferromagnetic case ($J_{ij} = +1$), where larger local fields are produced by larger neighboring spins $\sigma_j$.

### 3.1 Spin glasses: from rigorous results to numerical simulations

From a mathematical perspective, the fact that the interactions $\{J_{ij}\}$ are quenched random variables complicates the analysis with respect to uniform interactions. The Sherrington–Kirkpatrick model [52], in other words, the Edwards–Anderson model on a complete graph corresponding to its infinite-dimensional limit, has been at the forefront of theoretical developments in spin-glass research. This model undergoes a thermodynamic phase transition separating a high-temperature paramagnetic phase from a low-temperature spin-glass phase at an exactly known temperature. The existence of this phase transition and the low-temperature properties were first established using the replica method [44] and later proven rigorously [54]. The study on the domain-wall free energy [51], which incorporates the fluctuation effects at the mean-field level, has indicated that the lower critical dimension is 2.5, which lies between the dimensions of 2 and 3.

Mathematically rigorous results for the Edwards–Anderson model in finite dimensions are very few. In systems with random interactions, local regions may exhibit low probabilities but strong correlations, leading to anomalous singularities in the free energy and divergences in high-temperature expansions. In a specific random system, the existence of this type of singularity has been mathematically proven and is known as the Griffiths singularity [29]. This singularity emerges at the phase transition temperature when the random interactions are assumed to be uniform. In the Edwards–Anderson model, the Curie temperature of the ferromagnetic Ising model (with all $J_{ij}$ equal to $+J$) constitutes this

Griffiths temperature. Despite these difficulties, it has been proven that, at sufficiently high temperature, the Edwards–Anderson order parameter vanishes identically, and the spin-glass susceptibility remains finite in short-range spin-glass models [6, 25]. This means that the high-temperature phase is paramagnetic, although rigorous temperature bounds seem to be absent. These temperature regions are far from the spin-glass transition temperature $T_{SG}$ suggested by the numerical simulations mentioned below. One expects that a spin-glass phase cannot exist at temperatures higher than the Griffiths temperature, so the Griffiths temperature likely serves as an upper bound for $T_{SG}$. However, this seems not to be a rigorous statement.

Early numerical studies [12, 42] on domain-wall energies at zero temperature, though limited to small system sizes, were the first to propose the existence of a finite-temperature spin-glass transition in three dimensions and the absence of such a transition in two dimensions. These findings were subsequently strengthened by exact algorithms in two dimensions and more sophisticated heuristic algorithms [10], which allowed for larger system sizes and more accurate results. Following them, local Monte Carlo methods, particularly those using the heat-bath algorithm, played a crucial role in confirming these conclusions. These Monte Carlo studies provided direct evidence for a finite-temperature transition in three dimensions [7, 8, 46, 47] and the absence of such a transition in two dimensions [7, 34]. While neither has been proven rigorously, the fact that the ground state of the two-dimensional Edwards–Anderson model can be computed in a time polynomial in $N$[9, 55] is compatible with the hypothesis that complex phase transitions are unlikely to occur in systems where the ground state can be easily obtained. However, it should be noted that certain systems, such as the random-field Ising model [45], allow for efficient ground-state calculations yet still exhibit complex phase transitions at finite temperatures. These conclusions, both for three and higher dimensions as well as for two dimensions, were based on estimates of spin-glass order parameters. These order parameters examine the degree to which the equilibrium running averages of a given observable, such as the spin overlap between replicated systems, become independent of two independent starting configurations in Monte Carlo simulations ([7], Equation 4). Another route to studying spin glasses has consisted in analyzing the autocorrelation functions of observables (e.g., the value of $\sigma_k(t)$). Early results already pointed to a difference in the scaling behavior at late times ([46], Figure 7), [47], from which a finite spin-glass transition temperature in the range $T_{SG} \simeq 1.10 - 1.14$ was inferred. Although no consensus has been reached on the nature of the spin-glass phase, more recent studies have refined estimates of the spin-glass transition temperature $T_{SG}$ in three dimensions, with different estimates such as $T_{SG} = 1.1019(29)$[3] and $T_{SG} = 1.109(10)$[30], which combine simulations for rather small system sizes with empirical extrapolations to the thermodynamic limit.

Damage spreading in spin-glass systems was found as a dynamical anomaly in early numerical simulations [14, 18], which showed that it occurs at temperatures higher than the spin-glass transition temperature suggested by other studies. However, it remained unclear whether the anomaly was related to the spin glass transition itself or to the Griffiths singularity. The connection between damage spreading and coupling, which is the focus of this article, was recognized in Ref. [4].

## 3.2 From path coupling to scaling plots

In the finite-dimensional Edwards–Anderson model, we now consider the random-share coupling for the heat-bath algorithm of Equation 7. To establish coupling, we consider two arbitrary spin configurations as initial states of the two Markov chains and apply the path-coupling argument of Section 2.2. The two configurations differ in at most $N$ sites so that we can connect them by a path of at most $N$ neighboring configurations that differ by one spin only.

Let $\boldsymbol{\sigma}^A$ and $\boldsymbol{\sigma}^B$ be two such neighboring configurations (see the lhs of Figure 2) that differ by the spin $j$. The common random element $\{k, \Upsilon\}$ of Equation 6 contains the spin $k$ to be updated and the random number $\Upsilon$ required for the heat-bath step of Equation 7. With probability $p_{1\to 0} = 1/N$, the spin $j$ is updated. The field $h_j$ is the same for $\boldsymbol{\sigma}^A$ and $\boldsymbol{\sigma}^B$, and so is $\Upsilon$ in Equation 7. It follows that the distance decreases from 1 to 0 with $p_{1\to 0}$.

With probability $2d/N$, spin $l$, one of the $2d$ neighboring spins of $j$, is updated. The local fields $h_l(\boldsymbol{\sigma}^A)$ and $h_l(\boldsymbol{\sigma}^B)$ differ by exactly 2. The probability $p_{1\to 2}$ of making different decisions, which corresponds at most to the red region on the rhs of Figure 2, is at most equal to

$$\begin{aligned} p_{1\to 2} &= \frac{2d}{N} \max_h |\pi^+(h) - \pi^+(h \pm 2)| \\ &= \frac{2d}{N} [\pi^+(0) - \pi^+(-2)] = \frac{2d}{N} \left[ \frac{1}{2} - \frac{1}{1 + \exp(4\beta)} \right]. \end{aligned}$$

If $p_{1\to 0} > p_{1\to 2}$, the expected distance between $\boldsymbol{\sigma}^A$ and $\boldsymbol{\sigma}^B$ decreases after one step, for any choice of spin configuration and any choice of the couplings $\{J_{ij}\}$, which is the case at high temperature. This is also a condition where the damage caused by a single spin difference does not spread in the initial stage of the damage spreading under random-share coupling. It provides the upper bound of the damage spreading temperature. More details are discussed in Section 3.3. The limiting temperature for the application of the path-coupling argument is when $p_{1\to 0} = p_{1\to 2}$, which translates into

$$\beta_{\text{path}} = \frac{1}{4} \log \left( \frac{2d}{d-1} - 1 \right) = \frac{1}{2d} + \frac{1}{6d^3} + \frac{1}{10d^5} + \cdots,$$

and equivalently,

$$T_{\text{path}} = \frac{1}{\beta_{\text{path}}} = 2d - \frac{2}{3d} - \frac{8}{45d^3} + \cdots. \tag{8}$$

For $T > T_{\text{path}}$, we are assured of fast coupling in the Edwards–Anderson model. The argument also holds for sublattice parallel updates. As discussed, $T_{\text{path}}$ is obtained for any choice of interactions and any spin configuration. Consequently, $T_{\text{path}}$ is also the path-coupling bound for the ferromagnetic Ising model, although we know from monotonicity that fast coupling will take place down to the Curie temperature.

We now numerically evaluate the mean coupling time of the finite-dimensional Edwards–Anderson model in both two and three dimensions in view of the scaling analysis discussed in Section 2.3. The mean coupling time of the two-dimensional model was already evaluated under a random update rule, and it has been demonstrated that a dynamical phase transition occurs in

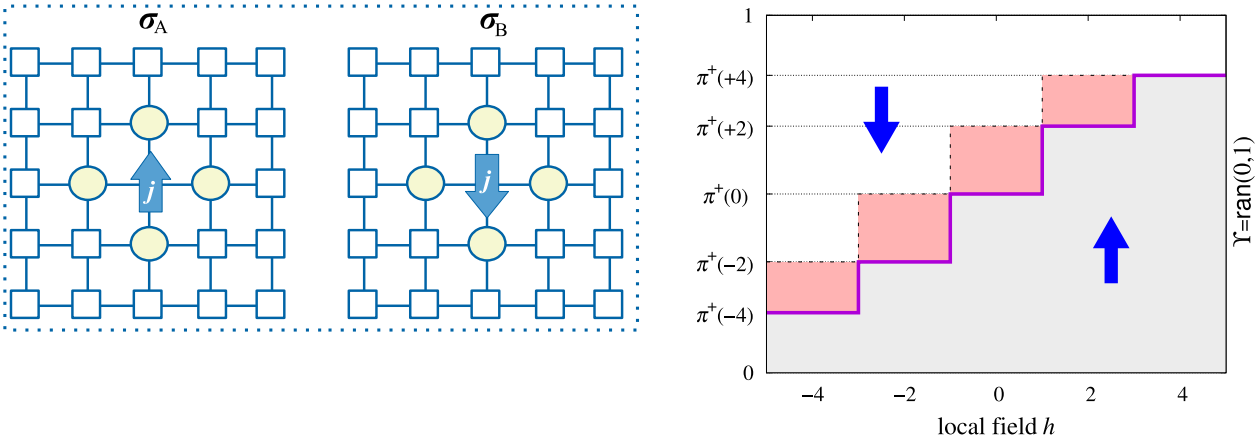


FIGURE 2
*Left*: Two spin configurations, $\boldsymbol{\sigma}^A$ and $\boldsymbol{\sigma}^B$, which differ at a single site indicated by arrows. The sites connected to it are marked with circles, and the sites connected to them are marked by squares, which represent arbitrary states, either up or down, that are common to both configurations. *Right*: The probability $\pi^+(h)$ of the next spin state being "up"(+) in the heat-bath algorithm for a two-dimensional Ising model, as a function of the local field $h$, following the form $\pi^+(h)$ of Equation 7. The next state becomes "up" if a random number ϒ falls within the gray region. The red region represents conditions where two spins, which differ by a local field of 2, result in different next states.

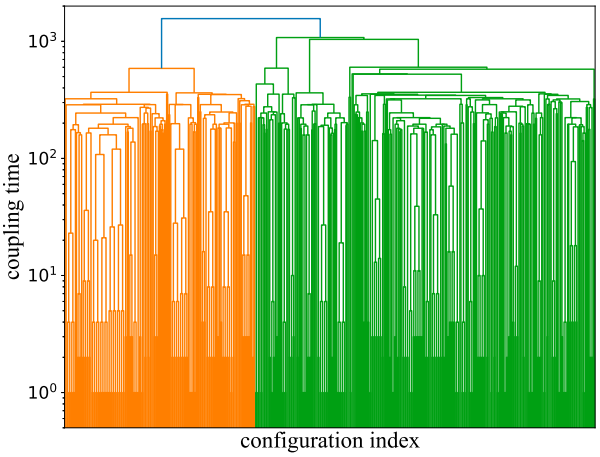


FIGURE 3
Dendrogram of configurations in the partial-survey approximation for the three-dimensional Edwards–Anderson model with parallel updates at $T = 3.90 \gtrsim T_{\text{coup}}$ and with $\mathcal{N}_0 = 512$. Any starting set with representative configurations in the two main branches (*orange*, *green*) gives the same coupling time, explaining the success of the partial survey.

which the size dependence of the coupling time qualitatively changes [4], confirming earlier results [14]. The mean coupling time results presented below are evaluated using the partial-survey approximation with the number $\mathcal{N}_0$ of randomly chosen initial conditions. The results obtained with different values of $\mathcal{N}_0$ are plotted at each data point, but they are completely contained within the size of the markers, thereby confirming that they are independent of $\mathcal{N}_0$. A dendrogram representation explains the independence of the mean coupling time of $\mathcal{N}_0$ (see Figure 3).

All the figures shown below represent results averaged over 4,096 realizations of interactions, independent of $N$, with error bars indicating sample fluctuations from these realizations. The first results for the three-dimensional Edwards–Anderson model are presented in the two panels of Figure 4, which show the estimated mean coupling time for the partial-survey approximation under the parallel and random updates. Although the two updates differ in the high-temperature limit, both exhibit a $N \log N$ behavior for system size $N$ at sufficiently high but finite temperatures. As the temperature decreases, the behavior of the $N$ dependence of the mean coupling time changes from slow to fast increase at a certain temperature. There is a slight, yet significant, difference in the transition temperature between the two updates, with a lower transition temperature observed for the parallel updates. This illustrates that coupling has no direct thermodynamic significance.

Figure 5 presents finite-size scaling plots of the mean coupling time for the three-dimensional Edwards–Anderson model, comparing both the parallel and random updates. The plot demonstrates that the scaling works well when the appropriate scaling parameters are chosen. This is consistent with the above argument that the transition temperatures, $T_{\text{coup}}$ or $\beta_{\text{coup}}$, are significantly different for the two update rules. In contrast, the precision of the scaling exponents, $\phi$ and $\omega$, is not as precise as that of the transition temperature, and it can be considered that these two rules yield almost the same values for these exponents. It remains unclear whether these exponents have a meaning analogous to the critical exponents of a second-order transition. Of particular interest is the exponent $\omega$, which represents the divergence of the characteristic scale as it approaches the transition temperature. Our results suggest that this exponent has the same value on both the high- and low-temperature sides of the transition temperature. This is comparable to the correlation length exponent.

An analogous scaling analysis for the two-dimensional Edwards–Anderson model is shown in Figure 6. The left panel is the analysis result of our own numerical simulations using the sublattice parallel update, while the right panel presents the scaling analysis based on numerical data using the random update from [4]. In both

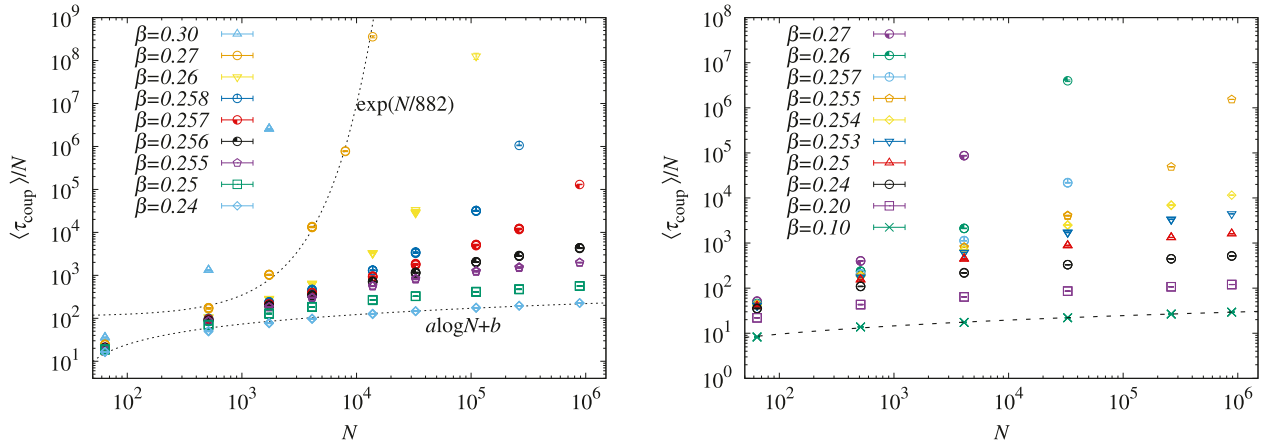


FIGURE 4
System-size $N$ dependence of the mean coupling time at various inverse temperatures in the three-dimensional Edwards–Anderson model. *Left*: Parallel update. *Right*: Random update.

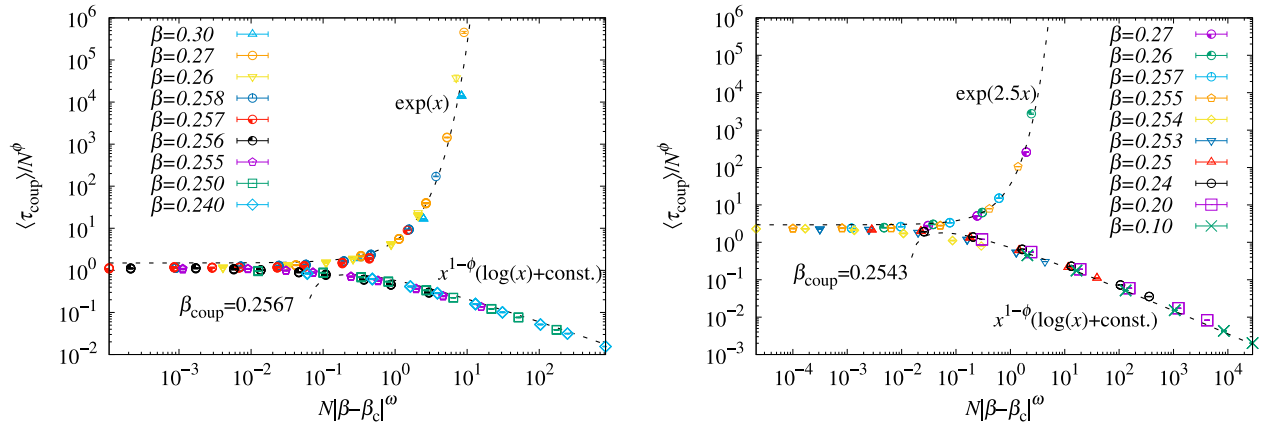


FIGURE 5
Finite-size scaling plot of the mean coupling time in the three-dimensional Edwards–Anderson model. *Left*: Parallel updates ($\omega \simeq 1.7$, $\phi \simeq 1.7$, and $\beta_{\mathrm{coup}} \simeq 0.2567$). *Right*: Random updates ($\omega \simeq 1.84$, $\phi \simeq 1.70$, and $\beta_{\mathrm{coup}} \simeq 0.2543$). Two dotted lines in each panel represent the expected high- and low-temperature asymptotic forms of the scaling function.

cases, the scaling is consistent with a phase transition in the mean coupling time. As observed in the three-dimensional model, $T_{\mathrm{coup}}$ depends on the underlying Markov chain, with a lower transition temperature for the parallel update. The scaling exponents depend on the dimensionality. However, the proper scaling variable may not be the number of spins, $N$, used here, but rather the linear dimension $L$. This suggests that the value of the exponents may depend on the dimensionality through the relationship $N = L^d$.

## 3.3 Path coupling and damage spreading for spin glasses

Table 1 summarizes the key temperatures discussed in previous sections, including $T_{\mathrm{path}}$ and $T_{\mathrm{coup}}$, as well as previously estimated results for $T_{\mathrm{SG}}$ and $T_{\mathrm{Griffiths}}$. This table demonstrates the differences in transition temperatures for both two- and three-dimensional Edwards–Anderson models, providing a detailed overview of the coupling and spin-glass transitions.

On the one hand, path coupling demonstrates that above $T_{\mathrm{path}}$, the uniform contraction between neighboring configurations leads to fast coupling. Below $T_{\mathrm{path}}$, there are spins $k$ (for example, those with $h_k = 0$) for which, at least initially, there is no such contraction. Nevertheless, as our numerical simulations show, fast $N$ log $N$ coupling also takes place in the window $T_{\mathrm{coup}} < T < T_{\mathrm{path}}$. The absence of a regime change at $T_{\mathrm{path}}$ can be illustrated, in the language of damage spreading, by following the mean damage as a function of time for two configurations that initially, at time $t = 0$, are neighboring. Above $T_{\mathrm{path}}$, the mean damage decreases exponentially for all times (see inset of Figure 7), whereas for $T < T_{\mathrm{coup}}$, it increases rapidly. In the window $T_{\mathrm{coup}} \lesssim T \lesssim T_{\mathrm{path}}$, the mean damage initially increases, as expected, but then turns around and again vanishes exponentially. This turning point seems to occur when the damage reaches a certain size, which grows as the temperature

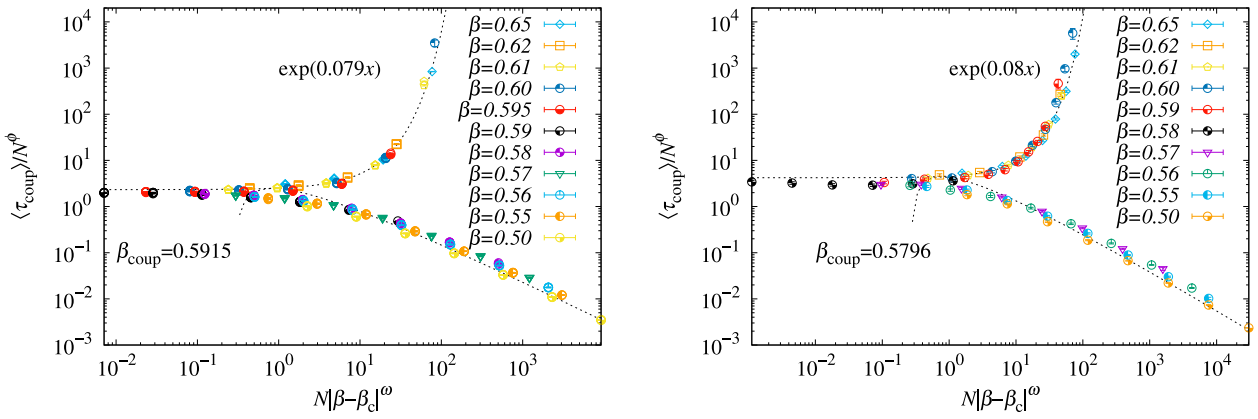


FIGURE 6
Finite-size scaling plot of the mean coupling time in the two-dimensional Edwards–Anderson model. *Left*: Parallel update (our simulations). The obtained parameters are $\omega \simeq 1.4$, $\phi \simeq 1.95$, and $\beta_{\text{coup}} \simeq 0.5915$. *Right*: Random updates (original data of Ref. [4]). The obtained parameters are $\omega \simeq 1.4$, $\phi \simeq 1.95$, and $\beta_{\text{coup}} \simeq 0.5796$. Two dotted lines in each panel represent the expected high- and low-temperature asymptotic forms of the scaling function.

TABLE 1 Spin-glass transition and coupling temperatures for the Edwards–Anderson model in two and three dimensions. $T_{\text{SG}}$ is the numerical estimate from Refs. [3, 30] in three dimensions and is expected [8, 34] to vanish in two dimensions. $T_{\text{coup}}$ is from Figures 5, 6, and $T_{\text{Griffiths}}$ is the Curie temperature of the ferromagnetic Ising model. Finally, $T_{\text{path}}$ is from Equation 8.

| Dimension $d$ | $T_{\text{SG}}$ | $T_{\text{coup}}$ (parallel) | $T_{\text{coup}}$ (random) | $T_{\text{Griffiths}}$ | $T_{\text{path}}$ |
|---|---|---|---|---|---|
| 2 | 0 | 1.69… | 1.72… | 2.269… | 3.640… |
| 3 | 1.1019 – 1.1090 | 3.89… | 3.93… | 4.51… | 5.770… |

approaches $T_{\text{coup}}$. This behavior can be understood in analogy with the characteristic diverging scale $N^*(\beta)$ in the finite-size scaling analysis of Equation 5, which suggests a picture similar to a critical phase transition, where the threshold damage size corresponds to the diverging scale near $T_{\text{coup}}$.

## 4 Coupling in hard spheres

In this section, we examine coupling for the hard-sphere system of statistical mechanics. For concreteness, we concentrate on the two-dimensional hard-disk model, which was the object of the historically first study using Markov chains [43]. The model has created an unabating series of works in mathematics, physics, and chemistry [40]. After an introduction to the model and to the Metropolis algorithm [35] that we will mostly consider, we review the very few known exact results on the model (Section 4.1) and then move on to the analysis of path coupling (Section 4.2) and to numerical calculations leading up to our scaling analysis. We finally discuss, following Ref. [32], what, precisely, the behavior of the algorithm teaches us about the physics of the hard-disk model (Section 4.3).

The model describes $N$ disks of radius $\sigma$ in a rectangular box with periodic boundary conditions. For simplicity, we assume the box to be a square of side length $L$. The center position of disk $k$ is given by $\mathbf{x}_k = (x_k, y_k)$ and in a "legal" configuration, any two disks cannot overlap (get closer than $2\sigma$), periodic boundary conditions being accounted for. The sample space $\Omega$ is now continuous, and the

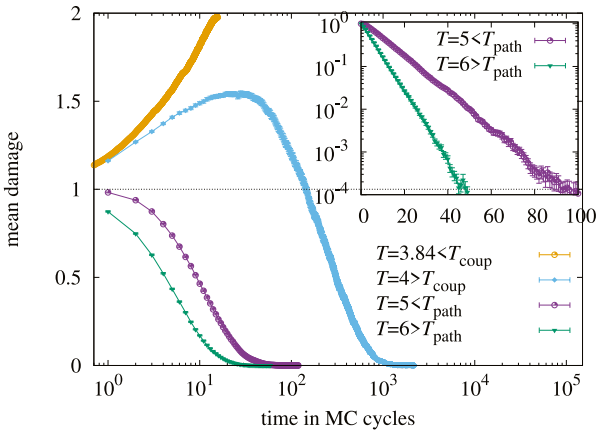


FIGURE 7
Damage evolution over time for two states differing by a Hamming distance of 1 as initial conditions in random updates of the three-dimensional Edwards–Anderson model. The size is $N = 64^3$, and the four temperatures shown are above and below both $T_{\text{path}}$ and $T_{\text{coup}}$. The inset shows the same plot on a semi-log scale.

statistical weight of a configuration $\mathbf{X} = \{\mathbf{x}_1, \ldots, \mathbf{x}_N\}$ is given by

$$\pi(\mathbf{X}) = \begin{cases} 1 & \text{if } \mathbf{X} \text{ is legal} \\ 0 & \text{else} \end{cases},$$

where, for simplicity, we have omitted the Cartesian $2N$-dimensional measure. The control parameter of this model is the density $\eta = N\pi\sigma^2/L^2$, the fraction of occupied space to the volume of the box.

We consider the "global" Metropolis algorithm: At each time step, and starting from a configuration $\mathbf{X}(t) = \{\mathbf{x}_1, \ldots, \mathbf{x}_N\}$, one random disk $k$ among the $N$ disks is sampled. A move of disk $k$ from $\mathbf{x}_k$ to a random position inside the simulation box $\mathbf{x}'_k = [\mathtt{ran}(0,L), \mathtt{ran}(0,L)]$ is attempted. If the configuration $\mathbf{X}'$, in which $\mathbf{x}$ is replaced by $\mathbf{x}'$ is legal, the move is accepted and otherwise rejected:

$$\mathbf{X}(t+1) = \begin{cases} \{\mathbf{x}_1, \ldots, \mathbf{x}_{k-1}, \mathbf{x}'_k, \mathbf{x}_{k+1}, \ldots, \mathbf{x}_N\} & \text{if legal} \\ \mathbf{X}(t) & \text{otherwise} \end{cases}.$$

Here, the new position is chosen within a square-shaped periodic window of length $L$ around the current position, whereas in the local Metropolis algorithm, the window size usually has a length on the scale of the inter-particle distance [36].

The random-share coupling for the global Metropolis algorithm uses the following random element:

$$\Upsilon_t = \{k, \mathbf{x}' = \{x, y\}\} = \{\underbrace{\mathtt{nran}(1,N)}_{\text{particle index } k}, \underbrace{\{\mathtt{ran}(0,L), \mathtt{ran}(0,L)\}}_{\text{proposed position } \mathbf{x}'=\mathbf{x}_k(t+1)}\}. \quad (9)$$

This coupling has been considerably refined [31, 32].

## 4.1 Rigorous results for the thermodynamics of hard spheres

Rigorous results on hard-disk (and hard-sphere) models are very few. It is known that the close-packing density $\eta = \pi/(2\sqrt{3})$ in two dimensions is characterized by the hexagonal packing [24]. It thus corresponds to an essentially unique configuration that has long-range orientational and positional order. For densities below the close-packing density, the absence of long-range positional order was established rigorously [50] so that there is no crystal (with long-range orientational and positional order) below close packing. Indications for a phase transition were first found in the 1960s [1, 40]. The existence of two phase transitions and of three phases (liquid, hexatic, and solid) as a function of density is now well accepted [5, 40]. As in the Edwards–Anderson model (where the temperature $T$ replaces the inverse of the density $\eta$ as a control parameter), a rigorous proof of a transition away from close packing is still lacking. At low finite densities, the convergence of the virial expansion was proven early on [38], establishing the existence of the liquid phase. It extends up to a density $\eta = 0.70$ and is followed by a window of coexisting liquid and hexatic regions (see Table 2 below).

## 4.2 Path coupling and scaling plots for hard disks

We now consider path coupling for hard disks, using the random map based on Equation 9 and a Hamming metric that counts the number of different disk positions in any two configurations. Let $\mathbf{X}^A$ and $\mathbf{X}^B$ be two neighboring hard-disk configurations that differ in the position of disk $j$ only (see Figure 8). Simplifying a coupling from Ref. [35], we use as the common random element $\{k, \Upsilon\}$ the

TABLE 2 Densities in the hard-disk system (see Equation 1 of Ref. [40]) for common definitions of densities). The homogeneous liquid phase empirically extends to a density of 0.70. The homogeneous hexatic phase is from 0.716 to 0.72. The density range from 0.70 to 0.716 corresponds to phase separation.

| Quantity | Density | Comment |
|---|---|---|
| $\eta_{\text{LP}}$ | 0.03619 | Convergence of virial expansion, historic first [38] |
| $\eta_{\text{path}}$ | 1/12 = 0.083 | Naive path-coupling density (Equation 12) |
| … | 1/8 = 0.125 | Improved path-coupling [35] |
| … | 0.154 | Path coupling, optimized metric [31] |
| … | 1/6 = 0.166 | Improved coupling of Ref. [32] |
| $\eta_{\text{coup}}$ | 0.128 | Empirical coupling density (Figure 9) |
| … | 0.29 | Empirical birth–death coupling density [4, 56] |
| $\eta_{\text{liquid–hex}}$ | 0.70 – 0.716 | Liquid–hexatic coexistence [1, 5] |
| $\eta_{\text{hex–solid}}$ | 0.72 | Hexatic–solid phase transition [5] |
| $\eta_{\text{pack}}$ | $\pi/(2\sqrt{3})$ = 0.907 | Close-packing crystal |

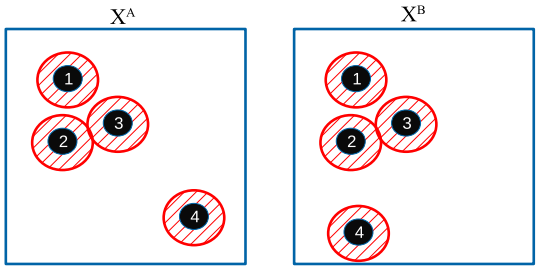


FIGURE 8
Hard-disk configurations, differing only in disk $j = 4$. Under the random-share coupling, the difference disappears if the disk $j$ is moved to a position outside the "halo" of other disks (see Equation 10). It is increased to two if the move of disk $k \neq j$ would overlap with $j$ in only one of the configurations (see Equation 11). Disks of radius $\sigma$ are shown with their $2\sigma$ halos.

disk $k$ to be updated and its new position, both identical for $\mathbf{X}^A$ and $\mathbf{X}^B$. With probability $1/N$, the disk $j$ is moved (that is, $k = j$). The move is accepted in both configurations if it stays away (by $2\sigma$) from the "halo" of all remaining disks in both configurations. This yields the probability of decreasing the Hamming distance from 1 to 0:

$$p_{1\to 0} \geq \frac{1}{N}\left(1 - \frac{N-1}{N} 4\eta\right). \quad (10)$$

On the other hand, the Hamming distance can be increased from 1 to 2 if a disk different from $j$ is moved less than $2\sigma$ away (that is, into the halo), of disk $j$ in one configuration but not in the other. The probability of increasing the Hamming distance from one to two can thus be bounded as:

$$p_{1\to 2} \leq \frac{N-1}{N}\left(\frac{8}{N}\eta\right), \quad (11)$$

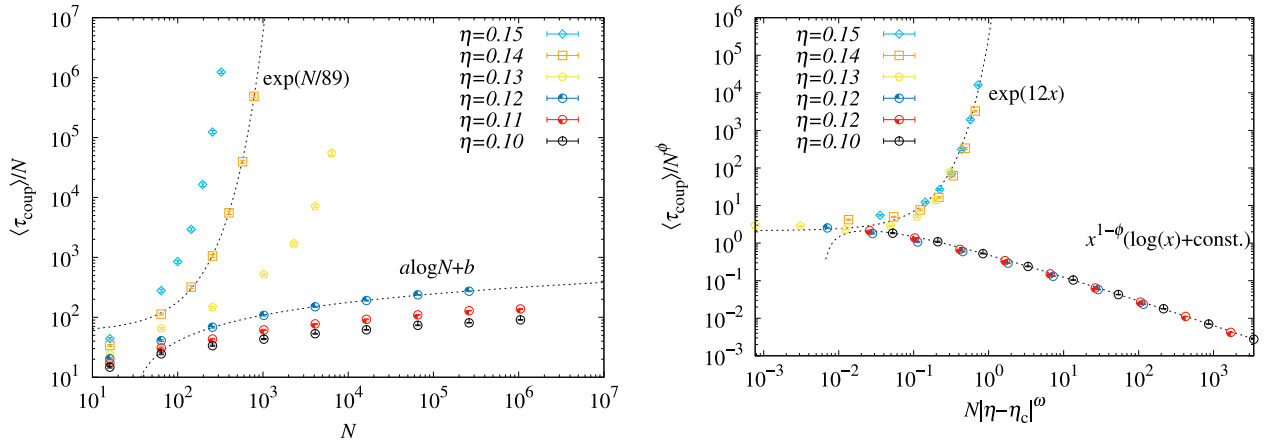


FIGURE 9
*Left*: System-size dependence of the mean coupling time at various densities in two-dimensional hard disks (data from Ref. [4]). *Right*: Finite-size scaling plot of the coupling time with parameters $\omega \simeq 1.6$, $\phi \simeq 1.75$, and $\eta_c \simeq 0.128$. The two dotted lines represent the expected high- and low-density asymptotic forms of the scaling function.

where the factor $8\eta/N$ on the rhs arises from the difference between two "halos" of area $4\pi\sigma^2$ for each of the disks $j$ in the two configurations.

Again, for $p_{1\to 0} > p_{1\to 2}$, the expected Hamming distance between $A$ and $B$ decreases after one step, for any two neighboring disk configurations, which can be assured for

$$\eta < \eta_{\text{path}} = \frac{1}{12}. \tag{13}$$

It follows [13] that the Hamming distance between configurations $A$ and $B$ that differ in the position of only one disk decreases in expectation at each step if the density is smaller than 1/12.

As with the Edwards–Anderson model, we now analyze the mean coupling time of the two-dimensional hard-disk model under the global Metropolis algorithm with the random-share coupling of Equation 9. In this case, we reanalyze the data obtained in Ref. [4], which we replot on the lhs of Figure 9. The analogous scaling ansatz again provides an excellent fit of the data. The critical exponents do not differ significantly from those found in the Edwards–Anderson model, suggesting the possibility of some underlying universality. However, uncovering the intricate physical picture behind this similarity remains an open question for future research. It should be noted that these critical exponents are not directly related to the critical phenomena of physical systems in the conventional sense. Rather, they characterize the "phase transition" in computational algorithms associated with the coupling of Markov chains. From an algorithmic perspective, these exponents are of significant interest as they provide insight into the inherent challenges in achieving fast coupling.

## 4.3 Advanced hard-disk couplings, physical implications

The coupling approach to the hard-disk system has been intensely studied in recent years, and the random-share coupling of Equation 9 only provides the simplest possible choice. A number of refined couplings have been proposed. The one proposed in Ref. [35] moves disks differently for the configuration $\mathbf{X}^A$ and $\mathbf{X}^B$ and reaches a path-coupling density of 1/8 (see Table 2 for an overview). Building on this coupling, optimizing the metric reaches a limiting density of 0.154, which was later improved for a different algorithm to 1/6. In addition to these rigorous bounds, numerical evidence for the birth–death algorithm [56] points to a coupling density of ~0.3 [4]. These densities, and especially the rigorously proven ones, are still quite far from the "empirical" transition density $\eta \sim 0.70$ of the liquid phase, which was only in recent years understood to be toward a hexatic, and which bounds on a region $\eta \in [0.7, 0.76]$ without a homogeneous solution, and then giving rise to a mixture of the hexatic and the liquid.

The crucial connection between fast coupling (thus, fast mixing) and physical ordering was made for the hard-sphere case in Ref. [32], where it was proven that $O(N \log N)$ random steps of the global Metropolis algorithm are insufficient to construct configurations with any kind of long-range order. Fast mixing of a single-particle algorithm, even a non-local one, thus implies that the resulting configuration (which is practically in equilibrium) has exponential spatial correlation functions. This, to all intents and purposes, shows the extension of the liquid phase. We believe that it does not, however, prove the convergence of the virial expansion [38] because of the possibility of a liquid–liquid phase transition, which cannot be captured in a mixing-time argument.

# 5 Conclusion

In this article, we have discussed the computational aspects of two of the most challenging models in statistical physics, namely, the Edwards–Anderson model and the hard-disk model. In both these models, there are almost no rigorous results about the phase transitions in non-trivial physical dimensions, that is, above two dimensions for the spin model and above one dimension (away

from close packing) for the particle system. Further connections are that the computational algorithms are mostly derivatives of the local-move heat-bath or Metropolis algorithm in both cases. Cluster algorithms have been developed for both systems [21, 34], but they have not really been useful in the physically interesting dimensions. Finally, the two models are united by the fact that they are truly challenging in their physical interpretation: For the Edwards–Anderson model, for a long time, even empirically, there was only a very rough agreed-on value of the transition temperature from the high-temperature paramagnetic phase, which was considerably sharpened in recent times only (see Table 1). No agreement has been reached on the nature of the low-temperature phase. For the hard-disk model, the now agreed-on transition scenario [5] was proposed only a decade ago, after more than 50 years of intense simulation. In that model, even the simplest algorithm, the local Metropolis algorithm, faces extreme challenges, as its irreducibility and ergodicity cannot be guaranteed in the constant-volume ensemble [11, 33].

In this context, the coupling approach provides an interesting yet incomplete view of the high-temperature/low-density phases. In the Edwards–Anderson model, one can easily establish the existence of a path-coupling temperature (see Equation 8), which we think provides a rigorous upper bound for the extension of the paramagnetic phase. For the hard-disk model, the program has been followed through completely, and the coupling result is the currently best lower bound for the extension of the liquid phase. It is fascinating how a result on the speed of a Monte Carlo algorithm can be derived from the behavior of two Markov chains (that is, from coupling) and can then be turned into a statement on the phase behavior. This fascination was sensed early on in the literature on damage spreading that, as we discussed, naturally connects to the path-coupling approach.

Damage spreading has created an extensive literature in physics, but, as we pointed out, that literature has concentrated on the specific random-share protocol, which gives the very low bounding density of Equation 12 when translated to the hard-disk context. In particle systems, there has been much progress from improved couplings and optimized metrics (see Table 2), which we hope can be ported to spin glasses and, more generally, to disordered systems. It would be interesting to see whether our scaling approach can be applied to these more advanced couplings.

## Data availability statement

The raw data supporting the conclusions of this article will be made available by the authors, without undue reservation.

## Author contributions

KH: writing–original draft and writing–review and editing. WK: writing–original draft and writing–review and editing.

## Funding

The author(s) declare that financial support was received for the research, authorship, and/or publication of this article. This research was supported by a grant from the Simons Foundation (Grant 839534, MET). This work was also supported by JSPS KAKENHI Grant Nos. 23H01095, and JST Grant Number JPMJPF2221. This research was conducted within the context of the International Research Project "*Non-Reversible Markov chains, Implementations and Applications.*"

## Acknowledgments

We thank J. L. Lebowitz for an inspiring discussion. KH would like to thank the Ecole Normale Supérieure, ENS, for their kind hospitality during a research stay, which provided a productive environment and variable support for the completion of this work. The authors thank the Supercomputer Center, the Institute for Solid State Physics, and the University of Tokyo for the use of the facilities.

## Conflict of interest

The authors declare that the research was conducted in the absence of any commercial or financial relationships that could be construed as a potential conflict of interest.

## Generative AI statement

The author(s) declare that no Generative AI was used in the creation of this manuscript.

## Publisher's note



## References

1. Alder BJ, Wainwright TE. Phase transition in elastic disks. *Phys Rev* (1962) 127:359–61. doi:10.1103/PhysRev.127.359

2. Aldous D, Diaconis P. Shuffling cards and stopping times. *The Am Math Monthly* (1986) 93:333–48. doi:10.2307/2323590

3. Baity-Jesi M, Baños RA, Cruz A, Fernandez LA, Gil-Narvion JM, Gordillo-Guerrero A, et al. Critical parameters of the three-dimensional Ising spin glass. *Phys Rev B* (2013) 88:224416. doi:10.1103/PhysRevB.88.224416

4. Bernard EP, Chanal C, Krauth W. Damage spreading and coupling in Markov chains. *EPL (Europhysics Letters)* (2010) 92:60004. doi:10.1209/0295-5075/92/60004

5. Bernard EP, Krauth W. Two-step melting in two dimensions: first-order liquid-hexatic transition. *Phys Rev Lett* (2011) 107:155704. doi:10.1103/PhysRevLett.107.155704

6. Berretti A. Some properties of random Ising models. *J Stat Phys* (1985) 38:483–96. doi:10.1007/BF01010473

7. Bhatt RN, Young AP. Search for a transition in the three-dimensional ±*J* Ising spin-glass. *Phys Rev Lett* (1985) 54:924–7. doi:10.1103/PhysRevLett.54.924

8. Bhatt RN, Young AP. Numerical studies of Ising spin glasses in two, three, and four dimensions. *Phys Rev B* (1988) 37:5606–14. doi:10.1103/PhysRevB.37.5606

9. Bieche L, Uhry JP, Maynard R, Rammal R. On the ground states of the frustration model of a spin glass by a matching method of graph theory. *J Phys A: Math Gen* (1980) 13:2553–76. doi:10.1088/0305-4470/13/8/005

10. Boettcher S. Stiffness of the Edwards-Anderson model in all dimensions. *Phys Rev Lett* (2005) 95:197205. doi:10.1103/PhysRevLett.95.197205

11. Böröczky K. Über stabile Kreis-und Kugelsysteme. *Ann Univ Sci Budapest Eötvös Sect Math* (1964) 7:79–82.

12. Bray AJ, Moore MA. Lower critical dimension of Ising spin glasses: a numerical study. *J Phys C: Solid State Phys* (1984) 17:L463–8. doi:10.1088/0022-3719/17/18/004

13. Bubley R, Dyer M. Path coupling: a technique for proving rapid mixing in Markov chains. In: 2013 IEEE 54th Annual Symposium on Foundations of Computer Science, Los Alamitos, CA, USA: IEEE Computer Society (1997). 223.

14. Campbell I, de Arcangelis L. On the damage spreading in Ising spin glasses. *Physica A: Stat Mech its Appl* (1991) 178:29–43. doi:10.1016/0378-4371(91)90073-l

15. Chanal C, Krauth W. Renormalization group approach to exact sampling. *Phys Rev Lett* (2008) 100:060601. doi:10.1103/PhysRevLett.100.060601

16. Chanal C, Krauth W. Convergence and coupling for spin glasses and hard spheres. *Phys Rev E* (2010) 81:016705. doi:10.1103/PhysRevE.81.016705

17. Creutz M. Monte Carlo study of quantized SU(2) gauge theory. *Phys Rev D* (1980) 21:2308–15. doi:10.1103/PhysRevD.21.2308

18. Derrida B, Weisbuch G. Dynamical phase transitions in 3-dimensional spin glasses. *EPL* (1987) 4:657–62. doi:10.1209/0295-5075/4/6/004

19. Ding J, Lubetzky E, Peres Y. The mixing time evolution of Glauber dynamics for the mean-field Ising model. *Commun Math Phys* (2009) 289:725–64. doi:10.1007/s00220-009-0781-9

20. Doeblin W. Exposé de la Théorie des chaînes simples constantes de Markoff à un nombre fini d'états. *Rev Math Union Interbalkanique* (1938) 2:77.

21. Dress C, Krauth W. Cluster algorithm for hard spheres and related systems. *J Phys A: Math Gen* (1995) 28:L597–L601. doi:10.1088/0305-4470/28/23/001

22. Dyer M, Sinclair A, Vigoda E, Weitz D. Mixing in time and space for lattice spin systems: a combinatorial view. *Random Struct Algorithms* (2004) 24:461–79. doi:10.1002/rsa.20004

23. Edwards SF, Anderson PW. Theory of spin glasses. *J Phys F: Metal Phys* (1975) 5:965–74. doi:10.1088/0305-4608/5/5/017

24. Fejes L. Über einen geometrischen Satz. *Mathematische Z* (1940) 46:83–5. doi:10.1007/BF01181430

25. Fröhlich J, Imbrie JZ. Improved perturbation expansion for disordered systems: beating Griffiths singularities. *Commun Math Phys* (1984) 96:145–80. doi:10.1007/BF01240218

26. Geman S, Geman D. Stochastic relaxation, Gibbs distributions, and the Bayesian restoration of images. *IEEE Trans Pattern Anal Mach Intell* (1984) PAMI-6:721–41. doi:10.1109/tpami.1984.4767596

27. Glauber RJ. Time-dependent statistics of the Ising model. *J Math Phys* (1963) 4:294–307. doi:10.1063/1.1703954

28. Griffeath D. A maximal coupling for Markov chains. *Z fr¨ Wahrscheinlichkeitstheorie Verwandte Gebiete* (1975) 31:95–106. doi:10.1007/bf00539434

29. Griffiths RB. Nonanalytic behavior above the critical point in a random Ising ferromagnet. *Phys Rev Lett* (1969) 23:17–9. doi:10.1103/PhysRevLett.23.17

30. Hasenbusch M, Pelissetto A, Vicari E. Critical behavior of three-dimensional Ising spin glass models. *Phys Rev B* (2008) 78:214205. doi:10.1103/PhysRevB.78.214205

31. Hayes TP, Moore C. Lower bounds on the critical density in the hard disk model via optimized metrics. *arXiv:1407.1930* (2014). doi:10.48550/arXiv.1407.1930

32. Helmuth T, Perkins W, Petti S. Correlation decay for hard spheres via Markov chains. *The Ann Appl Probab* (2022) 32. doi:10.1214/21-aap1728

33. Höllmer P, Noirault N, Li B, Maggs AC, Krauth W. Sparse hard-disk packings and local Markov chains. *J Stat Phys* (2022) 187:31. doi:10.1007/s10955-022-02908-4

34. Houdayer J. A cluster Monte Carlo algorithm for 2-dimensional spin glasses. *The Eur Phys J B - Condensed Matter Complex Syst* (2001) 22:479–84. doi:10.1007/PL00011151

35. Kannan R, Mahoney MW, Montenegro R. Rapid mixing of several Markov chains for a hard-core model. *Proc 14th Annual ISAAC (Springer, Berlin, Heidelberg), Lecture Notes Computer Sci* (2003) 663–75. doi:10.1007/978-3-540-24587-2_68

36. Krauth W. *Statistical mechanics: algorithms and computations*. Oxford University Press (2006).

37. Landau D, Binder K. *A guide to Monte Carlo simulations in statistical physics*. Cambridge University Press (2013).

38. Lebowitz JL, Penrose O. Convergence of virial expansions. *J Math Phys* (1964) 5:841–7. doi:10.1063/1.1704186

39. Levin DA, Peres Y, Wilmer EL. *Markov chains and mixing times*. American Mathematical Society (2008).

40. Li B, Nishikawa Y, Höllmer P, Carillo L, Maggs AC, Krauth W. Hard-disk pressure computations—a historic perspective. *J Chem Phys* (2022) 157:234111. doi:10.1063/5.0126437

41. Martinelli F. Lectures on Glauber dynamics for discrete spin models. In: P Bernard, editor *Lectures on Probability Theory and Statistics: Ecole d'Eté de Probabilités de Saint-Flour XXVII - 1997*. Berlin, Heidelberg: Springer Berlin Heidelberg (1999). p. 93–191.

42. McMillan WL. Domain-wall renormalization-group study of the three-dimensional random Ising model. *Phys Rev B* (1984) 30:476–7. doi:10.1103/PhysRevB.30.476

43. Metropolis N, Rosenbluth AW, Rosenbluth MN, Teller AH, Teller E. Equation of state calculations by fast computing machines. *J Chem Phys* (1953) 21:1087–92. doi:10.1063/1.1699114

44. Mezard M, Parisi G, Virasoro M. Spin glass theory and beyond. *World Scientific* (1986). doi:10.1142/0271

45. Nattermann T, Villain J. Random-field ising systems: a survey of current theoretical views. *Phase Transitions* (1988) 11:5–51. doi:10.1080/01411598808245480

46. Ogielski AT. Dynamics of three-dimensional Ising spin glasses in thermal equilibrium. *Phys Rev B* (1985) 32:7384–98. doi:10.1103/PhysRevB.32.7384

47. Ogielski AT, Morgenstern I. Critical behavior of three-dimensional Ising spin-glass model. *Phys Rev Lett* (1985) 54:928–31. doi:10.1103/PhysRevLett.54.928

48. Propp JG, Wilson DB. Exact sampling with coupled Markov chains and applications to statistical mechanics. *Random Structures and Algorithms* (1996) 9:223–52. doi:10.1002/(sici)1098-2418(199608/09)9:1/2<223::aid-rsa14>3.3.co;2-r

49. Randall D, Winkler P. Mixing points on an interval. In: C Demetrescu, R Sedgewick, R Tamassia, editors. *Proceedings of the seventh workshop on algorithm engineering and experiments and the second workshop on analytic algorithmics and combinatorics, ALENEX/ANALCO 2005*. Vancouver, BC, Canada: SIAM (2005). p. 218–21.

50. Richthammer T. Lower bound on the mean square displacement of particles in the hard disk model. *Commun Math Phys* (2016) 345:1077–99. doi:10.1007/s00220-016-2584-0

51. Franz S, Parisi G, Virasoro MA. Interfaces and lower critical dimension in a spin glass model. *J Phys France* (1994) 4:1657–67. doi:10.1051/jp1:1994213

52. Sherrington D, Kirkpatrick S. Solvable model of a spin-glass. *Phys Rev Lett* (1975) 35:1792–6. doi:10.1103/PhysRevLett.35.1792

53. Stanley HE, Stauffer D, Kertész J, Herrmann HJ. Dynamics of spreading phenomena in two-dimensional Ising models. *Phys Rev Lett* (1987) 59:2326–8. doi:10.1103/PhysRevLett.59.2326

54. Talagrand M. Spin glasses: a challenge for mathematicians: cavity and mean field models. In: *Ergebnisse der Mathematik und ihrer Grenzgebiete. 3. Folge A Series of Modern Surveys in Mathematics*. Springer (2003).

55. Thomas CK, Middleton AA. Exact algorithm for sampling the two-dimensional Ising spin glass. *Phys Rev E* (2009) 80:046708. doi:10.1103/PhysRevE.80.046708

56. Wilson DB. How to couple from the past using a read-once source of randomness. *Random Structures and Algorithms* (2000) 16:85–113. doi:10.1002/(SICI)1098-2418(200001)16:1⟨85::AID-RSA6⟩3.0.CO;2-H

# Frontiers in Physics

**Investigates complex questions in physics to understand the nature of the physical world**

Addresses the biggest questions in physics, from macro to micro, and from theoretical to experimental and applied physics.

## Discover the latest Research Topics

See more →

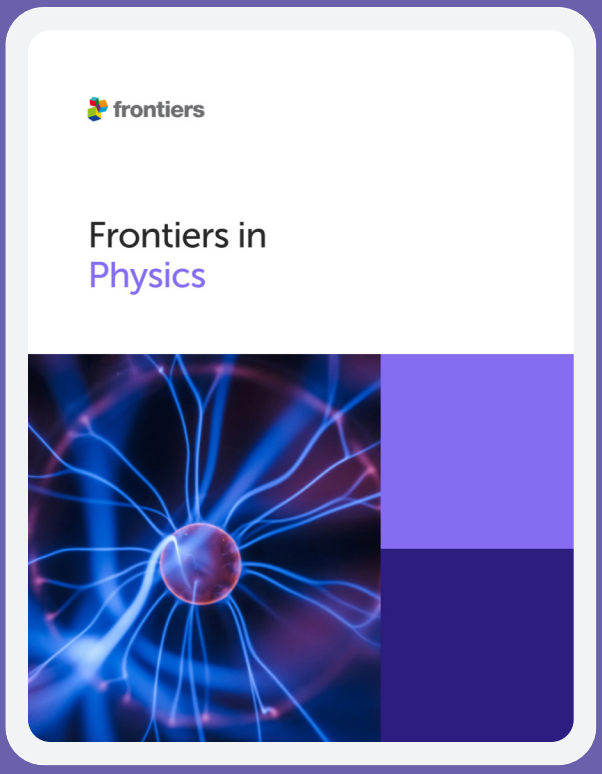


**Frontiers**

Avenue du Tribunal-Fédéral 34
1005 Lausanne, Switzerland
frontiersin.org

**Contact us**

+41 (0)21 510 17 00
frontiersin.org/about/contact